Doctoral Dissertations   Student Scholarship

Winter 2014

FULL-WAVEFORM AND DISCRETE-RETURN LIDAR IN SALT MARSH ENVIRONMENTS: AN ASSESSMENT OF BIOPHYSICAL PARAMETERS, VERTICAL UNCERTATINTY, AND NONPARAMETRIC DEM CORRECTION

Jeffrey Nickerson Rogers
University of New Hampshire, Durham

Follow this and additional works at: https://scholars.unh.edu/dissertation

FULL-WAVEFORM AND DISCRETE-RETURN LIDAR IN SALT MARSH
ENVIRONMENTS: AN ASSESSMENT OF BIOPHYSICAL PARAMETERS, VERTICAL
UNCERTATINTY, AND NONPARAMETRIC DEM CORRECTION

BY

JEFFREY N. ROGERS

B.A. Boston University, 1996

M.S. University of Maine, Orono, 1999

DISSERTATION

Submitted to the University of New Hampshire

In Partial Fulfillment of

The Requirements for the Degree of

Doctor of Philosophy

In

Earth and Environmental Science

December, 2014

This dissertation has been examined and approved in partial fulfillment of the requirements for the degree of Doctor of Philosophy in Earth and Environmental Science by:

Dissertation Director, Dr. Larry G. Ward, Research Associate Professor, Department of Earth Sciences, University of New Hampshire

Dr. Susan Adamowicz, Land Management Research & Demonstration Biologist, Rachael Carson National Wildlife Refuge, Maine

Dr. David M. Burdick, Research Associate Professor, Department of Natural Resources and the Environment, University of New Hampshire

Dr. Graham Giese, Senior Scientist, Department of Marine Geology, Center for Coastal Studies, Provincetown

Dr. Mary Martin, Research Assistant Professor, Earth Systems Research Center, University of New Hampshire

Dr. Christopher Parrish, Associate Professor, School of Civil and Construction Engineering, Oregon State University

On November 18th, 2014

Original approval signatures are on file with the University of New Hampshire Graduate School.

TABLE OF CONTENTS

DEDICATION

This dissertation is dedicated to my family, Kaden, Aidric, Ellowyn and especially to Stacy for her patience and support during this 10 year journey.

ACKNOWLEDGEMENTS

LIST OF TABLES

LIST OF FIGURES

ABSTRACT

FULL-WAVEFORM AND DISCRETE-RETURN LIDAR IN SALT MARSH ENVIRONMENTS:

AN ASSESSMENT OF BIOPHYSICAL PARAMETERS, VERTICAL UNCERTATINTY, AND

NON-PARAMETRIC DEM CORRECTION

by

Jeffrey N. Rogers

University of New Hampshire, December, 2014

High-resolution and high-accuracy elevation data sets of coastal salt marsh environments are necessary to support restoration and other management initiatives, such as adaptation to sea level rise. Lidar (light detection and ranging) data may serve this need by enabling efficient acquisition of detailed elevation data from an airborne platform. However, previous research has revealed that lidar data tend to have lower vertical accuracy (i.e., greater uncertainty) in salt marshes than in other environments. The increase in vertical uncertainty in lidar data of salt marshes can be attributed primarily to low, dense-growing salt marsh vegetation. Unfortunately, this increased vertical uncertainty often renders lidar-derived digital elevation models (DEM) ineffective for analysis of topographic features controlling tidal inundation frequency and ecology. This study aims to address these challenges by providing a detailed assessment of the factors influencing lidar-derived elevation uncertainty in marshes. The information gained from this assessment is then used to: 1) test the ability to predict marsh vegetation biophysical parameters from lidar-derived metrics, and 2) develop a method for improving salt marsh DEM accuracy.

Discrete-return and full-waveform lidar, along with RTK GNSS (Real-time Kinematic Global Navigation Satellite System) reference data, were acquired for four salt marsh systems characterized by four major taxa (*Spartina alterniflora*, *Spartina patens*, *Distichlis spicata*, and *Salicornia spp*.) on Cape Cod, Massachusetts. These data were used to: 1) develop an innovative combination of full-waveform lidar and field methods to assess the vertical distribution of aboveground biomass as well as its light blocking properties; 2) investigate lidar elevation bias and standard deviation using varying interpolation and filtering methods; 3) evaluate the effects of seasonality (temporal differences between peak growth and senescent conditions) using lidar data flown in summer and spring; 4) create new products, called Relative Uncertainty Surfaces (RUS), from lidar waveform-derived metrics and determine their utility; and 5) develop and test five nonparametric regression model algorithms (MARS – Multivariate Adaptive Regression, CART – Classification and Regression Trees, TreeNet, Random Forests, and GPSM – Generalized Path Seeker) with 13 predictor variables derived from both discrete and full waveform lidar sources in order to develop a method of improving lidar DEM quality.

Results of this study indicate strong correlations for *Spartina alterniflora* (r > 0.9) between vertical biomass (VB), the distribution of vegetation biomass by height, and vertical obscuration (VO), the measure of the vertical distribution of the ratio of vegetation to airspace. It was determined that simple, feature-based lidar waveform metrics, such as waveform width, can provide new information to estimate salt marsh vegetation biophysical parameters such as vegetation height. The results also clearly illustrate the importance of seasonality, species, and lidar interpolation and filtering methods on elevation uncertainty in salt marshes. Relative uncertainty surfaces generated from lidar waveform features were determined useful in qualitative/visual assessment of lidar elevation uncertainty and correlate well with vegetation

height and presence of *Spartina alterniflora*. Finally, DEMs generated using full-waveform predictor models produced corrections (compared to ground based RTK GNSS elevations) with R^2 values of up to 0.98 and slopes within 4% of a perfect 1:1 correlation. The findings from this research have strong potential to advance tidal marsh mapping, research and management initiatives.

CHAPTER I

INTRODUCTION

Today, 10% of the world's population lives within coastal regions with elevations of less than 10 m above sea level (Fitzgerald et al. 2008). However, land area for this same geographic region is only about 4% of the total Earth's land mass (Gedan et al. 2009). With the onset of rapid global climate change in the late twentieth and early twenty-first century, ecological systems, people and our infrastructure are potentially at risk. Coastal wetland systems are particularly sensitive and vulnerable to the effects of climate change (Erwin 2009).

Predictions of sea-level rise (SLR) for the next 100 years vary dramatically from 0.33 m to 1.32 m under an intermediate emission scenario (RCP 4.5) (Horton et al. 2014). As sea level rises, vulnerability of coastal regions to flooding caused by storm surges, astronomical tides and wave damage increases dramatically (Fitzgerald et al. 2008). In addition, the normal recurrence intervals for tidal flooding and storm patterns begin to exceed thresholds set by current natural conditions, making changes to manmade coastlines necessary such as adjustments to structures like seawalls. Wetland systems are extremely vulnerable to changes in quantity and quality of water (Erwin 2009). Therefore, due to their high environmental, economic and social value, salt marsh adaption to SLR is a concern for scientists and coastal managers (Craft et al. 2009).

Whether salt marshes are sustainable largely relates to small elevation differences within the marsh surface, which can affect inundation, sedimentation, salinity, and therefore available nutrients (Morris et al. 2002). Accurate salt marsh elevations are integral to understanding almost every aspect of salt marsh science and management including inundation, resiliency, and

the ability to adapt to SLR. To best monitor salt marsh health and response to SLR, detailed topographic information on the order of centimeters is often necessary.

Present investigative methods for collecting salt marsh elevation data involve field surveys using traditional survey equipment, Real Time Kinematic Global Navigation Satellite System (RTK GNSS), aerial photography interpretation, and photogrammetry. Acquiring terrain elevation data using these methods produces accurate, but in most cases, sparse data coverage and is typically costly and time consuming due to resource intensive field work (Green et al. 1996). Data acquisition becomes even more complicated as the size of the studied system increases (Butera 1983; Bork and Su 2007). Recently, remote sensing tools have been developed that demonstrate great promise to improve salt marsh data collection (Lee and Shan 2003; Marani et al. 2003; Argitas and Yang 2006; Belluco et al. 2006; Chust et al. 2008). Lidar has been identified as one of those tools and can be used for rapid survey of storm impacts, monitoring shoreline change, restoration planning, and flood hazard assessment (Brock and Sallenger 2001) and is often proposed as a substitute for field data collection in salt marshes (Montane and Torres 2006; Schmid et al. 2011). However, vegetation-induced elevation uncertainty is an intrinsic problem with using lidar in salt marsh environments. Appendix C contains a glossary of terms related to elevation uncertainty, as used in this dissertation.

For lidar to continue to be a viable technology in salt marsh research, the observed uncertainty in elevation needs to be less than the elevation ranges significant to marsh ecology (Sadro et al. 2007). For instance, if the lidar bias from vegetative impacts is larger than the elevation range determining salt marsh inundation, species dominance, and habitat, then the technology's usefulness for salt marsh research becomes questionable. Topographic lidar uncertainty in salt marsh environments and its removal has been to date an unresolved problem

(Schmid et al. 2011; Hladik and Alber 2012; Hladik et al. 2013). In general, uncorrected lidar datasets from salt marshes have been found to be inaccurate and insufficient for use in determining inundation frequency or response to SLR (Morris et al. 2005; Rosso et al. 2006; Torres and Styles 2007; Schmid et al. 2011; Hladik and Alber 2012). However, the extent to which lidar penetrates the salt marsh canopy and the methods used to correct vegetation-induced uncertainty and bias have not been thoroughly assessed (Populus et al. 2001; Gopfert and Heipke 2006; Rosso et al. 2006; Schmid et al. 2011; Hladik and Alber 2012; Hladik et al. 2013). Insufficiently understanding lidar accuracy within salt marsh environments contributes to significant errors in salt marsh research and our inability to effectively plan for their conservation and restoration.

Research to determine the degree to which lidar penetrates salt marsh canopy has started to shed light on this subject (Populus et al. 2001; Gopfert and Heipke 2006; Rosso et al. 2006; Schmid et al. 2011; Hladik and Alber 2012; Hladik et al. 2013). For instance, salt marsh species, seasonality, stem density, vertical density, and height influence lidar signal penetration properties (Hladik and Alber 2012; Rogers et al. 2015). Large differences in growth habit and leaf structure exist between various salt marsh species, affecting lidar response. *Spartina alterniflora* has long flat tapering leaves growing up to approximately 2.0 m in height, whereas *Spartina patens* is a low growing ~0.1-0.3 m thatch with narrow rolled, linear leaves (Tiner 1987). Salt marsh canopies range from 0.1 – 2.0 m and are typically less than the round-trip distance in air of the lidar pulse and resolving threshold for multiple returns (Schmid et al. 2011). All of these vegetation attributes are likely to contribute to lidar signal error and produce point clouds with numerous single returns that resemble bare-earth surfaces.

Recently, attempts have been made to not only understand the source and magnitude of salt marsh induced bias, but to improve lidar derived salt marsh digital elevation models (DEMs) by removing or reducing vegetation induced bias. Previous efforts at developing accurate correction techniques for removing vegetation induced lidar bias from salt marsh DEMs have involved filtering/interpolation/classification methods or algebraic functions of bias based on canopy height and density coverage (Rosso et al. 2006; Wang et al. 2009; Schmid et al. 2011). Filtering and interpolation methods can be suspect because of the scarcity of true ground returns from the low, dense-growing salt marsh vegetation, as well as the potential inaccuracies introduced by the uncertain separation of the ground and vegetation returns (Sadro et al. 2007; Wang et al. 2009; Schmid et al. 2011). While correlations exist between salt marsh vegetation canopy height, percent coverage and lidar bias (Populus et al. 2001; Gopfert and Heipke 2006; Schmid et al. 2011), they do not appear to be strong enough to explain the extent of bias observed.

There have been several innovative approaches to DEM correction that utilize discrete-return lidar (DRL) data and subtraction of species specific bias estimates (Sadro et al. 2007; Hladik and Alber 2012; Hladik et al. 2013). Field mapped and multi/hyperspectral derived vegetation GIS layers have been used in combination with a site specific determination of vegetation induced bias to remove a constant, species-based bias (Hladik and Alber 2012; Hladik et al. 2013). Although this method appears superior to other interpolation and filtering methods, it seems inadequate to address the ultimate goal. Correction techniques that are based on vegetation assume 1) *a priori* knowledge of species location, which is usually unavailable, inaccurate, or requires additional flight sensors, processing and interpretation that add to time, cost and introduced errors; and 2) that each area of vegetation that requires DEM modification

has a constant correction factor across its entire extent. It has been well documented that vegetation height, and therefore lidar bias, varies continuously, even within a species, along complex environmental gradients, which would make species-based correction methods challenging to implement.

Even after considering previous research contributions, there is a critical need to better understand the physical characteristics that affect vertical lidar uncertainty in salt marshes, such that coastal scientists can develop and use lidar DEMs with confidence in salt marsh research and management. While a significant amount of work has been done with DRL systems, full waveform systems have not been fully evaluated. Most of the methods discussed in the literature for full-waveform lidar processing to estimate surface characteristics (e.g., slope, and/or radiometric properties) or forest biomass (Drake et al. 2002; Wright and Brock 2002; Nayegandhi et al. 2006; Mallet and Bretar 2009) use computationally-complex signal processing approaches such as deconvolution or decomposition (Jutzi and Stilla 2006). Only a few studies have been conducted on the use of simple shape-based waveform metrics (Adams et al. 2012; Muss et al. 2013; Parrish et al. 2014) for estimation of various biophysical parameters or uncertainty. Since each salt marsh vegetation species should affect the shape of the return differently, it may be possible to use shape-based metrics to extract vegetation information.

Organization of the Dissertation

Three separate, but related, studies were conducted and written as individual research papers. As a result of being in manuscript format, each chapter contains its own Introduction, Methods, Results, Discussion and Conclusions. Chapter II provides additional background information on salt marsh formation, relationship with tidal datums, response to sea level rise

and a discussion on lidar sensor technology that expands upon the briefer narrative included in chapters III, IV, and V.

Chapter III evaluates an adapted method of in-situ digital photography (Möller 2006) that can rapidly assess salt marsh vegetation vertical biomass density, as well its light obscuration properties. Vertical vegetation biomass density is likely to be related to its opacity and therefore provides insight into lidar penetration characteristics. These data, along with other biophysical parameters collected in the field (including physical samples and those derived from photography), were used to examine relationships among the parameters and metrics extracted from lidar waveforms. The primary focus was on *Spartina alterniflora,* but other common and dominant salt marsh species were included. The hypothesis tested was that feature-based waveform metrics such as waveform width, waveform standard deviation, and amplitude contain information that can be used to estimate salt marsh biophysical parameters including vegetation height, stem density and biomass.

Chapter IV considers lidar uncertainty observed in salt marsh environments. Uncertainty from discrete return lidar (DRL) was analyzed by season (specifically, temporal differences between peak growth and senescent conditions), vegetation species, and lidar processing (interpolation and filtering) methods. In addition, using feature-based full-waveform analysis, additional information contained in lidar waveforms was used to create relative uncertainty surfaces (RUS) to assess variation in elevation uncertainty throughout the marsh. These spatial assessments of uncertainty assist in identifying where, within the marsh, are lidar elevations most reliable/suspect and where researchers should target additional field work to improve marsh elevation data or if the areas of high (or low) uncertainty overlap areas of particular concern, such as critical habitat. Combined with the quantitative analysis of the DRL data, this

information can assist coastal managers and scientists in more effectively utilizing lidar data of salt marshes.

Chapter V investigates the potential removal of vegetation-induced bias using full-waveform lidar feature-based metrics such as waveform width and amplitude, as well as salt marsh surface characteristics such as slope and rugosity derived from the DRL. These were used as inputs into nonparametric modeling algorithms. The research also developed models without full waveform inputs using only DRL derived salt marsh surface characteristics. Vegetative zone maps were created using the same modeling parameters and a training set of known vegetation species locations. All model predictor variables were derived from lidar without *a priori* knowledge of species. The overall goal was to create models to accurately correct salt marsh lidar DEMs for vegetative lidar bias.

Chapter VI provides final conclusions and potential research directions. Additional information regarding the research is included in the appendices. Appendix A is a report on camera calibration for the apparatus developed in Chapter III. Appendix B is a discussion of the various modeling algorithms used in Chapter V.

CHAPTER II

BACKGROUND

Salt Marsh Environments

A salt marsh is a saline wetland dominated by grasses and other plants that have adapted to periodic flooding usually caused by tidal forcing (Mitsch and Gosselink 2000). They are typically found in sheltered embayments throughout middle to high latitudes where wave energy is low (Kennish 2001). Salt marshes are among the most important ecosystems on Earth, known to be very biologically productive and an integral link in coastal food webs (Mitsch and Gosselink 2000). They provide habitat and refuge for juvenile fish and crustaceans, many of which are of high economic value (Dionne et al. 1999; Gedan et al. 2009). They serve as filtering systems for runoff and tidal waters, removing excess nitrogen, which can lead to eutrophication, including toxic algal blooms (Bertness et al. 2002). Salt marshes are biological sinks for atmospheric carbon dioxide (Broome et al. 1988; Chmura et al. 2003). Also, salt marshes limit flooding to coastal communities by acting as natural storage basins and reducing shoreline erosion as they attenuate wave energy (Gedan et al. 2009). The loss of these ecosystems and the services they supply would be staggering (Peterson et al. 2008). Researchers have even attempted to quantify the "cost" per hectare per year for equivalent ecosystem services that salt marshes provide (**Table 2.1**) (Costanza et al. 1997). Salt marshes have been destroyed, damaged or degraded by historical and present human activities. In some locales as many as 80% of salt marshes that once occurred have been lost to human development (Bertness et al. 2002). Although salt marshes are now protected from direct impacts by United States federal

and state laws, indirect impacts continue to degrade tidal marshes. For example, man-made structures such as roads, bridges, undersized culverts, and earthen dikes often present barriers to tidal exchange that results in peat oxidation, subsidence and degradation of habitat value (Roman et al. 1984; Boumans et al. 2002; Baily and Pearson 2007).

Salt marshes are considered good examples of ecosystem engineering, consisting of "organisms that directly or indirectly modulate the availability of resources to other species (other than themselves) by causing state changes in biotic or abiotic materials and in doing so modify, maintain and/or create habitats" (Jones et al. 1994). Salt marsh vegetation has adapted to periodic flooding and severe stress of salinity, soil waterlogging and soil phytotoxins caused by tidal forcing (Mitsch and Gosselink 2000). Characteristic patterns of vegetation zonation that are based on the vertical elevation gradient are often exhibited by salt marshes (Zedler et al. 1999; Morris et al. 2005). Subtle changes in surface elevation often produce differences in vegetation speciation and sediment accumulation as a function of the tidal regime, marsh surface elevation, inundation duration, and plant species competition (**Figure 2.1**) (Reed 2002; Shuman and Ambrose 2003; Silvestri et al. 2003; Konisky and Burdick 2004); (Bockelmann et al. 2002; Silvestri et al. 2003). Differences between what is salt marsh or unvegetated mudflat may be determined by just a few centimeters of elevation (Reed and Cahoon 1992). However, edaphic conditions such as nutrient availability, soil redox potential, organic soil content, sulfide concentrations, soil moisture, and porewater salinity also play a role in determining vegetation dominance (Morris and Bradley 1999; Mitsch and Gosselink 2000; Morris et al. 2005).

Geomorphically, a salt marsh is often separated from the tidal flat by a ramp in elevation or abrupt change in elevation caused by increased sedimentation and decreased erosion due to vegetation growth (Crooks et al. 2002). Marshes are typically considered either ramped or

platform depending on the level of maturity and the primary driver of accretion, bioproductivity or tidal sedimentation (Fitzgerald et al. 2008). Ramped marshes are more intertidal in nature, dominated by low marsh vegetation, *Spartina alterniflora*, and have high mineral sedimentation rates. These marshes are often considered immature and have not yet obtained equilibrium with sea level rise (SLR) (Morris et al. 2002). Platform marshes on the other hand are considered mature, having achieved dynamic stability relative to sea level and exhibit a platform-like morphology proceeded by either an erosion scarp or a short ramp of low marsh vegetation. These systems have a higher peat concentration due to organogenic accretion processes and low influx of tidal borne suspended mineral sediments (Fitzgerald et al. 2008). Platform marshes are also more susceptible to the threat of SLR because they accrete at slower rates and are composed primarily of vegetation less tolerant of inundation than low marsh systems.

Marsh morphology is primarily driven by hydrology and its interaction with sediment supply, which incorporates tidal influences but may also include groundwater and sheet flow (Varnell et al. 2003). A large number of factors are now known to influence salt marsh formation causing change in vertical elevations and accretion. These factors include organic and inorganic sediment supply, compaction, subsidence, edaphic conditions, climate, erosion, ice rafting and storm sediment, bioturbation and grazing, elevation, tidal range, flood regime, relative sea level rise, vegetation species competition and density, and anthropogenic impacts (**Figure 2.2**) (Redfield 1972; Cahoon et al. 1995; Roman et al. 1997; Orson et al. 1998; Schwimmer and Pizzuto 2000; Argow and Fitzgerald 2006; Goodman et al. 2007; Ward et al. 2008).

Vertical accretion of the marsh surface is attributable to a combination of two processes, mineral sediment deposition and organic matter accumulation (Redfield 1972; Warren and

Niering 1993; Morris et al. 2002). Deposition of suspended sediment is a primary driver of accretion in many salt marshes particularly in the intertidal low marsh region or fluvial systems. Marsh sediment accumulation rates have been observed to increase from the lower to upper reaches of the marsh system (Orson et al. 1990). Marsh vegetation creates hydraulic drag by reducing tidal flow and attenuating waves causing sediment to drop out of suspension (Morris et al. 2002; Möller 2006). In addition, it provides surface areas to collect sediment on its leaf and stalk structure (Morris et al. 2002). This accretion reduces water depths, hence the biofeedback drives the system toward equilibrium with sea level (Morris et al. 2002). Mineral sediments are found in high concentrations in fluvial dominated systems and near the marsh edge as a result of the reworking of tidal flat sediments (Stoddart et al. 1989; Ward et al. 1998). Deposition of this sediment decreases rapidly as a function of the distance from the marsh edge or channel system (Stoddart et al. 1989). Often mineral-rich, coarser-grained deposits can be found on natural levees around tidal channels.

Although the processes behind mineral sedimentation in marshes are widely understood it is only recently that the mechanisms for organic matter accumulation have been recognized (Nyman et al. 2006). High marsh areas accrete by a process known as organogenesis due to the infrequent flooding that occurs and the distance from sediment sources (Miller et al. 2001). In addition, it has been found that the primary growth mechanism in some coastal marshes is organogenic when mineral-based sediment is not available (Nyman et al. 2006). SLR in excess of marsh accretion rates can increase flooding stress on vegetation, stimulating growth through a positive feedback loop (Nyman et al. 2006). The process works through the production of a fibrous network of aquatic roots that develop just above the marsh surface (Nyman et al. 2006). Organic sediment development depends on factors such as dominant vegetation type and nutrient

availability. Also, salt water flooding reduces oxidation, which leads to preservation of organic materials resulting in marsh accretion. Less frequent flooding will lead to increased oxidation and therefore marsh subsidence. These organic sediments have lower bulk density when measured compared to mineral based accretion deposits (Kearney et al. 1994; Ward et al. 1998). Transgressive marshes will often exhibit large sequences of accumulation shifting between organogenic deposits to mineral based sediment where the reverse would represent a regression (Allen 1995).

Storm events appear to be a major factor in determining periodic, long-term sedimentation rates in some marshes. Everyday processes such as tidal inundation and precipitation are regular and predictable in their influence. However, low frequency, high magnitude events can provide episodic sediment accumulation that can substantially modify the marsh system in both positive and negative ways. Storms can affect salt marsh sediment and elevations by sediment deposition, erosion, vegetation disruption, compaction, soil shrinkage, soil swelling, and rending/folding of sediment (Cahoon et al. 1995; Cahoon 2006). Storm sediment can provide a quick infusion of mineral deposition stimulating organogenic accumulation through root growth (Cahoon 2006). Sedimentation rates in one marsh exceeded 24 mm/year for a single event (Roman et al. 1997). Storms can also cause major erosion or overwash deposits leading to an increased availability of sediment for marsh accretion (Ward et al. 1998; Ward et al. 2008). Geomorphology also likely plays a significant role in determining the amount and location of storm-related erosion or accumulation such as proximity to an inlet or flood tidal delta.

Sea Level Rise

Sea level is one of the most important elevation horizons in geomorphology having a direct influence on shoreline processes and features such as salt marshes. It is both a datum for measuring heights and a base level for erosion. There are two types of sea level rise (SLR) observed from a local or global perspective. Eustatic sea level is a simultaneous global change in world-wide water levels. Changes in eustatic sea level can be attributed to several factors with the most well-known being continental glaciation. Continental glaciation causes sea levels around the world to drop by interrupting the hydrologic cycle. Water is removed from the oceans via precipitation onto continental ice sheets locking it away and dropping world-wide sea levels (Boggs 1987). As ice sheets melt through changing long-term climatic conditions, large quantities of water are released increasing global ocean volumes and eustatic sea levels. Eustatic sea level curves are best approximations of SLR since they contain numerous unknowns in their calculation such as geoidal variability, thermal expansion of sea water and relative crustal movements (isostasy) (Barnhardt et al. 1995).

SLR can also be observed from a local or regional perspective, which is called relative sea level rise (RSLR). Relative sea level is the sum of all vertical movements at the coast (**Figure 2.3**) (Giese and Aubrey 1987; Barnhardt et al. 1995). In fact, the impacts of all sea level interaction with the coast are relative to local land levels and terms like emergent or submergent only reflect relative movement of land and sea in a regional context. This is a result of the Earth's crust being in a constant state of motion causing continents to be subjected to tectonic uplift, delta deposits to compact or subside, and coastlines to erode away. Also, continental ice sheets cause crustal depression and ultimately uplift when they melt known as isostatic adjustment. Even humans have affected relative sea level typically realized as local subsidence,

through the removal of aquifer water, mining of petroleum products, diking of salt marshes, and redirecting river flood waters. A positive movement of the sea inland is called a transgression and a negative movement is a regression. Unfortunately, the most widely accepted evidence of eustacy is also the same evidence for determining isostasy, which poses a problem for scientists studying SLR. Tropical islands make better locations to isolate eustatic sea level trends from the geologic record (Church et al. 2006).

The current cycle of SLR has been occurring since the last glacial ice sheet retreat. However, recent SLR (20th and 21st century) is largely thought to be caused by thermal expansion of sea water (Church et al. 2008). The oceans store more than 90 percent of the heat in the Earth's climate system and act as a temporary buffer against the effects of climate change (Barnett et al. 2005; Domingues et al. 2008). Heat transfer is constantly occurring between the atmosphere and the ocean's surface. When materials are heated they increase in volume through a process called thermal expansion. Heat that is transferred to the ocean increases the global volume of water resulting in a rise in eustatic sea level (Church et al. 2008). If the problem is overly simplified, based on globally averaged sea surface temperatures, a linear model of ocean heat uptake and thermal expansion can translate to a future trend in global sea level rise (Barnett et al. 2005). Small changes in the ocean's transport of heat or salt can have large effects on surface temperature, and ultimately on climate. Ocean warming and thermal expansion rates have been found to be 50 percent larger than previous estimates for the upper 700 m of the oceans and even greater for the upper 300 m (Barnett et al. 2005). Regional variations in sea level distribution are largely thought to be due to regional differences in ocean thermal expansion (Church et al. 2008). Although up to now thermal expansion is considered to be the major

contributor to SLR in the 20th and 21st century, ice melting will likely play a significant role in the long term (Church et al. 2008).

It has also been demonstrated that there are seasonal, annual and decadal variations in regional sea levels. Sea level responds to the radiative and mechanical forcing of the atmosphere (Plag and Tsimplis 1999). Seasonal and annual variations in pressure systems, wind, and temperature can cause an anticipated cycle to local and regional sea level (Harris 1963). For instance, the East Coast of North America typically has its lowest sea levels in late winter and its highest in the fall (Provost 1976). Long-term trends in sea level from tide gauge records clearly identify short-term variations on the sub decadal timescale (~5 years) (Plag and Tsimplis 1999; Reed 2002). Fluctuations in the interannual and decadal global circulation patterns such as El Nino-Southern Oscillation (ENSO) or the North Atlantic Oscillation (NAO) can cause significant variation in seasonal weather cycles and therefore sea level (Plag and Tsimplis 1999). In the short term, the increased recurrence intervals in storm frequency and severity are also a large, unpredictable driver that strongly influences regional/local SLR rates.

Eustatic sea levels have varied as much as 120 m between glacial and interglacial cycles (Church et al. 2008). In New England, the isostatic effects of glaciation have strongly influenced relative sea-level during the late Quaternary (Belknap et al. 1987a; Belknap et al. 1987b; Belknap and Shipp 1991; Kelley et al. 1992; Barnhardt et al. 1995; Barnhardt et al. 1997). Retreat of the ice sheets led to isostatic uplift, and sea level fell to approximately -60 m by 10.8 ka before present time (Barnhardt et al. 1995; Barnhardt et al. 1997). The timing and magnitude of coastal emergence varied widely due to variations in ice thickness and retreat. Over the last 7000 years sea level rose much more slowly and in the last several thousand years there has been little change in eustatic SLR rates, averaging an increase of approximately 1mm/year (Kelley et

al. 1995; Gehrels et al. 1996; Church et al. 2008; Fitzgerald et al. 2008). Sediment cores and salt marshes have shown that SLR in the 19th and early 20th century have increased, accelerating to 2 mm/year by around 1950 (Gehrels and Belknap 1993; Donnelly et al. 2004; Church et al. 2008). Satellite measurements by TOPEX and Jason-1 and tide gauge data of global sea levels from the last two decades show a steep increase in eustatic SLR in the last 10 years to about 3mm/yr (Church and White 2006). Evidence of this acceleration in SLR has been noted from other observations as well. Relative sea level has been rising at 3mm/yr for the last 40 years in Massachusetts with 2 mm/yr of that due to land subsidence (Giese and Aubrey 1987). However, a comparison of tide-gauge data with marsh basal peat dating in New England, over the last few decades indicates a three times increase in SLR acceleration (Donnelly et al. 2004). SLR predictions for the next century by various researchers differ significantly but all suggest a sharp increase in eustatic sea level elevation to as much as 1.32 m under an intermediate emission scenario (RCP 4.5) (**Figure 2.4**) (Church and White 2006; Horton et al. 2014).

Salt Marsh Response to Sea Level Rise

Salt marsh adaptability to eustatic and relative sea level rise is a concern for scientists and coastal managers. Marsh survival depends on an ability to maintain sediment accretion rates equivalent to the rate of sea level rise (SLR) and migrate landward, transgressing over high marsh communities onto the upland (Donnelly and Bertness 2001a; Mendelssohn and Kuhn 2003). Salt marshes could collapse if SLR accelerates faster than the marsh accretion rate (Hartig et al. 2002). Salt marshes are known to have maintained this equilibrium with sea level for approximately the last 4000 years by the accumulation of both mineral sediment and organic

matter (Redfield 1965; Redfield 1972). However with the predicted increases in global eustatic SLR in the next century, marsh survivability is unknown.

For salt marshes to keep up with SLR they must continue their process of self-maintenance where vegetation and decomposers interact with sea level to regulate the marsh elevation toward equilibrium (Morris et al. 2002). They must maintain sediment accretion and decomposition rates so surface elevation growth is comparable to the rate of SLR. At the same time, erosion at the seaward edge must be compensated by migration landward, transgressing onto the upland (Donnelly and Bertness 2001b; Mendelssohn and Kuhn 2003; Fitzgerald et al. 2008). A number of factors influence vertical accretion in salt marshes including organic and inorganic sediment supply and loss (erosion and oxidation of organics), compaction, ice rafting and storm sediment, elevation, tidal range, flood regime, relative sea level rise, and vegetation species composition and density (Redfield 1972; Roman et al. 1997; Orson et al. 1998; Argow and Fitzgerald 2006; Goodman et al. 2007). Low vertical accretion rates may suggest a marsh system is out of equilibrium with sea level (Ward et al. 1998). Anthropogenic obstructions to marsh transgressions are most likely to have the biggest impact on potential for system loss. Seawalls, steep slopes and other natural and anthropogenic features obstruct salt marsh migration (Fitzgerald et al. 2008). If SLR outpaces accretion marshes will collapse and there are barriers to migration marsh area will be lost through coastal squeeze, (Hartig et al. 2002; Fitzgerald et al. 2008). Possible salt marsh responses to sea level rise are outlined in **Figure 2.5**. With accelerating SLR a marsh can exhibit several different outcomes:

1)   <u>Transgression</u>: The salt marsh accretes at a pace at or above that of SLR that allows it to survive, transgressing landward, with low marsh migrating over the high marsh in a

landward direction while the seaward edge is eroded and reverts to intertidal mud flats (Donnelly and Bertness 2001b; Goodman et al. 2007).

2)   Barriers: The salt marsh meets a natural or man-made physical barrier such as a steep slope or seawall, preventing it from landward migration causing coastal squeeze (Donnelly and Bertness 2001b; Fitzgerald et al. 2008). In this case either the marsh elevations will increase only in a vertical direction reducing in aerial extent allowing it to survive or it will collapse as SLR exceeds the accretion capacity of low marsh vegetation (Reed 2002).

3)   Partial Collapse: The salt marsh is incapable of accreting at a rate that can keep up with sea level rise but the higher salinity tolerance, wider elevation range and accretion rates of low marsh vegetation permit it to rapidly colonize and migrate over the high marsh transitioning to a smooth cordgrass salt marsh. If SLR continues to increase, areas of low marsh will fall below its optimal elevation range, which leads to collapse (Morris et al. 2005).

4)   Collapse: The marsh is incapable of accreting through both mineral and organogenic methods at rates great enough for survival of increased SLR. The marsh surfaces collapse into tidal pools and mud flats, likely from high marsh to low marsh, as tidal channels and mosquito ditches allow penetration of salt waters deep into the high marsh system drowning the vegetation (Tolley and Christian 1999).

Salt marsh vegetation communities may or may not be able to respond to a rapidly accelerating sea level. Changes from high marsh dominated systems to low marsh have been documented in southern New England salt marshes (Warren and Niering 1993). Transitioning from one marsh type to another has been described as ecosystem state change (Miller et al. 2001). Also, additions of sudden and acute stressors such as storm induced wrack deposits to an already disturbed community can cause unexpected, severe changes (Brinson et al. 1995; Tolley

and Christian 1999). This type of local disturbance may produce differing results depending on its location in the wetland or the wetlands hydrogeomorphic class (Tolley and Christian 1999). Vegetation changes may be further indication of marsh systems not keeping up with sea level (Warren and Niering 1993; Roman et al. 1997).

Marsh accretion and subsidence as a response to SLR is not likely to be the only visible effects on systems. As sea level rises there will be an increase in tidal prism that will likely cause the enlargement of the marsh drainage networks (Ward et al. 1998; Hughes et al. 2009). A balance exists between erosion, mineral sedimentation, and organogenic deposition which makes the marsh particularly sensitive to changing conditions caused by more hydrologic flow over its surface (Morris et al. 2002). A submerging marsh system will alter its channel hydrology and geometry to adjust for changing flow rates and larger volumes of water (Ward et al. 1998). Headward erosion of existing creeks and new creek formation have been observed at several sites and is attributable to relative sea level rise (RSLR) in those regions (Hughes et al. 2009). At one site the erosion is likely caused by a combination of factors including bioturbation, increased infiltration, herbivory, and RSLR. Consumptions of vegetation by crabs and their burrows is the likely cause of additional instability found at one South Carolina marsh (Hughes et al. 2009). Creek network adjustments are likely to continue to occur with an acceleration of SLR (Marani et al. 2003).

Another impact of SLR on the marsh systems may involve past anthropogenic ditch construction. More than 90% of New England salt marshes have been ditched in an effort to control mosquito populations (Kennish 2001). Ditching increases the draining of porewater from the surrounding peat having a "drying effect" on the marsh; this fosters aerobic conditions, which can lead over time to marsh subsidence (Warren and Niering 1993). Ditching provides a

conduit for increased tidal inundation and the spread of *Spartina alterniflora* in-land. As sea level rises these ditch and creek conduits facilitate large amounts of water delivery to the upper marsh system not accustomed to regular flooding. Increased tidal inundation can lead to decreased belowground decomposition but also to hypoxic conditions decreasing bioproductivity and OM contribution to sediment 'growth' (Warren and Niering 1993; Miller et al. 2001). However, other research suggests that high marsh vegetation can be less biologically productive under increased inundation and higher salinities, further decreasing accretion and leading to possible dieback into open water pools (Adamowicz and Roman 2005). Vincent et al. (2014) found vegetation dieback strongly correlated with increased flooding from ditch plugs. Although, this is in direct conflict with research by Nyman et al. (2006) and Morris et al. (2002).

There are mixed conclusions as to long term response to sea level rise but most research suggests that salt marshes are stable relative to the present rate of SLR (Reed et al. 2007). As SLR has increased, so have the rates of salt marsh accretion and at least in the short term they are keeping pace with SLR (Roman et al. 1997; Goodman et al. 2007). One study of Maine salt marshes found that over a 17 year period, 7 out of 11 marshes achieved accretion with a positive balance to current rates of SLR at average rates of 2.8 mm/y (Goodman et al. 2007). However, sites where the marker horizon was lost to erosion were excluded, which skewed the mean. Another study in southern New England marshes found changes in vegetation exhibiting a rapid shoreward advancement of *Spartina alterniflora*, which was attributable to an increase in SLR (Donnelly and Bertness 2001b). SLR alone is not the only cause for concern regarding salt marsh response. Anthropogenic disturbances to sediment supply and reduced tidal exchange both may lead to increased subsidence, channel modification and changes to marsh

biogeochemistry that will play a role in how marshes respond to SLR (Hartig et al. 2002; Kirwan and Temmerman 2009).

There appears to be an optimum rate of RSLR leading to elevations where marsh plants experience an optimum depth for productivity and inundation depths exceeding the optimum are likely to lead to collapse (Morris et al. 2002). In addition, accelerated SLR and marsh response may not be linearly related and there may be regional differences or thresholds before signs of adjustment are visible (Fitzgerald et al. 2008). Estimates of long-term accretion often underestimate the more recent trends because of the time scale of the measurements (Kearney and Ward 1986; Orson et al. 1998; Ward et al. 1998). Marshes that only experience micro-tidal inundation are likely to experience greater declines than those with meso/macro tidal water levels because they rely more on organogenesis to support vertical accretion (Craft et al. 2009). Organogenic marshes with ramp morphology will likely show gradual and persistent loss while platform marshes will, at least initially, lose little areal extent (Miller et al. 2001; Fitzgerald et al. 2008). Some areas such as marshes on Chesapeake Bay are being replaced by open water and tidal flats at an alarming rate due to reduced sediment supply and accumulations rates below that of SLR (Kennish 2001).

Coastal managers often wish to preserve or restore salt marshes as a defense against SLR, (Gedan et al. 2009). The ability of salt marsh systems to attenuate waves and buffer against storm damage has been studied for years (Provost 1976; Möller et al. 2002; Möller 2006; Fitzgerald et al. 2008). Various forms of coastal protection date back about 3000 years to ancient civilizations (Charlier 2003). Manmade dikes and sea walls remain in many places along the world's coasts that prevent the sea's ability to shift inland and provide room for salt marsh development (Erwin 2009). Declining salt marsh area could lead to reduced shoreline protection

for coastal communities (Craft et al. 2009). In the case of dikes there appear to be three scenarios for adaptation: raising/reinforcing, realigning, and removing/restoring. It has been found that, in the long term, hard structure revetments are not sustainable solutions and in the short term often pass the problem further down the coast (Charlier 2003). In some cases coastal managers have begun a program of managed retreat where dikes and seawalls are removed , to return the land back to its natural condition ahead of SLR in order to create coastal flood protection (Hazelden and Boorman 2001; Gedan et al. 2009). However, large scale feasibility of this technique is currently unknown. Salt marsh restoration is an affordable and environmentally friendly approach to preventing coastal erosion.

Tidal Datums

Water level datums are elevations to which all water heights and depths are referenced (Brown and Kraus 1998). Tidal datums are time mean averages of water level measured from a gauge over a tidal datum epoch. The current nineteen year epoch, a period from 1960-1978, is used in tidal computations to average out the yearly variability for a period representing the regression of the moon's nodes and other nonlinear trends (Swanson and Thurlow 1979; Brown and Kraus 1998; Gibson and Gill 1999). Tidal datums are local vertical datums that can change significantly within a single geographic area. They are not considered geodetic datums which are fixed planes such as North American Vertical Datum 1988 (NAVD88). As relative sea level rises, all tidal datums such as Mean High Water (MHW), Mean Low Water (MLW), and Mean Sea Level (MSL) need to be recalculated and adjusted upward accordingly (Giese and Aubrey 1987). This may not be a linear relationship with increases of SLR as there may be other changes such as basin resonance to consider. The accuracy of a tidal datum depend on the

accuracy of the measurement system, the surveying done between the gauge and a geodetic benchmark, and the equations used to process the collected data (Brown and Kraus 1998). Using only a 12 month epoch as opposed to 19 years, one researcher determined that the probable error would be as much as 1.5 cm for a tidal gauge on the Atlantic coast (Swanson 1974).

Mean Lower Low Water (MLLW) is the national standard datum for all nautical charts, tide tables, and bathymetric maps in the United States adopted by the National Oceanic and Atmospheric Administration National Ocean Survey NOAA NOS (Swanson and Thurlow 1979). Before 1979, there was not a national standard and every region had its own specific datums. The definition of MLLW is as follows:

> "The arithmetic mean of the lower low water heights of a mixed tide observed over a specific 19-year Metonic cycle (the National Tidal Datum Epoch). Only the lower low water of each pair of low waters of a tidal day is included in the mean. For stations with shorter series, simultaneous observational comparisons are made with a primary control station in order to derive the equivalent of a 19-year value." (Schureman 1975)

Using this same method all other datums are calculated (Swanson and Thurlow 1979) such as Mean Low Water (MLW) and Mean High Water (MHW) being the one used to depict the Continually Updated Shoreline Project (CUSP) (**Figure 2.6**). MLW and MHW are the averages of all the low waters and high waters including lows and both highs, respectively, in the calculation. Lowest or Highest water calculations use only the lowest or highest of each pair of tide in a day.

The Relationship of Salt Marshes to Tidal Datums

It has been presumed for many years that a relationship exists between salt marsh vegetation growth and the tidal datum of mean high water (MHW) (Chapman 1940; Redfield and Rubin 1962; Redfield 1972; Provost 1976). The MHW line is considered by many as the transition line between regular flooding and irregular flooding of the marsh platform. However, the elevation of MHW differs between sites due to differences in geography, basin resonance, restrictions, bottom contours, prevailing winds and currents (Bockelmann et al. 2002). Inundation is typically calculated by relating shore height to inundation frequency from regional tide gauge data (Bockelmann et al. 2002). In that study, Bockelmann (2002) found a curvilinear relationship between inundation frequency and shore height. Shore height correlated only weakly with inundation frequency over large distances, where distances of 2.5-5 km had as much as 25% differences from regional based MHW and differences of 300% in inundation frequency (Bockelmann et al. 2002). Locally produced datums based on inundation frequency were found to be better at predicting the occurrence of dominant plant species over tidal datums based on regional tide gauge data (Bockelmann et al. 2002).

A review of salt marsh studies in the United States by another researcher over an approximately 20 year time span showed low correlation between MHW and *Spartina alterniflora* (Mckee and Patrick 1988). However, this analysis was based on disparate studies with different sampling methods and regional-based datum comparisons. Yet another research team found no consistent correlation between *S. alterniflora* and MHW as it is tied to NGVD and defined on the NOAA nautical charts (Lefor et al. 1987). They found that regional based MHW does not seem adequate for this type of analysis and is ideally developed for each individual site since biological response depends on local conditions (Lefor et al. 1987). Most researchers do

agree, however, that there does appear to be some agreement between occurrence of salt marsh vegetation and local tidal datums (Redfield 1972; Lefor et al. 1987; Gehrels and Belknap 1993; Bockelmann et al. 2002; Morris et al. 2002; Li et al. 2009).

Spartina alterniflora is almost always the most seaward emergent plant on the Atlantic coast of North America and its lowest elevation occurrence appears close to MSL. There are different ecological forms of *S. alterniflora*, tall, medium, and short-form. One study (Lefor et al. 1987) showed that 98.4% of tall-form *S. alterniflora* observations appeared at or below MHW with a peak occurrence of 15 cm below and all onsite observations of *Spartina alterniflora* were between 0-50 cm below (Lefor et al. 1987). *Spartina patens* was found largely 10-15 cm above MHW . There also appears to be a consistent correlation between *Iva frutescens* at the upland edge with Highest High Tides (Provost 1976; Lefor et al. 1987). Research in South Carolina has been conducted using lidar to determine a marsh elevation distribution curve as it relates to vegetation growth, Mean High Water (MHW) and SLR within an individual salt marsh (Morris et al. 2002; Morris et al. 2005).

Lidar Systems

Lidar (light detection and ranging) is an airborne remote sensing technology that can be used to provide high-resolution elevation data over large areas using laser range finding. Pioneered by NASA in the early 1970s, lidar became commercially available and viable for thescientific and engineering communities starting around the mid-1990s, with ongoing development continuing today (Irish and Lillycrop 1999). Lidar is an active remote sensing technique, meaning it uses its own source of electromagnetic radiation, rather than relying on reflected sunlight. Airborne lidar systems are composed of three fundamental components (each

with a host of subcomponents): 1) a laser scanner that transmits pulses towards the earth's surface (usually creating a swath on the surface using some form of scan mechanism, such as an oscillating scan mirror), 2) an integrated Global Navigation Satellite System (GNSS) - Inertial Navigation System (INS) for generating blended navigation solutions, consisting of 3D position and orientation of the sensor along the flight track, and 3) a receiver. Datasets produced from lidar are typically three-dimensional point clouds of X-Y-Z laser impacts with physical objects, which are typically vegetation, manmade structures, or the ground. Spatial coordinates of lidar points are determined by using the laser ranges, scan angles, blended navigation solution, and calibration data in the laser geolocation equation. The increased availability of lidar is largely related to the increases in computing power, data storage and enhanced GNSS accuracies (Mallet and Bretar 2009).

There are two different types of lidar systems in use today: discrete-return lidar (DRL) and full-waveform recording (Mallet and Bretar 2009). DRL systems use a hardware-based ranging system comprised of a constant fraction discriminator and time interval meter. Elevation is determined by recording the elapsed time between the emission of a short duration laser pulse and the arrival of the reflection of that pulse at the sensor's receiver. When this time is multiplied by the speed of light, it results in a measurement of the round-trip distance traveled, half of which is the distance between the sensor and the target (Bachmann 1979; Lefsky et al. 2002b). Discrete systems often have high spatial resolution because of their small diameter footprint (0.2-3.0 m diameter). DRL systems initially recorded only the first or first and last pulses returned to the sensor; however, many sensors today are designed to record multiple reflections (Lefsky et al. 2002b). Multiple-return systems are typically used to study forest canopy and can discriminate low-intensity signals out of the noise (Mallet and Bretar 2009). In

most available systems the minimum detectable distance between two echoes are greater than 1.5 m (Lefsky et al. 2002a).

Full-waveform datasets are collected with pulsed lidar systems recording a complete time series of backscattered energy with a digitizer and a high capacity storage device. Laser pulse intensity in the return signal is dependent on the power of the system's initial pulse, the fraction of the pulse intercepted by a surface, the reflectance of the intercepted surface and the fraction of the pulse that is returned in the direction of the sensor. Since vegetation, soil and other objects have a rough surface at infrared (IR) wavelengths, targets scatter energy, some of which returns to the sensor (Wagner et al. 2008). Full-waveform backscatter allows the user to detect the vertical distribution of targets and can resolve multiple surfaces with a distance of less than 0.15 m (Mallet and Bretar 2009). Waveform digitizing systems such as the Enhanced Lidar Visual Interactive System (ELVIS) have the ability to record intensity of the return pulse, which can better characterize canopy structure but typically have larger diameter footprints on the order of 10 m (Lefsky et al. 2002b). At the present time, end users of topographic lidar (e.g., coastal scientists) rarely have access to waveform data, either because the data were collected with a hardware-based ranging (i.e., discrete return) system without a separate waveform digitizer, or because the service provider was only required to provide downstream products, such as point clouds and DEMs.

Lidar sensor platforms produced by various manufacturers have many similar characteristics. Some of the main differences in technical specifications include the laser's wavelength, power, pulse duration/repetition rate, beam size and divergence angle. NIR lasers are most commonly used for vegetative and topographic surveys because of their high vegetation reflectance (Lefsky et al. 2002b). Two of the most commonly used NIR laser wavelengths are

1550 nm and 1064 nm. Water in terrestrial lidar systems is typically observed as a data void as most of the beam energy is absorbed or specularly reflected away from the receiver. Full waveform bathymetric systems, such as SHOALS 3000 and CZMIL utilize both a NIR laser and a green laser near 532 nm due to its better penetration of shallow water (Lefsky et al. 2002b). In bathymetric systems the infrared beam is reflected by the water surface allowing a calculation of water depth by the time difference of the NIR backscatter and the green laser backscatter from the seafloor. Water clarity and bottom type reflectivity properties are the most limiting factors for depth detection (Irish and Lillycrop 1999). In some sensors, another band of energy is also recorded called the Raman (645 nm) red energy. Raman results from the excitation of the water molecules by the laser energy (Irish and Lillycrop 1999; Pe'eri and Philpot 2007). Full waveform data processing techniques involve the decomposition of the returned backscatter into relevant peaks to generate denser point clouds then would be available from discrete pulsed systems (**Figure 2.7**) (Wagner et al. 2008; Mallet and Bretar 2009). Even though Radar (Radio detection and ranging) remote sensing and research on backscatter characteristics has been utilized since the 1970s, comparatively little is known about the lidar scattering properties of vegetation and other terrain surfaces (Wagner et al. 2008).

Some factors known to degrade the vertical accuracy of lidar by 5 to 10 cm (or greater) are uncertainties in the post-processed trajectory, scan angle uncertainty, ranging uncertainty, and calibration issues (Shrestha and Carter 1998; Lefsky et al. 2002b). These estimates are consistent with the literature provided by the lidar instrument manufacturers, such as Optech. However, the accuracy of data sets varies from survey to survey and also depends upon surface type (road, bare sand, vegetation, or mud).

Laser and physical components

The laser portion of the lidar instrument emits NIR laser pulses between 1064 and 1550 nm in wavelength at frequencies of up to 500 kHz. These pulses are reflected off a rotating mirror that rotates in a sweep perpendicular to the flight direction. There are several types of mirror configurations that have advantages and disadvantages operating in in-line, oscillating and conic geometries (Kukko and Hyyppa 2009). When a mirror rotates left and right it is called a saw-tooth scanner. This type of configuration has the disadvantage that the mirror does not continually rotate at the same speed but rather has to slow to a stop before rotating in the opposite direction (Fowler 2001). However, oscillating scanners produce a higher footprint density in the cross-track direction and sparser in the along-track direction (Kukko and Hyyppa 2009). Another configuration is the rotating polygon, which only moves in one direction at a constant rate. A disadvantage to this type of mirror is a potential systematic bias due to the data being collected in one direction with no fixed stop position to indicate the extent of a swath (Fowler 2001). Many providers prefer the mirror scanning system and programmatically disregard the swath edges to remove those sources of error (Fowler 2001).

There are a number of potential sources of error within the laser components of the Lidar system. These are laser range errors, pulse rate and stability, beam divergence errors, and mechanical errors associated with the equipment such as scan angle errors, mirror misalignments, timing errors, aircraft navigation and bore-sight (Fowler 2001; Kukko and Hyyppa 2009). The uncertainty in the laser range measurement is approximately 2 cm (Habib et al. 2009). Each coordinate is time-tagged, defining its position in both time and space. Accurate timing is very important for post-processing correction between all the various components. Any timing bias or discrepancy could cause major systematic errors.

Lidar point density determines the level of ground topographic detail that can be resolved. Point density is determined by five different factors (Kukko and Hyyppa 2009):

1)   Laser pulse rate: The Laser pulse rate, also known as pulse frequency rate (PFR), will increase the data density as the pulse rate is increased.

2)   Flight altitude: Flight altitude determines the width of the swath (assuming a constant scan angle) and the proximity between laser points. The higher the flight altitude, the lower the point density (assuming other variables remain constant). The Laser beam diverges into a conic shape as a function of altitude increasing the size of the footprint, which typically ranges from 0.6m to 2.5m (Kukko and Hyyppa 2009). As a rule of thumb, horizontal accuracy is often claimed to be between $1/5500^{th}$ and $1/1000^{th}$ the flight altitude (Toyra et al. 2003; Hodgson and Bresnahan 2004; Habib et al. 2009; Optech 2009).

3)   Laser scan angle: At a set altitude and a constant laser frequency, a smaller scan angle will increase the density of points collected. The highest accuracy typically occurs at the scan line nadir and decreases as the swath angle increases (Hodgson et al. 2005). Scan angle has an estimated uncertainty on the order of 0.009 ° (Habib et al. 2009).

4)   Aircraft speed: Flight speed will influence point density by increasing or decreasing the spacing between scan lines. Decreased flight speed leads to increased point coverage.

5)   Swath overlap. The closer the centerlines of the aircraft flight tracks, the greater the swath overlap and, therefore, denser the dataset.

Atmospheric conditions are known to degrade the laser coordinates of vertical surface points by refraction off of aerosols, excessive humidity, and low-lying clouds (Shrestha and

Carter 1998; Lefsky et al. 2002b).   Atmospheric attenuation can dampen the amplitude of lidar waveforms and reduce the ranging accuracy. Surface scattering of the laser as it impacts a material or at an angle to a surface also lead to further degradation of the returning lidar pulse (Kukko and Hyyppa 2009). The low horizontal positional accuracy of lidar has been known to be a contributing factor in influencing vertical uncertainty (Hodgson and Bresnahan 2004; Raber et al. 2007).

Global Navigation Satellite System

Global Navigation Satellite System (GNSS) provide the positioning for the aircraft and, after post processing, the lidar data points. GNSS measurements of aircraft location are typically the biggest limiting factor for determining lidar instrument position accuracy (King 2009). With the establishment of good static ground base station(s), lidar flight position errors can be minimized, but not dismissed (King 2009). Ionospheric effects are a potential source of error but can be negated by cancellation using a base station and a rover (aircraft) unit over short distances of 10-20 km and using dual-frequency receivers. Tropospheric delay at the elevation angle and azimuth of each satellite, also known as Zenith Total Delay (ZTD), is another source of uncertainty, but can almost fully cancel with a static base station (King 2009). For baselines longer than 10-20 km, uncertainties from these sources can increase to as much as 0.2-0.3 m, but are more typically 0.05-0.1 m.   The time of day and satellite constellation has a large impact on the quality of the GNSS signal. Surveys should only be planned on days of optimum satellite geometry.

Inertial Measurement Unit

The inertial measurement unit (IMU), the key component of the GNSS-aided inertial navigation system (INS), uses orthogonal triads of accelerometers and gyros to measure angular rate and acceleration along 3 axes. Typically these units provide accuracies in the blended (Kalman filtered) navigation solution of 0.01 to 0.05 degrees in pitch and roll, while heading uncertainty can be a bit higher. For example Optech's ALTM 3100 using the Applanix POS/AV-510 integrated GNSS-INS system has the following uncertainties, Roll 0.005º, Pitch 0.005º, Yaw 0.008º (Optech 2005).

Various types of random noise in the above system components can lead to lidar point cloud accuracy problems. Positional noise in the aircraft GNSS will cause similar noise in the point cloud that are independent of the flying height, look angle, and direction. Angular noise in the attitude or mirror angles can affect the horizontal coordinates in the point cloud more than the vertical but are dependent on the flying height and look angle. Finally, range noise usually affects the vertical component of the point cloud and is independent of the system flying height but dependent on the look angle and flight direction (Habib et al. 2009).

Figures and Tables

Table 2.1: Salt marsh ecosystem services and associated cost presented in 1994 US dollars. (After Gedan et al. (2009)).

Ecosystem Service	Examples of Human Benefits	Average Value (Adj. 2007 $ ha^{-1} year^{-1})
Disturbance Regulation	Storm protection and shoreline protection	$2,824
Waste Treatment	Nutrient removal and transformation	$9,565
Habitat	Fish and shrimp nurseries	$280
Food Production	Fishing, hunting, gathering, aquaculture	$421
Raw Materials	Fur trapping	$136
Recreation	Hunting, fishing, birdwatching	$1,171
Total		**$14,397**
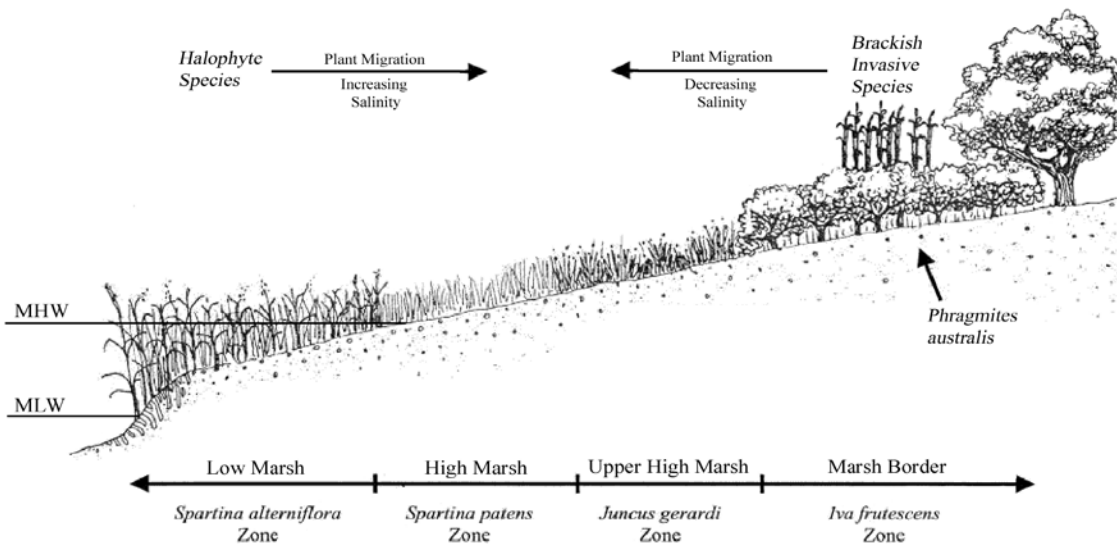
Figure 2.1: Cross section of a typical New England salt marsh illustrating the tidal zonation of saltmarsh vegetation and plant succession migration direction based on increasing or decreasing salinity concentrations. Tidal datums Mean High Water (MHW) and Mean Low Water (MLW) are shown. (After Bertness et al. (2002)).
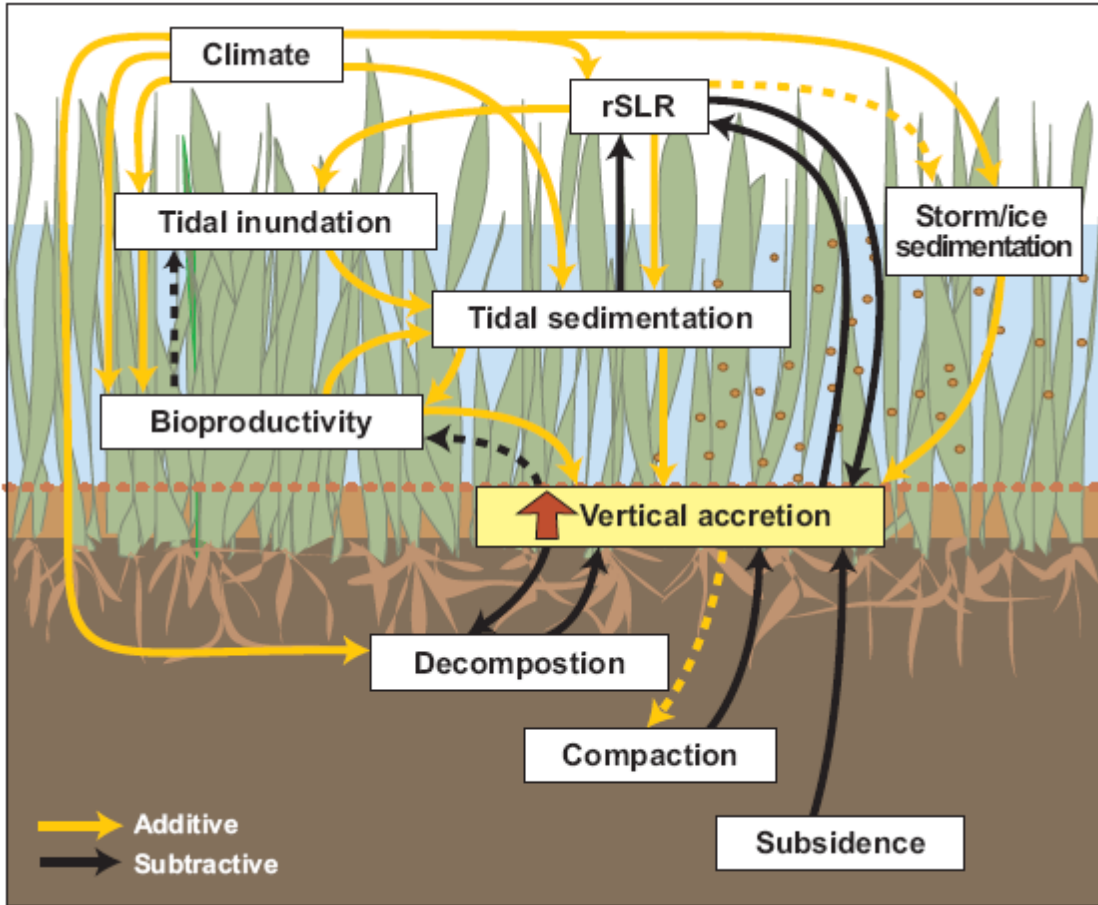
Figure 2.2: Marsh processes that affect vertical accretion of salt marsh environments. (After Fitzgerald et al. (2008)).
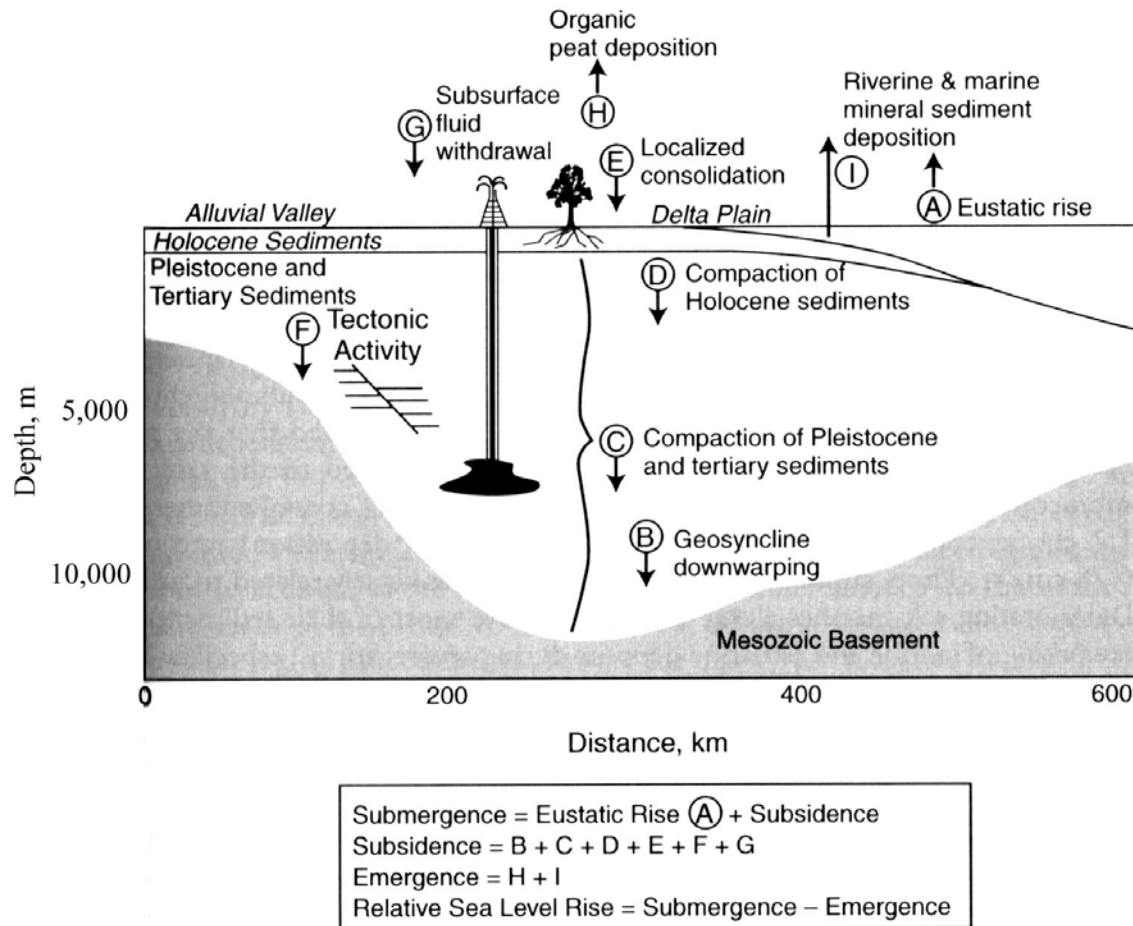
Figure 2.3: Diagram depicting various factors that influence Relative Sea Level Rise for the Mississippi Delta. (After Mitsch and Gosselink (2000)).
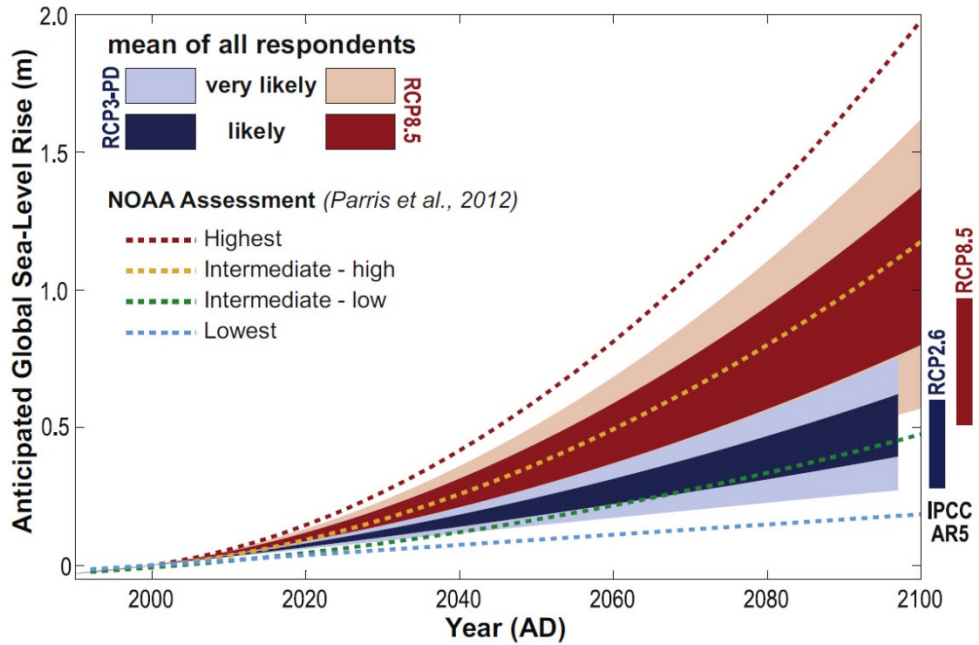
Figure 2.4: Sea Level Rise predictions for the next 100 years. (After Horton et al. (2014)).
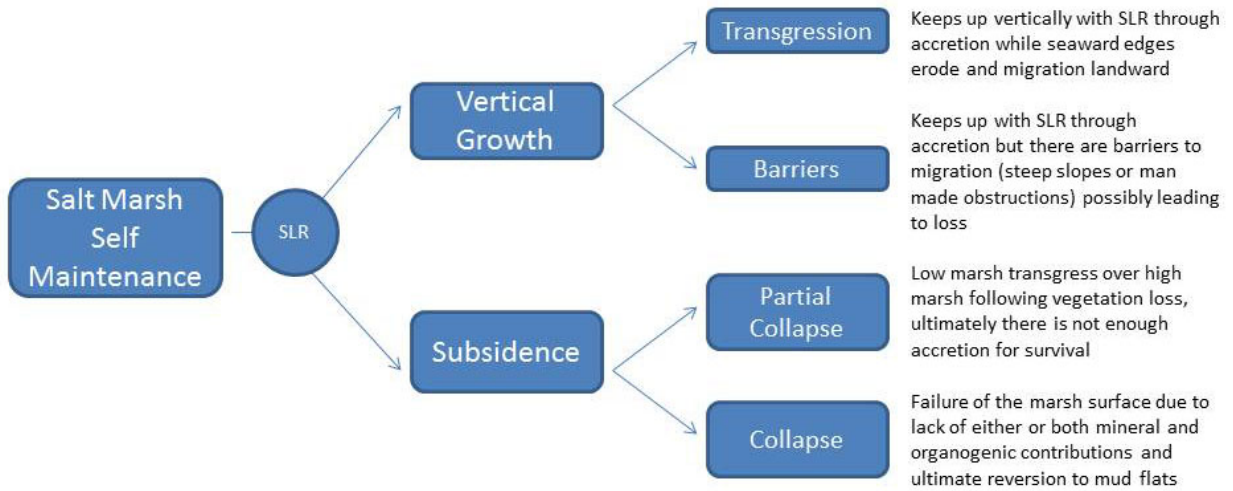
Figure 2.5: Flow chart of possible outcomes to salt marsh systems in response to accelerating Sea Level Rise.
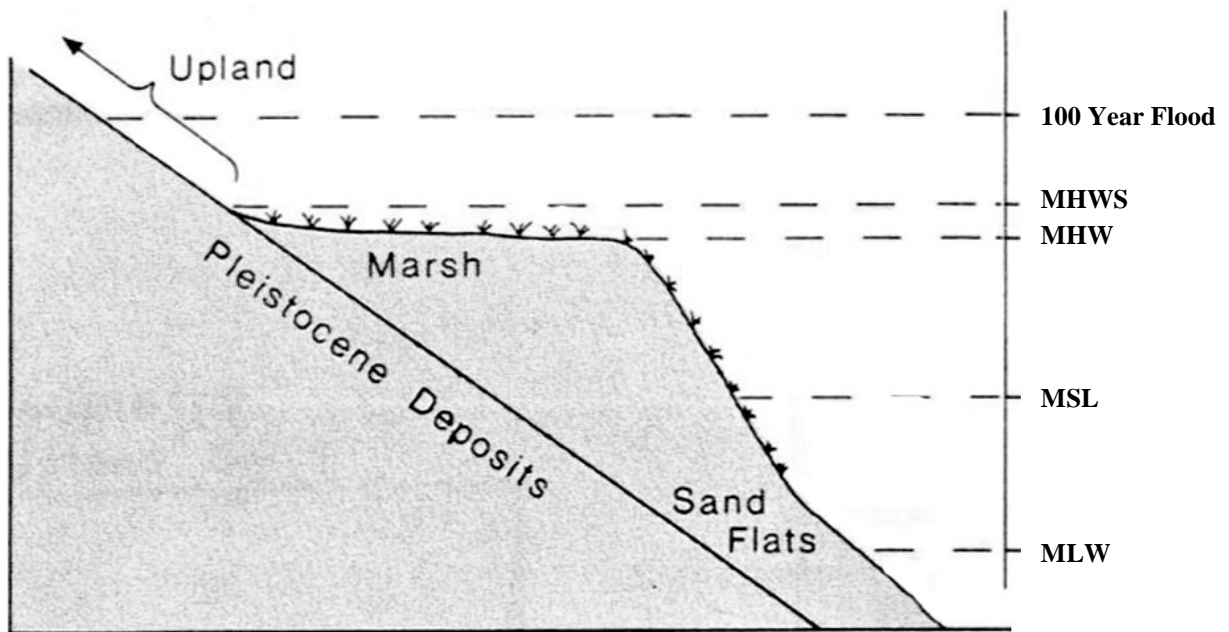
Figure 2.6: Commonly used tidal datums. (After Giese and Aubrey (1987)).
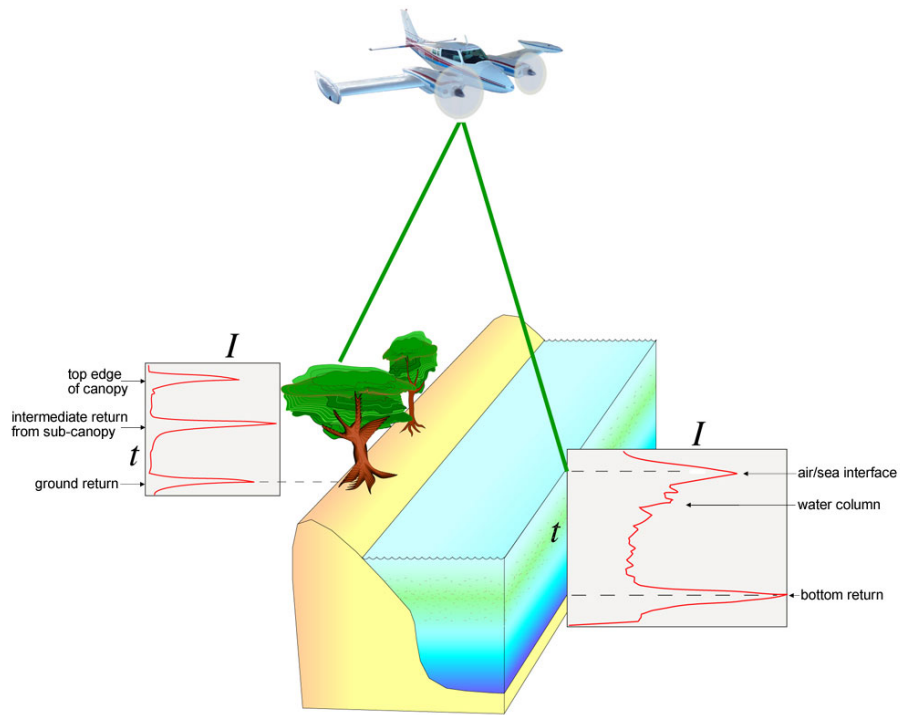
Figure 2.7: Sample full-waveform returns from a green lidar system in terrestrial and bathymetric applications. The graph on left shows full waveform green laser returns for terrestrial vegetation while the right graph shows returns from within the water column. (After Wright and Brock (2002)).

CHAPTER III

EVALUATION OF FIELD-MEASURED VERTICAL OBSCURATION AND FULL

WAVEFORM LIDAR TO ASSESS SALT MARSH VEGETATION BIOPHYSICAL

PARAMETERS

Published as:

Abstract

Local, high-resolution, accurate data sets are needed to support restoration and other management initiatives in coastal salt marshes, yet field collections of site-specific vegetation data is often impractical. In this study, a novel combination of full-waveform light detection and ranging (lidar) and field techniques for assessing the distribution of aboveground biomass throughout its height and its light blocking properties were investigated. Using new field methods, strong correlations were observed ($r > 0.9$) between subsamples' vertical biomass (VB), the distribution of vegetation biomass by height, and vertical obscuration (VO), the measure of the vertical distribution of the ratio of vegetation to airspace, for *Spartina alterniflora*. Also, it was found that simple metrics derived from the lidar waveforms, such as waveform width, can provide new information to estimate salt marsh vegetation parameters. The strong correlations between field-collected biophysical parameters and metrics derived from lidar data suggest that remote sensing methods can be used to estimate some vegetation biophysical

parameters such as plant height and proportion of vegetation area (PVA) using smaller, more targeted field surveys. Future work will be needed to verify the extensibility of the methods to other sites and vegetation types.

Introduction

Salt marshes are important habitats providing valuable ecosystem functions such as fish nursery habitat, carbon storage, shoreline protection services, and others (Costanza et al. 1997; Chmura et al. 2003; Chmura et al. 2012). Therefore, coastal change, salt marsh inundation and adaptation caused by sea level rise are of great concern for scientists and coastal managers, who require timely methods to monitor impacts over short and long temporal periods (Brock and Sallenger 2001). Advances in remote sensing technologies such as airborne light detection and ranging (lidar) for topographic/nearshore elevation surveys have led to more responsive, data rich, and accurate mapping of many terrestrial and aquatic environments including salt marshes (Lee and Shan 2003; Marani et al. 2003; Argitas and Yang 2006; Belluco et al. 2006; Chust et al. 2008; Schmid et al. 2011; Hladik and Alber 2012; Hladik et al. 2013).

Previous salt marsh lidar research has dealt mostly with discrete return datasets, which are readily available for many coastal areas but provide limited information about the structure of the vegetation (Rosso et al. 2006; Schmid et al. 2011; Hladik and Alber 2012). To compensate for a lack of information regarding the vegetation, additional research has been conducted using data fusion methods between discrete return lidar and hyper- or multi-spectral data to increase the contextual information available for analysis (Dubayah and Drake 2000; Anderson et al. 2008; Millette et al. 2010; Swatantran et al. 2011; Hladik 2012; Hladik et al. 2013; Schalles et al. 2013). However, a relatively new capability in commercial, topographic lidar that offers promise

for salt marsh vegetation mapping is the recording and analysis of full waveform datasets. Salt marsh vegetation with heights significantly less than the width of the transmit laser pulse typically show return waveforms that contain just a single peak (**Figure 3.1**) (Parrish et al. 2014). Nevertheless, the waveforms may contain information that will assist in the analysis of vegetation. Specifically, the shape of the received pulse is expected to vary across the marsh as a function of the terrain and vegetation characteristics. An advantage to waveform shape-based metric analysis is that observable details, such as vegetation biophysical parameters, might be overlooked based solely on height-based metrics derived from discrete lidar datasets (Muss et al. 2013). Additionally, waveform shape-based metrics may prove useful when there is no *a priori* knowledge of vegetation species distribution.

While a significant amount of work has been done on the processing of lidar waveforms to estimate surface characteristics (e.g., slope, and/or radiometric properties) or forest biomass (Drake et al. 2002; Wright and Brock 2002; Nayegandhi et al. 2006; Mallet and Bretar 2009), most of the methods discussed in the published literature involve sophisticated, computationally-complex signal processing approaches such as deconvolution (Jutzi and Stilla 2006). To date, only a few studies have been conducted on the use of simple shape-based waveform metrics (Adams et al. 2012; Muss et al. 2013; Parrish et al. 2014) for estimation of biophysical parameters. The basic premise is that, since each salt marsh vegetation species should affect the shape of the return differently, by analyzing shape-based metrics it may be possible to extract information about the nature of the vegetation.

This study tests a novel combination of full-waveform lidar and field-based methods. The field techniques used were developed to extract vegetation characteristics from digital photography (Zehm et al. 2003; Neumeier 2005; Möller 2006) and were adapted for this lidar

investigation. In research conducted by Möller (2006), vertical plant density was determined from digital photographs and related to roughness coefficients for water flow across the marsh. In this research, the vertical plant density and distribution were expected to have a measurable effect on the lidar pulse returns. Vertical profiles of salt marsh vegetation obscuration (VO) [%] and biomass by height (VB) [g/m^3] were investigated in their undisturbed growth position using in-situ digital photography. These data, along with other biophysical parameters collected in the field (including physical samples or those derived from photography), were used to examine relationships among the parameters and metrics extracted from lidar waveforms. The primary focus was on *Spartina alterniflora*, but other common and dominant salt marsh species were also included in the study. The hypothesis is tested that some simple waveform metrics such as waveform width, waveform standard deviation, and amplitude contain information that can assist in estimating salt marsh biophysical parameters such as vegetation height, stem density and biomass.

Methods

Study Areas and Ecosystem Description

The study sites comprised four mesotidal salt marshes (Hatches Harbor, Moors marsh, Pamet River marsh, and Great Island - Middle marsh) on the protected bay coast of Cape Cod, Massachusetts, USA (**Figure 3.2**), with field investigations conducted between July and August, 2010. This part of Cape Cod Bay exhibits a semidiurnal tide with a mean range of ~2.83 m (NOAA, 2013). All the marshes are largely low marsh dominated by *Spartina alterniflora* (smooth cordgrass) growing upon sandy substrata with typically a small rim of high marsh platform. Marsh sites were chosen based on their proximity to each other to maximize the data

collected from a 40 km^2 lidar flight area, the availability of large stands of as many major marsh species as possible, and the ability to collect the field data within a specified time window around the July, 2010 overflight conducted by the National Center for Airborne Laser Mapping (NCALM). In general, wind conditions at the sites averaged 2.5-5.3 m/sec (NNW) during most survey days, but occasionally reached up to 7.6 m/sec. Multiple sample locations for each vegetation species type were collected to determine reproducibility of the results and investigate variability within each species type.

Hatches Harbor, a 2.2 km^2 (1.2 km^2 unrestricted with full tidal flow, 1 km^2 restricted with partial flow) salt marsh located at the eastern-most tip of Cape Cod, is one of the youngest marshes in the northeastern United States, due to the timing of the Provincetown sand spit formation (Uchupi et al. 1996; Portnoy et al. 2003). Dominant plants that form large monoculture stands are *S. alterniflora*, *Salicornia bigelovii* and *Salicornia depressa.* (succulent forbs) (Portnoy et al. 2003).

Moors marsh (2.0 km^2) is located behind a long, 1.6 km rock breakwater that allows water to flow through its porous structure. Monitoring during this study with pressure transducers found the amplitude of the natural tides were muted by 2-4 cm and had a temporal lag of up to 30 minutes. This marsh, like Hatches Harbor, is dominated by *S. alterniflora* with sporadic large monocultures of *Salicornia spp.* There is a small fringe of high marsh located at the shoreward edge dominated by *Spartina patens* (salt marsh hay).

Pamet marsh (2.0 km^2) has two distinct branches: the Little Pamet River, which heads north, and the main Pamet River, which lies to the east of an old railroad causeway built on the marsh. Both sides of the railroad dike are considered unrestricted with full tidal flow exchange with Cape Cod Bay. Each location exhibits a slightly different morphology and vegetation. The

Little Pamet has a low lying marsh morphology dominated by *S. alterniflora* with very little high marsh platform. The Pamet marsh morphology has a more significant portion of high marsh platform with *S. patens* and *Distichlis spicata*. A large segment of the marsh appears to be in collapse, exhibiting complex patterns of deterioration and the formation of numerous tidal channels, mudflats, and shrinking islands (Smith 2009).

Great Island - Middle Marsh (0.3 km^2) is a small back-barrier marsh with a broad high marsh platform dominated by *S. patens* and *D. spicata*. Of the four marshes investigated, this is the only one that contains extensive ditching that predates a 1947 aerial photograph. There is a large expanse of high marsh plateau with dense stands of *S. alterniflora* in its lower reaches and channels (**Figure 3.3**). However, extensive areas of bare ground were formed at this site due to marsh wasting (Smith 2009).

Homogeneous, near monoculture stands for three major species and one genera (*S. alterniflora, S. patens, D. spicata*, and *Salicornia spp.*) were commonly found at the study sites and so were chosen for analysis. Salt marshes exhibit vegetation zonation based on elevation and plants adaptations to the harsh conditions (Bertness and Ellison 1987). Different marsh species have varying morphologies as well as growth habits. Measurements of salt marsh vegetation above-ground biomass may be useful for determining lidar penetration properties, but only if measured for the vertical distribution of biomass (VB). Variability in growth habit and height within one community is also common.

This study investigates two forms of *Spartina alterniflora* (medium form (MF) 50-100 cm and tall form (TF) >100 cm) in the analysis. The mean sample height for *S. alterniflora* (tall and medium) out of 13 stations was 115 cm, with a minimum height of 60 cm, a maximum height of 170 cm and a standard deviation of 34 cm. Regional differences in vegetative zonation,

communities, and structure exist between northern and southern salt marshes (Ewanchuk and Bertness 2004). *S. alterniflora* has at least two distinct variations or ecophenes, short-form (SF) <80 cm and tall-form (TF) >100 cm, caused by edaphic factors in northern marshes (Anderson and Treshow 1980). In some locations, three ecophenes are sometimes defined as 0-50 cm (SF), 50-100 cm (MF), >100 cm (TF) (Reimold et al. 1973; Ornes and Kaplan 1989; Wiegert and Freeman 1990; Pennings and Bertness 2001; Hladik and Alber 2012). Tall-form typically grows along estuarine creeks with semidiurnal flooding and can exceed 2 m in height. In contrast, short-form is typically found in high marsh areas with higher salinity, sulfide concentrations and/or lower redox potential (Mitsch and Gosselink 2000).

Vegetation Photographic Measurements

The development of an in-situ, field-based tool for measurement of the vertical mass distribution and light blocking properties of shorter, coastal grasses is needed for assessing lidar penetration properties. In addition, it will assist in developing new ways to perform calibration and validation ("cal/val") of overhead remote sensing data. Therefore, an apparatus was designed and built to measure VO consisting of 3 main components: a downward-looking camera on a tripod pole, a mirror at a 45 degree angle to the ground, and a red background board with a calibration scale (**Figure 3.4**). A collapsible A-frame was constructed out of lightweight aluminum to house a 0.35 m by 1.38 m flat mirror. The camera used was a Casio EX-Z35 12.1 megapixel digital camera with a 3x zoom, an aperture of f3.1-5.6, and a focal length of 35.5-106.5mm (Shutter speed 1/2000 second, aperture 3.1W, and depth of field 8.76 m). This camera was mounted and leveled on a standard tripod, which was extended and inserted into an arm of the A-frame so that the camera field of view was centered on the mirror where distortion due to

camera optics is minimized (Straatsma et al. 2008). Lastly, a 0.75 m x 1.5 m red foamcore backboard on a frame of wood was constructed with a pre-attached vertical scale of alternating white and black centimeter squares. The board also had a pre-calibrated optical depth scale (the distance from the board to the base of the mirror) to facilitate rapid setup of the board for the two optical depths used in this project. Since the optimal optical depth for each vegetation species was unknown, the background was first set at 25 cm from the mirror and imaged multiple times before resetting the background to 10 cm for a second series of images. The resulting pixel resolution was approximately 1.8 mm and 1.6 mm GSD (Ground Sample Distance), respectively, at each ground sample station.

Planimetric (areal) vegetation coverage is an important measurement that is expected to relate to data obtained from remote sensing systems, due to the similarities in viewing geometries (i.e., near nadir). Planimetric photos were taken prior to any site disturbance by the equipment. The camera was set on the tripod at a height of approximately 2 m and a planimetric photo of the ground and calibration rod was captured with the same digital camera used for the profile photography. Excessive shadows caused by direct sunlight were found to be a challenge for both the planimetric and profile photography. Therefore, several methods were used to reduce the exposure and influence of direct sunlight such as choosing field days with diffuse illumination conditions, positioning equipment so the image was not in direct sunlight, and the use of a shade umbrella when the other two methods were not possible.

Biomass Measurements

The calibration of the digital photography required physical biomass measurements and an understanding of its vertical distribution above ground. The methodology used to determine

biomass and vertical density are similar to the methods used by several other researchers (Zehm et al. 2003; Neumeier 2005; Nobis and Hunziker 2005; Möller 2006) and employed a standard 0.25 x 0.25 m quadrat, a calibrated staff for height measurement, and a 3 cm tall ring of PVC pipe (10.16 cm inner diameter), through which the vegetation samples were pulled for subsequent measurement (**Figure 3.5**).

The vegetation samples were washed and dried to remove all moisture before measuring. The in-situ sample was carefully cut into 5 cm lengths starting from the base of the stalk (ground) and measured for mass by height, representing the VB measured height. This produced 359 subsamples of mass at specific heights for comparison to the photographic data. Because VB samples were a subset of the quadrat, their combined biomass is the equivalent of a standard quadrat biomass measurement. Stem density [n/m^2] was also counted from the physical quadrat for *S. alterniflora* and from the in-situ samples for *S. patens*, *D. spicata*, and *Salicornia spp*.

Ground Photography Image Processing/Analysis

For each sample location surveyed, the highest quality image from each optical depth was selected based on clarity of focus, image rotation, contrast, and position. Histogram processing was then applied to adjust for varying illumination levels (e.g., due to differing sun angles or atmospheric conditions), such that the backgrounds were consistent across images. The resulting images were comprised of vegetation, background (air space), and a scale bar.

VErtical vegetation STructure Analysis (VESTA) and Sidelook software was used to analyze the vertical vegetation structure from the digital photography (Zehm et al. 2003; Nobis and Hunziker 2005). Color photography taken in the field was run through a threshold tool using the green band to create a binary image with pixels classified as vegetation (black) or airspace

(white) (**Figure 3.6**). Tabular data of VO were generated by counting vegetation pixels vs. airspace by height in incremental bins of 5 cm by 33 cm (width of usable image on mirror), which correspond with the same biomass height increments collected in the field/laboratory work. For a specified height bin, VO is computed as:

$$vo = 100 \times \frac{Num\ veg\ pixels}{Total\ pixels} \qquad (1)$$

An uncertainty analysis of VO was performed modeling each component uncertainty (e.g., lens distortion, mirror parameters, mixed pixels, and threshold), and was determined to be on the order of 1-2%, which is an order of magnitude better than what can be obtained from the lidar data. Total Vertical Obscuration (TVO), defined as the VO for the entire height of the vegetation (i.e. VO for the entire image) was computed. This quantity was then multiplied by the image area computed as the product of image width (0.33 m) and vegetation height to obtain a parameter referred to as Proportion of Vegetation Area (PVA) [m^2].

Planimetric image vegetation coverage was also extracted from the collected digital photography. It was determined that the best approximation of down-looking vegetation coverage could be obtained using the same green band histogram threshold contrast between the vegetation and the dark ground surface/leaf litter. Excessive light colored leaf litter in the image may overestimate ground cover while dark shadows on the vegetation stems may underestimate ground cover. Although shadows and leaf litter may slightly positively or negatively influence the overall calculation of vegetation cover, contrast of the ground with live vegetation was considered as the best approximation ground cover conditions.

Lidar Data Processing

A July, 2010 lidar survey flown specifically for use in this study was compared with the field collected data. The lidar flight was conducted by the NCALM using an Optech GEMINI Airborne Laser Terrain Mapper (ALTM) and an Optech 12-bit IWD-2 intelligent waveform digitizer (**Table 3.1**). The sites in this study were comprised of marsh vegetation, "bare earth" and water (i.e. no trees, buildings, or other structures), so the data were almost entirely composed of single-return only pulses. A Trimble NetR5 base station network with cellular-based correction and a Trimble R8 Model 3 Real Time Kinematic (RTK) GPS rover was used in the field data collection. The equipment provided an RMS of < 1 cm in the horizontal and 2cm in the vertical for each of the 27 ground sample stations. The field and airborne data were collected within two weeks of one another.

Waveforms were selected for the 27 sample locations from the larger database by developing a custom workflow using ArcGIS, QCoherent LP360 and MATLAB to extract lidar waveforms and compute waveform shape-related metrics for the closest lidar point to the center of each of the 27 sample locations, typically within 0.5m radius. For this study five simple metrics were computed from the received return waveform: waveform width (full width half maximum [FWHM]), sample skewness (a skewness measure of the waveform vector elements), waveform amplitude, waveform standard deviation, and Pearson's 1st skewness coefficient (mean – mode)/standard deviation (Parrish et al. 2014). Skewness is a measure of the asymmetry between the upper and lower sides of a distribution, where a longer tail to the lower portion would indicate positive skewness. Comparisons of the extracted waveform metrics to physically and photographically collected data were made to investigate the relationships to biomass density, VO and cumulative biomass.

Results

Vertical Biomass (VB) and Obscuration (VO)

The first relationships investigated were between field collected plant biomass and vertical obscuration to determine a possible connection with lidar signal loss and the potential for using full waveform data to detect salt marsh vegetation biophysical parameters. Linear, Pearson's correlations between the 359 VO and VB height subsamples were computed from the 27 sample locations surveyed in this project (**Table 3.2**) and all correlations reported are significant with a $p < 0.05$ unless otherwise noted. Comparison of all vegetation samples across all species as a group exhibited a correlation between VO and VB of $r = 0.59$ (312 df) [degrees of freedom (df = n-2)], $p < 0.05$ and $r = 0.53$ (357 df), $p < 0.05$ for the 10 and 25 cm optical depths, respectively (**Table 3.3**). Examining specific species, *S. patens* and *Salicornia spp.* exhibited weak correlations compared to *D. spicata* and *S. alterniflora*. The best VO to VB results were from *S. alterniflora*, which showed a correlation of $r = 0.80$ (216 df) and $r = 0.70$ (245 df), for the 10 cm and 25 cm optical depths, respectively (**Figure 3.7a**). Individual *S. alterniflora* samples performed even better, often with results of $r > 0.90$. For example, sample GA3 had a correlation coefficient of 0.97 (20 df) (**Figure 3.7b**). A notable improvement in species correlation also was observed when the MF and TF *S. alterniflora* ecophenes were separated (Table 3). As subsets, the *r* value obtained was MF 0.89 (93 df) for the 10 cm optical depth and 0.85 (93 df) for the 25 cm optical depth, while TF improved to 0.84 (120 df) for the10 cm optical depth and 0.77 (152 df) for the 25 cm optical depth (**Figure 3.7c, d**). The Pamet marsh TF *S. alterniflora* samples exhibited low correlation due to windy conditions (WNW winds at approximately 7.6 m/sec) in the marsh resulting in the topmost leaves blowing out of the image and sample PA5 was removed entirely from all analyses for this reason. In most

cases greater coefficients were observed in the sample groups using the 10 cm optical depth, but individual samples seemed to correlate better using the 25 cm optical depth.

Height Assessment

Recording field measurements of vegetation heights directly with a calibrated staff can often be subjective because each observer or even the same observer on multiple visits may record stature differently for the same stand (Zehm et al. 2003; Neumeier 2005; Straatsma et al. 2008). To evaluate the consistency of the methods, an assessment was conducted of field-observed height as it compared with the VB sample heights, which was determined by extending the in situ collected plants to their full length. A comparison utilizing samples of all species surveyed for field observed height to VB sample measured height for the 25 cm optical depth exhibited an $r = 0.97$ (25 df) (**Figure 3.8a**). However, only the *S. alterniflora* indicated a similar correlation, $r = 0.97$ (11 df). Field observations of *S. alterniflora* heights were consistently lower than VB measured heights by a mean of 4.5 cm but *S. patens*, *D. spicata* and *Salicornia spp.* was found to have no significant correlation and exhibited lower measurements by a mean of 20 cm.

A similar comparison was made between field observations of vegetation height and photographically-derived vegetation heights from the VO binary images. All samples collected had a linear correlation with $r = 0.97$ (25 df) for the 25 cm optical depth (**Figure 3.8b**). As with the previous mentioned analysis, the *S. alterniflora* samples in this comparison demonstrated better results with an $r = 0.89$ (11 df) for the 25 cm optical depth and no significant correlation observed for the other surveyed species. Also, field observations were consistently lower than photographically derived heights with *S. alterniflora* exhibiting a mean difference of 8.6-14 cm and the other taxa differing by a mean of 10.4-16.8 cm**.**

Lidar Waveform Analysis

The results of the lidar waveform analysis are presented in terms of Pearson's correlation coefficient (r) since the goal of this initial test was merely to determine whether there were any relationships between the variables. Several of the parameters correlated well with waveform width and waveform standard deviation (**Table 3.4**). Evaluating all samples without speciation often yielded the best results. A strong positive linear relationship was observed between the width of the lidar waveform return and the height of the vegetation $r = 0.82$ (25 df) (**Figure 3.9a**). Within the subset of *S. alterniflora* samples, the parameters vegetation height exhibited a correlation to waveform width with an $r = 0.75$ (11 df).

Waveform amplitude correlated with planimetric obscuration with an $r = 0.71$ (25 df) for all samples and $r = 0.62$ (11 df) for the subset of *S. alterniflora* (**Figure 3.9b**). Sample skewness was found to correlate with quadrat stem density, which had an $r = 0.63$ (25 df), while Pearson's 1st skewness coefficient showed no significant correlations with any vegetation metrics. Using Proportion of Vegetation Area (PVA), the ability to relate the VO measurements from the field photography to the waveform shape metrics was tested. PVA was found to correlate well with waveform width $r = 0.73$ (25 df) (**Figure 3.9c**).

Having found some significant correlations, simple and multiple linear regressions were used to investigate the ability to predict the vegetation biophysical parameters from the best performing waveform metrics found in **Table 3.4** (**Table 3.5**). It is important to note that waveform width and waveform standard deviation are nearly collinear (Parrish et al. 2014), which is to be expected, as they are both measures of the spread of the return pulse. Waveform parameters were evaluated and those that were found to be highly correlated were removed from further analysis. Most of these multiple parameter combinations yielded little or no

improvement with the additional parameter in the regression. However, it was observed that in several instances improvements to *r* values were observed when including an additional waveform parameter. The regression of vegetation height on waveform width improved from r^2 = 0.68 to R^2 = 0.72 with the addition of waveform amplitude (note that r^2 is used to denote the coefficient of determination in the case of simple linear regression, while R^2 is used in the case of multiple regression). Most notably, the regression of vegetation height on waveform standard deviation improved from r^2 = 0.53 to R^2 = 0.74 with the addition of amplitude (**Table 3.5**).

Discussion

Biomass and Obscuration

While previous research has documented relationships between the total above-ground biomass of *S. alterniflora* and its height (Howes et al. 1986; Morris and Haskin 1990), this research investigated the distribution of mass throughout plant height for several species and then compared the biomass density to its light blocking properties (**Figure 3.6**). The research presented here suggests a strong linear relationship between VO and VB particularly for *S. alterniflora* (**Figure 3.7**). Other researchers working with different vegetation species, including some in European salt marshes, also found similar relationships (Zehm et al. 2003; Möller 2006). However, in the case of this study not all species investigated exhibited strong correlations. Thus, vegetation species appears to be a key determinant of the nature of the relationship. The vertical growth habit of the *S. alterniflora* makes it ideal for analysis by the VO and VB methods. *S. alterniflora* stalks typically grow vertically 20 cm – 200 cm with narrow leaves at the top. Spacing between individual plants varies, but is normally several centimeters, providing sufficient void space for analysis. Temporal variation is also dramatic between peak growth

conditions and senescence with stalks tending to fall over or even stripped from the marsh due to ice from winter conditions in northeastern U.S. salt marshes (Ewanchuk and Bertness 2004).

The relationship of obscuration to biomass may also be further refined by looking at *S. alterniflora's* two ecophenes assessed in this study, MF and TF. Correlation was significantly higher when they were individually analyzed, where Pearson's correlation coefficients increased from around 0.80 to 0.89 for MF and 0.84 for TF at the 10 cm optical depth. It appears these ecophenes may have subtly different biomass and obscuration properties in addition to their differing heights. *Distichlis spicata*, in the limited number of sample locations used in this study also exhibited a vertical growth habit. However, *D. spicata* and *S. patens* more often form a thick mat or thatch-like structure low to the ground, approximately 15-30 cm in height and with a high stem density. *Salicornia spp.* was also evaluated and initially thought would perform well, but did not appear to support a relationship between VO and VB despite its typically upright growth habit. Its dense interlocking stems created an almost opaque wall obscuring the background board to nearly the top of the vegetation, regardless of the optical depth used for the imagery.

Vegetation Height

Comparisons among the field observed heights, physical biomass measured heights and photographically-derived heights show strong correlations with physical or photo derived measurements having a positive bias with respect to field observation in all cases (**Figure 3.8a, b**). Field observed heights were consistently lower than the VB measured heights and photographically derived heights, particularly with the low growing species such as *S. patens*, *D. spicata*, and *Salicorina spp*. In comparison to VB sample heights measured physically the bias is

clearly due to the growth habit of the vegetation. These plants consistently had heights 14 to 20 cm higher than the field approximation because their leaves and stems lie flat against the ground. The height measured from VB samples in this case created an incorrectly assumed upright growth habit that does not typically occur for these species and therefore the VB method is not an effective method to determine vertically distributed biomass for these species.

Photo-derived and the field measured heights also displayed high correlation with r of between 0.96-0.97 for the two optical depths, which is consistent with the results reported by Zehm et al. (2003) using similar techniques. However, although smaller than the measured sample height bias, a positive bias with a mean of 9 cm was still observed. The source of this bias is most likely due to the steep viewing angle between the observer and the lower portion of the stadia rod when measuring low growing vegetation. As a consequence, field observations were consistently lower in this class of vegetation. *Spartina alterniflora* photographic derived height measurements were also positively biased over field observations by 4.5 cm (10 cm) and 8.6 cm (25 cm), which may be a function of detecting the fine leaf details in the imagery that a field observer would have difficulty measuring. Although the field observed method was clearly the fastest method for determining vegetation height, it was not always the most accurate. The digital photographic approach is useful for comparing small differences or percentile thresholds that cannot be achieved by visual estimates in the field alone (Neumeier 2005).

Waveform Lidar

The strength of linear relationships between five simple, shape-based waveform metrics and the collected biophysical parameters were assessed. It appears that some of the simple shape-based metrics show promise in predicting various vegetation characteristics in addition to

predicting lidar bias (Muss et al. 2013; Parrish et al. 2014). As demonstrated in **Table 3.4**, a moderate to strong relationship was found between several of the measured biophysical parameters with waveform width or waveform amplitude. Each of the highlighted relationships appears to have a logical basis. For example, the relationship between waveform width and vegetation height can be can be attributed to the fact that the convolution of the laser pulse with an extended target (i.e., taller vegetation, although still less than half the transmit pulse width, converted to a range) will result in greater spreading of the return pulse (**Figure 3.9a**). Also, waveform amplitude appears to increase with increased planimetric obscuration, which can be explained by the fact that dense, healthy vegetation results in higher amplitude returns, especially at the near infrared wavelength of the laser (**Figure 3.9b**). Similarly, waveform width was expected to increase with increasing PVA, since, in areas of higher TVO, the pulse does not penetrate the lower layers of the vegetation, which would increase spreading of the return pulse (**Figure 3.9c**).

Visible on these graphs (**Figure 3.9**) is a clustering of points of non-*S. alterniflora* species that, when taken without the *S. alterniflora* data points, exhibit almost no correlation. All of the non-*S. alterniflora* species found and sampled in the marshes have nearly the same characteristics and growth habit, such as height (~20-35 cm), planimetric obscuration, and PVA. Therefore it is quite logical that clustering would occur, and a lack of correlation is not unexpected. *Spartina alterniflora* in these marshes was observed to include all of the ecophenes (SF, MF, TF) varying in height from 5 cm to 200 cm. However, the samples of *S. alterniflora* collected and analyzed for this study did not include a representative selection of SF samples (<50 cm) and only used MF (50 cm – 100 cm) and TF (>100 cm) samples. *Spartina alterniflora* exhibited a stronger correlation with the waveform metrics analyzed than the non-*S. alterniflora*

species due to the natural variability in its growth height, planimetric obscuration, etc. For example, in our analysis of waveform width and vegetation height if samples of SF *S. alterniflora* with heights less than 50 cm were to be added, the correlation with the waveform width would likely have been much stronger even without the addition of the other species. The non-*S. alterniflora* species fill in the gap in the height distribution and increase the coefficient of determination. It is only when all the species found in the marsh, varying in all vegetative characteristics, such as height from 0 – 2 m, that a strong relationship starts to appear.

The results of multiple linear regressions were also promising. Waveform amplitude and waveform standard deviation accounted for nearly 75% of the variability in vegetation height. In addition, waveform width and amplitude accounted for 60% of the variability in quadrat stem density. It should be emphasized that the lidar system used in this study had a long transmit pulse width of ~12 ns at 70 kHz PRF (Table 1). Further research is needed to assess whether the methods developed here are applicable to lidar systems with shorter pulse widths. For example, with much shorter transmit pulse widths, the returns from marsh vegetation may be multi-modal, necessitating a modification of the waveform processing algorithm. Another possible extension involves computing and applying corrections to the waveform features for variable incidence angle. In previous work, Parrish et al. (2014) investigated the effects of pulse broadening with incidence angle, using the geometric pulse stretching model of Abdallah et al. (2012), and found it to be negligible with the low flying height (600 m), narrow beam divergence (0.25 mrad) and relatively small scan angles (+/- 21°), similar to those used in this study. This finding is consistent with that of Bretar et al. (2009). Likewise, in an empirical study using different sediment types (e.g., sand and gravel), Kukko et al. (2008) found the decrease in signal amplitude to be negligible for incidence angles up to 20°. However, these authors examined only

the change in incidence angle on the target surface, and not the slight increase in target range that also occurs with increasing scan angle (assuming constant flying height and surface elevation and a scan mechanism that scans back and forth through nadir). Thus, another recommended topic for further research is to compute range-based corrections to the waveform metrics to see if this changes the correlations with vegetation biophysical parameters.

Conclusion

The primary conclusions from this study can be summarized as follows: (1) There is a clear relationship between VB density and VO, and this relationship is species dependent; (2) The VO method provides an alternative to field-based height data collection. Field-based collection can be more efficient, but when consistent, quantifiable, high-detail data are needed, the VO method is superior; (3) The vertical biomass (VB) and vertical obscuration (VO) methods are measurements that can yield important information for use in future salt marsh and lidar investigations; (4) Simple, shape-related lidar waveform return metrics may be useful in estimating salt marsh biophysical parameters. It was found that waveform width and amplitude had significant correlations with vegetation height, planimetric obscuration, and PVA. Waveform data can offer additional information about the target not available in discrete-return data. However, there were differences between species specific and non-speciated results. These differences were likely a result of varying growth habits (vegetation height, density, and planimetric coverage). Some analyses performed better on a specific species, namely *S. alterniflora*, while others were improved by including all species, which likely fill a gap in parameter variability such as height.

Field techniques for data collection are accurate but often cumbersome in salt marsh environments. However, for projects covering large spatial extents (100s to 1000s of km^2) it is typically cost- and time-prohibitive to collect field data over the entire project area. Full-waveform lidar holds the promise of providing more accurate salt marsh elevation models by detecting the ground/vegetation measurements within the discrete lidar dead zone of 2 or more meters (Nayegandhi et al. 2009). It may also have the ability to detect coastal vegetation biophysical parameters. The results of this study suggest that, in such situations, it may be possible to gain at least a coarse understanding of the vegetation biophysical parameters across the entire project area from analysis of the lidar data alone, to support conservation and management initiatives, while minimizing the amount of expensive, time-consuming field work that needs to be performed. It is recommended that the methods developed in this study be tested further, ideally with larger sample sizes than were logistically feasible in this work. Specific goals of the follow-on studies should include assessing : a) the ability to extend these methods to geographic locations with differing vegetation and geomorphology, b) how well the regression coefficients hold from one site or region to another, and c) the extensibility of the methods to lidar systems with shorter transmit pulse widths.
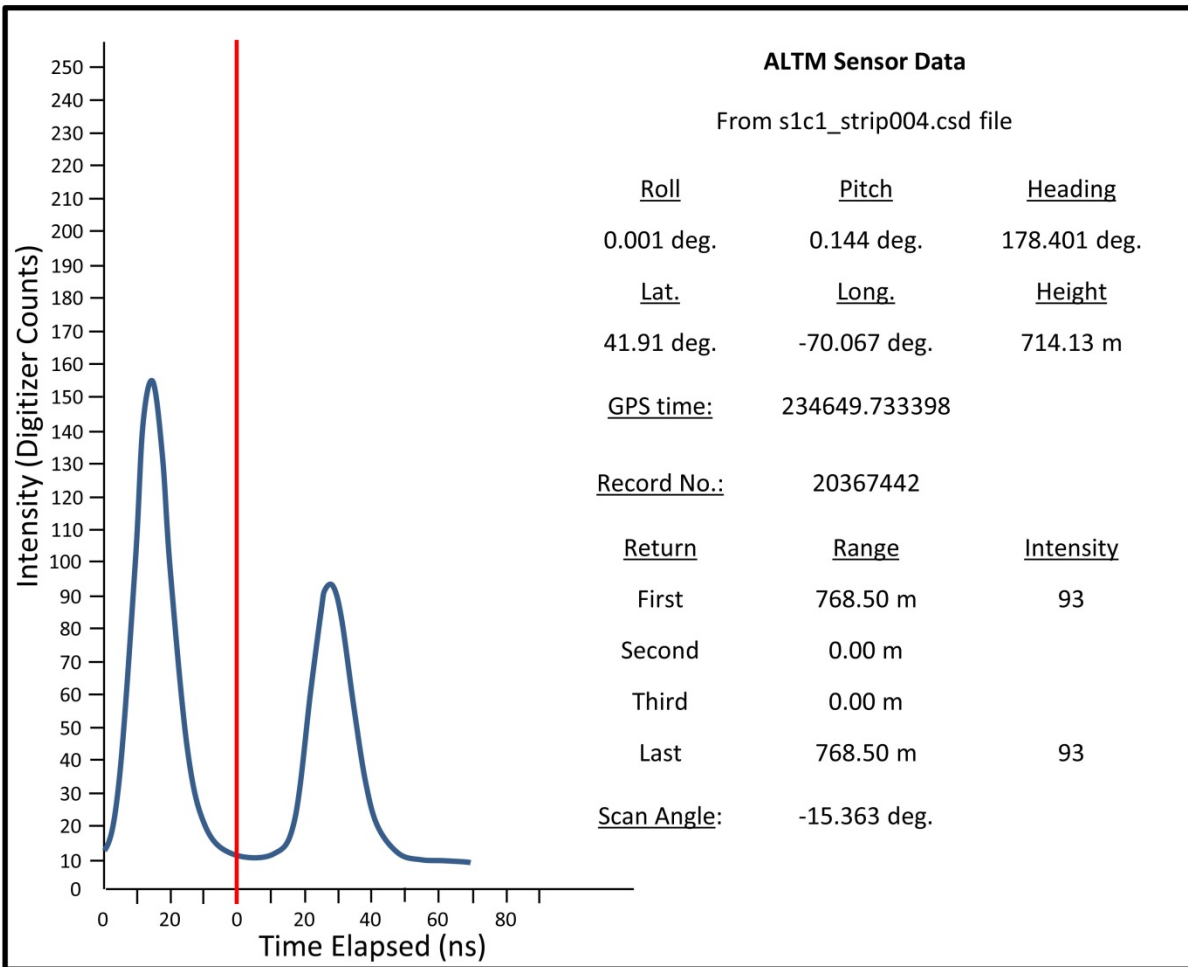
Figure 3.1: Example of a typical transmit pulse (to the left of the vertical dashed line) and return waveform (right of the dashed line) in a salt marsh (sample location GA3). Note that, although the return contains only a single peak, its shape may be influenced by the salt marsh vegetation, in which case there may be an observable relationship between shape-based metrics extracted from the waveform and vegetation biophysical parameters of interest.
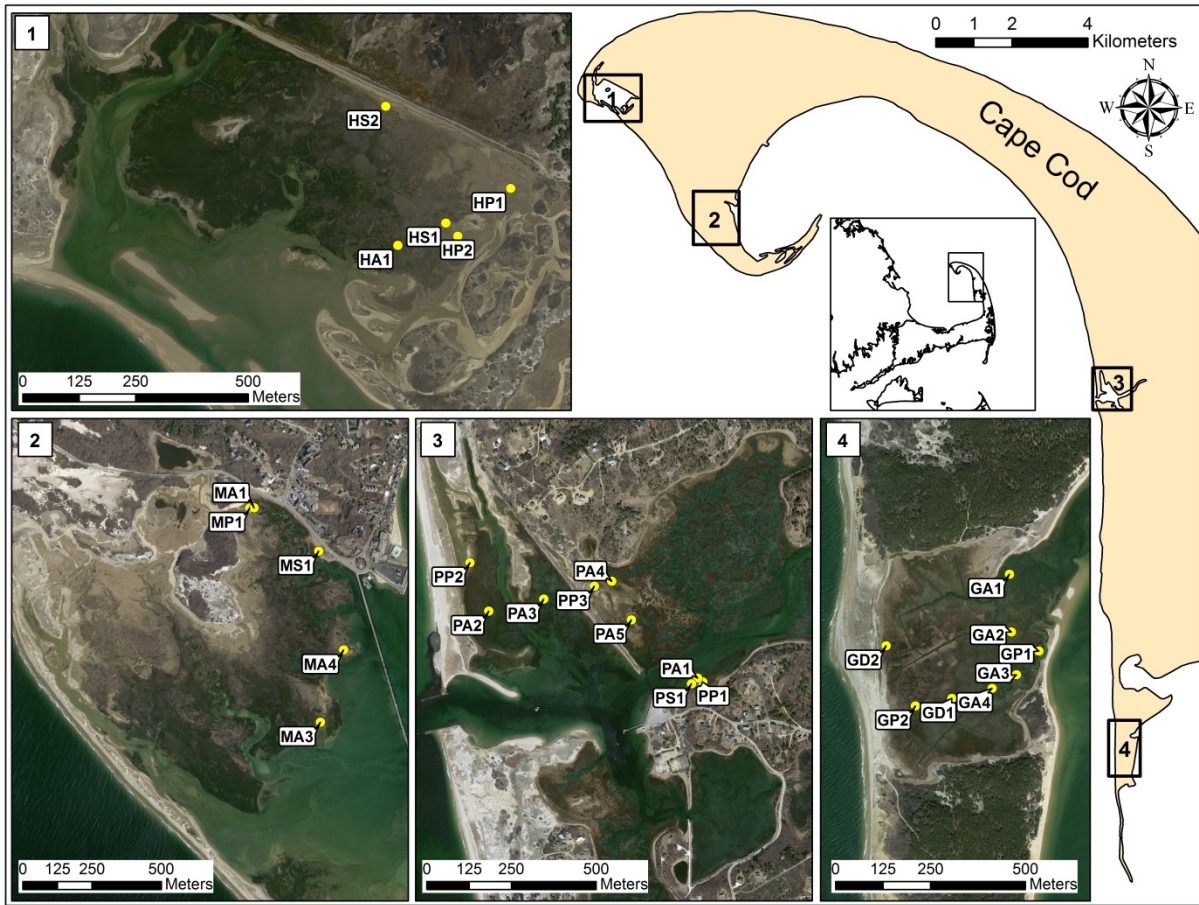
Figure 3.2: Site locus map and field sites. Insets are 1) Hatches Harbor, 2) Moors marsh, 3) Pamet marsh, and 4) Great Island – middle marsh. Labeled dots represent the 27 sampling locations.

Figure 3.3: Great Island - Middle Marsh tidal channel and *Spartina alterniflora*.
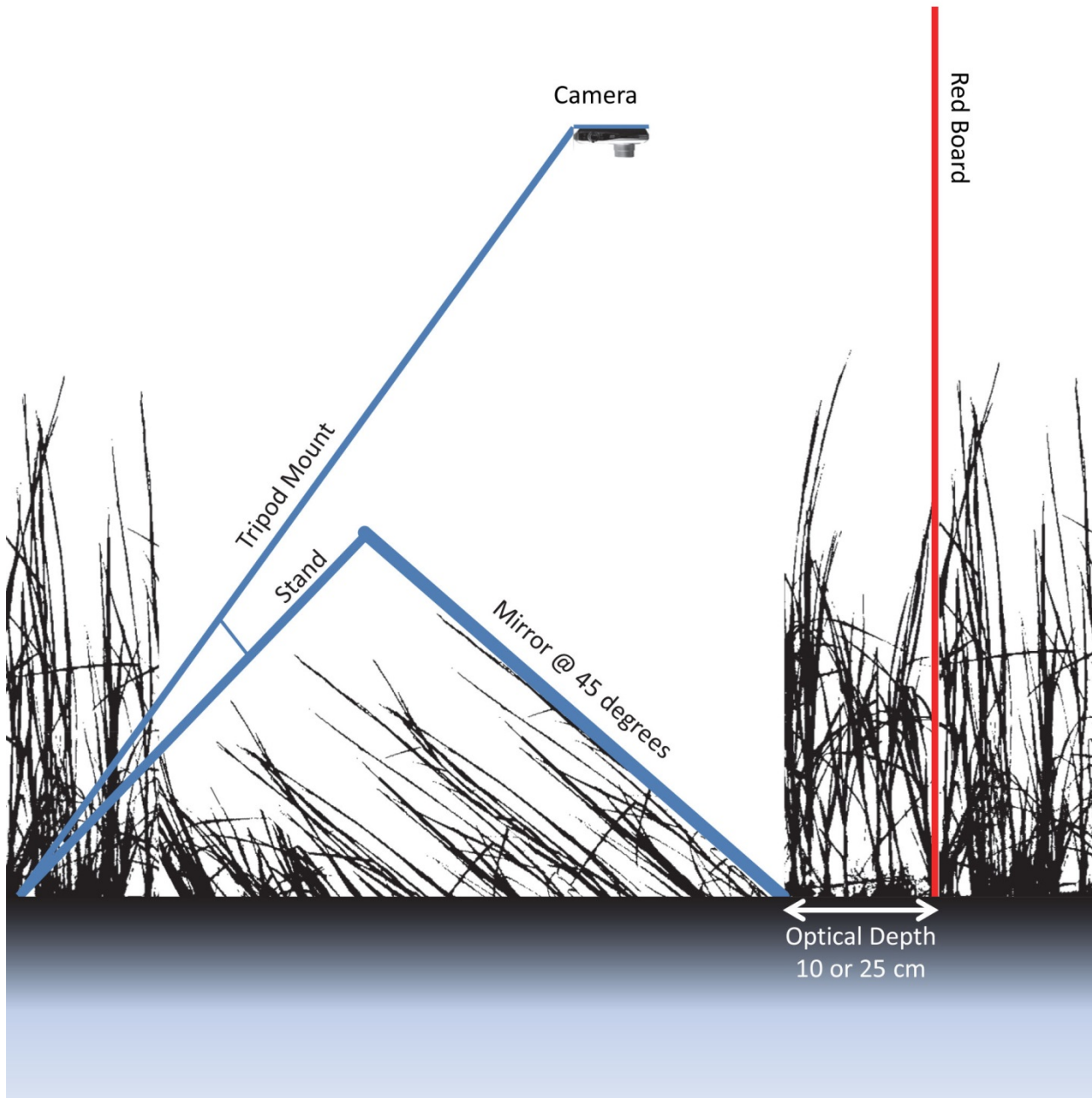
Figure 3.4: Camera and mirror equipment used to capture in-situ digital photography of salt marsh grasses.

Figure 3.5: *S. alterniflora* **vegetation sample plot HA3 with quadrat and in-situ sampling ring. The sampling occurs in front of the mirror after capturing the digital photographs.**
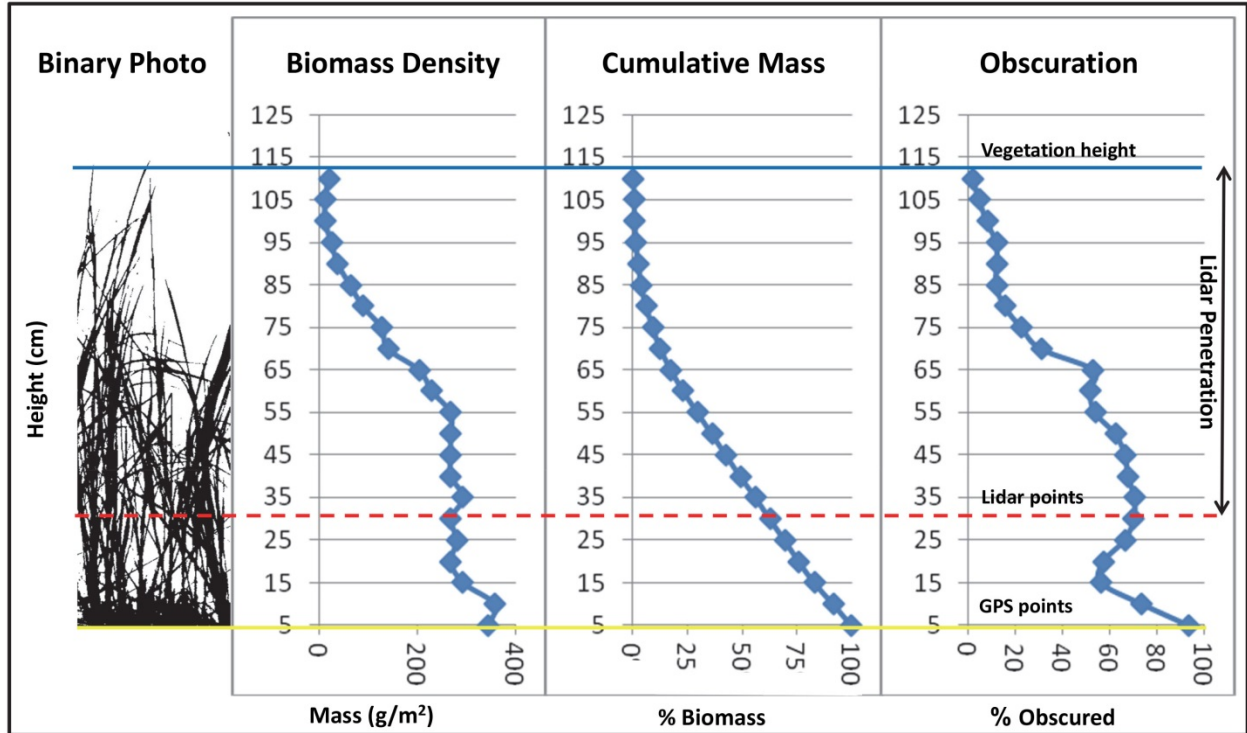
Figure 3.6: Binary vegetation image, vertical biomass density plot (VB), cumulative biomass %, and vertical obscuration (VO) for *Spartina alterniflora* sample location GA3 on Great Island. Yellow line is ground as determined from surveyed RTK GPS (GPS points), Red dashed line is the lidar elevation from the closest lidar return (lidar points), and Blue line is measured vegetation height from photo measurements (vegetation height). Due to the analysis groupings of 5 cm increments the first label reads 5 cm (0-5 cm) not 0.

Table 3.1: Flight parameters of NCALM July 20th, 2010 lidar data set.

Flight Parameter	Value
Flying Speed	60 m/sec
Altitude	600 m
Swath Overlap	50%
Laser Beam Divergence	0.25 mrad
Pulse Rate	70 kHz
Transmit Pulse Width	12 ns
Scan Rate	40 kHz
Scan Angle	± 21º
Point Density	5 pts/m^2
Laser Footprint	0.15 m

Table 3.2: Pearson's correlations between VB and VO at each of the field sample locations. "n" is the number of subsamples per sample location used in the calculation (i.e. number of 5 cm increments).

Species	Site	Location	10 cm Optical Depth		25 cm Optical Depth	
			r	n	r	n
S. alterniflora	Great Island	GA1	0.90	24	0.96	24
		GA2	0.81	15	0.83	15
		GA3	0.90	22	0.97	22
		GA4	0.88	22	0.94	22
	Moors Marsh	MA1	0.96	16	0.84	16
		MA3	0.92	28	0.94	28
		MA4	0.96	12	0.97	12
	Hatches Harbor	HA1	0.97	19	0.94	19
	Pamet Marsh	PA1	0.73	27	0.90	27
		PA2	-	-	0.89	29
		PA3	0.75	14	0.92	17
		PA4	0.94	16	0.96	16
		PA5	0.44	27	0.67	29
S. patens	Pamet Marsh	PP1	0.90	7	0.94	7
		PP2	0.93	5	0.94	7
		PP3	0.98	8	0.89	9
	Moors Marsh	MP1	0.25	4	0.80	7
	Great Island	GP1	0.22	8	0.39	8
		GP2	0.81	6	0.97	6
	Hatches Harbor	HP1	0.88	8	0.98	8
		HP2	0.99	8	0.82	9
Salicornia spp.		HS1	0.62	5	0.82	5
		HS2	0.63	5	0.87	7
	Pamet Marsh	PS1	0.91	7	0.97	7
	Moors Marsh	MS1	0.99	5	0.97	5
Distichlis spicata	Great Island	GD1	0.91	6	0.92	6
		GD2	0.69	5	0.73	5

Table 3.3: Correlation between VB and VO by species, site and ecophene with the number of sample locations (N) used in its calculation and subsamples (n). All correlations are significant with p < 0.05 except for *Salicornia spp*. 10 cm optical depth. Sample PA5 was excluded due to image problems caused by wind.

Analysis	10 cm Optical Depth		25 cm Optical Depth		N
	r	n	*r*	n	
All locations and species	0.59	285	0.53	326	26
All *S. alterniflora*	0.80	212	0.70	243	12
All Medium-form *S. alterniflora*	0.91	71	0.89	71	5
All Tall-form *S. alterniflora*	0.85	141	0.78	172	7
All non *S. alterniflora* species	0.46	73	0.46	83	14
Great Island - all *S. alterniflora*	0.84	81	0.84	81	4
Great Island - Medium-form *S. alterniflora*	0.83	13	0.81	13	1
Great Island - Tall-form *S. alterniflora*	0.87	68	0.93	68	3
Pamet - all *S. alterniflora*	0.79	56	0.52	87	4
Pamet - Medium-form *S. alterniflora*	0.90	30	0.91	30	2
Pamet - Tall-form *S. alterniflora*	0.71	26	0.46	57	2
Moors - all *S. alterniflora*	0.78	56	0.76	56	3
Moors - Medium-form *S. alterniflora*	0.94	28	0.88	28	2
Moors - Tall-form *S. alterniflora*	0.92	28	0.94	28	1
Hatches - Tall-form *S. alterniflora*	0.97	19	0.94	19	1
All *Distichlis spicata*	0.84	11	0.84	11	2
All *S. patens*	0.46	42	0.42	52	8
All *Salicornia spp.*	0.38	20	0.51	20	4
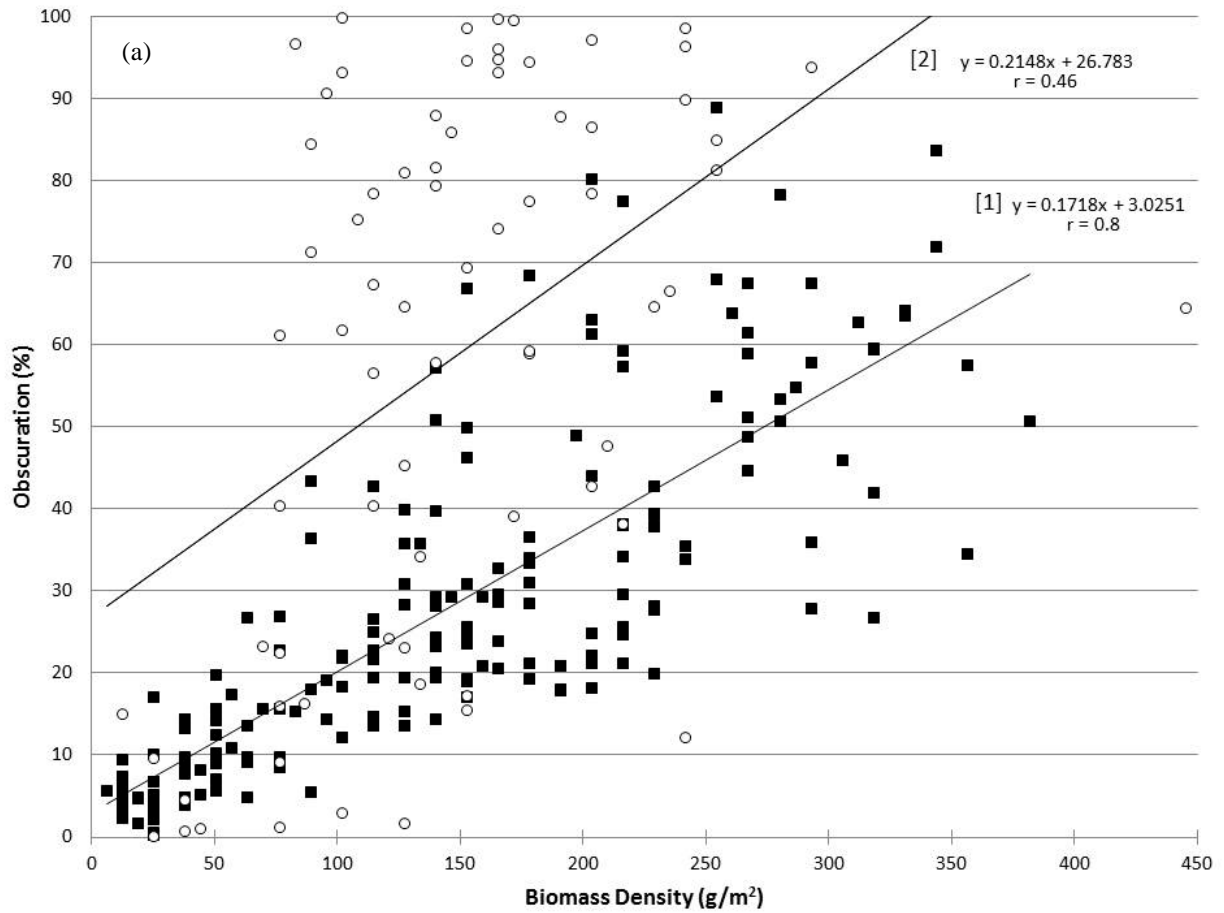
Figure 3.7a: Relationship of vertical obscuration with vertical biomass density for an optical depth of 10 cm. Solid square markers are all *S. alterniflora* samples represented by regression equation [1] and open circle markers are all other species represented by regression equation [2].

(b)

y = 0.23x + 0.6339

r = 0.97
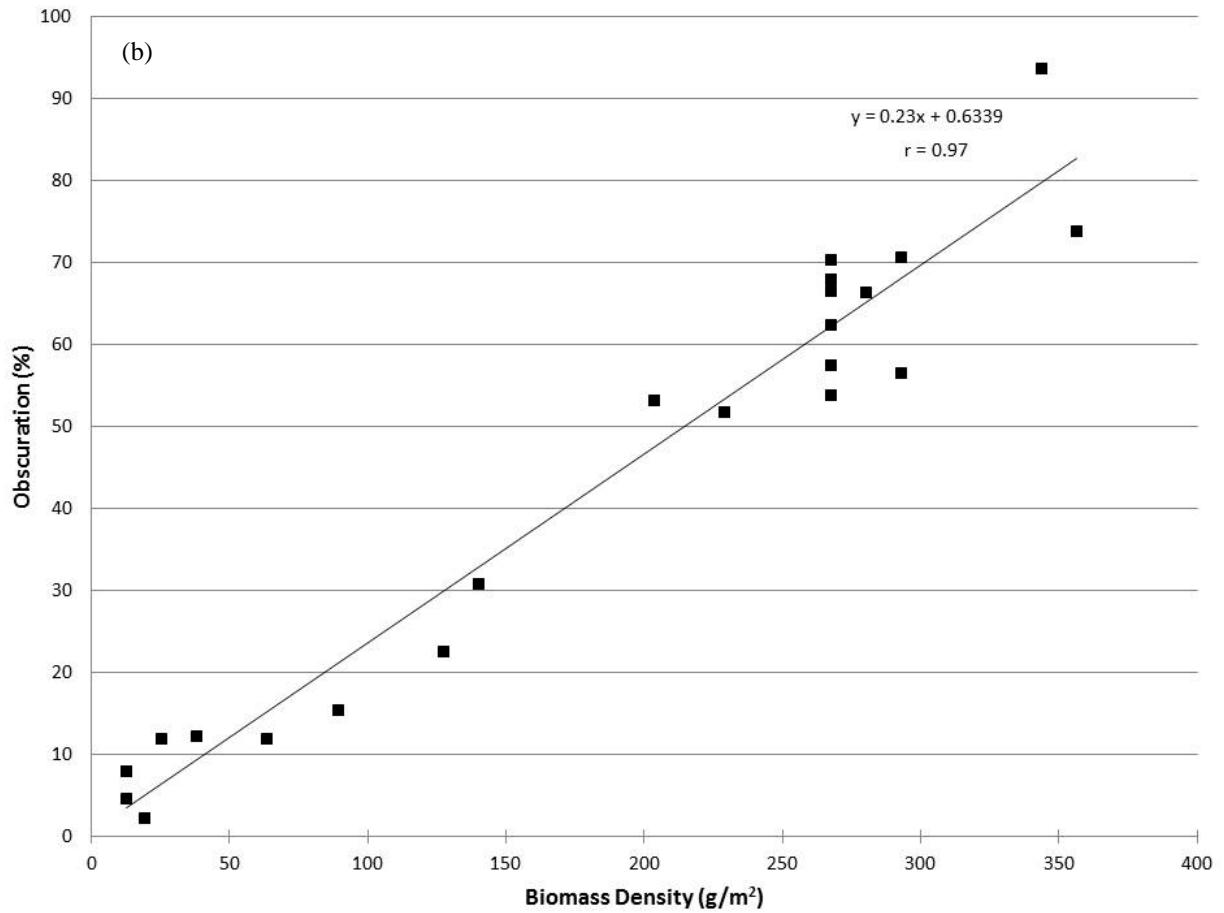
Figure 3.7b: Relationship of vertical obscuration with vertical biomass density for an optical depth of 25 cm for the *S. alterniflora* sample location GA3 from Great Island - Middle Marsh.
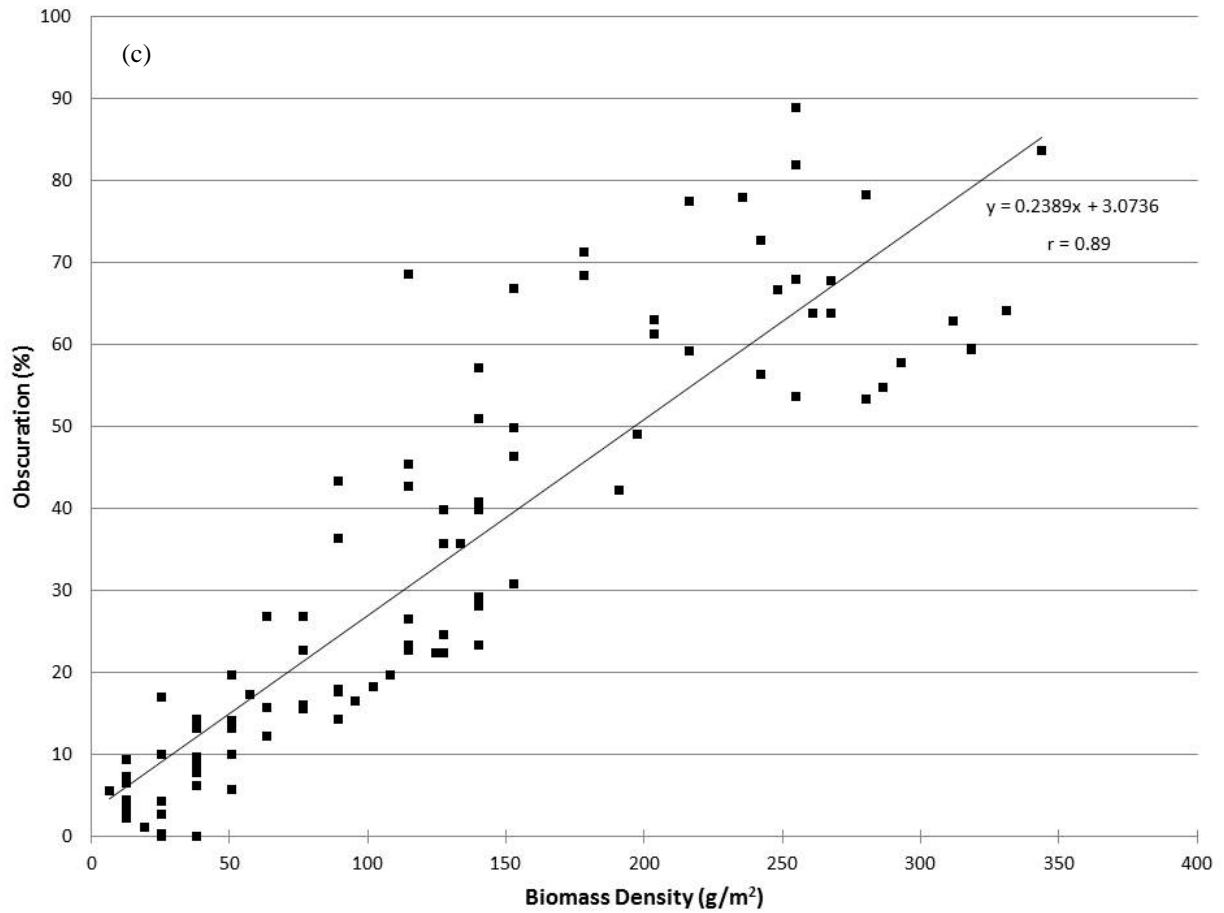
Figure 3.7c: Relationship of vertical obscuration with vertical biomass density for an optical depth of 10 cm for Medium-form *S. alterniflora* samples at all field locations.
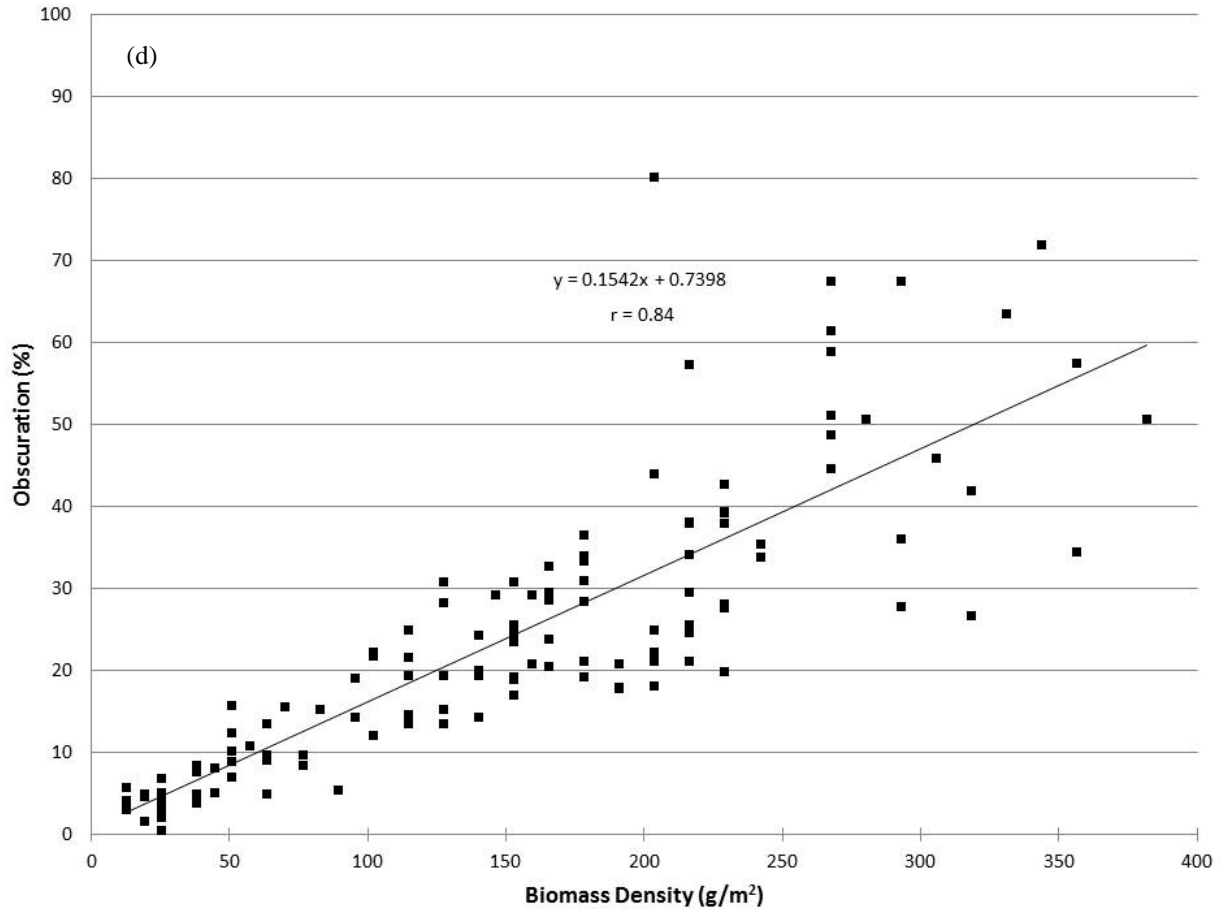
Figure 3.7d: Relationship of vertical obscuration with biomass density for an optical depth of 10 cm for Tall-form *S. alterniflora* samples at all field locations.
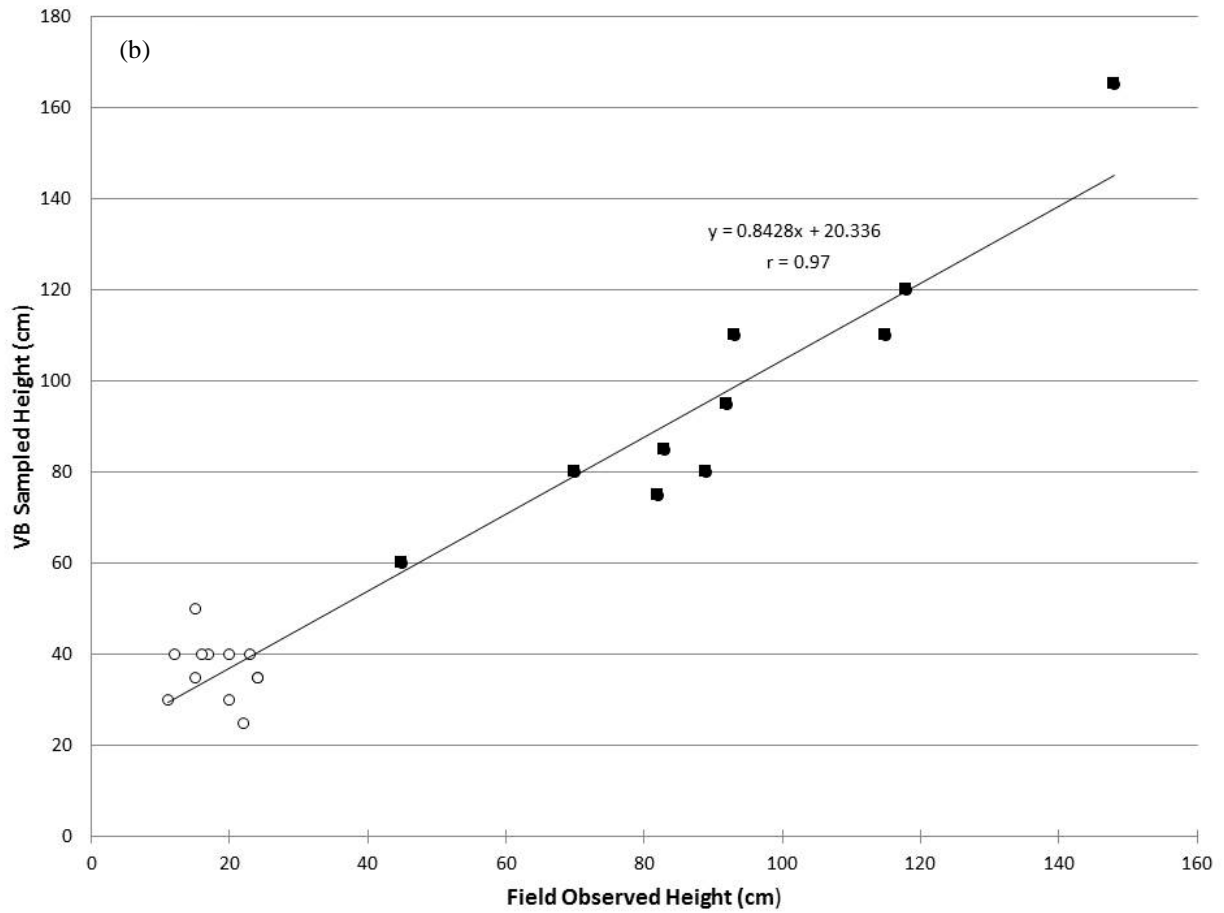
Figure 3.8a: Relationship of Vertical Biomass sample heights from the in-situ biomass samples with field observed height measurements. Solid square markers are *Spartina alterniflora* samples and open circle markers are all other species. All samples combined have an *r* = 0.97 (25 df), p <0.05, while the subset of *S. alterniflora* samples has an *r* = 0.94 (11 df), p <0.05.
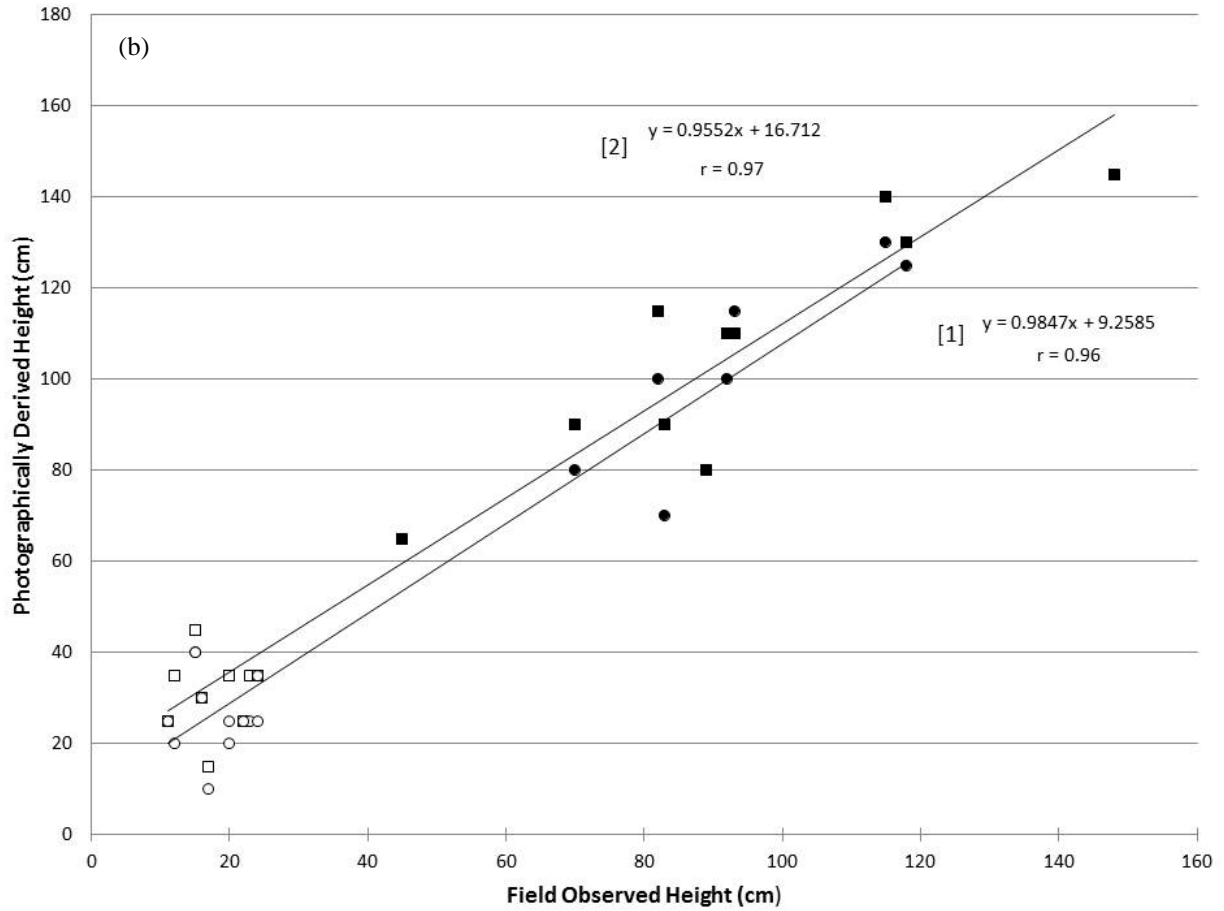
Figure 3.8b: Relationship of photographically derived heights with field observed height measurements. Circle markers are 10 cm optical depth represented by regression equation [1] and square markers are 25 cm optical depth represented by regression equation [2]. *Spartina alterniflora* samples are solid markers while open markers represent all other species. The subset of this data that contains *S. alterniflora* samples has an *r* = 0.83 (10 df), p <0.05 and *r* = 0.84 (11 df), p <0.05 for 10 cm and 25 cm optical depths.

Table 3.4: Results of Pearson's correlations (*r*) of biophysical parameters on waveform metrics for all vegetation species and the subset of *Spartina alterniflora*. Gray shaded cells have a p value <0.05 (df = 24).

Parameters	Width		Sample Skewness		Amplitude		Waveform Standard deviation		Pearson's 1st Skewness	
	All	*S. alterniflora*	All	*S. alterniflora*	All	*S. alterniflora*	All	*S. alterniflora*	All	*S. alterniflora*
Photographic Vegetation Height	0.82	0.75	0.5	0.17	0.57	0.17	0.73	0.78	0.4	0.37
Planimetric Obscuration	0.47	0.14	0.6	0.33	0.71	0.62	0.1	0.3	0.1	0.2
Quadrat Stem Density	0.58	0.66	0.6	0.35	0.73	0	0.35	0.48	0.4	0
Quadrat Biomass Density	0.41	0.2	0.3	0.22	0.53	0.14	0.17	0.22	0	0.14
Proportion of Vegetation Area (25cm)	0.73	0.57	0.5	0	0.39	0.61	0.62	0.46	0.4	0.24
Proportion of Vegetation Area (10cm)	0.49	0.14	0.3	0.14	0.26	0.28	0.33	0	0.2	0
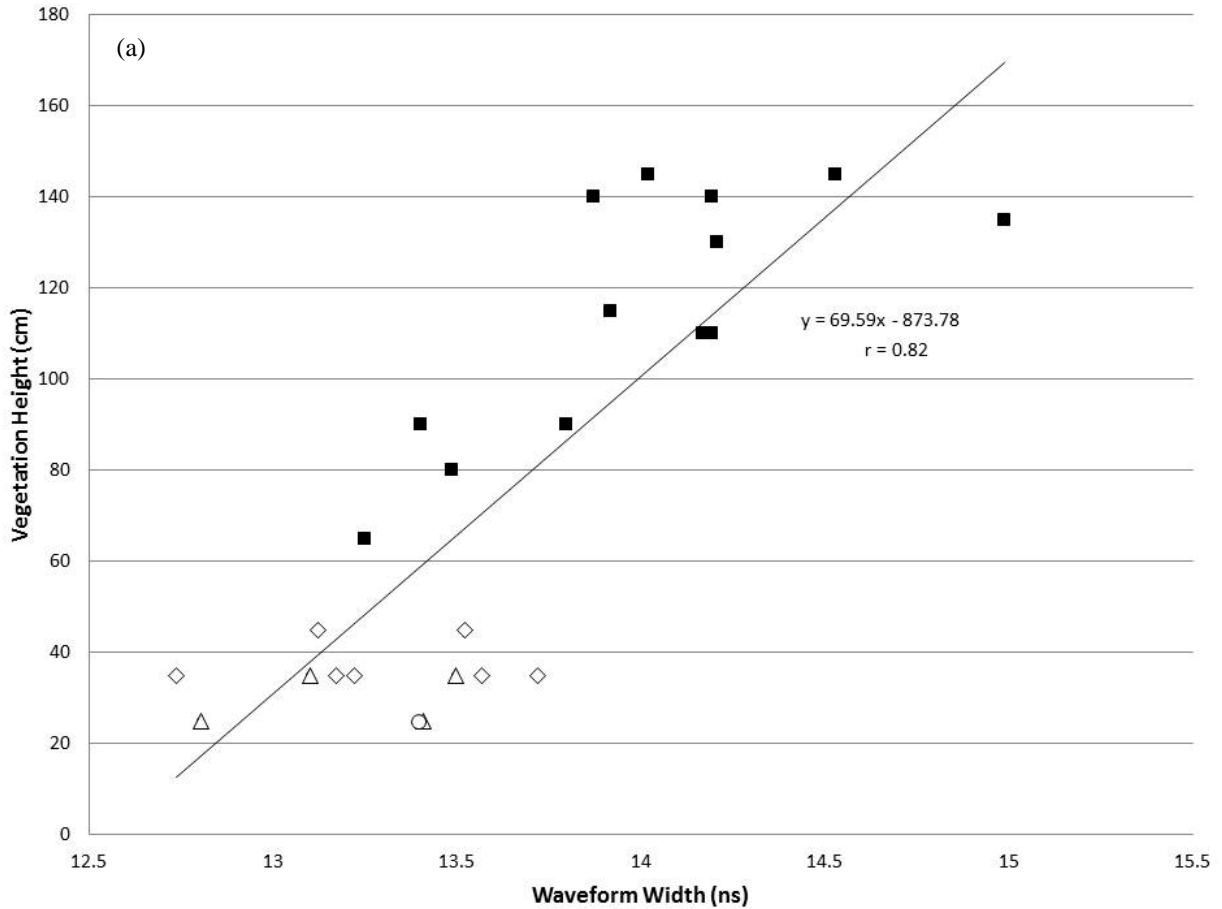
Figure 3.9a: Relationship of waveform width with vegetation height as derived from the digital photographs. Sample symbols are as follows: solid square markers are *Spartina alterniflora*, open circle markers are *Distichlis spicata*, open diamonds are *Spartina patens* and open triangles are *Salicornia spp*.
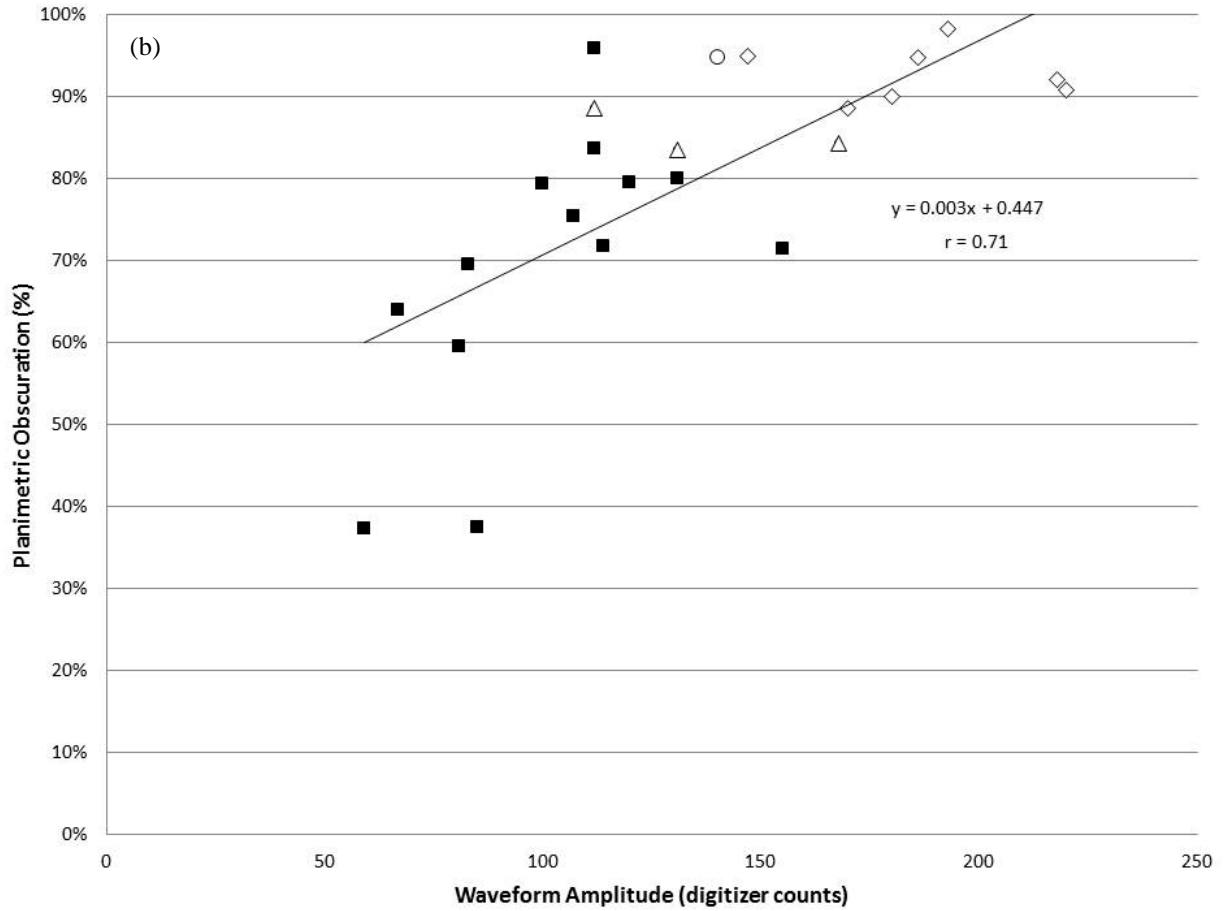
Figure 3.9b: Relationship of waveform amplitude with planimetric obscuration. Sample symbols are as follows: solid square markers are *Spartina alterniflora***, open circle markers are** *Distichlis spicata***, open diamonds are** *Spartina patens* **and open triangles are** *Salicornia spp***.**
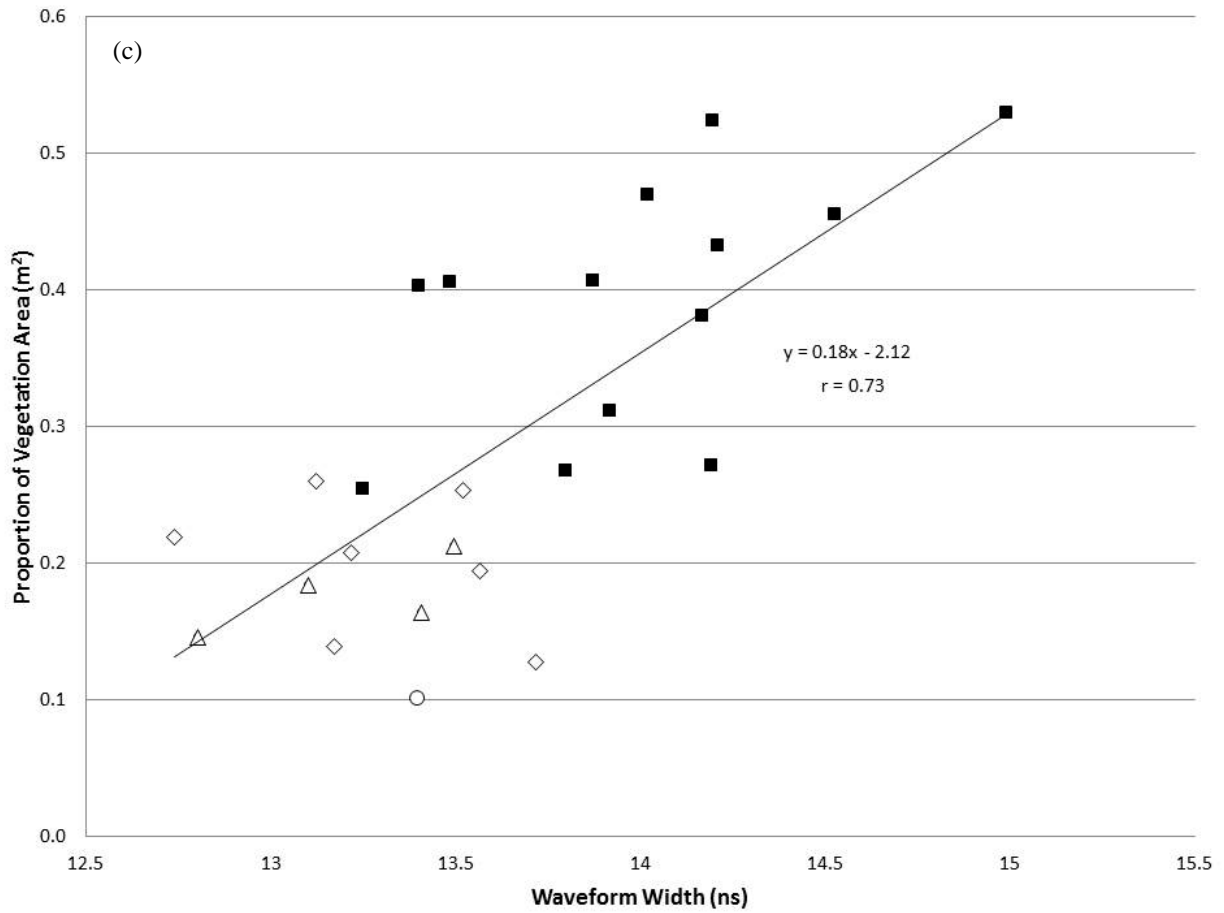
Figure 3.9c: Relationship of waveform width with proportion vegetation area. Sample symbols are as follows: solid square markers are *Spartina alterniflora*, open circle markers are *Distichlis spicata*, open diamonds are *Spartina patens* and open triangles are *Salicornia spp*.

Table 3.5: Results of multiple linear regressions (R^2) of biophysical parameter with waveform metrics. Bold with underline represent improved results.

	Waveform Width and Sample Skewness	Waveform Width and Amplitude	Waveform Width and Waveform SD	Sample Skewness and Amplitude	Sample Skewness and Waveform SD	Amplitude and Waveform SD
Vegetation Height	0.68	**<u>0.72</u>**	0.68	0.38	0.57	**<u>0.74</u>**
Planimetric Obscuration	0.32	0.53	0.49	0.53	0.36	0.51
Quadrat Stem Density	0.47	**<u>0.6</u>**	0.38	0.58	0.42	**<u>0.6</u>**
Quadrat Biomass Density	0.18	0.32	0.27	0.32	0.05	0.29
PVA (25 cm)	0.54	0.54	0.54	0.23	0.42	0.47

CHAPTER IV

ASSESSMENT OF ELEVATION UNCERTAINTY IN SALT MARSH ENVIRONMENTS

USING DISCRETE-RETURN AND FULL-WAVEFORM LIDAR

Abstract

Lidar data can serve as an important source of elevation information for studying, monitoring and managing salt marshes. However, previous studies have shown that lidar data tend to have lower vertical accuracy (i.e., greater uncertainty) in salt marshes than in other environments. This increase in vertical uncertainty hinders the ability to analyze very small elevation differences, which can be ecologically significant. For coastal scientists and managers to effectively evaluate and use lidar data in salt marshes, a better understanding of the vertical uncertainty is needed. Specifically, the factors affecting the uncertainty: plant species, season, and lidar processing methods must be investigated. This study addresses this need using discrete-return (DRL) and full-waveform lidar, along with RTK GNSS reference data, for four marshes on Cape Cod, Massachusetts (USA). The lidar bias (mean elevation residual when comparing lidar elevation against GNSS ground truth) and standard deviation were computed across: all four marsh systems, four major taxa (*Spartina alterniflora*, *Spartina patens*, *Distichlis spicata*, and *Salicornia spp.*) using varying interpolation and filtering methods. The effects of seasonality (temporal differences between peak growth and senescent conditions) were also investigated using lidar data acquired in the summer and following spring. Relative uncertainty surfaces (RUS) were computed from lidar waveform-derived metrics and examined for their utility and correlation with individual lidar residuals. The results clearly illustrate the importance

of seasonality, species, and lidar interpolation and filtering methods on elevation uncertainty in salt marshes. Results demonstrate that RUS generated from lidar waveform features are useful in qualitative/visual assessment of lidar elevation uncertainty and correlate well with vegetation height and presence of *Spartina alterniflora*. Knowledge of where DRL uncertainty persists within salt marshes and the effect of various techniques of bias removal implemented to date should lead to the development of better correction methods and DEMs with higher value to salt marsh researchers and planners.

Introduction

Salt marshes are tidally influenced, halophytic grasslands found in middle and high latitudes around the globe (Mitsch and Gosselink 2000). They are among the most productive ecosystems on the planet and provide valuable services to both the natural and human built environments such as fish nursery habitat, carbon storage, sediment traps, water filtration, and shoreline protection (Costanza et al. 1997; Mitsch and Gosselink 2000). Whether salt marshes thrive, survive or fail (and are replaced by other coastal habitat, e.g., mudflats) generally relates to very small variations in elevation, which affects inundation, available nutrients, sedimentation and salinity (Morris et al. 2002). To monitor their health and response to changes in sea level rise (SLR), detailed topographic information on the order of centimeters is necessary. However, acquiring accurate terrain elevation data can be difficult and is typically costly and time consuming if traditional data collection methods are used (Green et al. 1996). Lidar has been identified as a valuable tool for rapid survey of storm impacts, monitoring shoreline change, restoration planning, and flood hazard assessment (Brock and Sallenger 2001) and is often

proposed as a substitute for field-based datasets collected by either conventional survey instruments or more modern GNSS devices (Montane and Torres 2006; Schmid et al. 2011).

Lidar's usefulness in salt marsh studies is a function of the uncertainty of lidar-derived elevation relative to the elevation range of ecological importance (Sadro et al. 2007). For example, lidar in a salt marsh environment is ineffective where its elevation/vertical uncertainty (due to vegetative variation and other factors) is greater than the elevation range determining inundation, species dominance and habitat. In addition to impacts from vegetation, systematic and nonsystematic factors known to degrade the laser coordinates of points by centimeters to decimeters include sensor position and orientation (the post-processed navigation solution from the integrated GNSS/INS system), scan angle, calibration and environmental parameters such as soil saturation (Shrestha and Carter 1998; Lefsky et al. 2002b; Hodgson and Bresnahan 2004; Hopkinson et al. 2004). Based on all of these factors but, especially the vegetation and environmental parameters, uncorrected lidar datasets generally have relatively high vertical uncertainty in salt marsh environments and may be inadequate to determine inundation extent and frequency (Morris et al. 2005; Rosso et al. 2006; Schmid et al. 2011; Hladik and Alber 2012), key factors influencing salt marsh health.

Research to determine the extent to which lidar achieves salt marsh canopy penetration has started to shed light on vegetation effects (Populus et al. 2001; Gopfert and Heipke 2006; Rosso et al. 2006; Schmid et al. 2011; Hladik and Alber 2012; Hladik et al. 2013; Rogers et al. 2015). Species stem density, vertical density, height, and seasonality likely influence lidar signal penetration properties in salt marsh environments. In addition to the physical attributes of vegetation height, leaf morphology and growth habit may also be factors influencing lidar signal returns (Hladik and Alber 2012; Rogers et al. 2015). Leaf structures and growth habit vary

greatly from species to species. For example *Spartina alterniflora* has long flat tapering leaves and grows to a height of up to 2.0 m, while *Spartina patens* has narrow linear leaves that are rolled within a low growing ~0.1-0.3 m thatch in a "cow lick" pattern (Tiner 1987). All of these vegetation attributes are likely to contribute to lidar error, while leading to point clouds that are difficult to distinguish visually from bare-earth surfaces.

Notwithstanding the contributions of previous research, there is a need to better understand the factors affecting the vertical uncertainty of lidar data in salt marshes, such that coastal scientists and managers can make informed decisions related to: a) when and how to use lidar data in salt marsh research, b) restoration planning, and c) sea-level rise studies. This study addresses this need, using lidar data and RTK GNSS ground truth, for four salt marshes on Cape Cod, Massachusetts. Variables investigated include: season (specifically, temporal differences between peak growth and senescent conditions), vegetation species, and lidar processing (interpolation and filtering) method.

Another important aspect of this study is the use of full-waveform lidar, which records a time-series of backscattered signal strength for each laser pulse. Received signal strength is a function of the peak transmitted pulse power, the fraction of the pulse intercepted by a surface, the reflectance of the intercepted surface, the angle of incidence, and the fraction of the pulse that is returned in the direction of the sensor. Since vegetation, soil and other objects have a rough surface at near infrared (NIR) wavelengths, targets scatter energy, only some of which returns to the sensor (Wagner et al. 2008) **(Figure 4.1)**. Full-waveform data can better characterize canopy structure (Drake et al. 2002; Lefsky et al. 2002b; Anderson et al. 2008) allowing the user to detect the vertical distribution of targets, and has been shown to improve range resolution (Mallet and Bretar 2009). Salt marsh canopies typically range from 0.1 – 2.0 m depending on

species type and salinity regime and latitude. These heights are often less than the transmitted laser pulse width of the lidar system (converted from a temporal duration to a corresponding round-trip distance in air) and resolving threshold for discrete-return lidar (DRL) (Schmid et al. 2011). Therefore, full-waveform systems may allow for analysis and feature discrimination at a level of detail not possible with DRL systems.

Techniques for working with full-waveform that are discussed in the literature typically involve sophisticated, computationally-complex signal processing approaches such as deconvolution and decomposition (Jutzi and Stilla 2006). Only a few studies have been conducted on the use of simple feature-based waveform metrics (Adams et al. 2012; Muss et al. 2013; Parrish et al. 2014; Rogers et al. 2015). In this study, simple shape-based waveform features are used to create relative uncertainty surfaces (RUS) and assess spatial variation in elevation uncertainty throughout the marsh. These spatial assessments of uncertainty assist in answering the following types of questions: 1) where within the marsh are the elevations most reliable or suspect; 2) do the areas of high (or low) uncertainty overlap areas of particular concern, such as species transitions or critical habitat; and 3) if resources were available to support acquisition of GNSS reference data within only a portion of the marsh, where should these efforts best be concentrated to achieve the greatest improvement in the marsh elevation data? Combined with the quantitative analysis of the DRL data, this information can assist coastal managers and scientists in more effectively utilizing lidar data of salt marshes.

Methods

Four separate mesotidal salt marshes on protected coasts of Cape Cod, Massachusetts, USA were investigated. The marsh sites chosen contained representative stands of the dominant

plant species for the area (*Spartina alterniflora* Loisel*, Spartina patens, Distichlis spicata*, and *Salicornia spp.)* and were in close proximity of the marshes to each other, allowing field data to be collected within a specified time window around a lidar overflight. The sites from north to south are Hatches Harbor marsh (1.2 km^2), Moors marsh (2.0 km^2), Pamet River marsh (2.0 km^2), and Great Island - Middle marsh (0.3 km^2) **(Figure 4.2)**. The area has a semidiurnal tide with a mean range of ~2.83 m (NOAA 2013). All the marshes surveyed in this study are largely *Spartina alterniflora* (smooth cordgrass) dominated low marsh environments with a sandy substrate. Typically, there is a small border of high marsh located at the upland border dominated by *Spartina patens* (salt marsh hay), *Distichlis spicata* (spike grass) and *Salicornia spp.* (glasswort) (Portnoy et al. 2003) **(Figure 4.3)**. At two of the sites, Pamet River and Great Island, a large segment of the marsh appears to be in collapse, exhibiting extensive areas of bare ground due to a form of marsh wasting (Smith 2009).

The salt marsh vegetation in the study sites were characterized by homogeneous, near monoculture stands for three major species and one genus (*Spartina alterniflora, Spartina patens, Distichlis spicata*, and *Salicornia spp.)*. The vegetation demonstrated zonation patterns which are driven by small scale elevation changes and edaphic conditions (Bertness and Ellison 1987). Within an individual vegetative community, variability in growth habit and height was also common. *Spartina alterniflora* had three distinct variations or ecophenes observed at these sites and other marshes caused by edaphic factors: 0-50 cm (short form [SF]); 50-100 cm (medium form [MF]); and >100 cm (tall form [TF]) (Reimold et al. 1973; Anderson and Treshow 1980; Ornes and Kaplan 1989; Wiegert and Freeman 1990; Pennings and Bertness 2001; Hladik and Alber 2012). Tall-form typically grew along estuarine creeks with semidiurnal flooding and exceeded 2 m in height in some locations. In contrast, short-form was typically

found in high marsh areas with higher salinity, sulfide concentrations and/or lower redox potential (Mitsch and Gosselink 2000).

Lidar Data Collection

The National Center for Airborne Laser Mapping (NCALM) collected 37 km^2 of lidar data for this study on July 20th, 2010 during peak biomass at the daily predicted low tide ($\pm$ 90 minutes). The instrument used was an Optech GEMINI Airborne Laser Terrain Mapper (ALTM) and an Optech 12-bit IWD-2 intelligent waveform digitizer mounted in a twin-engine Cessna 337 Skymaster (see flight parameters in **Table 4.1**). The DRL points were collected via the Optech hardware-based ranging system comprised of a constant fraction discriminator and time interval meter. Return waveforms were digitized with a 1 ns sampling period and provided in Optech's NDF binary format with an IDX index file. The sites investigated in this research contained low growing marsh vegetation, "bare earth" and water and did not include trees, buildings, or other structures. Therefore, the data were almost entirely composed of single returns (Rogers et al. 2015). Elevations were initially transformed to NAVD88 using GEOID03 and later updated using GEOID09 with NOAA's Vertical Datum Transformation (VDatum) version 3.2 (NOAA NGS's latest geoid model, GEOID 12a, did not become available until after the majority of the data processing for this study was completed.)

Additionally, data were used from the lidar for the North East Project funded primarily by the American Recovery and Reinvestment Act (ARRA) of 2009 and led by the United States Geological Survey (USGS). These data were collected for all of Cape Cod on May 5, 2011 under senescent conditions and 9 months after the NCALM flight. The lidar data were acquired with an Optech GEMINI ALTM during predicted spring low tides ($\pm$ 90 minutes) at an altitude

of 1,000 m AGL, a pulse rate of 100 kHz with an average nominal post spacing of 0.45 m, and spot illumination size of 0.23 m (**Table 4.1**). The data were collected and processed by the provider to meet a vertical accuracy of $RMSE_z$ of 9.25 cm in the "open terrain" land cover class, and elevations were referenced to NAVD88 using GEOID09.

Field Data Collection

A detailed set of 3,446 ground-control points (GCPs) was established in various zones that included tidal sandflats, low marshes, and high marshes. Additionally, hard surfaces such as roads and parking lots in close proximity to the marshes were surveyed to analyze for overall lidar dataset accuracy. Marsh surface elevations and hard target ground elevations were collected with a Trimble NetR5 base station network with cellular-based correction and a Trimble R8 Model 3 Real Time Kinematic (RTK) GNSS rover. Special care was needed to ensure vertical accuracy when using the rover unit in marsh environments (Torres and Styles 2007). A survey antenna rod was modified with a 12 cm diameter flat base to prevent the rod from sinking into the unconsolidated mud and peat. Ground elevations were recorded in arbitrary transects through the marsh with the average point density of 5-7 per m^2. The equipment manufacturer specifies the RTK-GPS rover mode provides an RMSE of < 1 cm in the horizontal and 2 cm in the vertical. All collected elevations were referenced to NAVD88 using GEOID09 (the same geoid model used with the lidar data). At most of the locations, dominant vegetation species and vegetation heights were logged (where vegetation was present) for later comparisons with the lidar dataset. The field data collected by the RTK GNSS were periodically checked to verify that accuracy standards were maintained. Elevation of a known benchmark was surveyed with the same Trimble device for comparison and occupied for >4 hours for a full

OPUS solution. Also, temporary benchmarks were established by occupying the same, hard surface locations several times throughout the field day and the residuals were calculated to compare any variations found in the coordinates. Each elevation residual (or individual "vertical difference" or "vertical error") ΔZ was calculated as:

$$\Delta Z_i = Z_{lidar} - Z_{GPS} \qquad [1]$$

The sample standard deviation (the spread of the elevations about the mean) for the repeatedly RTK GNSS surveyed temporary benchmark was determined to be 0.006 m. RTK GNSS measurements for the surveyed benchmark with OPUS elevation solution were determined to have an $RMSE_z$ of 0.006 m. The vertical root mean square error is given by the following equation:

$$RMSE_z = \sqrt{\frac{\sum_{i=1}^{N}(\Delta Z_i)^2}{N}} \qquad [2]$$

Discrete-Return Lidar Processing

NCALM provided as part of its data deliverable a LAS file of last return lidar points and a "bare-earth" grid, with point classification performed in TerraSolid TerraScan software. Upon visual inspection of the "bare-earth" grid, the filtering method for ground appeared too aggressive with large sections of a 14 m wide by 1.6 km long stone dike completely decimated (**Figure 4.4**). This issue may have any number of causes and is likely a result of specific parameter settings. However, because complete control was needed over the gridding and filtering process and those software settings could not be altered, this data deliverable was not chosen as the sole source for analysis. Discrete lidar return data from both temporal datasets were preprocessed using QPS Fledermaus 7.43 from the original LAS point cloud data. Data

evaluation and cleaning were performed using the PFM 3D point cloud editor to remove artifacts and erroneous or non-natural points that could influence the ΔZ or gridding results. After cleaning, the point clouds were converted to raster grids with 1 m^2 pixel size using several different algorithms, (inverse distance weighted [IDW] 1x, IDW 3x, minimum bin, maximum bin). IDW 1x used an inverse distance weighted average of only the points that fell within the 1 by 1 m cell, while the IDW 3x used a weighting of all lidar returns within a 3 by 3 m grid area surrounding the target cell. The IDW 1x method provides a better estimate of the value of each pixel based on the available lidar returns without any influence of the surrounding points, while IDW 3x method smooths the data slightly and suppress high-frequency noise. The minimum bin and maximum bin filtering methods use the lowest or highest value of all the lidar returns found in the grid cell size and ignores all other values in the cell. Data were then imported into ESRI ArcGIS 10 for point feature and grid based analysis using Spatial Analyst.

Overall lidar relative accuracy was evaluated using hard surface control data collected with the RTK GNSS on flat surfaces such as roads and parking lots (Rosso et al. 2005; Sadro et al. 2007). These surfaces should provide the best lidar return, produce minimal scatter, and will not be influenced by variable conditions such as overlying vegetation or soil moisture content. Elevation residuals (ΔZ) were calculated for all hard surface points (n = 101) and then the mean was used to obtain estimates of lidar bias (Latypov 2002; Brovelli et al. 2004; Rosso et al. 2006) (**Figure 4.5**). Lidar bias is defined as the mean elevation residual:

$$\mu_l = \frac{\sum_{i=1}^{N} \Delta Z_i}{N} \qquad [3]$$

It is important to note that, due to how elevation residual is defined (Eq. 2), a positive bias indicates that the lidar elevations are generally above (i.e., higher than) the reference elevations. In this study it was found that the lidar underestimated the RTK GNSS elevations of hard

surfaces with a bias of -0.087 m and -0.044 m for the NCALM and ARRA datasets respectively **(Table 4.2)**. Accuracies between flights were calculated from the same hard target data points to determine any global bias that may prevent an accurate assessment. The non-vegetation-induced bias was then removed to allow for unbiased comparisons between flights (Rosso et al. 2006) and the field collected elevations. After non-vegetation-induced bias removal, the salt marsh vegetation was analyzed in a similar manner looking at differences between lidar derived elevation grids, surveyed ground elevations (n = 2,898) and field collected information such as vegetation species or plant height. All regressions and Pearson correlations reported in this paper are significant with a $p < 0.05$ unless otherwise noted.

Relative Uncertainty Surfaces

Lidar waveforms were extracted by developing a custom workflow using ArcGIS, QCoherent LP360 and MATLAB to compute waveform shape-related metrics. Extending previous work (Parrish et al. 2014; Rogers et al. 2015), the ability to create relative uncertainty surfaces (RUS) from features computed from lidar waveforms was evaluated. This process entailed first computing lidar echo width and for each lidar point within each marsh. The regression equations obtained from the best-fitting regressions of lidar residuals (ΔZ) on waveform features developed in Parrish et al. (2014) were then applied to every lidar waveform return within a subset of the project sites. The equation used was as follows with *w* representing waveform width (full width half maximum [FWHM]) and μ_w representing waveform mean (a measure of the center of the return pulse):

$$\widehat{\Delta Z} = f \cdot x \qquad [4]$$

where $\mathrm{x} = [1 \quad w \quad \mu_w \quad w \cdot \mu_w]^T$ and $\mathrm{f} = [9.0696 \quad -0.6419 \quad -0.3055 \quad 0.0207]^T$ for

Moors Marsh and $\mathrm{f} = [2.3250 \quad -0.1726 \quad 0.0334 \quad -0.0029]^T$ for Pamet Marsh. The output

was scaled to an arbitrary range of 0-1 (with 1 representing the highest relative uncertainty),

interpolated to a regular grid (1 m grid spacing) using an inverse distance weighting (IDW)

interpolation, and imported into an ArcGIS project containing imagery and other data layers for

visual analysis. The reason for scaling to the arbitrary range [0 to 1] is to emphasize that the

intended use of these RUSs is to visually analyze spatial variation in relative uncertainty across a

marsh, rather than to determine an exact value of ΔZ (with physically-meaningful units, such as

meters) at a particular geographic location. The RUS grid was then lowpass filtered (using a 3x3

lowpass filter in the spatial domain) to remove high frequency noise and produce a smoother

grid. This process workflow is illustrated graphically in **Figure 4.6**.

Results

Vegetation-induced bias was investigated across all four marsh sites using a comparison

of 2,648 field RTK GNSS measurements with lidar derived elevations from the July 20th, 2010

NCALM dataset. The reason for focusing on primarily on bias, rather than on standard deviation

and/or $RMSE_z$, is that previous studies (Populus et al. 2001; Morris et al. 2005; Torres and Styles

2007; Schmid et al. 2011; Hladik and Alber 2012) have shown that salt marsh vegetation

introduces errors in lidar data that are generally systematic (i.e., a high bias), rather than random.

However, an important component of the analysis included also computing the standard

deviation and $RMSE_z$ for each site and verifying that the following relationship is satisfied for

large sample sizes:

$$\mathrm{RMSE_z}^2 \approx \mu^2 + \sigma^2 \qquad\qquad [5]$$

where μ is the bias and σ is the standard deviation.

Discrete-Return Lidar Uncertainty Analysis

Several different gridding interpolation and filtering methods were assessed on the NCALM dataset for their effectiveness in producing accurate ground estimates. However, all methods evaluated in this study produced DEMs with still significant positive bias. Using one of the most common interpolation methods, IDW, with a weight of 1 cell, it was found that the lidar measurements exhibited a positive bias of 0.14 m (σ = 0.17 m) over the ground control data (**Figure 4.7**). When separated by species type, most of the overall vegetation bias could be attributed to *Spartina alterniflora* with an observed bias of 0.23 m (σ = 0.2 m) (**Table 4.3**). Using an IDW 3x (interpolation with a weight of 3x3 cells) did not produce significant differences from the IDW 1x results. The Terrascan filtered grid exhibited a modest improvement over the IDW method with a positive bias of 0.11 m (σ = 0.14 m) (**Figure 4.8**). A species-based review of the Terrascan grid was similar in its results with a majority of the overall bias attributed to *Spartina alterniflora*. *Spartina alterniflora* always appears to have the highest bias, regardless of the processing method used.

The final methods evaluated were minimum and maximum bin filtering of the LAS data where the lowest or highest elevation reading in a defined grid cell, in this case 1 m^2, is used and all other values that occur in that grid cell are ignored. As in Schmid, Hadley and Wijekoon (2011), the minimum bin method generally improved results over the IDW method reducing some positive data drift above the 1:1 correlation line to lower the overall bias to 0.09 m (σ =

0.15 m) (**Figure 4.9**). However, it increased the number of negative residuals but decreased the standard deviation.   It was initially anticipated that: a) maximum bin would provide a determination of vegetation height, and b) the difference of maximum bin and minimum bin would have a correlation with bias.   However, no strong relationships were found to support these assumptions.

The ARRA May 5th, 2011 dataset was also evaluated with the same gridding and filtering methods with the exception of Terrascan, which was unavailable. This dataset represented leaf-off conditions with the marsh in its least vegetated state. As expected, this dataset was much improved over leaf-on conditions with overall bias of 0.04 m ($\sigma = 0.06$ m) (**Figure 4.10**). It is interesting to note that the *Spartina patens* and *Distichlis spicata* were now the two species with the largest bias. Using the minimum bin approach on this dataset further reduced the overall bias but increased the standard deviation.

The results of the NCALM dataset at individual marsh sites are generally consistent with the overall lidar bias described above and are presented in **Table 4.4**.   Using the IDW 1x interpolation method, the NCALM dataset had a range of bias in vegetated areas of 0.10 to 0.22 m across all sites. *Spartina patens*, *Distichlis spicata*, and *Salicornia (sp)* had biases very consistent with the overall bias (i.e., the mean across species). However, *Spartina alterniflora* demonstrated the most variation with a site specific range from 0.16 m to 0.35 m. Results from the ARRA early season flight appear to be more varied and inconsistent at the marsh level than the peak season dataset (**Table 4.5**). There appeared to be fewer patterns of bias for individual species. At this early season flight date *Spartina patens*, *Distichlis spicata*, and *Salicornia (spp)* appear to produce larger bias than *Spartina alterniflora*.

Overall bias and standard deviation are summary statistics frequently reported to quantify the error of lidar data sets, but observing frequency of residuals reveals a distribution of lidar error unique to each species surveyed (**Figure 4.11**). Three of the four target species had unimodal distributions, while one, *S. alterniflora*, was clearly multimodal. Due to its three distinct ecophenes, each distribution was also plotted. The short-form *S. alterniflora* residual distribution had a bias of 0.12 m (σ = 0.12 m) (n = 509). It has a similar peak as the other shorter species but with a slightly longer tail. The medium-form *S. alterniflora* exhibited a bias of 0.23 m (σ = 0.17 m) and also had an extended tail towards higher residuals (n = 530). Lastly, the tall-form *S. alterniflora* showed a broad distribution with a bias of 0.41 m (σ = 0.21 m) (n = 349).

The role of vegetation height as a source of lidar bias was likewise examined. The mean height for all vegetation at 2,648 RTK GNSS locations was 0.46 m (σ = 0.38 m), with a minimum height of 0.02 m and a maximum recorded height of 1.95 m. *Spartina alterniflora* was significantly taller than the three other major species present in these marshes (**Table 4.6**). The mean height for *Spartina alterniflora* (short, medium and tall forms combined) was 0.68 m (σ = 0.38 m), with a minimum height of 0.03 m, a maximum height of 1.95 m. Lidar residuals (the difference between the NCALM IDW 1x grid and RTK GNSS elevation), plotted with the recorded vegetation heights at the same locations exhibited an r^2 = 0.49 (n = 2,648) (**Figure 4.12**). A regression of only the *S. alterniflora* locations exhibited an r^2 of 0.36 (n = 1,473). The bias to height ratio (the mean of the ratio of lidar residuals to vegetation heights) was calculated for each species and represents the amount of lidar bias as a function of the vegetation height. The overall bias to height ratio was 34% for all vegetation species at the four field sites. Three of the individual species surveyed, *Spartina alterniflora*, *Spartina patens*, and *Distichlis spicata*,

had a bias to height ratio of 35%, while *Salicornia (spp)* was observed to have a lower ratio of 25%.

Temporal Analysis

To look at the effects of seasonal vegetation growth on the lidar accuracy, a comparison of the May 2011 lidar data with the July 2010 dataset was conducted at the same 2,810 ground control points. It was assumed prior to data collection that the July data set, acquired at peak vegetation conditions, would display increased elevation bias over the near-senescent early May flight. The results support this assumption, with the July dataset displaying an overall increase in bias of 0.1 m (**Table 4.7**). A graph of this comparison exhibits a strong positive bias above the 1:1 correlation line (**Figure 4.13**). When evaluated by species, GCP locations where *Spartina alterniflora* was dominant exhibited the most significant increase in elevation bias of 0.18 m. However, very little change or slight negative change was observed for the other high marsh species surveyed.

To qualitatively and quantitatively evaluate change due to growth/seasonal variation, a difference map was created by subtracting the grid of the May flight from the July flight (**Figure 4.14**) producing a visual representation of the changes occurring across the marsh. Overall, there was a net positive increase in marsh elevations as recorded by the DRL system. Clear patterns of tall vegetation near the tidal channels and in the lowest reaches of the marsh are evident and correspond with the distribution of *Spartina alterniflora* observed during fieldwork and with aerial photography. These areas of intense change ranged up to 1 m in height in tight concentrations. Based on an analysis of 381,654 pixels of marsh surface in a subset of Moors marsh, the mean difference was 0.27 m ($\sigma = 0.19$ m) with a minimum of -0.34 m, maximum of 1

m (**Figure 4.15**). It is interesting to note that there were very few pixels that indicated a negative change between leaf-on to leaf-off conditions within the marsh subset analyzed. The presumed underlying cause of the temporal change is the growth of the vegetation. Evaluating the grid difference with the field measured vegetation heights exhibited a correlation with an $r^2 = 0.59$ (n = 789) (**Figure 4.16**). However, a comparison between observed lidar residuals ($\Delta Z = $ IDW 1x – RTK GNSS) with the difference between the ARRA May 5th, 2011 and the NCALM July 20th 2010 lidar flights for the Moors marsh site had an $r^2 = 0.91$ (n = 785) (**Figure 4.17**) indicating that the residuals are indeed associated with areas of taller vegetation.

Relative Uncertainty Surfaces

The next step in this study was to build upon previous work using lidar waveform feature-based metrics as they relate to both vertical uncertainty and vegetation height (Parrish et al. 2014; Rogers et al. 2015). Using the regression equation above [4] from Parrish, Rogers and Calder (2014), each individual waveform was mapped to an uncertainty value and then normalized to a relative value between 0-1 before gridding. The RUS were obtained in this manner for Moors marsh and Pamet marsh (**Figure 4.18**). Qualitatively these maps display intricate detail as to the spatial variability in vertical error. Visual inspection of the RUSs indicated that the areas of greatest uncertainty correspond with distributions of MF and TF *Spartina alterniflora*.

Several quantitative analyses were conducted on these uncertainty surfaces to determine how well they represent ground conditions. The results of the RUS analysis are presented in terms of Pearson's correlation coefficient (*r*) since the goal was to merely determine whether there were any relationships between the variables. The first was a comparison between the

waveform relative uncertainty value and the discrete-return lidar residuals (ΔZ) at Pamet marsh, which exhibited a correlation of $r = 0.86$ (n = 271) (**Figure 4.19**). As lidar residuals and vegetation height are assumed to be correlated, a comparison of the waveform uncertainty value and vegetation height was also conducted (**Figure 4.20**), which produced an $r = 0.85$ (n = 268). Lastly, the temporal analysis conducted between the July, 2010 and May 2011 flights produced a detailed difference map attributable to seasonal vegetation growth. A subset of this grid sharing the same spatial extent as the waveform RUS grid was produced and the values of waveform uncertainty and temporal difference for each grid cell were compared. This procedure created a database of 380,024 values, which when plotted was extremely difficult to interpret visually, due to tens of thousands of points plotting on top of one another. To refine the results to an interpretable graph, a random subset of 2,000 points was extracted (**Figure 4.21**). The overall r was 0.82 (n = 380,024), and four individual subsets of 2,000 randomized points had r values of 0.81, 0.89, 0.82, and 0.86.

Discussion

Discrete Lidar Uncertainty

Comparison of DRL with RTK GNSS ground-truth elevations yielded interesting, if not unexpected, results. Overall, ground elevations were not well mapped in either the spring or fall flights by the lidar sensor within vegetated portions of the marsh. However, the spring dataset resulted in measurements closer to ground (bias of 0.04 m, $\sigma = 0.06$ m) because senescent vegetation was flattened or removed over the winter. A positive lidar bias of 0.14 m ($\sigma = 0.17$ m) was observed in the vegetated salt marsh surfaces of the July flight (**Table 4.3**). When individual vegetation species were separated, a majority of the bias can be attributed to just one

species during the July flight. *Spartina alterniflora* produced a bias of 0.23 m (σ = 0.20 m), while the three other species in this study had a combined bias of approximately 0.05m (σ = 0.06 m). The vertical growth habit of *Spartina alterniflora* is very different from the other species surveyed, which are low growing matt-like plants with mean heights less than 0.22 m (**Table 4.6**). *Spartina alterniflora* was observed to grow vertically with stalks 4 – 5 cm apart and 0.2 – 2.0 m in height with narrow, interlocking leaves near the top of the canopy. This growth form appears to greatly impact lidar pulse returns (Rogers et al. 2015). A regression of lidar residuals and recorded vegetation heights at GCPs exhibited a significant, but moderate coefficient of determination, r^2 = 0.49. The association is similar to that found by Schmid et al. (2011), and displayed significant scatter suggesting high variability within the vegetation and the possibility of other factors influencing the increased lidar residuals such as stem density, biomass density, or proportion vegetative area (PVA) [a measure of the cross-sectional area and the light obscuring properties of the vegetation] (Rogers et al. 2015).

Using various gridding and filtering methods, it may be possible to improve the overall DEM quality and lower lidar bias. For instance, using a minimum bin approach produced an improvement to overall lidar bias from 0.14 m (σ = 0.17 m) down to 0.09 m (σ = 0.17 m) when compared with the inverse distance weighting method for the July flight (**Table 4.3**). This is also consistent with findings by Schmid et al. (2011), but minimum bin can have certain disadvangates. For example, in the ARRA data in this study, minimum bin reduced the bias, but increased the standard deviation. Additionally, in non-vegetated, open terrain areas, minimum bin often favors lowest points that are erroneous (these would normally have been ignored, filtered out, or averaged into a series of points within a grid cell). Thus, minimum bin can produce poor results in areas such as mud/sand flats or steeper slopes of tidal streams (Schmid et

al. 2011). There is a large difference of effectiveness of minimum bin between the shorter species and the taller *S. alterniflora* (**Table 4.4**). Maximum bin filtering did not perform as well as was initially expected. A strong correlation between the difference of maximum and minimum bin with either the field collected vegetation height or the observed lidar residuals would have been a strong case supporting the use of these methods as part of a DEM improvement strategy.

Intuitively, it appears that without an effective correction technique to remove lidar bias from DRL datasets, minimizing bias in salt marsh environments requires that lidar flights should be coordinated during leaf-off, senescent conditions. However, senesced vegetation from the previous growing season also appears to impact the DRL pulse returns (**Table 4.3**) (Schmid et al. 2011; Hladik and Alber 2012). Winter/early spring flights during senescent conditions are not always logistically feasible and in the case of storm assessments, coastal areas must be surveyed immediately. Furthermore, in some locations such as in the southeastern United States, the vegetation does not fully senesce. The May dataset, as a result of the season, had an overall lidar bias of 0.04 m, which was a 0.10 m reduction over the July dataset. This reduction in bias is the direct result of the vegetation being dead and/or removed from the marsh. These findings are consistent with those of other researchers (Morris et al. 2005; Montane and Torres 2006; Schmid et al. 2011). Montane and Torres (2006) found senescent vegetation in a South Carolina to have an overall bias of approximately 0.07 m. Another consideration is that when surveying colder northern climates is the impact of heavy winter snow/ice that can be present on the marsh surface. The weight of the snow/ice sometimes compress or strip the vegetation (i.e, *Spartina alterniflora* stalks) to the ground line (Ewanchuk and Bertness 2004). In addition, ice can even

temporarily depress the marsh surface (Argow and Fitzgerald 2006) or permanently alter marsh surface elevations by rafting vegetation/sediment (Redfield 1972; van Proosdij et al. 2006).

This research shows changes in DEM surfaces derived from DRL between senescent and peak-growth conditions, leading to detailed maps of growth-induced bias (**Figure 4.14**). This finding further supports DRL flight planning during senescent marsh conditions. The Moors marsh difference surface exhibited significant correlation to vegetation height and lidar residuals during the July flight. It seems natural that seasonal variations in elevation detected by DRL would be related to observed lidar residuals and vegetation heights. Yet even more interesting was the difference surface's strong relationship with the observed lidar residuals ($r^2 = 0.91$) compared to the difference surface plotted vs. vegetation height ($r^2 = 0.59$). A correlation of lidar residuals directly with vegetation height across all four marsh sites only yielded an r^2 of 0.49. Previous research has suggested that lidar bias may correspond to roughly half the canopy height of a given vegetation class (Populus et al. 2001) or that vegetation height alone was not enough to explain positive bias and that vegetation density also plays a role (Gopfert and Heipke 2006). Schmid et al. (2011) suggested that the product of percent coverage (amount of the ground covered by vegetation) with vegetation height was a better correlation with lidar bias than strictly height. As demonstrated in this study by an overall bias to height ratio of 34%, the lidar bias appears to be less than the half of the canopy height estimate provided by other researchers. This is despite the data being collected during peak-growth conditions where previous researchers were working with senescent vegetation datasets. Even with a high PRF (pulse repetition frequency) of 125 kHz (Hladik and Alber 2012) and a small footprint lidar, poor lidar penetration is achieved with potentially less than 3% of lidar returns from the ground surface likely to be recorded (Wang et al. 2009). The lower r^2 value found for seasonal difference to

vegetation height as compared with temporal difference surface's strong relationship with the observed lidar residuals suggests that some other parameters such as planimetric obscuration (percent coverage) or biomass density must also influence lidar penetration and pulse return (Schmid et al. 2011; Rogers et al. 2015).

Relative Uncertainty Surfaces

In previous studies, simple, shape-related lidar waveform metrics were found to be predictive in estimating uncertainty and salt marsh biophysical parameters (Parrish et al. 2014; Rogers et al. 2015). Waveform features such as width and amplitude had significant correlations with lidar uncertainty, vegetation height, planimetric obscuration, and Proportion Vegetation Area (a ratio of the vertical obscuration [%] to the cross-sectional area of the measurement) (Rogers et al. 2015). In fact, waveform amplitude and waveform standard deviation accounted for nearly 75% of the variability in vegetation height (Rogers et al. 2015). The insights from those studies led to the creation of the RUSs. As noted earlier, the motivation for describing these surfaces as "relative" and recording grid values using an arbitrary, unitless scale of 0-1, as opposed to reporting either estimated residuals or standard uncertainty values in units of meters, is to avoid overstating the ability to predict elevation uncertainty from the waveform features. Research showed that the waveform features used to generate these surfaces were successful, on average, in predicting close to 60% of the total variation in DRL residuals across marshes (Parrish et al. 2014). That analysis indicated that the strength of residual prediction is sufficient for creating the RUS qualitative product shown in **Figure 4.18**, which provides a visual representation of the general variation of lidar uncertainty across the marsh. However, if the term "relative" were to be dropped and individual pixel values were assigned physically-

meaningful residual units (e.g., meters), there may be a tendency to misuse these data layers by placing too much faith in the exact value recorded at an individual pixel. Further research needs to be conducted using waveform feature metrics before more confidence can be given to these grids for project planning requiring highly accurate residual estimates.

Attempts were made at analyzing and interpreting the RUSs by comparing them to independently collected field data. The waveform uncertainty value correlated well with the discrete-return lidar bias and vegetation height. Also, the RUS displayed strong correlation with the temporal difference (ΔZ_t) between the July and May flights. The RUS surface is a strong indicator of lidar bias and can be used for qualitative analysis. Tall-form and medium-form ecophenes of *Spartina alterniflora* with vegetation height ranges of 0.5 – 2.0 m corresponded well to the higher values in the RUS. It appears likely that the waveform characteristics implemented in the RUS could be used to detect and map the boundary between high and low marsh environments with some degree of accuracy, since that boundary represents not only a change in vegetation species but also height. A qualitative product such as RUS can help plan projects even if exact uncertainty is not known or surface correction is not possible. For instance, identifying areas within the marsh where the elevations are the most reliable or potentially suspect could guide attention and resources to only the areas that require it. RUS might target field data collection, GNSS acquisition efforts, estimate vegetation height, or correlate with critical wildlife habitat and specific vegetation species of interest. RUSs may also be used to quickly identify and monitor locations of change within the marsh since areas of higher uncertainty should be related to vegetation height, which in most cases will imply changes in inundation frequency. Increased inundation could be a result of SLR or may also represent areas that are subsiding due to other factors. MF and TF *S. alterniflora* have been shown to

correlate with RUS and grow at elevations optimal for that species (Morris et al. 2005). If areas on the high marsh platform, which normally is populated by *S. patens*, suddenly begin to exhibit high RUS values, then further investigation would be necessary to determine the potential cause.

In previous studies, various attempts have been made to understand salt marsh lidar bias and improve the lidar produced DEM through interpolation method, point cloud filtering, or classification (Morris et al. 2005; Rosso et al. 2006; Torres and Styles 2007; Wang et al. 2009; Schmid et al. 2011). In addition there have been several innovative approaches to DEM correction using vegetation mapping, both field and hyperspectral, and the determination and removal of constant, species-based mean correction values (Hladik and Alber 2012; Hladik et al. 2013). However this method, although an improvement on previous correction attempts, is ultimately limited because it assumes 1) *a priori* knowledge of species location, which is usually unavailable, woefully inaccurate, or requires additional sensors, processing and interpretation that add to cost, time and introduced errors; and 2) that each vegetation species requiring a DEM correction has a constant correction factor across its entire extent. As evidenced in this paper and visually presented in **Figure 4.11**, different marsh species, in particular the often spatially dominant *S. alterniflora*, have different ranges of bias that fall in a continuous distribution rather than a constant. This range of bias is presumably influenced by vegetation height, stem density, planimetric obscuration, biomass density, and growth habit (Schmid et al. 2011; Hladik and Alber 2012; Rogers et al. 2015). Using full-waveform lidar datasets, such as those used to create the RUS products, allows an interpretation of the uncertainty based on a spectrum of results rather than a constant. Future work will attempt to exploit the full-waveform's enhanced information and capabilities to develop new correction methods.

Conclusion

Vegetation-induced lidar uncertainty continues to be a challenge to researchers and coastal managers wanting to use lidar for fine topographic analysis in salt marshes. As in other environments, lidar uncertainty varies as a function of the terrain and vegetation cover type. The following conclusions can be drawn from this investigation: 1) DRL returns in salt marsh environments include positive bias regardless of flight capture season. Positive lidar bias of 0.14 m (σ = 0.17 m) was observed across all survey locations in the peak vegetation dataset. A majority of the bias can be attributed to just one species, *Spartina alterniflora*; 2) custom interpolation and filtering techniques such as minimum bin may improve overall accuracy but can introduce additional errors, potentially creating negative bias considerations while not addressing a majority of the species-specific bias; 3) different marsh species have diverse ranges of bias that fall in a continuous distribution of residuals rather than a constant value. While most species observed in this study have unimodal distributions, *S. alterniflora* has a multimodal distribution as a result of its three distinct ecophenes. This multimodal distribution complicates currently developed correction techniques; 4) temporal measurements of change in vegetation-induced-bias between peak and senescent growth conditions are possible from lidar datasets. This finding further supports DRL flight planning during senescent marsh conditions and the ability of the sensor to discriminate small vegetation-induced elevation changes; 5) waveform feature metrics can be used to create RUSs that are useful to predict regions of variable uncertainty that can be confidently used for targeted ground truth or other field work activities.

The results of this study suggest that it may be possible to achieve at least a coarse understanding of lidar bias across an entire marsh from analysis of the lidar data alone without the *a priori* knowledge of vegetation species location. RUS maps can be used to minimize the

amount of expensive, time-consuming field work, target specific habitats or possibly monitor marsh change over time as it may relate to SLR and restoration initiatives. Achieving this goal will require further research to extend analyses to marshes in different regions of the country with differing vegetation species and further develop a correction technique using full-waveform feature-based uncertainty surfaces to improve lidar accuracy in salt marsh environments.
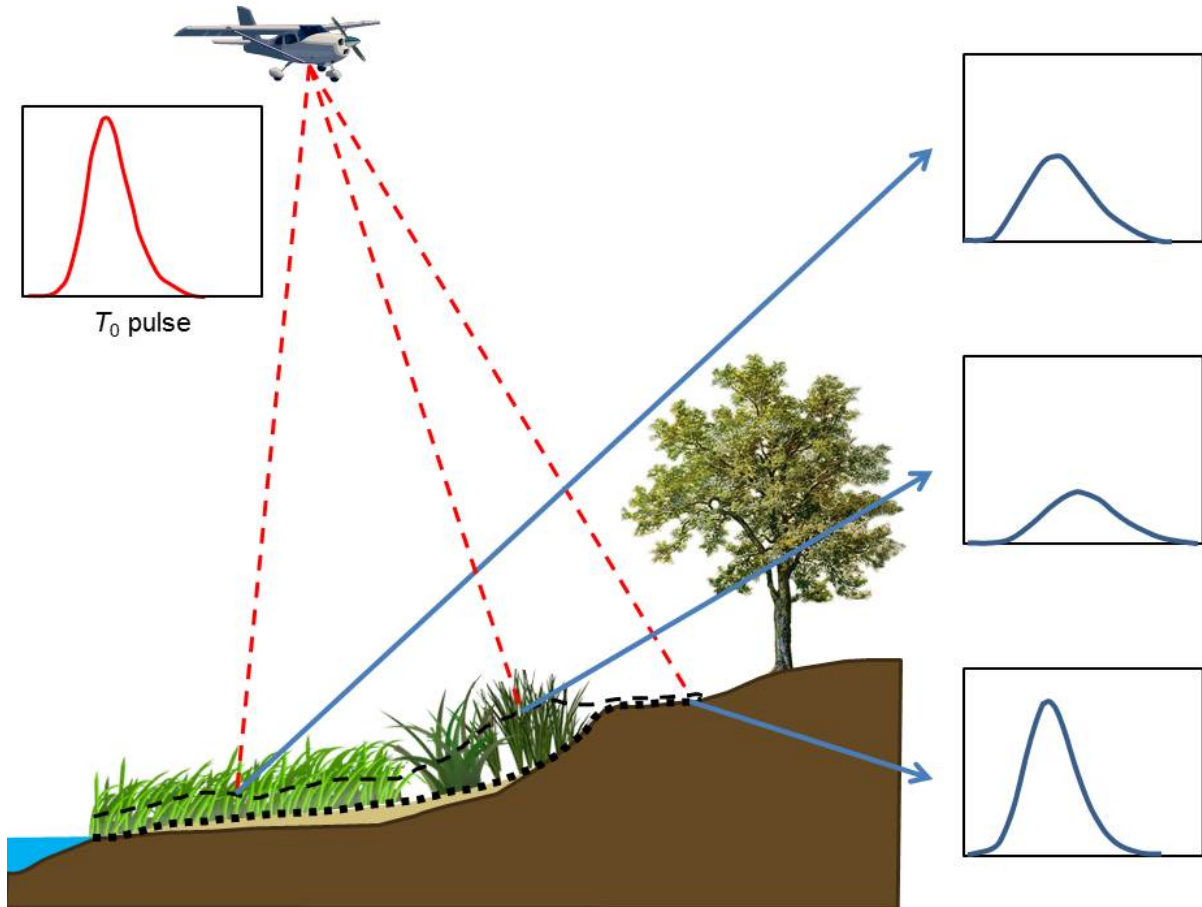
Figures and Tables

Figure 4.1: Lidar flight over a salt marsh. Black dotted line is ground measured with a RTK GNSS. Black dashed line is discrete lidar data returns of "ground." Also shown is the transmitted lidar pulse, T_0, and the single pulse full-waveform returns based on the intercepted terrain and cover for three selected locations (arrows).
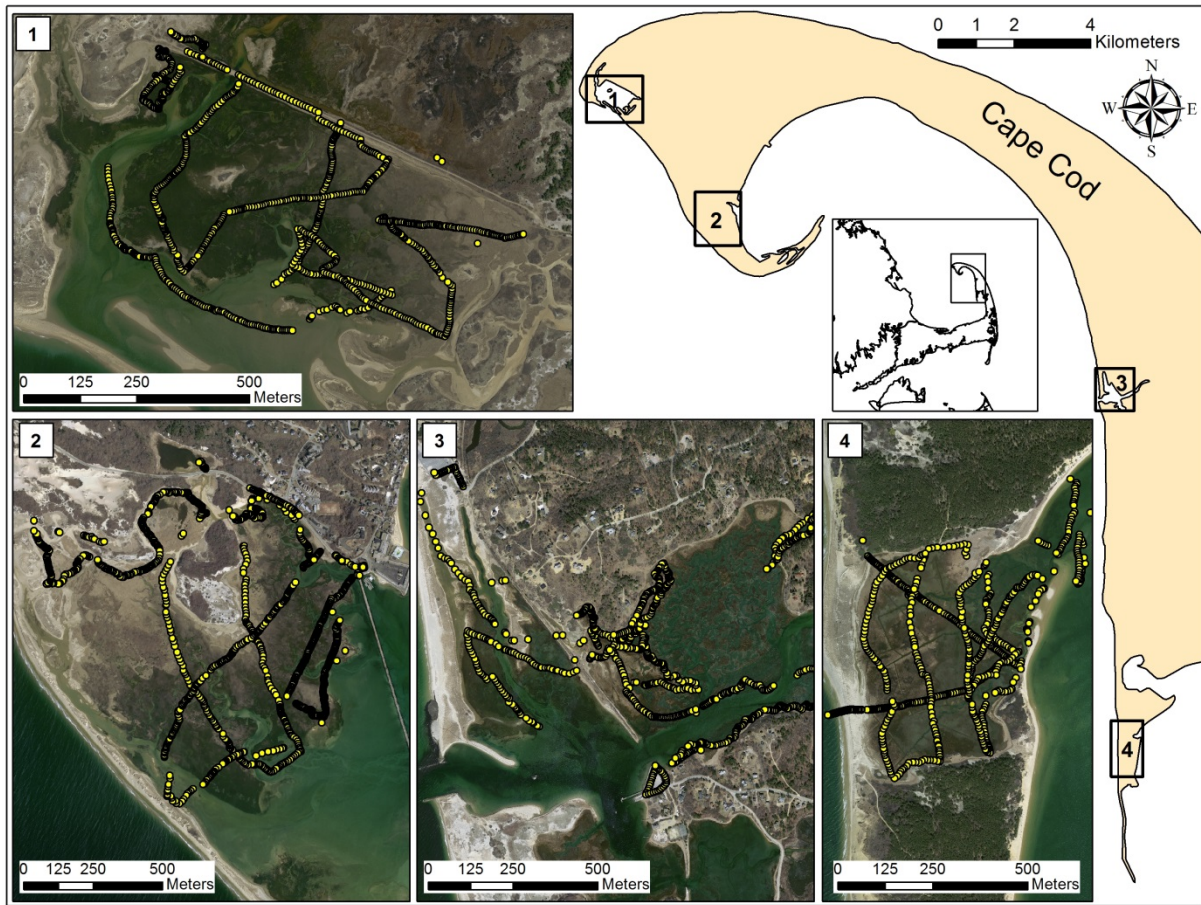
Figure 4.2: Site locus map and RTK GNSS points. Insets are 1) Hatches Harbor, 2) Moors marsh, 3) Pamet marsh, and 4) Great Island – Middle marsh.

Table 4.1: Flight parameters of NCALM July 20th, 2010 and ARRA May 5th, 2011.

Flight Parameter	NCALM	ARRA
Flying Speed (m/sec)	60	54
Altitude (m)	600	1371
Swath Overlap (%)	50	30
Laser Beam Divergence (mrad)	0.25	0.25
Pulse Rate Frequency (kHz)	70	145
Transmit Pulse Width (ns)	12	12
Scan Rate (kHz)	40	54
Scan Angle (degrees)	± 21	± 28
Point Density (pts/m^2)	5.00	3.93
Laser Footprint Diameter (m)	0.15	0.28
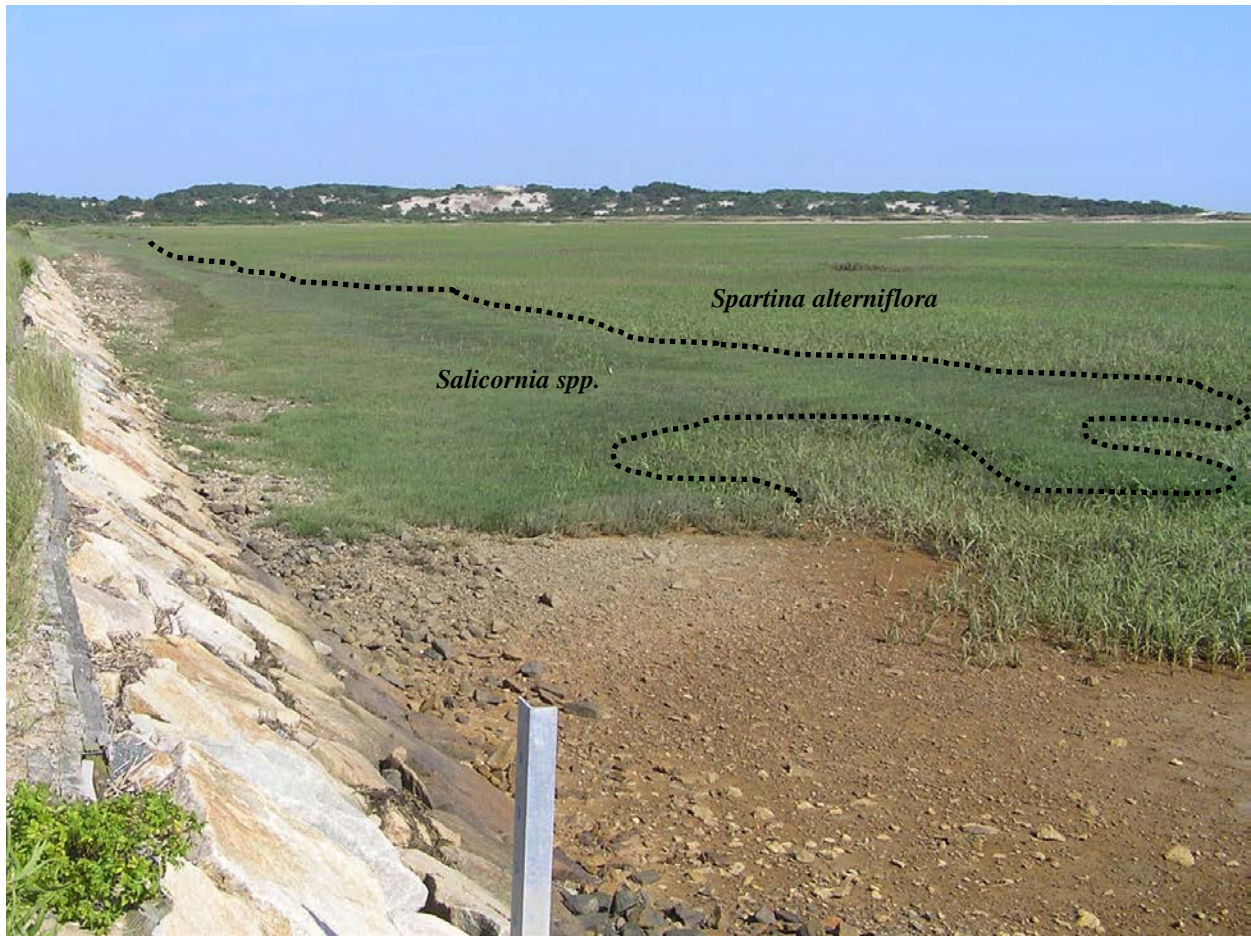
Figure 4.3: Hatches Harbor - *Spartina alterniflora* **and** *Salicornia spp.* **zonation along a man-made dike.**
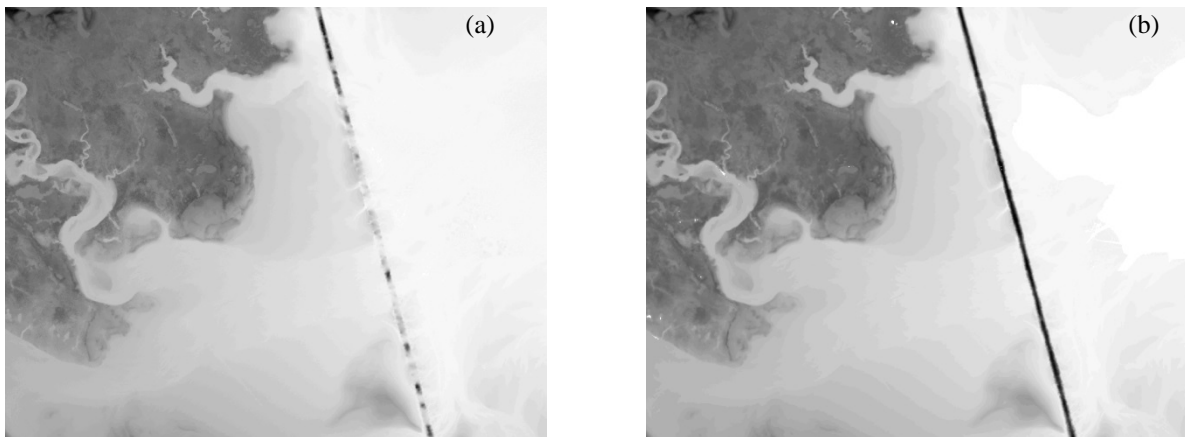
Figure 4.4: (a) Terrascan classified ground elevation grid of Moors marsh delivered from by the lidar provider. (b) IDW (1 cell weighting) grid produced from the LAS data of last returns. The 14 m linear stone dike is largely absent from the provided terrascan grid likely due to program settings.

Table 4.2: Hard target difference (m) between lidar measurement on pavement and RTK GNSS (n = 101) for each lidar flight.

	NCALM	ARRA
Mean	-0.087	-0.044
Min	-0.250	-0.243
Max	0.128	0.200
StDev	0.072	0.102
RMSE$_z$	0.113	0.110
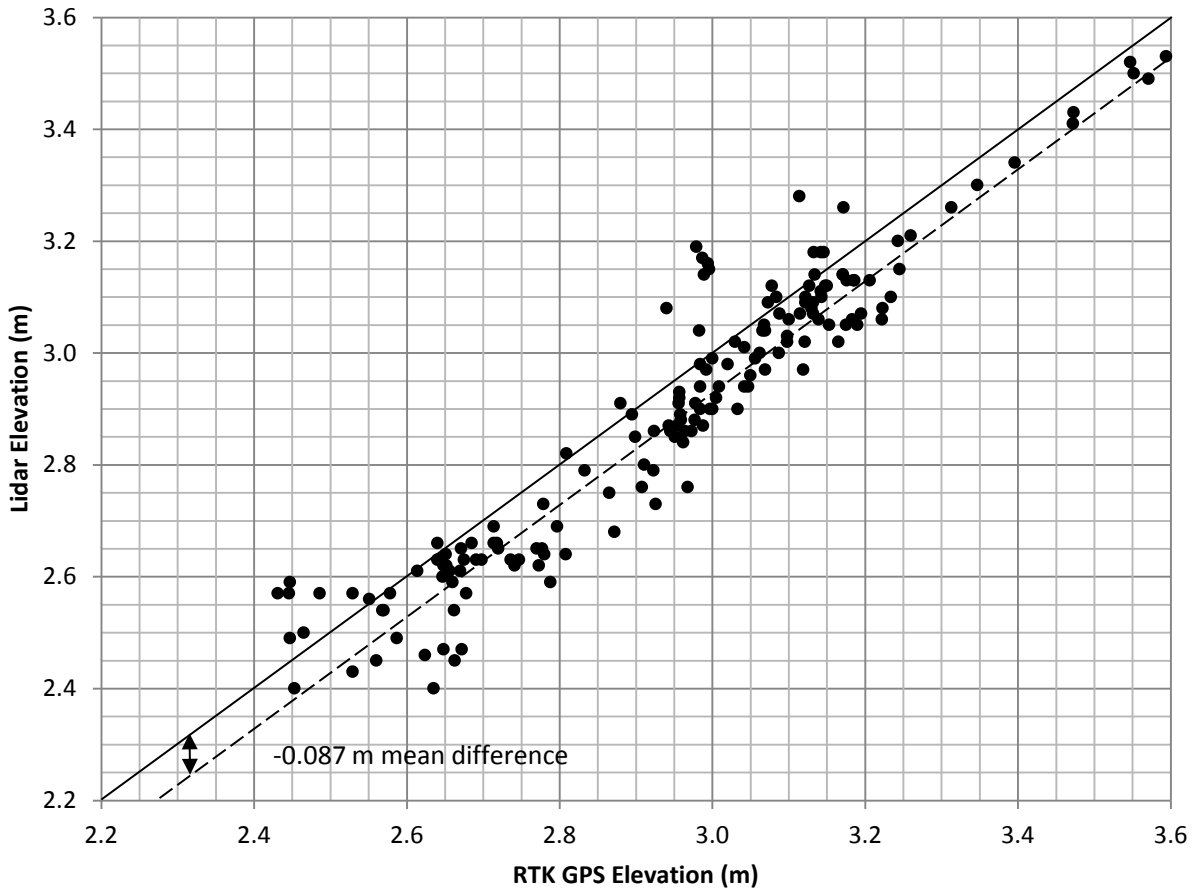
Figure 4.5: Scatter plot of RTK GNSS elevation against NCALM lidar elevation NAVD88 (n = 101) on hard targets (pavement). Solid line is a 1:1 correlation where the dashed best fit line has the same slope but is offset by a mean difference of -0.087 m.
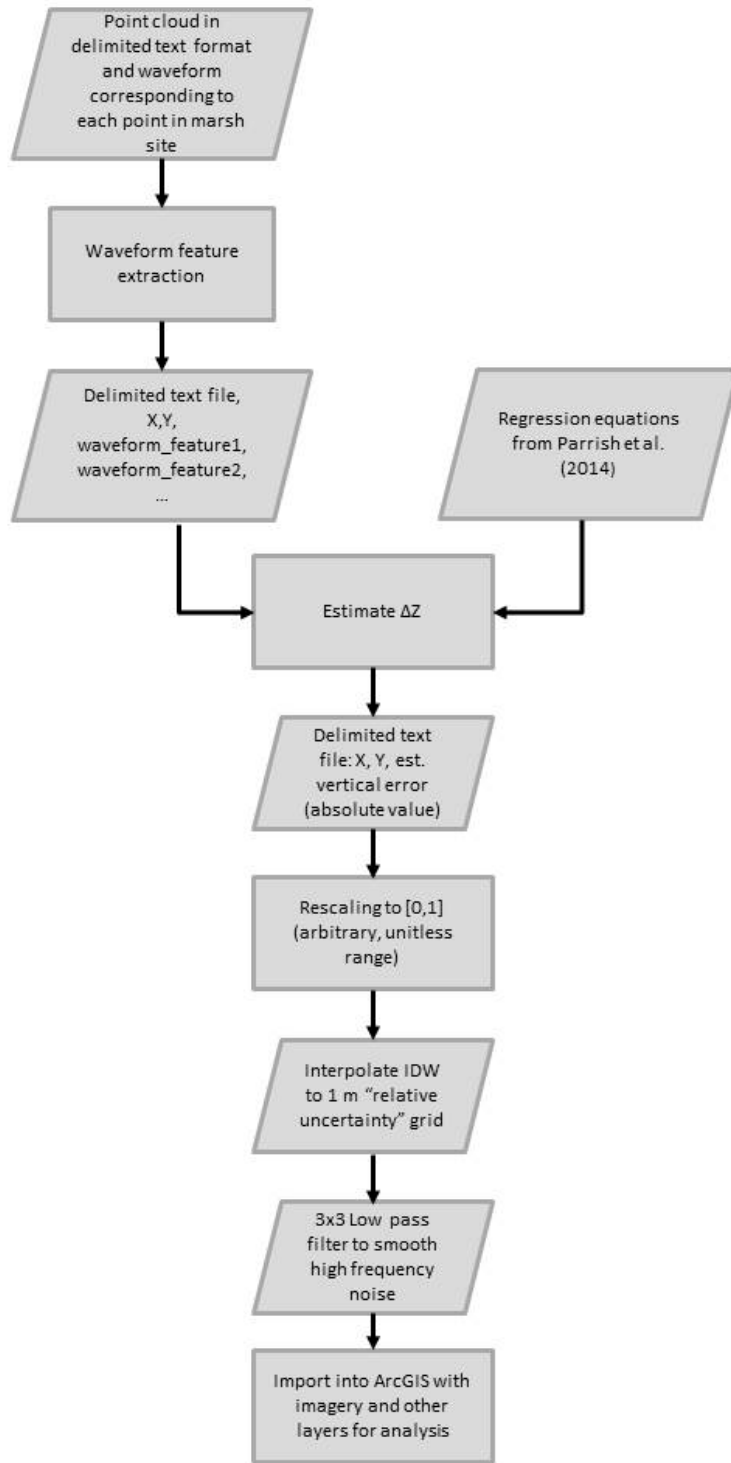
Figure 4.6: Workflow diagram for generation of relative uncertainty surfaces (RUS).

Table 4.3 –Difference (m) of Lidar and RTK GNSS by gridding method across all sites (all measurements in meters)

Grid Method	Species	N	Mean	Min	Max	Stdev	RMS
NCALM 7/20/10 IDW1x	All Vegetation	2648	0.14	-0.34	1.12	0.17	0.22
	S. alterniflora	1390	0.23	-0.34	1.12	0.20	0.30
	S. patens	709	0.05	-0.24	0.21	0.06	0.07
	Distichlis spicata	136	0.06	-0.06	0.15	0.04	0.07
	Salicornia spp.	413	0.05	-0.13	0.33	0.06	0.08
NCALM 7/20/10 IDW3x	All Vegetation	2648	0.14	-0.22	1.13	0.17	0.22
	S. alterniflora	1390	0.22	-0.22	1.13	0.19	0.29
	S. patens	709	0.05	-0.22	0.20	0.05	0.07
	Distichlis spicata	136	0.06	-0.06	0.14	0.04	0.07
	Salicornia spp.	413	0.05	-0.13	0.30	0.06	0.08
NCALM 7/20/10 Minimum Bin	All Vegetation	2648	0.09	-0.57	1.03	0.15	0.18
	S. alterniflora	1390	0.16	-0.57	1.03	0.18	0.24
	S. patens	709	0.01	-0.28	0.19	0.06	0.06
	Distichlis spicata	136	0.02	-0.10	0.10	0.04	0.05
	Salicornia spp.	413	0.01	-0.23	0.26	0.06	0.06
NCALM 7/20/10 Terrascan Ground	All Vegetation	2648	0.11	-0.60	0.91	0.14	0.18
	S. alterniflora	1390	0.18	-0.60	0.91	0.17	0.25
	S. patens	709	0.04	-0.11	0.20	0.04	0.06
	Distichlis spicata	136	0.05	-0.07	0.12	0.04	0.06
	Salicornia spp.	413	0.04	-0.13	0.28	0.05	0.07
ARRA 5/5/11 IDW1x	All Vegetation	2648	0.04	-0.50	0.29	0.06	0.08
	S. alterniflora	1390	0.04	-0.50	0.29	0.06	0.07
	S. patens	709	0.06	-0.27	0.23	0.07	0.09
	Distichlis spicata	136	0.09	-0.03	0.17	0.04	0.10
	Salicornia spp.	413	0.01	-0.20	0.23	0.05	0.05
ARRA 5/5/11 Minimum Bin	All Vegetation	2648	0.02	-1.40	0.23	0.10	0.10
	S. alterniflora	1390	0.02	-1.12	0.23	0.08	0.08
	S. patens	709	0.02	-1.40	0.23	0.12	0.12
	Distichlis spicata	136	0.06	-1.33	0.18	0.13	0.14
	Salicornia spp.	413	-0.01	-1.07	0.21	0.10	0.10

Figure 4.7: Scatter plot of RTK GNSS to NCALM July lidar elevations NAVD88 across all four marsh sites using the IDW 1x grid (n = 2,805). *Spartina alterniflora* **is represented by an open circle and all other species are represented by closed circle. The solid line represents 1:1 correlation.**
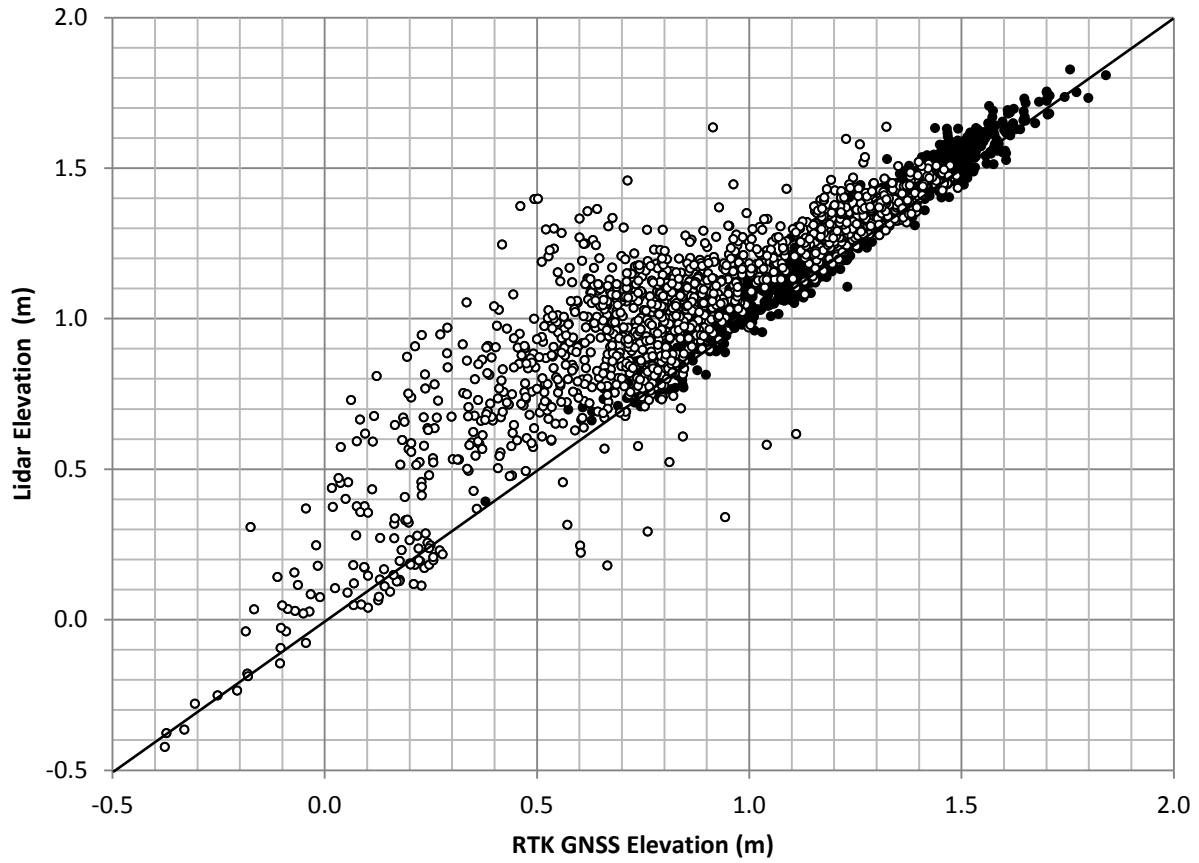
Figure 4.8: Scatter plot of RTK GNSS to NCALM July, Terrascan ground filtered lidar elevations NAVD88 across all four marsh sites using the IDW 1x grid (n = 2,805). *Spartina alterniflora* **is represented by an open circle and all other species are represented by closed circle. The solid line represents 1:1 correlation.**
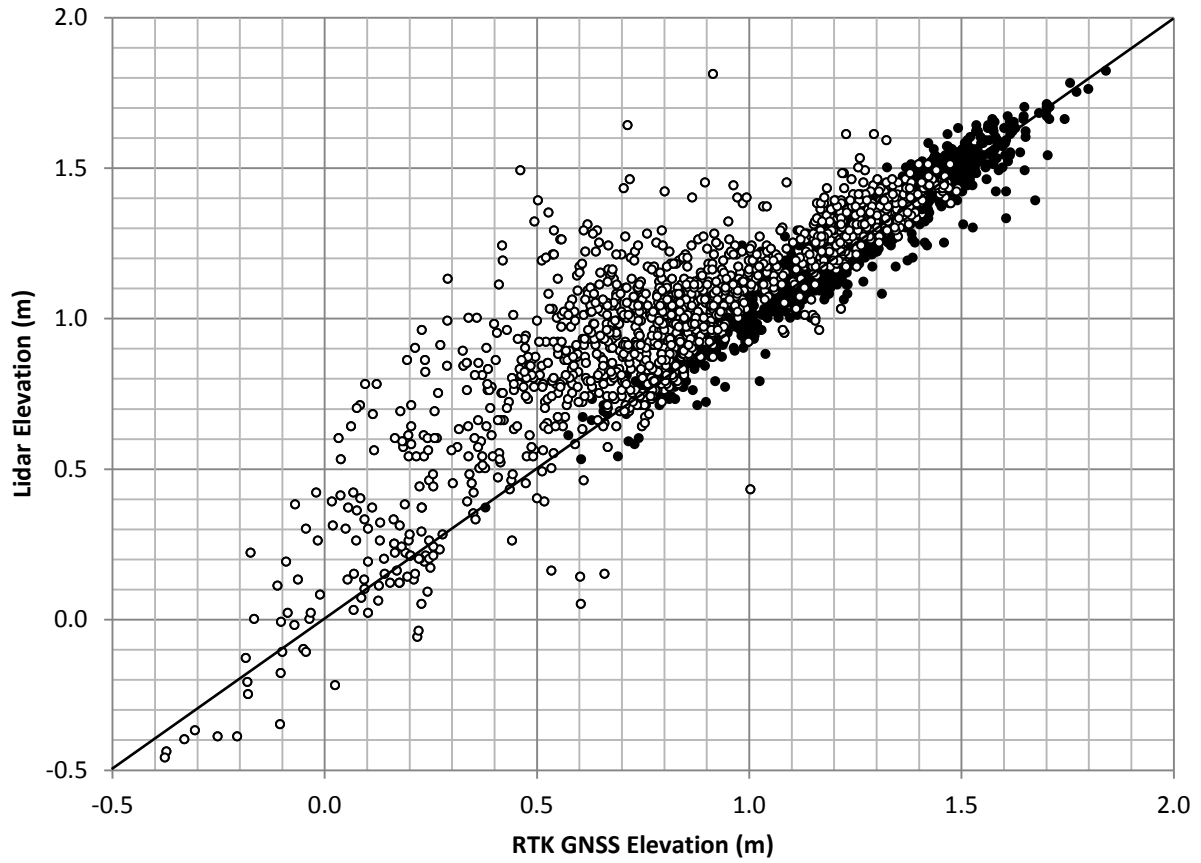
Figure 4.9: Scatter plot of RTK GNSS to NCALM July lidar elevations NAVD88 across all four marsh sites using the Minimum Bin grid (n = 2,805). *Spartina alterniflora* **is represented by an open circle and all other species are represented by closed circle. The solid line represents 1:1 correlation.**
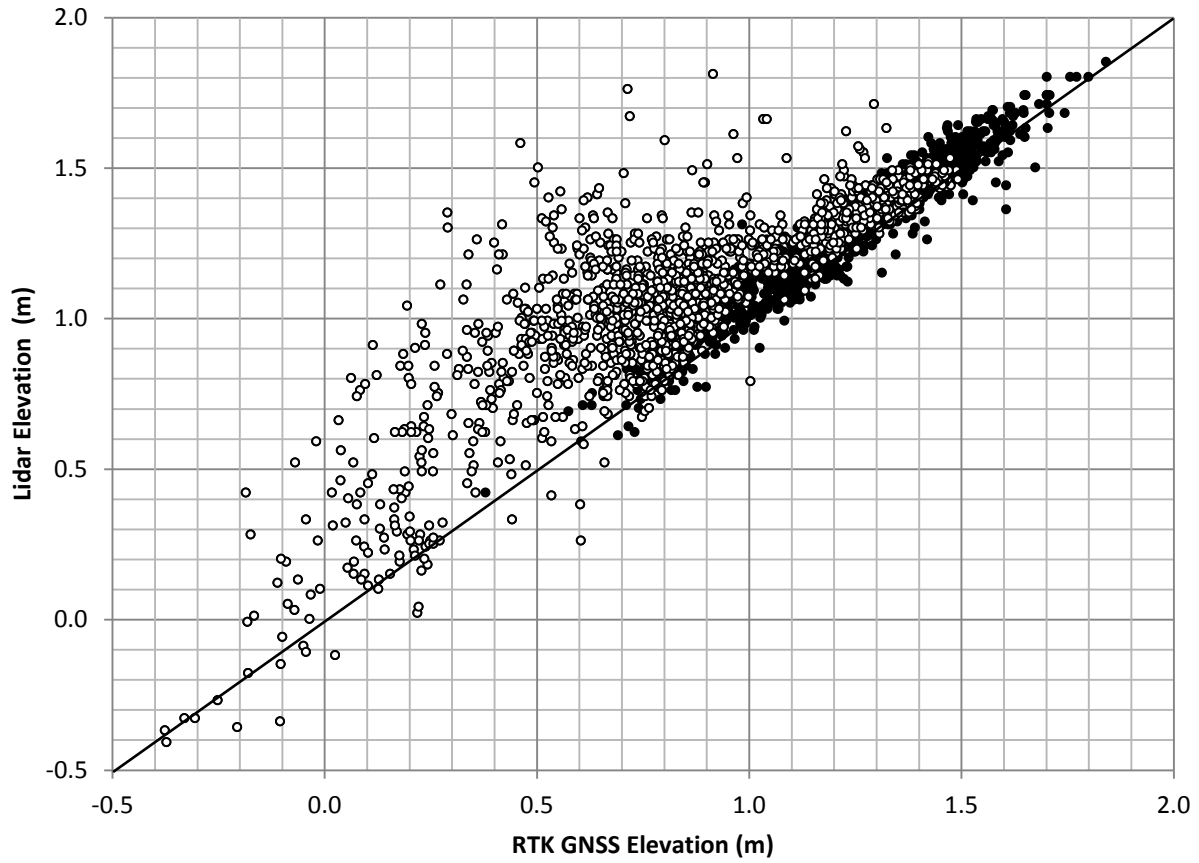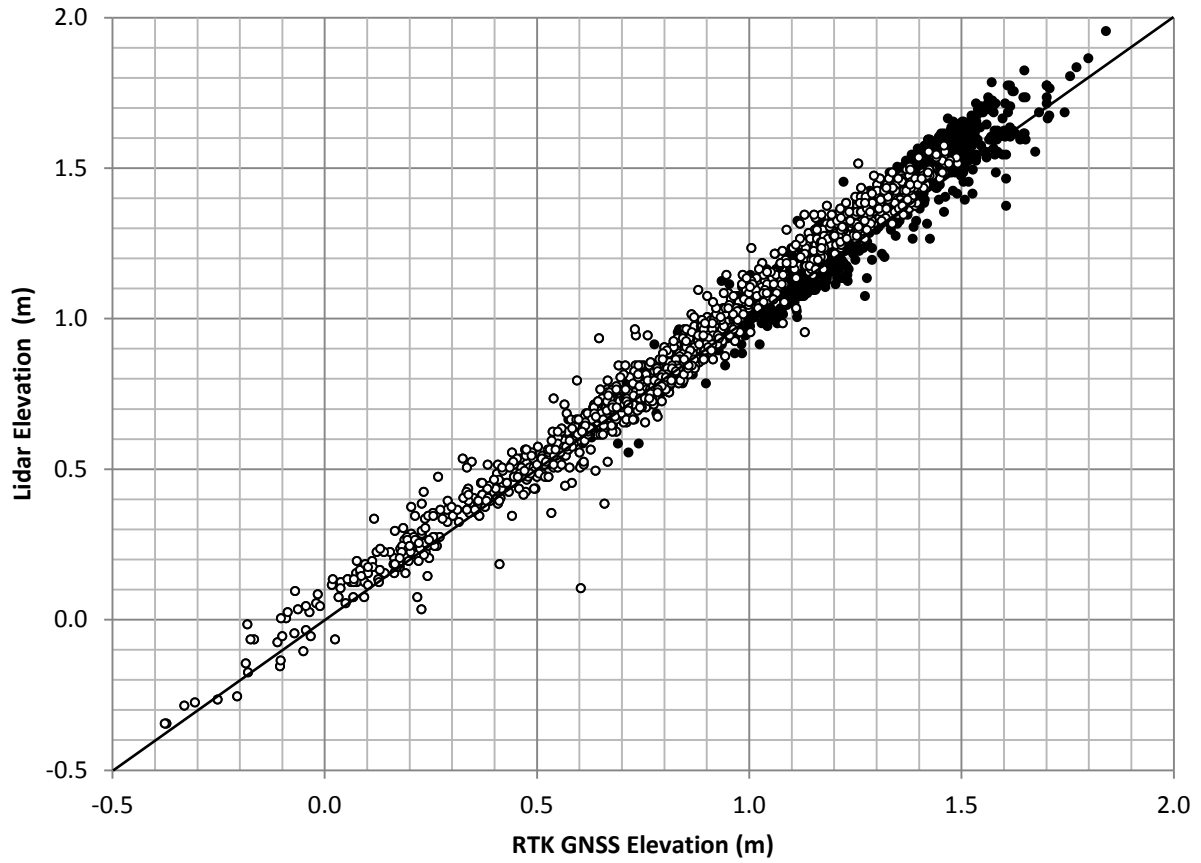
Figure 4.10: Scatter plot of RTK GNSS to ARRA May lidar elevations NAVD88 across all four marsh sites using the IDW 1x grid (n = 2,805). *Spartina alterniflora* **is represented by an open circle and all other species are represented by closed circle. The solid line represents 1:1 correlation.**

Figure 4.11: Frequency of occurrence for lidar residuals by vegetation species using the IDW 1x grid (n = 2,805) across all four marsh sites. The thick solid line represents the combined total of all *S. alterniflora* ecophene residuals [SF - Short Form (<0.5 m), MF -Medium Form (0.5 - 1 m), TF - Tall Form (>1 m)].

Table 4.4: Difference (m) of lidar and RTK GNSS by marsh for NCALM Flight

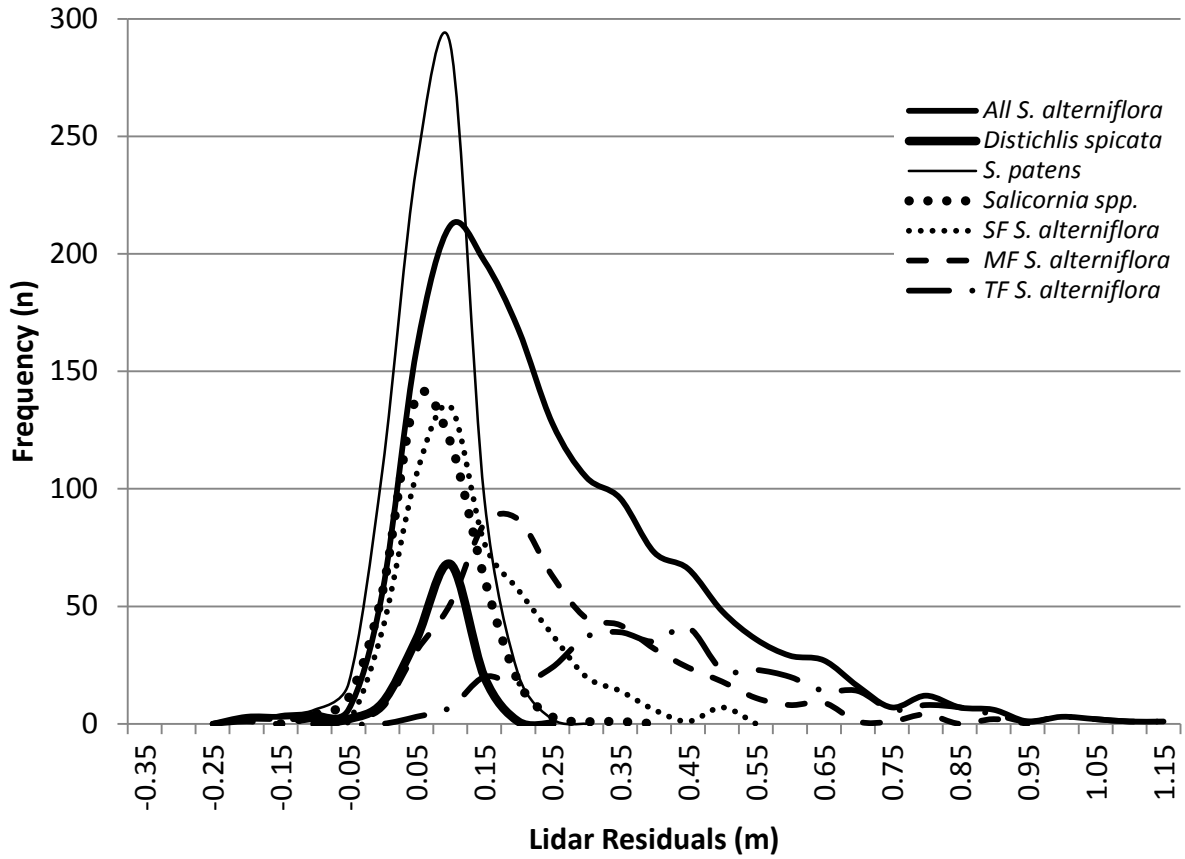| Marsh	Species	N	IDW - 7/20/10					Minimum Bin - 7/20/10				
			Mean	Min	Max	Stdev	RMS	Mean	Min	Max	Stdev	RMS
Great Island	Vegetation	532	0.11	-0.14	0.90	0.14	0.18	0.08	-0.23	0.90	0.14	0.16
	Spartina alterniflora	271	0.16	-0.06	0.90	0.18	0.24	0.13	-0.08	0.90	0.17	0.22
	Spartina patens	183	0.05	-0.06	0.17	0.04	0.07	0.02	-0.16	0.13	0.04	0.05
	Distichlis spicata	57	0.07	-0.02	0.15	0.03	0.08	0.04	-0.05	0.10	0.03	0.05
	Salicornia spp.	19	0.06	-0.05	0.21	0.06	0.09	0.03	-0.08	0.14	0.05	0.06
Hatches Harbor	Vegetation	775	0.10	-0.24	0.55	0.11	0.15	0.05	-0.51	0.52	0.10	0.12
	Spartina alterniflora	406	0.16	-0.14	0.55	0.11	0.20	0.10	-0.51	0.52	0.11	0.15
	Spartina patens	121	0.02	-0.24	0.19	0.06	0.07	-0.02	-0.27	0.19	0.07	0.07
	Distichlis spicata	57	0.07	-0.14	0.15	0.04	0.08	0.03	-0.23	0.10	0.05	0.06
	Salicornia spp.	237	0.05	-0.13	0.18	0.05	0.07	0.01	-0.23	0.16	0.06	0.06
Moors Marsh	Vegetation	819	0.22	-0.34	0.96	0.20	0.30	0.15	-0.55	0.83	0.18	0.23
	Spartina alterniflora	449	0.35	-0.34	0.96	0.18	0.39	0.26	-0.55	0.83	0.17	0.31
	Spartina patens	294	0.05	-0.17	0.21	0.06	0.08	0.01	-0.28	0.19	0.06	0.06
	Distichlis spicata	3	0.01	-0.02	0.03	0.03	0.02	-0.01	-0.03	0.01	0.02	0.02
	Salicornia spp.	56	0.05	-0.20	0.30	0.06	0.08	0.01	-0.28	0.16	0.06	0.06
Pammet Marsh	Vegetation	679	0.13	-0.23	1.12	0.19	0.23	0.06	-0.57	1.03	0.16	0.18
	Spartina alterniflora	347	0.20	-0.23	1.12	0.24	0.31	0.12	-0.57	1.03	0.21	0.24
	Spartina patens	159	0.06	-0.09	0.21	0.05	0.08	0.01	-0.25	0.18	0.07	0.07
	Distichlis spicata	65	0.05	-0.06	0.13	0.04	0.07	0.01	-0.10	0.09	0.04	0.04
	Salicornia spp.	103	0.06	-0.09	0.33	0.07	0.09	0.01	-0.13	0.26	0.07	0.07

Table 4.5: Difference (m) of lidar and RTK GNSS by marsh for ARRA Flight

| Marsh	Species	N	IDW - 5/5/11					Minimum Bin - 5/5/11				
			Mean	Min	Max	Stdev	RMS	Mean	Min	Max	Stdev	RMS
Great Island	Vegetation	532	0.09	-0.20	0.23	0.05	0.10	0.06	-1.40	0.23	0.12	0.13
	Spartina alterniflora	271	0.07	-0.06	0.23	0.05	0.09	0.05	-1.12	0.23	0.09	0.10
	Spartina patens	183	0.11	-0.16	0.21	0.04	0.12	0.08	-1.40	0.23	0.12	0.15
	Distichlis spicata	57	0.12	0.03	0.17	0.03	0.12	0.08	-1.33	0.18	0.19	0.21
	Salicornia spp.	19	0.05	-0.20	0.23	0.09	0.10	0.04	-0.33	0.21	0.11	0.12
Hatches Harbor	Vegetation	775	0.01	-0.28	0.20	0.04	0.04	-0.02	-1.25	0.21	0.11	0.11
	Spartina alterniflora	406	0.02	-0.28	0.20	0.04	0.05	-0.01	-0.87	0.21	0.09	0.09
	Spartina patens	121	-0.01	-0.23	0.11	0.05	0.05	-0.04	-1.25	0.11	0.16	0.16
	Distichlis spicata	57	0.11	-0.03	0.17	0.04	0.12	0.07	-1.33	0.18	0.20	0.21
	Salicornia spp.	237	-0.01	-0.11	0.09	0.03	0.03	-0.03	-1.07	0.07	0.11	0.12
Moors Marsh	Vegetation	819	0.02	-0.50	0.17	0.05	0.06	0.00	-1.29	0.19	0.08	0.08
	Spartina alterniflora	449	0.02	-0.50	0.17	0.05	0.06	0.00	-0.47	0.19	0.06	0.06
	Spartina patens	311	0.03	-0.27	0.14	0.06	0.06	-0.01	-1.29	0.11	0.09	0.09
	Distichlis spicata	3	0.05	0.01	0.11	0.05	0.07	0.00	-0.05	0.06	0.05	0.04
	Salicornia spp.	56	-0.01	-0.14	0.17	0.04	0.04	-0.01	-0.24	0.16	0.07	0.07
Pamet Marsh	Vegetation	679	0.08	-0.20	0.29	0.05	0.09	0.04	-0.38	0.22	0.06	0.07
	Spartina alterniflora	347	0.08	-0.18	0.29	0.05	0.09	0.04	-0.38	0.22	0.06	0.07
	Spartina patens	164	0.09	-0.20	0.23	0.05	0.10	0.05	-0.27	0.17	0.05	0.07
	Distichlis spicata	65	0.09	0.01	0.16	0.03	0.09	0.05	-0.05	0.15	0.04	0.06
	Salicornia spp.	103	0.06	-0.10	0.19	0.04	0.08	0.03	-0.21	0.12	0.04	0.05
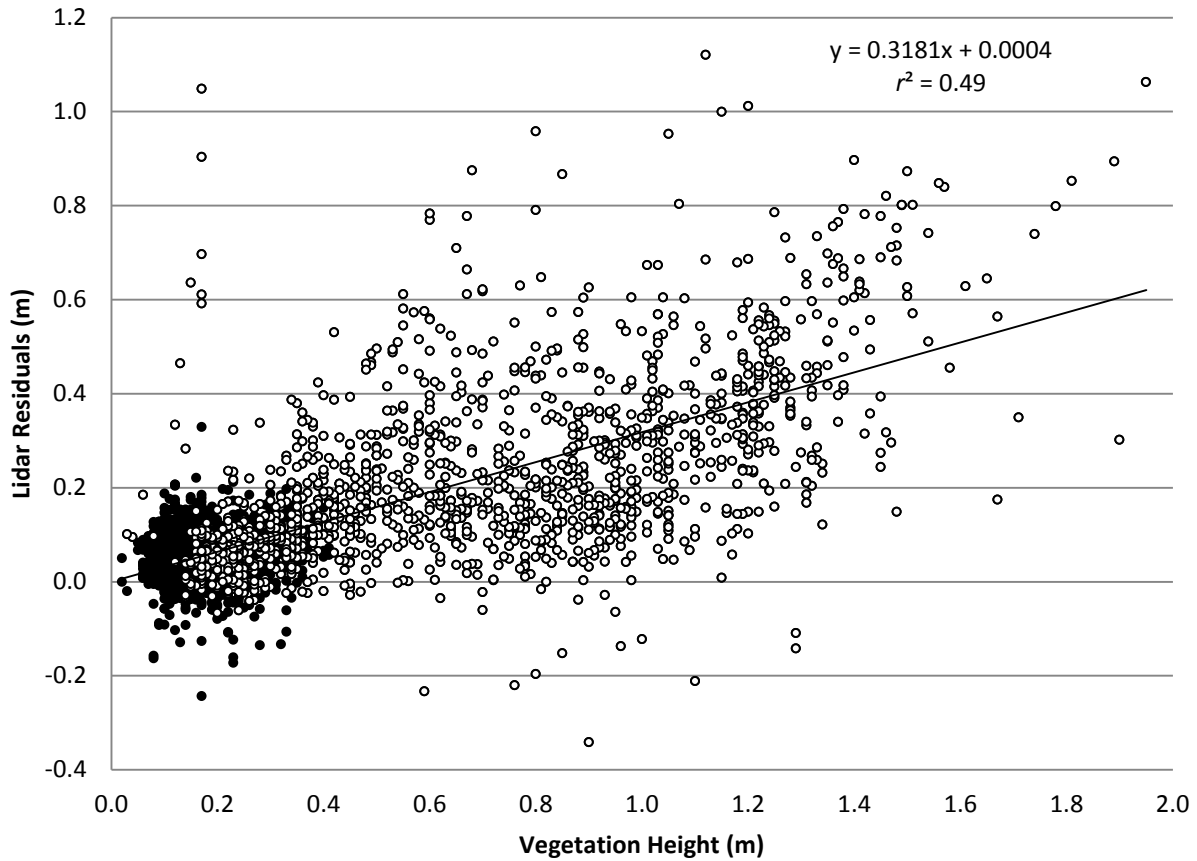
Figure 4.12: Scatter plot of lidar residuals across all four marsh sites using the IDW 1x grid (n = 2,805) and field measured vegetation height. *Spartina alterniflora* **is represented by an open circle and all other species are represented by closed circle. A regression of only the** *Spartina alterniflora* **exhibits an** r^2 **of 0.36 (n = 1,473)**

Table 4.6: Vegetation heights (cm) across all four marsh sites collected during the NCALM July 20th **2010 lidar flight. The bias to height ratio (BHR) is the mean of the ratio of lidar residuals to vegetation heights.**

Analysis	N	Mean	Min	Max	SD	BHR
All Vegetation	2648	46.6	2	195	38.3	34%
Spartina alterniflora	1473	68.8	3	195	38.5	35%
Spartina patens	781	18.0	2	41	7.8	35%
Distichlis spicata	136	22.3	8	42	8.5	34%
Salicornia spp.	258	19.4	5	27	5.1	25%

Table 4.7: Difference between the ARRA May 5th, 2011 and the NCALM July 20th 2010 lidar flights across all four marsh sites (n = 2,648)

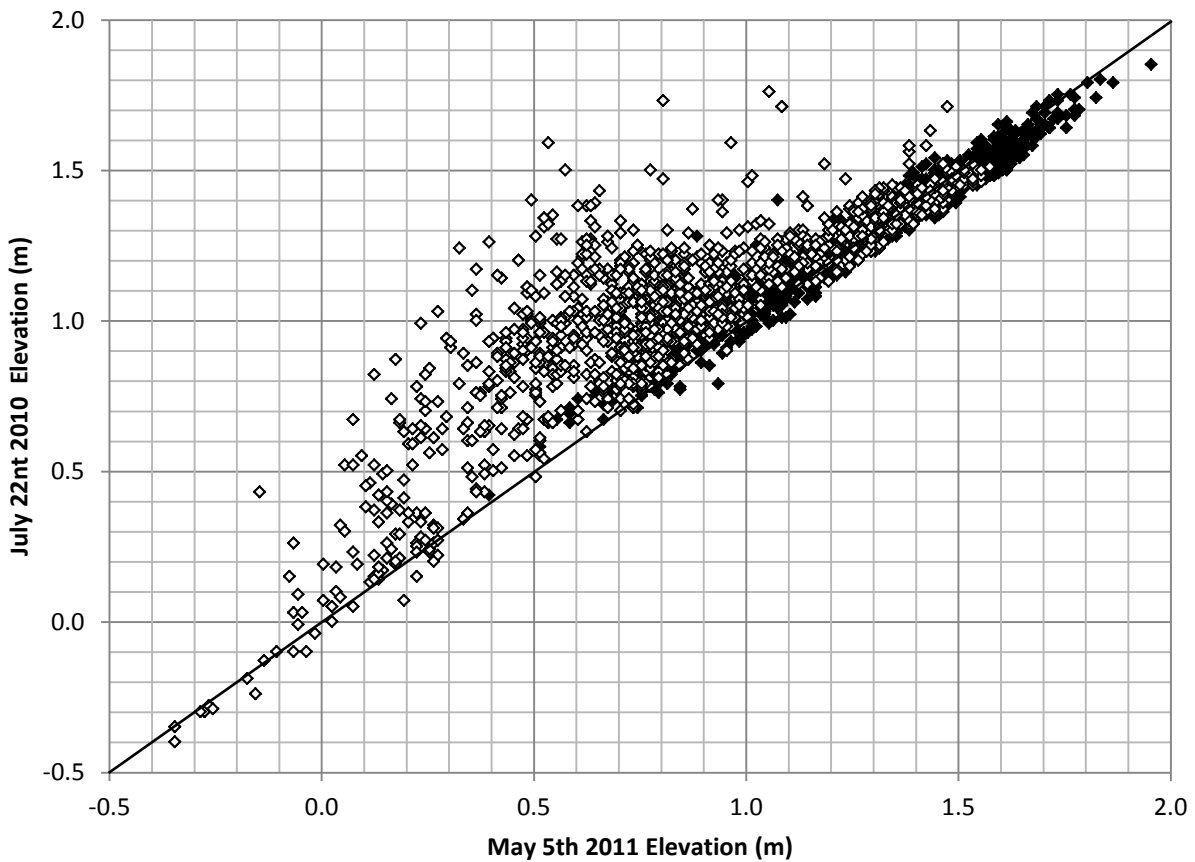| Analysis	N	Mean	Min	Max	SD	RMS
All Vegetation	2648	0.10	-0.14	1.06	0.17	0.20
Spartina alterniflora	1390	0.18	-0.12	1.06	0.19	0.26
Spartina patens	709	-0.01	-0.11	0.20	0.05	0.05
Distichlis spicata	136	-0.03	-0.10	0.06	0.03	0.05
Salicornia spp.	413	0.04	-0.14	0.40	0.06	0.07

Figure 4.13: Plot of lidar elevation NAVD88 from the ARRA May 5th, 2011 flight and the NCALM July 20th 2010 flights across all four marsh sites. The solid line represents 1:1 correlation. *Spartina alterniflora* **is represented by an open circle (n = 1,473) while all other survey vegetation species are represented by a closed circle (n = 1,337).**
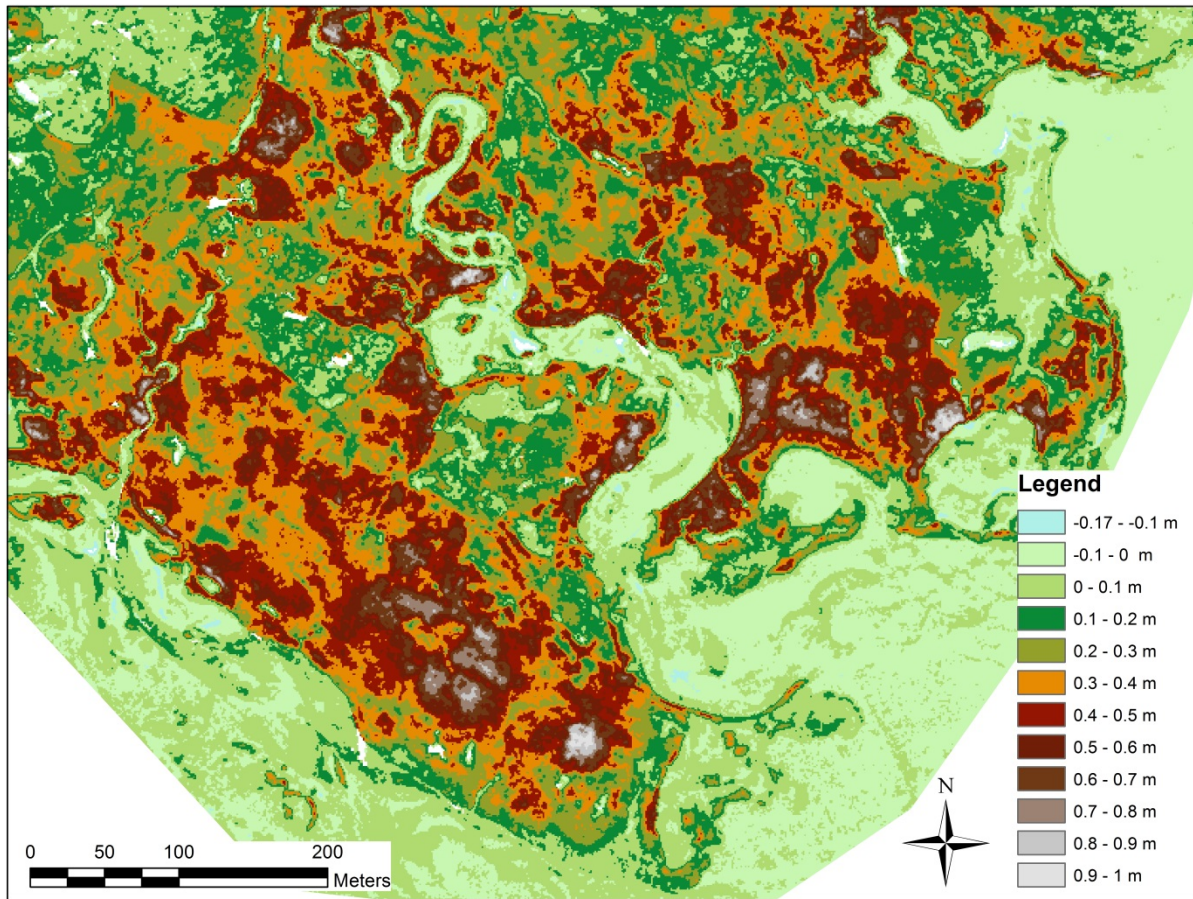
Figure 4.14: Difference map of increased marsh surface elevations from the ARRA May 5th, 2011 and the NCALM July 20th 2010 lidar flights for Moors marsh.
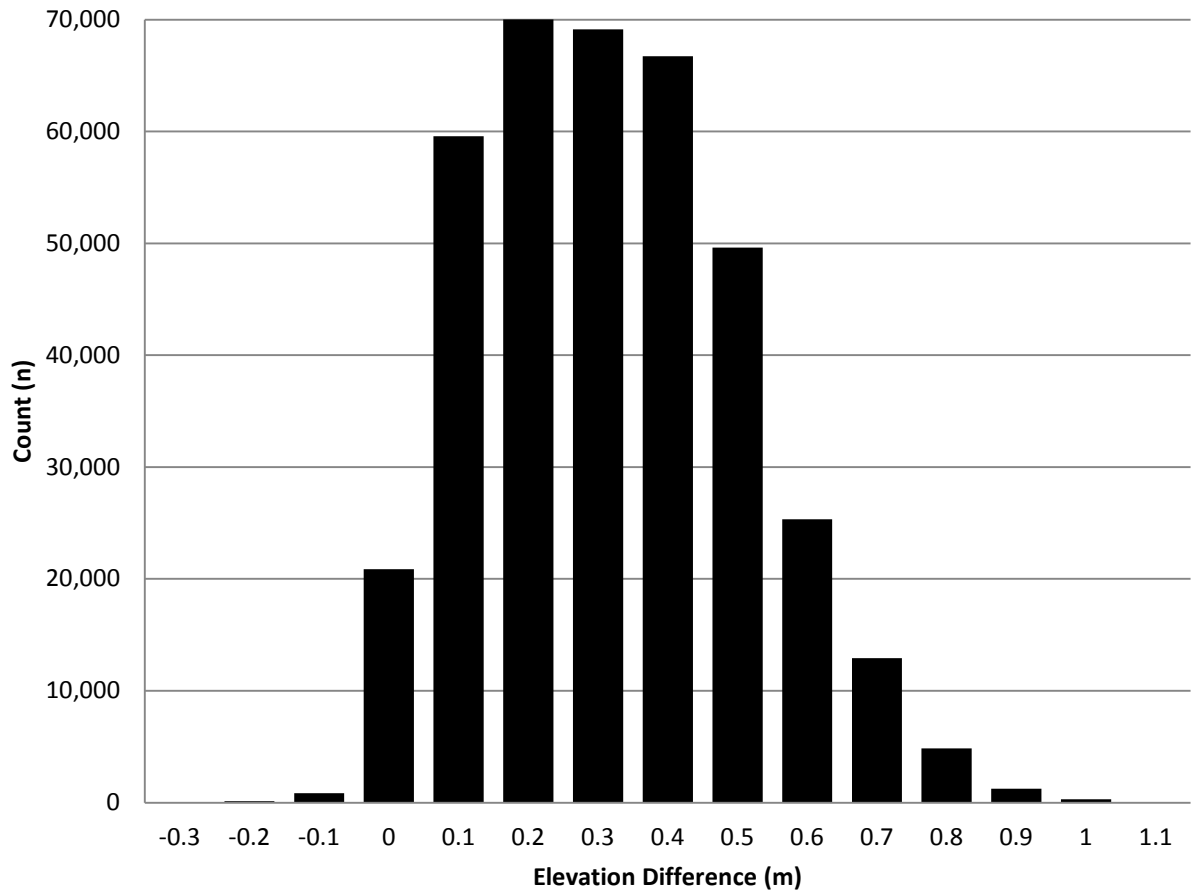
Figure 4.15: Histogram of marsh surface elevation differences from grids of the ARRA May 5th, 2011 and the NCALM July 20th 2010 lidar flights (n = 381,654) for Moors marsh.
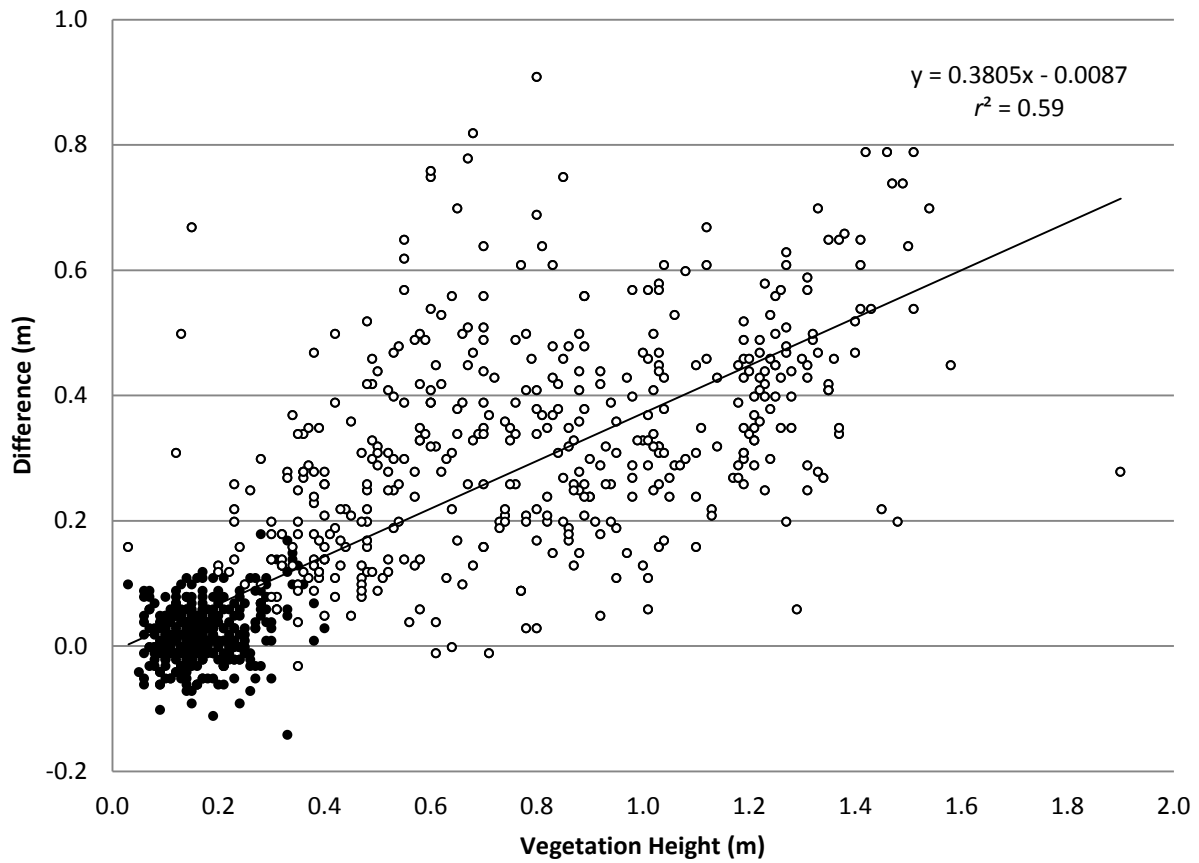
Figure 4.16: Relationship of the elevation difference between the ARRA May 5th, 2011 and the NCALM July 20th 2010 lidar flights with field recorded vegetation height (n = 788) across all four marsh sites. *Spartina alterniflora* **is represented by an open circle (n = 436) while all other vegetation species surveyed are represented by a closed circle (n = 352).**
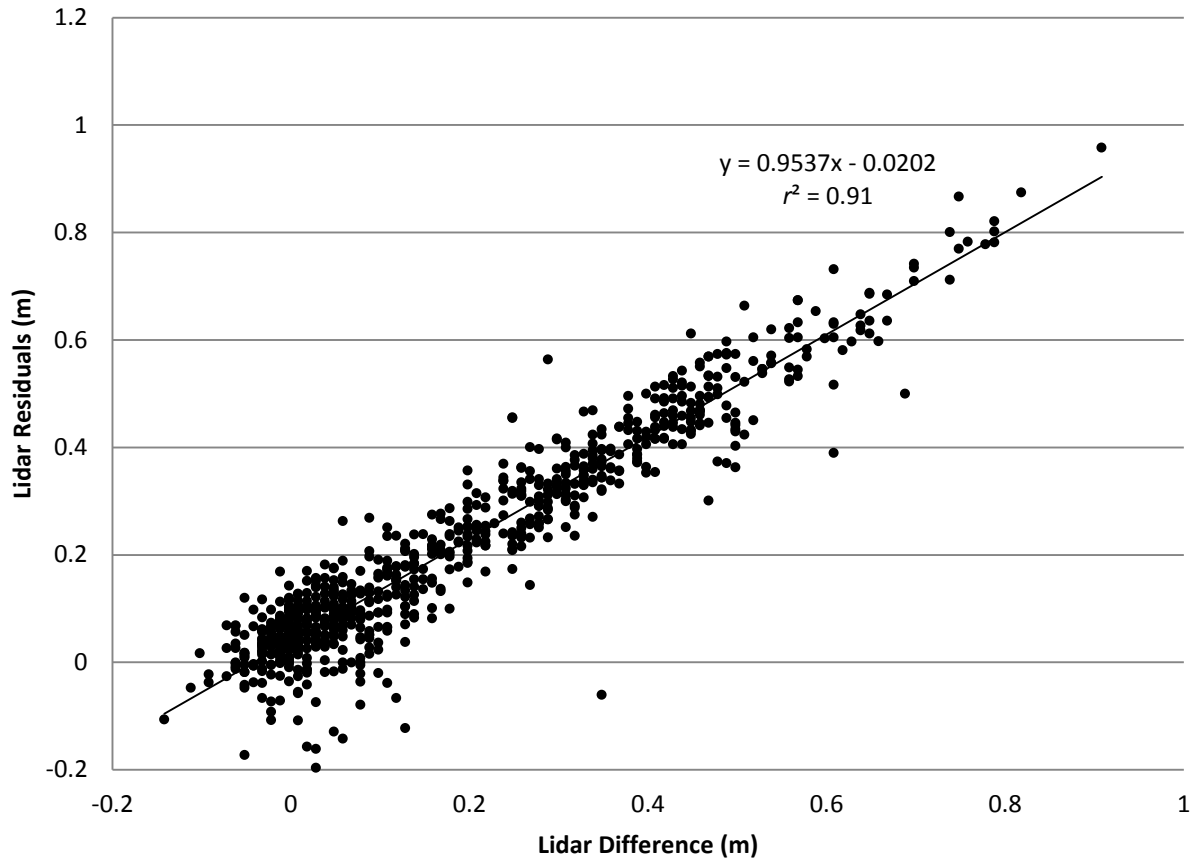
Figure 4.17: Relationship of elevation residuals (ΔZ = IDW 1x – RTK GNSS) with the difference between the ARRA May 5th, 2011 and the NCALM July 20th 2010 lidar flights (n = 785) for the Moors marsh site.
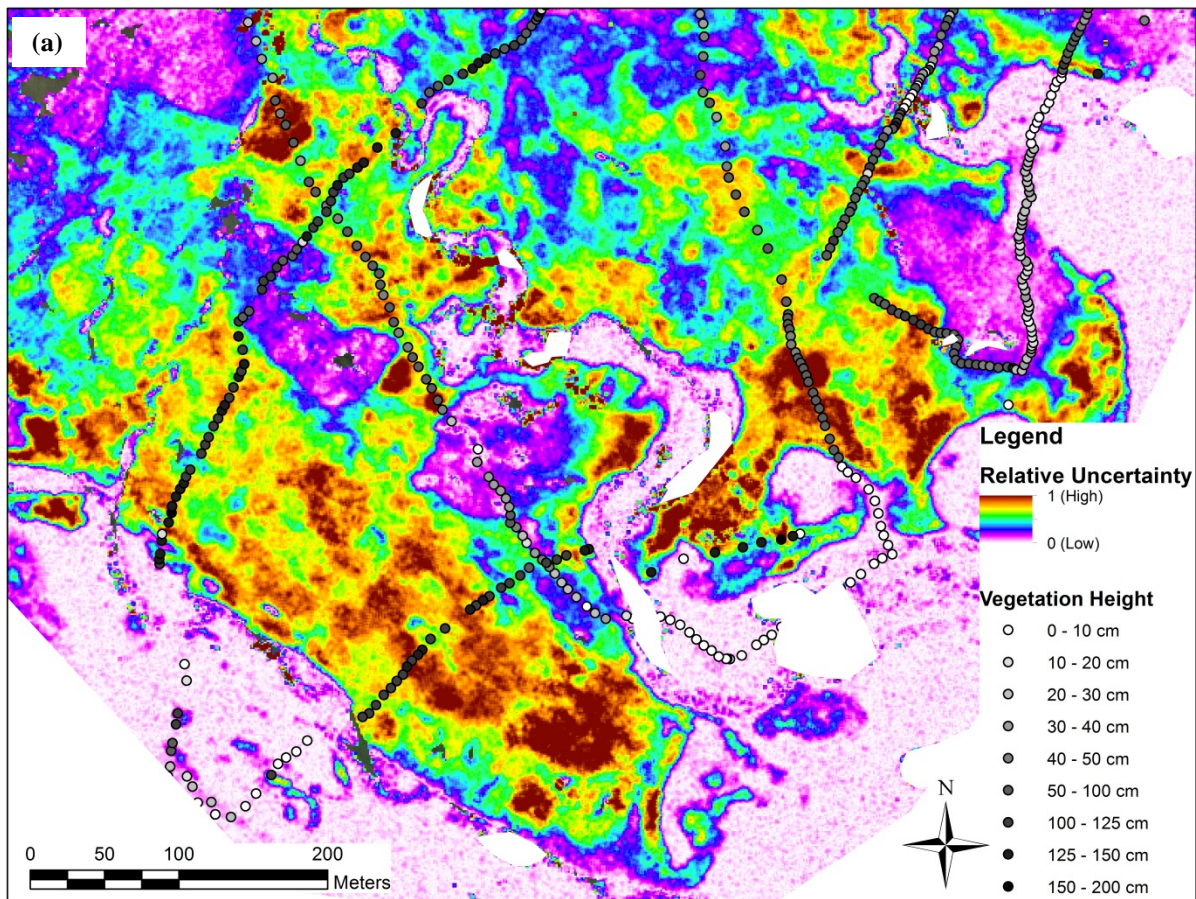
Figure 4.18a: Relative uncertainty surface (RUS) for Moors marsh developed from lidar waveform shape metrics. Note that relative uncertainty surfaces contain unitless values scaled to the range [0-1]. This product is intended to provide a depiction of the general variation in elevation uncertainty across the marsh. Field locations are color coded by vegetation height and plotted over the RUS for general comparison.
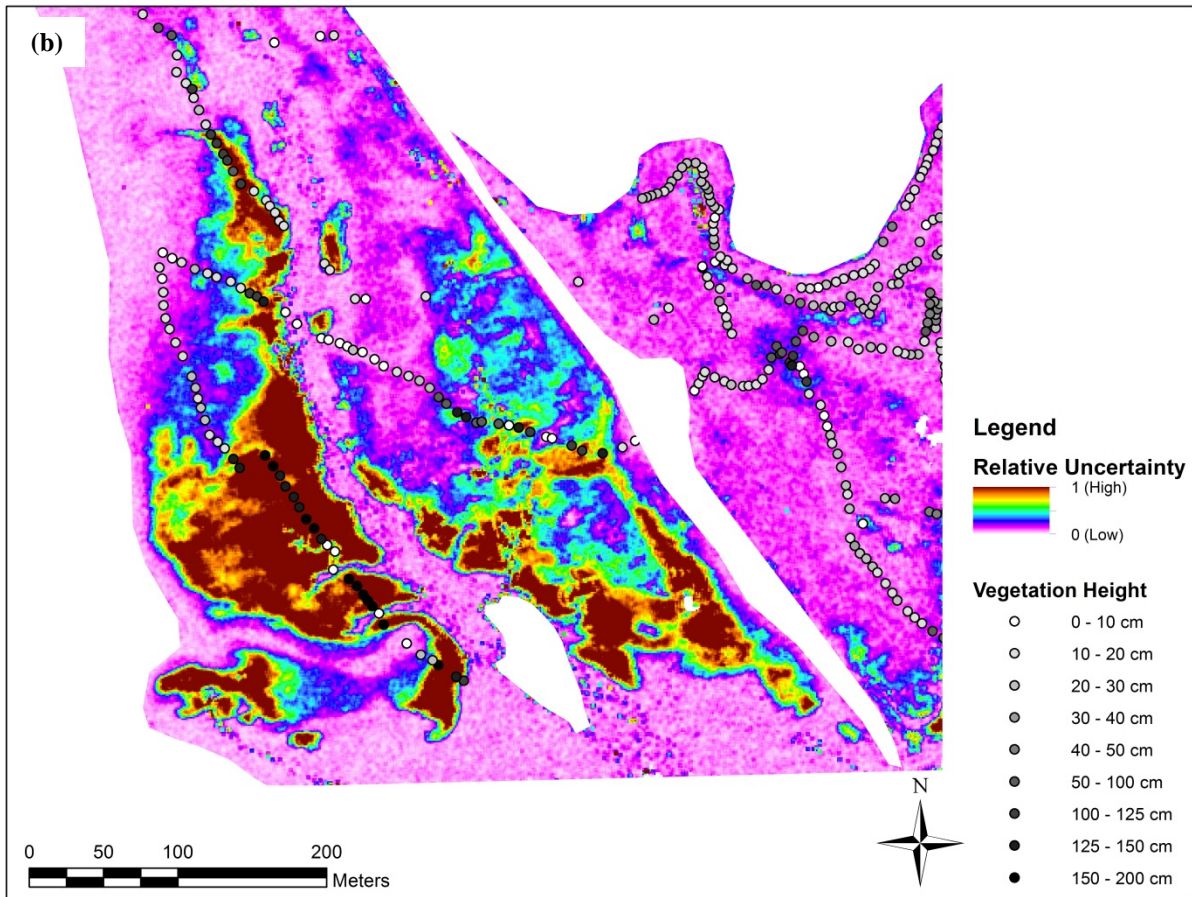
Figure 4.18b: Relative uncertainty surface (RUS) for Pamet marsh developed from lidar waveform shape metrics. Note that relative uncertainty surfaces contain unitless values scaled to the range [0-1]. This product is intended to provide a depiction of the general variation in elevation uncertainty across the marsh. Field locations are color coded by vegetation height and plotted over the RUS for general comparison.
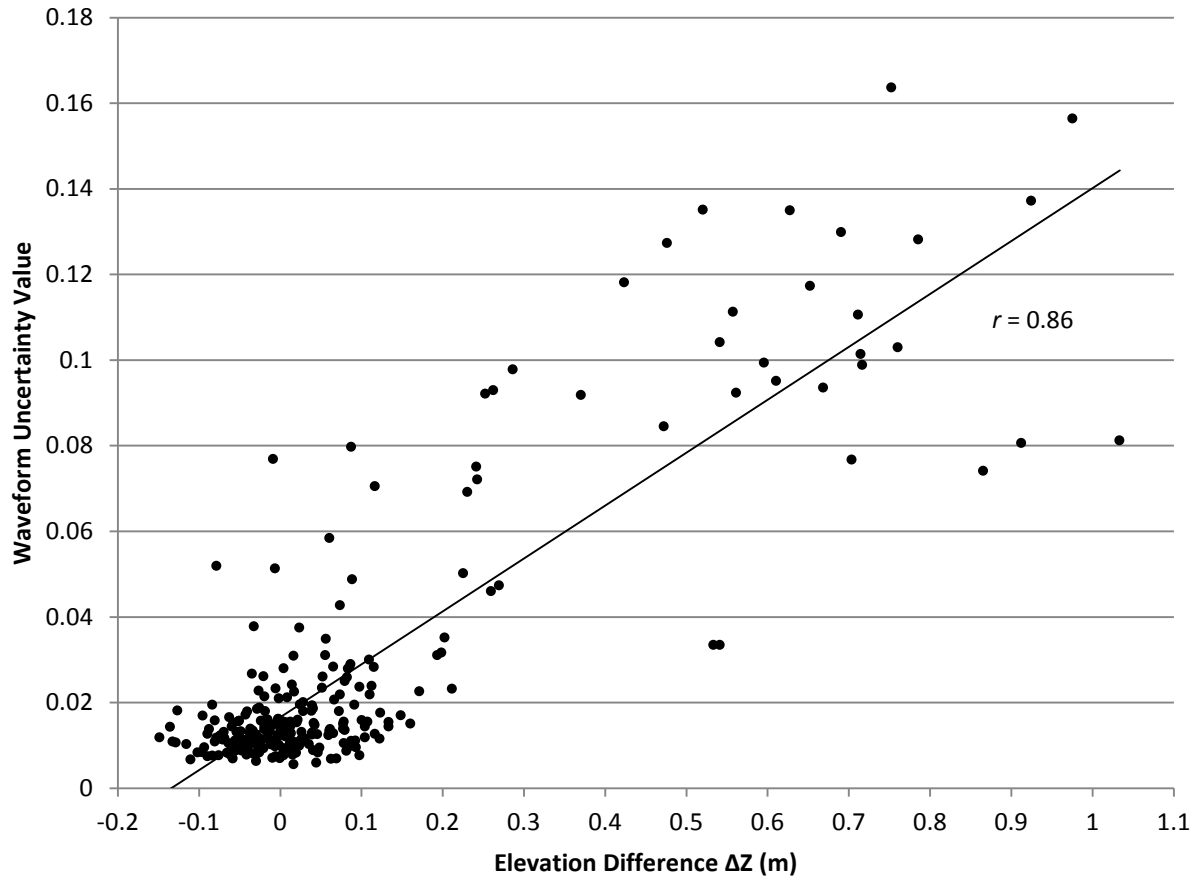
Figure 4.19: Relationship of the waveform relative uncertainty value with lidar bias (ΔZ) for all vegetation types (n = 271) at Pamet marsh from the NCALM July 20th, 2010 dataset. The Pearson correlation coefficient (*r*) is presented.
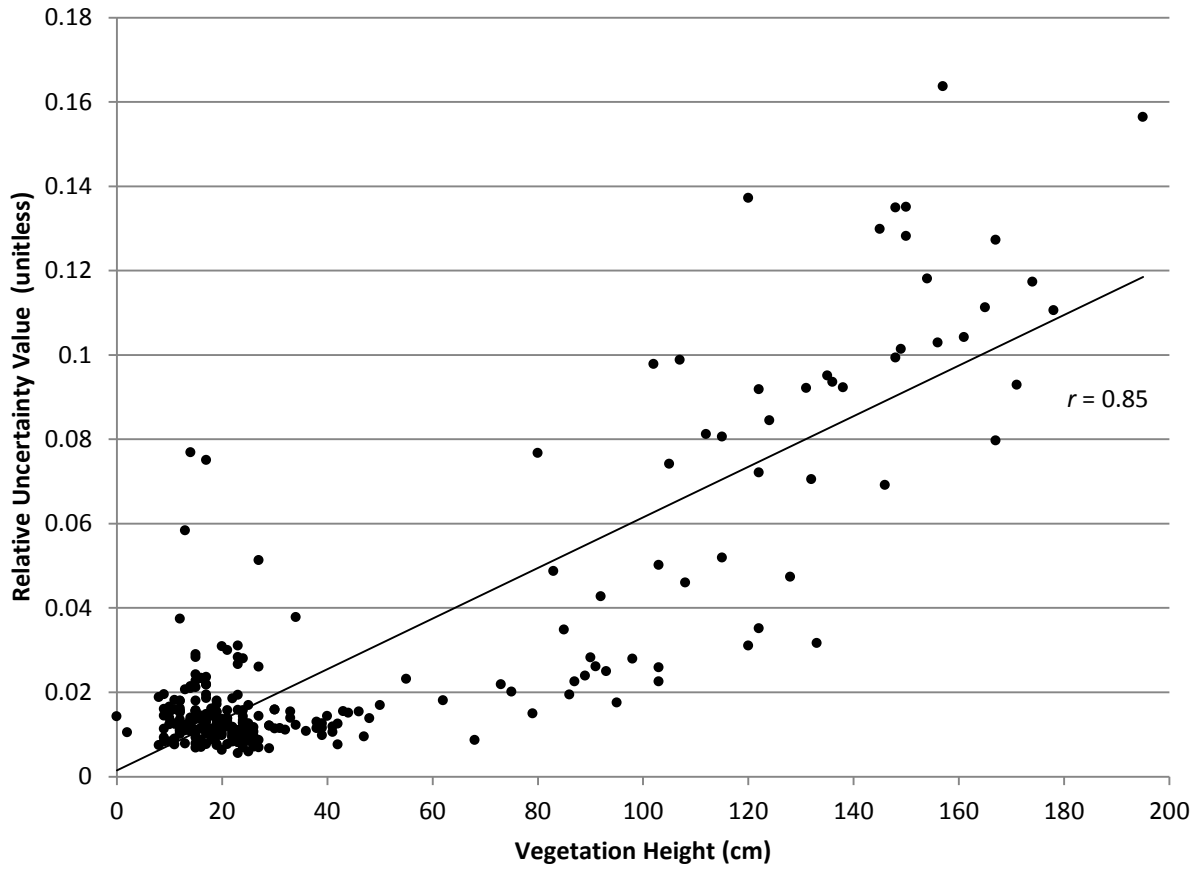
Figure 4.20: Relationship of the waveform relative uncertainty value with vegetation height for all vegetation types (n = 268) at Pamet marsh from the NCALM July 20th, 2010 dataset. The Pearson correlation coefficient (*r*) is presented.

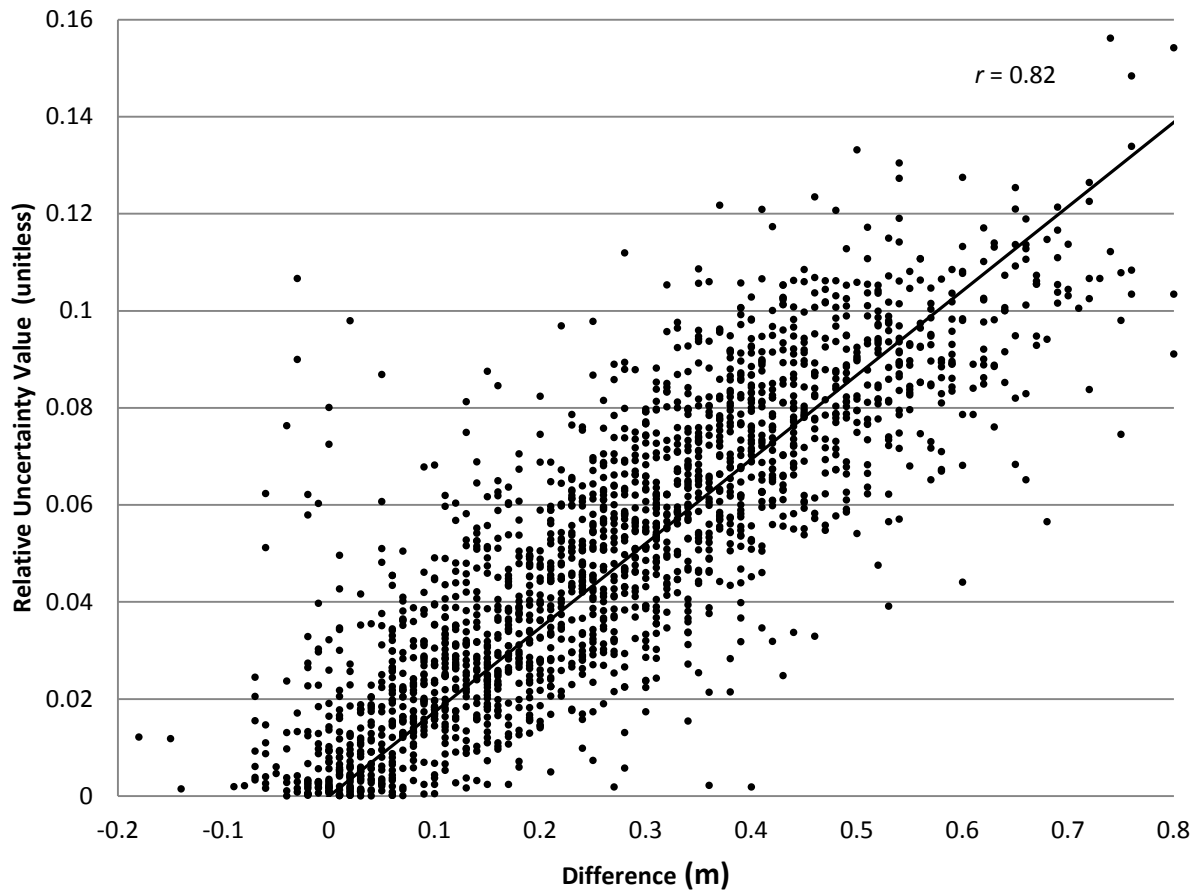**Figure 4.21: Relationship of the waveform relative uncertainty value with randomly selected subset of difference measurements (n = 2,000) at Moors marsh from grids of the ARRA May 5th, 2011 and the NCALM July 20th 2010 lidar flights. The Pearson correlation coefficient (*r*) is presented.**

CHAPTER V

IMPROVING SALT MARSH DIGITAL ELEVATION MODEL ACCURACY WITH FULL-
WAVEFORM LIDAR AND NONPARAMETRIC PREDICTIVE MODELING

Abstract

While lidar has emerged as the preferred technology for a wide variety of elevation
mapping applications, the usefulness of lidar for salt marsh mapping remains questionable. Salt
marsh vegetation tends to increase the vertical uncertainty in lidar-derived elevation data to the
point that the data can become ineffective for analysis of topographic features governing tidal
inundation as well as vegetation zonation. Previous attempts at improving lidar data of salt
marshes have ranged from simply computing and subtracting off the global elevation bias for the
entire data set to computing vegetation-specific, constant correction factors, which can be used
along with an existing habitat map to apply separate corrections to different areas within a study
site. It is hypothesized that correcting salt marsh lidar data by applying location-specific, point-
by-point corrections, which are computed from lidar waveform-derived features, tidal-datum
based elevation, distance from shoreline and other variables using nonparametric regression will
produce better results. Real time kinematic (RTK) Global Navigation Satellite System (GNSS)
measurements of ground elevation were collected at both vegetated and unvegetated surfaces for
three marshes in Cape Cod, Massachusetts, to be used as learn/test samples for model
development and evaluation. Five different model algorithms for nonparametric regression were
evaluated with the same dataset. TreeNet stochastic gradient boosting algorithm consistently

produced the best results. Using all predictor variables, including those derived from full-waveforms, it was found that the TreeNet model produced an R^2 value of 0.98 (n = 785) and slopes within 4% of a 1:1 correlation with ground elevations measured directly with RTK GNSS. Uncorrected lidar in vegetated areas exhibited a positive (high) bias of 0.24 m with a 0.23 m standard deviation, when tested against the ground control data. The correction essentially eliminated the overall elevation bias (μ = 0.00 m). An even more significant and interesting result is that, when examining the error statistics for the entire data set, the point-by-point elevation correction also enabled the standard deviation of elevation residuals about the mean to be reduced from 0.23 m to 0.07 m. Models using only DRL predictor variables performed well but were less accurate as those using full-waveform predictors. Lastly, models were constructed to predict the vegetative zone (high marsh or low marsh). All models were then scored on a full dataset of over 500,000 points to create corrected DEMs and classification maps of vegetation. Besides the initial discrete lidar elevation, waveform width was found to be the most important predictor of bias and habitat type in nearly all models developed. The methods tested here appear very promising for correction of salt marsh lidar data and do not require an existing habitat map.

Introduction

A salt marsh is a saline wetland dominated by grasses and other plants adapted to periodic flooding usually as a result of tidal forcing (Mitsch and Gosselink 2000). They are found throughout middle to high latitudes and exhibit characteristic patterns of vegetation zonation that are often based on a vertical elevation gradient (Zedler et al. 1999; Morris et al. 2005). Salt marshes provide valuable ecosystem functions, such as critical wildlife and

biodiversity support, water quality improvement, and coastal storm protection (Costanza et al. 1997; Mitsch and Gosselink 2000). Geomorphically, a salt marsh is often separated from the tidal flat by a ramp or abrupt change in elevation caused by increased sedimentation, peat development and decreased erosion due to vegetation (Crooks et al. 2002; Fagherazzi et al. 2006). These low-lying landforms are poised systems, balancing accretion and storage with erosion and oxidation of sediments in response to tidal flooding (Roman and Burdick 2012) and, therefore, are sensitive to increases in water levels resulting from sea level rise (SLR). In general, very small variations in elevation, which affect inundation, available sediments, nutrients and salinity, determine whether salt marsh species thrive, survive or fail (Morris et al. 2002). Therefore, SLR associated with climate change is a major cause of concern for coastal scientists and managers.

Accurately determining salt marsh elevation is fundamental to understanding almost every aspect of marsh system science and management including response to SLR and storm surge inundation in terms of adaptation and resiliency. However, obtaining high-resolution, high-accuracy digital elevation models (DEMs) of salt marshes can be difficult, costly, and time consuming using traditional data collection methods (Green et al. 1996). The importance of lidar (light detection and ranging) for conducting rapid surveys of salt marshes has been recognized (Brock and Sallenger 2001), and the technology is often proposed as a substitute for field-based data sets collected by either differential leveling or RTK GNSS (Real-Time Kinematic Global Navigation Satellite System) (Montane and Torres 2006; Schmid et al. 2011).

An inherent problem with the use of lidar in salt marsh systems is that the vegetation typically increases the vertical uncertainty. That uncertainty can be quantified empirically as the root mean square error (RMSE), obtained by comparison against RTK GNSS, as follows:

$$RMSE = \sqrt{\frac{1}{N}\sum_{i=1}^{n}(Z_i - Z_{i,c})^2} \qquad (1)$$

Where Z_i is the ith lidar-derived elevation and $Z_{i,c}$ is the corresponding ground control elevation. The RMSE can also be decomposed into the bias, μ (the mean difference between what the lidar determines to be bare earth elevation and ground control) and standard deviation of elevation differences about the mean, σ. For large sample sizes, N, it is expected that the following relationship will hold:

$$RMSE^2 \approx \mu^2 + \sigma^2 \qquad (2)$$

For lidar to remain a valuable technology in salt marsh research and planning, the observed uncertainty in elevation needs to be less than the elevation ranges of ecological importance (Sadro et al. 2007). For instance, if the uncertainty due to vegetative impacts on the lidar signal is greater than the elevation range determining inundation, species dominance, and habitat, then the lidar is not useful for restoration planning, hydrologic modeling, and SLR studies. Quantifying uncertainties of salt marsh lidar data and applying corrections to produce an accurate DEM (to within 4-7 cm) has, to date, been an unresolved problem. In general, uncorrected lidar datasets from salt marshes lack sufficient accuracy for use in the tasks mentioned above (Rosso et al. 2006; Schmid et al. 2011; Hladik and Alber 2012). However, research to determine the extent to which lidar penetrates the salt marsh canopy and methods to correct for vegetation-induced elevation uncertainty have begun to achieve results (Populus et al. 2001; Gopfert and Heipke 2006; Rosso et al. 2006; Schmid et al. 2011; Hladik and Alber 2012; Hladik et al. 2013; Rogers et al. In Review).

Previous Research

Prior attempts at developing correction techniques for vegetation-induced lidar uncertainty have involved: 1) subtracting off a global (i.e., computed for the entire data set) elevation bias; 2) filtering/interpolation/classification methods, algebraic functions based on canopy height and density coverage; and 3) subtraction of species-specific bias based on vegetation cover maps (Rosso et al. 2006; Wang et al. 2009; Schmid et al. 2011; Hladik and Alber 2012; Hladik et al. 2013; Rogers et al. In Review). Because of the spatial variation in elevation uncertainty across a marsh (Parrish et al. 2014), subtracting off a global bias tends to overcorrect the elevation error in some places and undercorrect it in others. Filtering and interpolation correction methods are greatly hindered by the dearth of true ground returns from the low, dense growing salt marsh vegetation and the potential inaccuracies introduced by uncertainty in the separation of ground and vegetation returns (Sadro et al. 2007; Wang et al. 2009; Schmid et al. 2011; Rogers et al. In Review). While relationships between vegetation canopy height, percent coverage and lidar uncertainty have been observed (Populus et al. 2001; Gopfert and Heipke 2006; Schmid et al. 2011), these methods can also fail to produce the desired level of elevation correction in a salt marsh.

Advancements in salt marsh DEM correction methods have been made by conducting species-specific elevation correction (Sadro et al. 2007; Hladik and Alber 2012; Hladik et al. 2013). Since the error is primarily attributable to vegetation and tends to be species-dependent, this method vastly improved DEM accuracy by focusing the appropriate amount of correction where it is needed. Yet a requirement of vegetation-based correction techniques is *a priori* knowledge of species distribution. From past project experience, existing vegetation maps are typically unavailable, too outdated, too coarse, or too inaccurate for many project sites. If a

project required collecting this information, it would also necessitate additional fieldwork or multi/hyperspectral sensor data, as well as the processing and interpretation that add to cost, time and introduced errors. However, even if this vegetation information were always available and accurate, it has been observed that some salt marsh species correspond to different ranges of elevation uncertainty that fall in a continuous distribution rather than a constant (Rogers et al. In Review). Lidar uncertainty is presumably influenced by vegetation height, stem density, biomass, and species growth habit (Schmid et al. 2011; Hladik and Alber 2012; Rogers et al. 2015). These vegetation characteristics vary over the marsh surface as a function of edaphic conditions (nutrients, salinity, sulfide concentrations, lower redox potential) as well as other factors (Mendelssohn et al. 1981; Bertness and Ellison 1987; Mitsch and Gosselink 2000; Byrd and Kelly 2006). For example, medium-form *Spartina alterniflora* has a height range of 50 – 100 cm, and one would expect the observed lidar uncertainty to have a range as well. It seems unlikely that each vegetation species/ecophene region would require a constant DEM correction factor across its entire extent (Hladik and Alber 2012; Hladik et al. 2013).

Full-waveform and Nonparametric Modeling Approach

An alternate method to the problem of salt marsh lidar elevation correction involves the use of full-waveform lidar systems. Full-waveform equipment records the time series of backscattered energy with a digitizer and a high-capacity storage device. The amplitude of the laser return is dependent on the power of the peak transmitted pulse, the surface-intercepted fraction of the pulse, the surface reflectance, the incidence angle, and the fraction of the pulse returned toward the sensor (Lefsky et al. 2002b). As a result only a small fraction of the transmitted energy from the initial pulse returns to the sensor from the ground target (Wagner et

al. 2008). Ground targets, such as vegetation, soil and other objects tend to have a rough surface at the near infrared (NIR) wavelengths commonly used in topographic lidar and scatter lidar energy diffusely, at least as a first-order approximation. Water is often observed as a data void since most of the energy at NIR wavelengths is absorbed or undergoes specular reflection in a direction away from the sensor, although some strong returns from near-nadir beams (i.e., directly below the aircraft) are often observed.

Full-waveform digitizing systems can reveal the vertical distribution of the targets and can resolve surfaces closer together in the range direction than discrete-return lidar (DRL) systems (Drake et al. 2002; Lefsky et al. 2002b; Anderson et al. 2008; Parrish et al. 2011). Data processing techniques for full-waveform lidar usually involve computationally-complex decomposition or deconvolution (Jutzi and Stilla 2006) of the returned backscatter into relevant peaks to generate denser point clouds then would be available from DRL systems (Wagner et al. 2008; Mallet and Bretar 2009). Studies utilizing simple, feature-based waveform metrics have started to demonstrate utility in the waveform data beyond these resource intensive approaches (Adams et al. 2012; Muss et al. 2013; Parrish et al. 2014; Rogers et al. 2015; Rogers et al. In Review).

In a previous study by the authors, it was observed that distributions of vegetation height display unique, species-based characteristics (**Figure 5.1**) (Rogers et al. In Review). While this relationship appeared to be particularly true with *S. alterniflora* and *Salicornia spp.*, *S. patens* and *D. spicata* maintain very similar growth characteristics and range of elevation dominance. Additionally, there is a known association between elevation and vegetation height such that as marsh elevation decreases the vegetation height increases (**Figure 5.2**). It has also been determined that individual marsh species exhibit varying ranges of elevation uncertainty unique

to their growth and form (Schmid et al. 2011; Hladik 2012; Rogers et al. In Review). Therefore, the ability to discriminate between species using these and other observable characteristics and relationships might play a role in determining a lidar elevation correction strategy. Furthermore, a relationship between metrics derived from lidar waveform features (in particular waveform width's association with elevation uncertainty and vegetation height) (Parrish et al. 2014; Rogers et al. 2015), suggest that a non-parametric modeling approach might lead to a successful correction technique.

Investigating problems with numerous independent variables and complex, possibly nonlinear response curves require the use of machine learning, nonparametric modeling. Unlike typical statistical analysis of dependent and independent variables that utilize single or multiple regression to make predictions of variable outcome, nonparametric modeling does not necessitate any hypothesis concerning variable distribution as prerequisite to analysis (Bourennane et al. 2014). Nonlinear approaches are often required in environmental modeling problems due to the complex and often concealed relationships between predictor variables (Tayyebi and Pijanowski 2014).

This research investigates the following: 1) the potential removal of vegetation-induced elevation uncertainty using full-waveform lidar feature-based metrics such as waveform width and amplitude, as well as salt marsh surface characteristics such as slope and rugosity derived from the DRL, as inputs into a battery of nonparametric modeling algorithms; 2) the use of nonparametric modeling and DRL-derived salt marsh surface characteristics (i.e. no full-waveform inputs included) to remove vegetation-induced uncertainty; and 3) creation of a vegetative zone maps using the same modeling parameters and a training set of known vegetation species locations. The ultimate goal of this work is to enable generation of models

that can correct salt marsh lidar-derived DEMs to a level suitable for ecological applications. Also, it may be possible to derive vegetative classification maps from lidar data (with limited ground truth efforts) that could assist with locating habitat, research planning, or vegetation modeling.

Methods

The study sites were comprised of three individual, mesotidal salt marshes (Moors marsh: 2.0 km^2; Pamet River marsh: 2.0 km^2; and Great Island Middle marsh; 0.3 km^2) located on protected shorelines of Cape Cod, Massachusetts (**Figure 5.3**). These marshes were selected based on the following criteria: 1) they are physically close to one another but hydrologically separate, 2) they contain large stands of the major marsh species present in northeastern United States, and 3) they are accessible, enabling collection of field data within a narrow time window around the capture of a lidar overflight conducted by the National Center for Airborne Lidar Mapping (NCALM). This area of Cape Cod Bay exhibits semidiurnal tides with a mean range of ~2.83 m (NOAA 2013).

Vegetative Community

Low marsh environments dominated by *Spartina alterniflora* (smooth cordgrass) are most commonly found in the studied marshes, but it was also common to find small topographic highs (typically isolated) and a narrow border of high marsh located in the landward portion of the marshes that are dominated by *S. patens* (salt marsh hay), *D. spicata* (spike grass) and *Salicornia spp.* (glasswort) (Portnoy et al. 2003) **(Figure 5.4)**. The marsh vegetation demonstrates zonation driven by small scale elevation changes and edaphic conditions (Bertness

and Ellison 1987). Varying plant morphologies and growth habits are employed by the vegetation to adapt to the harsh conditions found in tidal marshes.

Within each vegetative community there was variability in growth habit and height. For example, *Spartina alterniflora* at these sites has three distinct variations or ecophenes caused by edaphic factors, often reported as short form (0-50 cm; SF), medium form (50-100 cm; MF), and tall form (>100 cm; TF) (Reimold et al. 1973; Anderson and Treshow 1980; Ornes and Kaplan 1989; Wiegert and Freeman 1990; Pennings and Bertness 2001; Hladik and Alber 2012). Tall-form *S. alterniflora* ranges up to 2 m in height and was typically found at lower elevations with semidiurnal flooding and along estuarine creeks. In contrast, SF *S. alterniflora* is commonly found in high marsh depressions with higher salinity, greater sulfide concentrations and/or lower redox potential (Mitsch and Gosselink 2000).

Lidar Data Collection

Approximately 37 km^2 of lidar data was collected by The National Center for Airborne Laser Mapping (NCALM) on July 20th, 2010 centered on the daily predicted low tide (± 90 minutes). An Optech GEMINI Airborne Laser Terrain Mapper (ALTM) and an Optech 12-bit IWD-2 intelligent waveform digitizer were mounted in a twin-engine Cessna 337 Skymaster. Data were collected at a pulse repetition rate of 70 kHz and a flight speed of 60 m/sec and altitude of 600 m (**Table 5.1**) during peak biomass. DRL was collected using the Optech hardware-based constant fraction discriminator and time interval meter. Waveform data were delivered in Optech's NDF binary format with an IDX index file and sampled at 1 ns intervals. The salt marshes studied are comprised of low-growing marsh vegetation, "bare earth" and water features and did not include trees, buildings, or other structures such that the dataset was almost

entirely composed of single return pulses (Rogers et al. 2015). Elevations delivered in NAVD88 were converted to a local tidal datum, mean high water (MHW), using NOAA's Vertical Datum Transformation (VDatum) version 3.2 (Yang et al. 2013).

Field Data Collection

To characterize the salt marsh environment, ~2,800 ground control points (GCPs) were established in various zones including tidal sandflats, low marsh, and high marsh. Hard surfaces such as roads and parking lots in close proximity to the marshes were also surveyed to analyze the overall lidar dataset accuracy (Rogers et al. In Review). Marsh surface elevations and hard target GCPs were collected with a Trimble NetR5 base station network with cellular-based correction and a Trimble R8 Model 3 RTK GNSS rover. Due to the conditions found in salt marsh environments, special care was needed when using the rover to ensure vertical accuracy (Torres and Styles 2007). A GNSS survey rod was modified with a 12 cm diameter flat base to keep the rod from depressing into the unconsolidated mud and peat. Transects were taken through the marsh to record ground elevations, with an average point spacing of 5-7 m. The GNSS equipment provided an RMSE of < 1 cm in the horizontal and 2 cm in the vertical (based on comparisons against geodetic control within the survey site), with elevations referenced to NAVD88 using GEOID09 (the latest NGS geoid model available at the time that the majority of work in this study was completed). At each location surface conditions were recorded such as the presence of sand, mud or dominant vegetation species and canopy height for later use in the model.

Model Predictor Variables

A custom process was developed with ArcGIS10, QCoherent LP360 and MATLAB to extract lidar waveforms from the provided data files and compute waveform shape-related metrics. This research is a continuation of previous work on waveform shape metrics by the authors (Parrish et al. 2014; Rogers et al. 2015; Rogers et al. In Review). Each lidar point within a subset of the studied marshes had a number of waveform features calculated, including lidar echo width, mean, area under the curve (AUC), skewness, and peak amplitude (**Table 5.2**). Each of the feature metrics was then exported as an individual ASCII file and gridded in ArcGIS Spatial Analyst using an inverse distance weighting (IDW) with a 1 m cell size.

The DRL dataset used to produce predictor variables for the model included uncorrected starting elevations and other surface measures such as rugosity and slope (**Table 5.2**). Lidar LAS files were preprocessed using QPS Fledermaus 7.43 from the original LAS point cloud data. Lidar data evaluation and cleaning were performed using the PFM 3D point cloud editor to remove artifacts as well as erroneous or non-natural points that could influence the gridding results. Elevations were converted to MHW in VDatum v. 3.2 and gridded using an IDW interpolation method with a cell size of 1 m and a weighting value of 1 (only values within that cell were used in the cell value calculation) (Rogers et al. In Review). Grids of surface slope (the rate of change in value from each cell to its neighbors (Burrough and McDonell 1998)), and three measures of curvature (fourth-order polynomials of a surface on a cell-by-cell basis - curvature, profile curvature and planimetric curvature (Zevenbergen and Thorne 1987)), were calculated with ArcGIS v10. Rugosity, which is a measure of surface roughness (Sappington et al. 2007), was calculated using Benthic Terrain Modeler for ArcGIS10.

Distance from shoreline was the only model input variable not taken directly from the lidar dataset. It was critical that the elevation data used in this research be referenced to a local tidal datum such as MHW as opposed to NAVD88 orthometric heights or NAD83 ellipsoid heights because salt marsh vegetation speciation is tidally driven. A relationship has been established between tidal datum elevations (i.e. Mean High Water [MHW]) and the frequency of salt marsh species occurrence (Lefor et al. 1987; Mckee and Patrick 1988; Morris et al. 2005). Therefore a tidal datum is the best possible method to analyze difference in topographic height and speciation that will assist with model pattern recognition. Another reason the MHW datum was chosen was to be consistent with the NOAA Continually Updated Shoreline Product (CUSP). MHW shoreline was extracted from the lidar following procedures similar to those used by NOAA NGS (Graham et al. 2003; White et al. 2011). Also referenced was a 2009 MassGIS high resolution (0.3 m pixel) orthophoto captured one year prior to the lidar survey. The final shoreline was an interpretation of these datasets and represents the lowest extent of vegetation, which is approximately the -1 MHW contour line, with deep water channels greater or equal to 1 m in width extending into vegetated areas.

The target variable, RTK GNSS data for "true" ground elevation in MHW, point file (n = 785) was the subset of total available field data (n > 2800) that overlapped the extracted waveform datasets. The data file also included the dominant vegetation species found at each location and was intersected with the multiple predictor grid layers calculated above. Using the "extract multivalues to point" utility in ArcGIS10, all XY locations were attributed with the corresponding waveform or surface values found in **Table 5.2**. Distance to shoreline was calculated in meters for each point using a "multiple minimum distance" script in ArcGIS and the positive direction was defined to be shoreward of this line.

Models and Model Construction

The complex and often nonlinear relationships between predictors can be extracted using nonparametric, computer-based, predictive modeling with the 13 predictor variables available in this study (**Table 2**), without any prior assumptions as to the distribution of the variables. All models were created using Salford Predictive Modeler version 7.0, a commercially available software by Salford Systems (www.salford-systems.com). A battery of five nonparametric and one parametric model runs was conducted on the target variable with the available predictor dataset to determine the most predictive models. The available data from the three study marshes were combined into one database and then partitioned into "learn" (n = 560 [71%]) and "test" (n = 225 [29%]) datasets. The modeling software randomly selects records from the provided dataset based on the user preference of the required test partition size. The commonly-referenced standard is an 80/20 split of learn to test records. However, in this analysis a slightly more robust testing sample size was established to ensure model accuracy on the independent dataset. The test data are held back from the model development process making them completely independent of the model learn data and are used solely for model validation. Models were then evaluated for their performance using three criteria: 1) a high regression coefficient of determination (R^2) returned from the model with the independent test dataset; 2) similar regression coefficients values between learn and test datasets; and 3) the closeness of fit of the final regression equation line to a perfect 1:1 correlation. Therefore, a perfect model would produce an R^2 value equal to 1 and an equation of y = x. A summary of each of the model algorithms employed in this study can be found in **Table 5.3**. An algorithmic-level description of the different models is available in the references listed in the last column of **Table 5.3**. In the implementation of each of the following models, the algorithm rules were

selected to maximize the accuracy and then tested on the independent test dataset. Final models were then scored against the complete marsh-wide grid of 525,941 records with each of the above predictor variables available for every XY point/cell in the grid.

Results

Full-waveform lidar was collected and available for the entire geographic area covering the selected salt marshes. However, only subsets of waveform data from each of the three marshes were used due to extraction and processing time constraints. Therefore, the model training dataset included only field data that were bound by the extracted subset of full-waveform data (n = 785 total across the three marshes) (**Figure 5.3**). This same subset of ground control data was also used for the DRL model runs for consistency and comparability between the various models.

Ground Detection Correction Models Using Full-waveform Features

The results of five different regression-based nonparametric models and one parametric model are presented in **Table 5.4**. The dataset used for these model runs included all available waveform metrics as well as those predictors derived from the DRL elevation data from the same flight (**Table 5.2**). The resulting models produced "test" sample regression coefficients ranging from R^2 = 0.919 to 0.963 with regression line slopes from 0.897 to 0.982 and y intercepts near 0. The top two most successful models were TreeNet and MARS with test sample R^2 values of 0.96 and slopes within 4% of a 1:1 correlation. Since the learn and test sample results were very close in R^2 value, the model was scored (run) against all of the available data with ground truth RTK GNSS elevations (Learn + Test samples, n = 785) and plotted with the original uncorrected lidar

data to visualize the improvement. The TreeNet algorithm produced slightly better results than MARS on the independent test sample with a tighter linear clustering for the scored dataset of all available data with an R^2 of 0.982 (**Figure 5.5a**). The MARS model results appear to be a little more scattered than the TreeNet model with additional negative residuals (**Figures 5.5b**).

When investigating variable importance among the various nonparametric models produced, there is an apparent trend (**Table 5.5**). The obvious and most influential variable when calculating corrected elevation is starting elevation. After calculating the most important variable, the modeling software then assigns it a score of 100 and all other variables are rescaled relative to the most important variable. The second most important variable in 4 of 5 nonparametric models was waveform width. The CART model used distance from shoreline as the second and waveform width as the third most important variables. The predictive power of waveform width is consistent with previous findings by the authors in relation to observed lidar uncertainty and vegetation characteristics such as height (Parrish et al. 2014; Rogers et al. 2015; Rogers et al. In Review). However, the third most important variable was not consistent across models. In two of five cases (TreeNet and Random Forest) that variable was distance from shoreline but in the MARS and Generalized Path Seeker models, curve and waveform amplitude respectively were the third most important variable.

Bias caused by the salt marsh vegetation on lidar returns was evident in the uncorrected dataset by comparing the vegetated field RTK GNSS measurements used in this study (n = 694, 91 GCPs were bare ground) with lidar derived elevations from the NCALM dataset (Rogers et al. In Review). Lidar measurements exhibited a positive bias of 0.24 m over the ground control data (**Table 5.6**). Separated by species type, most of that overall vegetation bias can be attributed to just *S. alterniflora* with an observed bias of 0.35 m. The other species surveyed (*S. patens*, *D.*

spicata, and *Salicornia spp.*), had a bias of between 0.05 to 0.06 m with standard deviations ranging from 0.05 to 0.08 m. The resulting "corrected" elevations from the TreeNet and MARS models were evaluated in a similar manner to the uncorrected lidar and exhibited an overall bias of 0.00 and standard deviation, σ, of 0.07 m compared to the ground control data. After correction, the biases of *S. alterniflora* and the other species were reduced substantially (0.01 to 0.02 m; **Table 5.6**). The MARS model correction produced similar results, but with a slightly larger standard deviation ($\mu = 0.00$ m; $\sigma = 0.10$ m), and less reduction in bias for the shorter species compared with the TreeNet model results. The frequency distribution of uncorrected residuals demonstrated a range of lidar error unique to each species surveyed (**Figure 5.6**). Three of the four target species had similar residual distributions but *S. alterniflora* was offset and had a long, asymmetric tail. A histogram of the TreeNet corrected residuals illustrates a tight grouping around 0 m with only *S. alterniflora* exhibiting small shoulders on either side (**Figure 5.7**).

Ground Detection Correction Models Using Discrete-Return Lidar Predictors

Using the same algorithms as implemented with the full-waveform dataset, new model runs were conducted with only predictors derived from the DRL elevation data such as rugosity and slope (**Table 5.2**). These models, without the use of the waveform feature-based metrics, produced test sample regression coefficients ranging from 0.828 to 0.911 and regression line slopes from 0.799 to 0.913 with intercepts a little below 0 (**Table 5.4**). TreeNet and Random Forest (RF) created the two most successful models with test sample R^2 values of approximately 0.91 and slopes within 9% and 14% of a 1:1 correlation, respectively. The TreeNet algorithm (**Figure 5.8a**) had slightly more scatter on the scored dataset of all available data than the RF

algorithm (**Figure 5.8b**). However, the TreeNet model results had a significantly better slope line and y intercept than RF. The RF results had residuals that suggested a more pronounced overestimation of bare ground (sandflats) and underestimated high marsh vegetation. Both models with only DRL data contained significantly more scatter and underestimation than models developed using all of the waveform predictors. Variable importance for the DRL-based models also showed starting elevation was most influential, with the second most important variable typically being rugosity (**Table 5.7**). Model variation in variable importance was illustrated in the CART model, which considered distance from shoreline as the second most important variable and rugosity the third.

The top two DRL-based models, TreeNet and Random Forest, were also evaluated on their ability to remove overall lidar bias as well as species bias (**Table 5.6**). The TreeNet corrected data exhibited an overall bias, μ, of -0.01 (σ = 0.14 m), but species contributions varied widely (-0.05 to 0.10; **Table 5.6**). The Random Forest model correction produced a similar overall bias, μ, of -0.01 (σ = 0.11 m. However, the shorter vegetation species had a tendency to be underestimated, producing negative bias of between -0.07 and -0.08 m. A TreeNet residuals histogram exhibits a symmetric grouping around 0 m with *S. alterniflora* with moderate shoulders on either side (**Figure 5.9**).

Vegetation Classification Models

Based on the strong relationships between waveform-based metrics and vegetation biophysical parameters (Rogers et al. 2015), predictive modeling was also evaluated as a method to classify salt marsh vegetation strictly from lidar data and without the use of spectral properties typically used in vegetation classification. Dominant species or ground type had been collected

as part of the field data for the 785 RTK GNSS locations across the three marshes that overlapped the extracted waveform data footprint. A model developed to separately classify the three major species and one genus (*S. alterniflora, S. patens, D. spicata*, and *Salicornia spp.*) did not produce useful results due to similarities in growth characteristics and waveform response that created considerable confusion. Therefore, a simplified approach was attempted, relying on zonation to classify vegetation.

Salt marsh ecologists often refer to the vegetative zonation within the marsh system as high marsh (HM) and low marsh (LM) and these designations represent the species present as well as the frequency of inundation, which are integrally related. High marsh vegetation species in northeastern United States marshes include *S. patens*, *D. spicata*, *Salicornia spp.* and often short-form *S. alterniflora*, while the low marsh is comprised primarily of medium and tall-form *S. alterniflora.* The zonation model employed only three classes: bare ground (GR); high marsh (HM); and low marsh (LM). Three model algorithms were evaluated and their prediction success, the ability to discriminate between the three classes, is presented in a confusion matrix (**Table 5.8**). The TreeNet model produced the highest success rate with an overall classification success of 92% in the independent test dataset with the lowest success in the GR class. Random Forest and CART models also performed well with prediction success in the mid-80th percentile. Variable importance of each of the three zonation models was evaluated (**Table 5.9**) and as with the waveform based elevation correction models found in **Table 5.4**, the three most important predictors were waveform width, starting lidar elevation, and distance from shoreline.

The models were scored against the complete lidar dataset for Moors marsh of 525,941 grid cells with all 13 predictors to create classified grids of vegetation. As a reference and for comparison, a vegetation zonation map was created using traditional aerial photo interpretation

146

and ground-truth data (**Figure 5.10**). The field map displays a system dominated by low marsh with a large central channel and several scattered high marsh regions, which are presumably topographic highs. Comparisons between maps generated by the various classification models produced similar predictions, with some performing better in high marsh and others better at discriminating between low marsh and unvegetated tidal flats (**Table 5.8**). The best performing model, TreeNet, produced a classification map that is reasonably close to the field map (**Figure 5.11**). Data gaps are typically water features such as salt ponds that are shown as white. The resultant grid distinctly displays the two vegetative regions. The model appeared to have some difficulty in interpreting bare ground just inside the shoreline contour and confused it with high marsh vegetation. It has been reported that classification of multi/hyperspectral imagery of *S. alterniflora* also has difficulty in this zone due to spectral confusion with mixed pixels that include mud: "the *Spartina* problem" (Hladik et al. 2013). The cause in this case is not likely the same but may be in part due to the presence of large mats of macroalgae on rocks (*Ascophyllum nodosum var. scorpioides* and *Fucus vesiculosus var. spiralis*). These macroalgae were not evaluated in this study but are commonly found in the intertidal zone and might produce similar waveform response to high marsh vegetation based on its biophysical characteristics. There were also several high marsh areas identified by the model that were not interpreted as high marsh (SF *S. alterniflora*) from either the field or aerial survey. A subsequent site visit to the marsh confirmed that these were indeed areas that should be classified as high marsh that were missed from the aerial photo interpretation.

Discussion

Nonparametric DEM Correction

The predictive modeling developed in this research provides a viable alternative to previous methods of DEM correction. Applying nonparametric modeling on a location-specific, point-by-point basis, reduced not only the global bias, but also the standard deviation of elevation residuals when an empirical accuracy assessment for the entire data set was performed. The models developed using both full-waveform and DRL surface predictors were successful at adapting to each pixel's varying predictors, eliminating a majority of the vegetation-induced bias. The models accomplished this without *a priori* knowledge of vegetation species location and using only a single remote sensing platform. Although many of the algorithms evaluated in this study provided good results, the TreeNet algorithm consistently provided the best performance. The final model achieved an exceptional R^2 of 0.96 on the test dataset and 0.98 on the combined learn and test datasets, which dropped the overall bias from the uncorrected 0.24 to 0.0 m, and, interestingly, also reduced the standard deviation, σ, from 0.23 to 0.07 m.

These strong results may suggest that the model may be subject to an overfitting of the data. While this is a valid consideration, it should be noted that the model algorithms used in this study, in particular TreeNet, are designed to be resistant to overfitting. TreeNet uses several regularization techniques to minimize overfitting such as a gradual buildup of the model through successive gradient boosting iterations (trees). Variables are introduced one at a time but are only permitted to adjust the model outcome by very small coefficients (Friedman 2002). Increasing the number of trees reduces the error on the learn dataset and the software determines the optimal tree that minimizes overfitting and error. In addition, another method of overfitting regularization employed by TreeNet consists of the subsample size, which is a constant fraction

of the size of the training set. A small subsample size introduces randomness into the algorithm by forcing the regression trees to be fit to reduced datasets at each boosting iteration (Friedman 2002). Nevertheless, one final method of ensuring validity of the models (i.e. absence of overfitting), would be the comparison of the results of multiple nonparametric algorithms. The results from the various algorithms based on very different mathematical formulas and concepts produced a cluster of similar results giving further indication that the data were not overfit.

The set of predictors appears to be sufficient to provide discriminatory power and high predictive model accuracy. In some of the models this list could be paired back and still achieve similar results. In addition to starting elevation, waveform width appears to be the variable with the strongest predictive power, although several other predictors such as distance from shoreline, rugosity and waveform amplitude also played key roles in some models. Previous research has suggested that the relationship between waveform width and vegetation height or lidar uncertainty has strong predictive power (Parrish et al. 2014; Rogers et al. 2015; Rogers et al. In Review). This relationship can be attributed to the convolution of the laser pulse with an extended target (i.e., taller vegetation results in greater spreading of the return pulse) (Rogers et al. 2015). Distance from shoreline also played a key role in the developed models. As distance increased from the shoreline (i.e. the lowest elevational extent of vegetation), the vegetation height was likely to decrease as well. Although variations in rugosity (surface roughness) were slight across much of the uncorrected DEM surface, there were perceptible differences between vegetation species, presumably representative of growth habits, which were used in the correction process. For example, *S. alterniflora* stands appeared to have greater rugosity than the high marsh species. The predictive power of waveform amplitude was likely due to increased planimetric obscuration (i.e. vegetation coverage) with vegetation height, especially at the near

infrared wavelength of the laser (Rogers et al. 2015). Not surprisingly, waveform amplitude and waveform standard deviation (a collinear variable with waveform width used in this study) were found to account for nearly 75% of the variability in vegetation height (Rogers et al. 2015).

The coupling of nonparametric modeling tools and GIS has become standard practice in many different environmental fields such as land use, geomorphology, soil science, and wildlife habitat (Gutierrez et al. 2009; Timm and McGarigal 2012; Bourennane et al. 2014; Meissner et al. 2014; Tayyebi and Pijanowski 2014). An uncorrected lidar DEM for Moors Marsh displays highly variable elevations with undulating clusters of vegetation growth (**Figure 5.12**). However, the scored results from the TreeNet full-waveform model for the same geographic area produced a vastly improved DEM over the uncorrected lidar dataset and suggest that the model performs extremely well at removing vegetation-induced uncertainty (**Figure 5.13**). All high elevation clustering visible in the uncorrected DEM was removed and a smooth topographic surface was uncovered. Topographic highs hidden in the original DRL dataset are now plainly visible after model correction. Species-based correction methods have been found to create step like patterns in marsh DEMs when transitioning from one species polygon to another and step removal required additional smoothing algorithms that would increase DEM inaccuracy (Hladik et al. 2013). This was particularly true within the ecophenes of *S. alterniflora* (Hladik et al. 2013). A map depicting the difference between the uncorrected lidar and the full-waveform corrected DEMs confirms the extent of vegetation-based uncertainty reduction (**Figure 5.14**). A continuous surface is produced, rather than stepped platforms. Although the overall DEM bias was clearly improved with species-based correction methods (Hladik et al. 2013), nonparametric modeling with full-waveform predictors improves bias removal while compensating for changing vegetation conditions on a pixel by pixel basis creating more accurate DEMs.

The small footprint, full-waveform data used in this project is still relatively new and not commonly included in lidar surveys. Therefore, since most researchers may not have access or the ability to process this type of data for some time, elevation correction of the raw salt marsh lidar DEM using only DRL data sources (i.e. no waveform model predictors) would be valuable as an alternative to full-waveform based correction even if it were slightly less accurate. However, there is one waveform-based parameter that is regularly supplied with DRL systems. In addition to recording return pulse time to correspond with elevation, most topographic lidar systems record the intensity, or the amplitude (typically scaled to an arbitrary range of 0-255), of the return pulse. Lidar intensity is in essence the amplitude of the return pulse, and is a function of the reflectivity of the surface at the laser wavelength (as well as range, incidence angle, and other variables). Since amplitude was found to correlate well with some salt marsh biophysical parameters (Rogers et al. 2015) and was a moderate contributor in the full-waveform model, intensity was included in the DRL based models. The lidar intensity value provided with the NCALM data delivery was uncalibrated but since the data were collected for all three marshes with the same sensor and in one continuous flight, intensity values by ground feature type from site to site are not expected to vary.

As anticipated, the DRL-based model did not produce corrected DEMs of similar quality to models created using waveforms. The use of the DRL data predictors and intensity did improve the resulting DEM over the uncorrected lidar with an $R^2 = 0.93$ and with a slope within 9% of a 1:1 correlation. The use of this type of model may be acceptable in some circumstances where partial correction is better than correction accomplished by some other means or no correction at all. This is particularly the case when data acquisition does not specify recording full-waveform returns or when processing historical DRL datasets. Scored results for the full

geographic area produced an improved DEM (**Figure 5.15**) over the uncorrected lidar dataset (**Figure 5.12**). Differences between the uncorrected and the DRL corrected DEMs suggest that the model performs reasonably well at removing vegetation-induced uncertainty (**Figure 5.16**). Although, a comparison of the waveform model difference map (**Figure 5.14**) and the DRL model difference map (**Figure 5.16**) reveals that the DRL model under-corrected elevations in areas of tallest vegetation and over-corrected in areas with the shortest vegetation (**Figure 5.17**). This is particularly prevalent in areas that could be identified as SF *S. alterniflora*.

Vegetation Classification

Salt marsh vegetation mapping is traditionally performed using field based data, aerial interpretation or classification from spectral signatures found in multi/hyperspectral imagery to show patterns in time and space as plants respond to changes in important drivers like hydrology, sea level, and sediment supply (**Figure 5.10**) (Kirwan et al. 2011; Konisky 2012). A logical extension of the uncertainty correction modeling was to test its ability to map vegetation. Due to the similarities in biophysical characteristics between some of the vegetation found at this and other northeastern United States salt marshes, mapping in a general sense, if not wholly by species, is still of value. Using a combination of predictor variables including waveform width, rugosity, and distance from shoreline, several useful models were created. A three zone model (high marsh, low marsh, and bare ground) produced the lowest error rate with an overall classification success of 92%. Such maps are commonly used by salt marsh scientists to investigate marsh habitat and monitor changes in the marsh over time due to tidal restrictions, restored flow after a restoration project, storm assessment, or the potential impacts or monitoring of SLR. Once an appropriate shoreline file is chosen or created, salt marsh mapping using full-

waveform lidar and nonparametric, predictive modeling could be automated and provide standardized results with minimal human input or interpretation, which may allow for rapid, unbiased assessments of vegetation zones. Although future research is needed to assess its full capabilities, this new vegetation classification method may also prove to be more efficient and more accurate than the traditional methods currently being employed.

It is important to note that these maps are created solely from lidar data and without the use of any spectra derived from aerial photography or multi/hyperspectral imagery. There is little if any spectral difference between the three ecophenes of *S. alterniflora* (Schmidt and Skidmore 2003; Artigas and Yang 2005) and using traditional remote sensing classification methods often results in considerable confusion among the classes. Overall classification accuracies from other studies using spectral signatures or hybrid approaches of lidar and hyperspectral imagery ranged from 59% to >90% (Rosso et al. 2006; Wang et al. 2007; Hladik et al. 2013). That the nonparametric modeling of the full-waveform metrics could achieve similar or better results without the use of spectra is significant. The classification based on lidar modeling appears a viable alternative to differentiate salt marsh vegetation into identifiable regions or classes. One possible future research direction could be to add spectral values from the various bands of multi/hyperspectral imagery as predictor variables to the waveform model to produce potentially highly accurate vegetation classification maps.

Conclusion

The utility of salt marsh DEMs based on lidar is weakened by vegetation-induced uncertainty, which continues to challenge researchers and coastal managers who desire to use high resolution lidar datasets for regional or site-specific analysis. Without a satisfactory

correction method, lidar-based DEM models are often not suitable for restoration planning, hydrologic modeling, storm impact analysis, SLR adaptability studies or other applications where fine topographic details are necessary. The conclusions drawn from this research are as follows: 1) nonparametric predictive modeling techniques, coupled with full-waveform shape-based metrics, provide a powerful tool to reduce elevation uncertainty due to salt marsh vegetation, even during peak vegetation growth conditions. The highest performing model produced an R^2 of 0.98, a slope within 4% of a 1:1 correlation, and reduced bias, μ, from 0.24 m to 0.00 m, and standard deviation, σ, from 0.23 to 0.07 m; 2) in addition to DRL starting elevation, waveform width was determined to be the most significant predictor variable in nearly all models that used waveform feature-based metrics; 3) moderately successful models can be built from predictors based solely on DRL sources (with intensity), which may provide adequate correction in some circumstances particularly when working with historic datasets. The best models resulted in an R^2 of 0.92, slopes within 9% of 1:1 correlation, and reduced bias to -0.01 m, and standard deviation to 0.14 m; 4) accurate salt marsh zone classification maps (overall classification accuracy >90%) can be created using only a lidar data source and without multi- or hyperspectral imagery.

Full-waveform lidar combined with predictive modeling tools appears to deliver highly accurate salt marsh elevation models by reducing vegetation-induced lidar uncertainty. The developed model reduced systematic and random error for the entire data set by applying location-specific, point-by-point corrections obtained via the nonparametric regression methods. Corrected elevation surfaces will be tremendously useful to support coastal research and management objectives, while also minimizing the amount of expensive, time-consuming field work. The ability to properly correct salt marsh DEMs should allow the creation of better

inundation models such as SLAMM (Sea- Level Affecting Marshes Model) (Chu-Agor et al. 2011) and the detailed assessment of the impacts of sea level rise on marsh health and resilience. Corrected DEMs should also help to plan and monitor the results of salt marsh restoration projects. The five nonparametric models created in this study employed different algorithms to reduce elevation uncertainty, yet provided a relatively narrow range of results. The use of multiple algorithms producing similar results provides further validation of a successful outcome despite the complex variable relationships and interactions.

Further research needed includes: a) assess whether models created in this study can be successfully scored against full-waveform data from other northeastern salt marshes without reworking the developed model; b) extend this type of analysis to marshes in different regions of the country with differing vegetation species; c) analyze full-waveform data taken from marsh systems in winter (senescent conditions) to determine if this technique is adaptable to data collected at different times of the year.
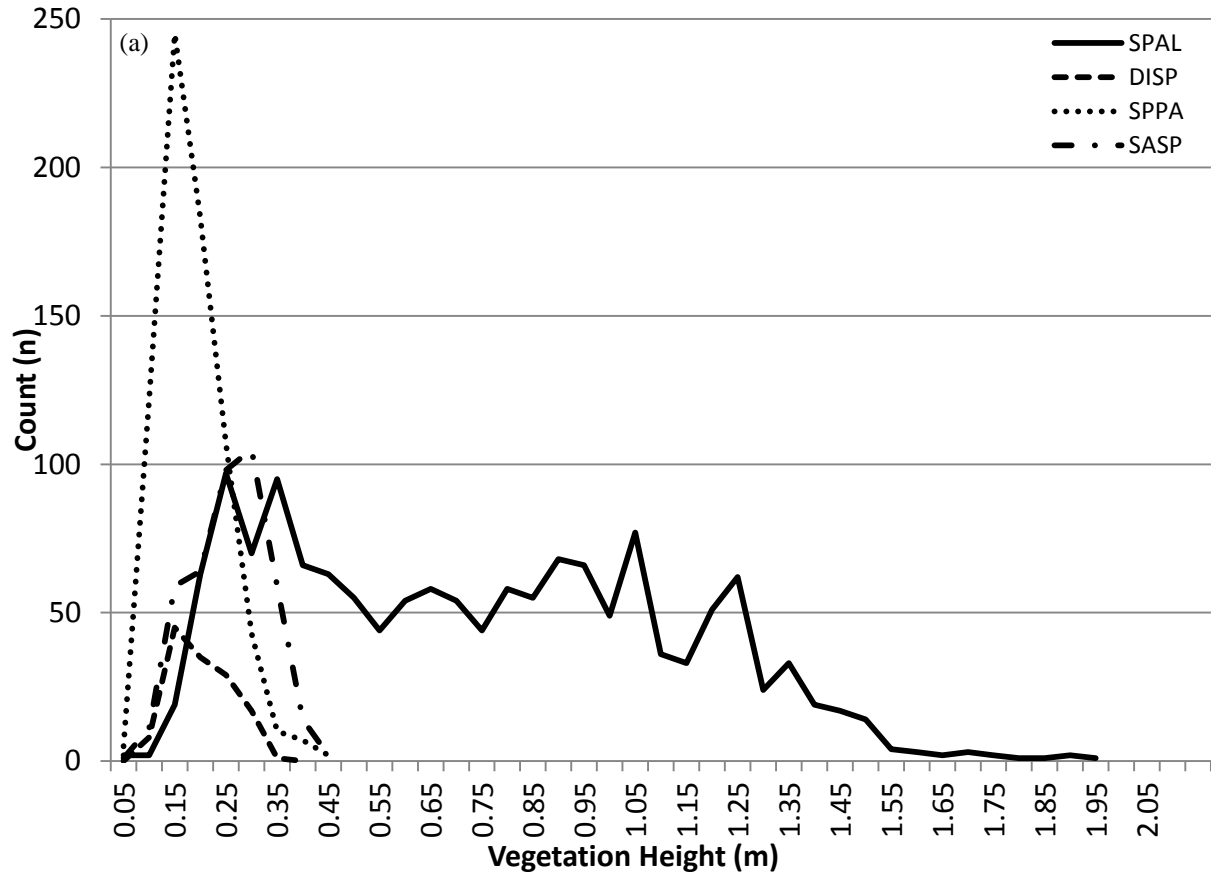
Figure 5.1a: Histogram of vegetation height for each of the surveyed species (n = 2,899). (SPAL - *Spartina alterniflora***, DISP -** *Distichlis spicata***, SPPA -** *Spartina patens***, SASP -** *Salicornia spp.***)**
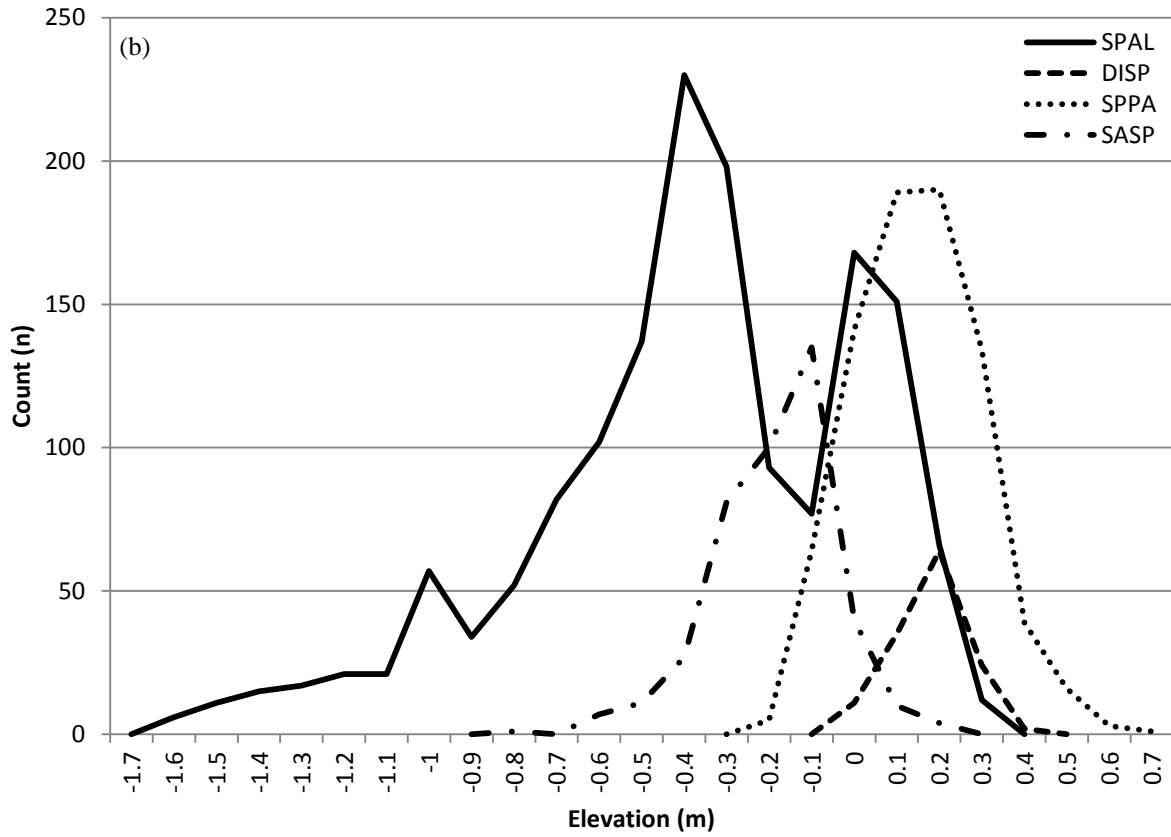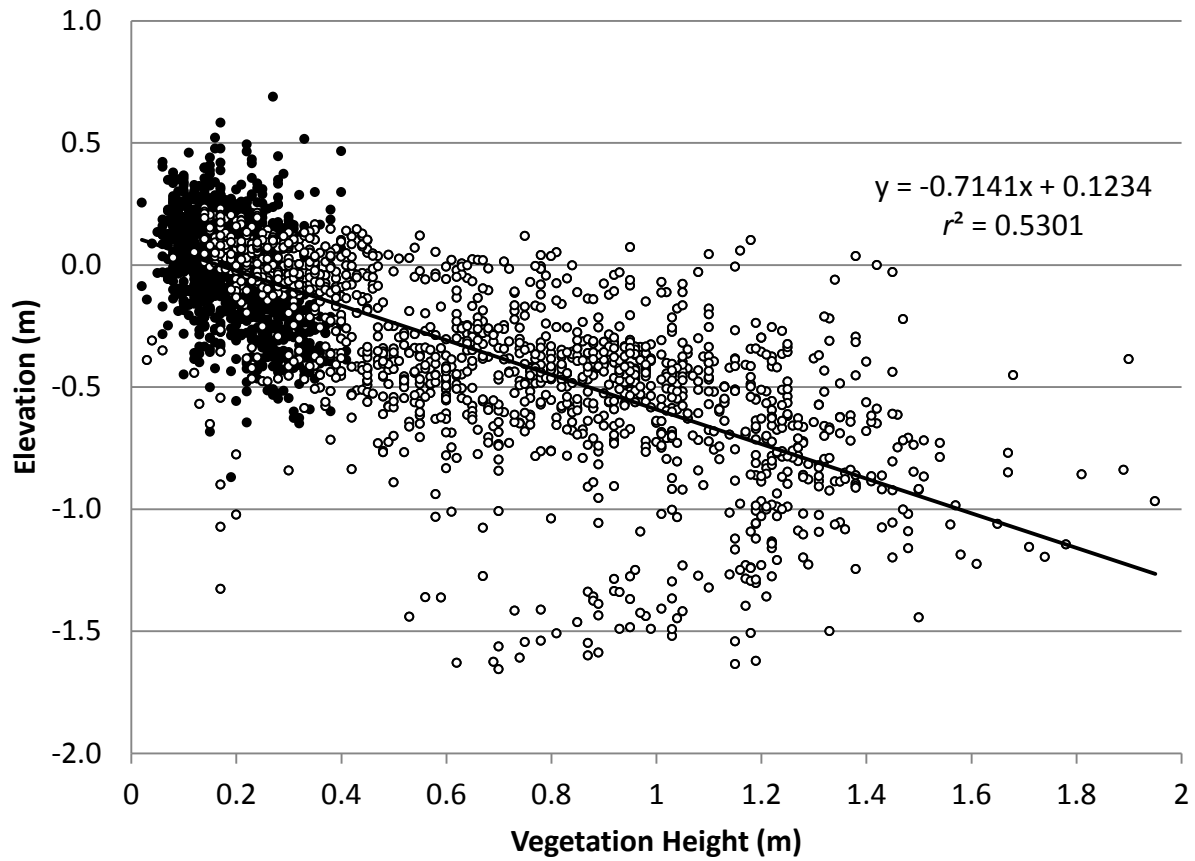
Figure 5.1b: Frequency of occurrence by elevation range (MHW) for each vegetation species (n = 2,899). (SPAL - *Spartina alterniflora***, DISP -** *Distichlis spicata***, SPPA -** *Spartina patens***, SASP -** *Salicornia spp.***)**

$$y = -0.7141x + 0.1234$$
$$r^2 = 0.5301$$

Figure 5.2: Scatterplot of vegetation height and terrain elevation (MHW) at each RTK GNSS location (n = 2,899). Open circles are *Spartina alterniflora* and closed circles are all other species (*Spartina patens*, *Distichilis spicata*, and *Salicornia spp.*).
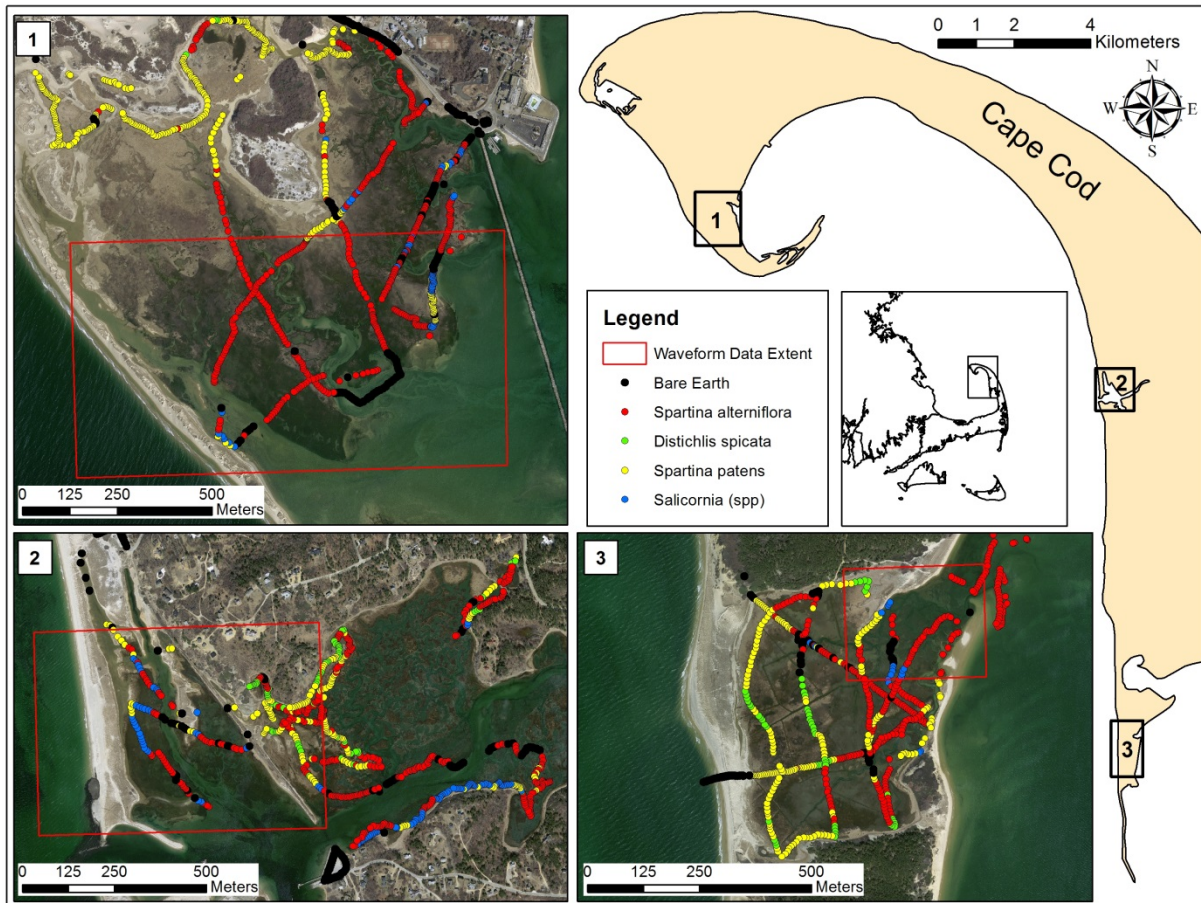
Figure 5.3: Site locus map. Insets are 1) Moors marsh, 2) Pamet marsh, and 3) Great Island – middle marsh. RTK GNSS points are color coded by dominant vegetation species/ground type. Red boxes are the extent of Full-waveform data used in the model creation analysis.

Figure 5.4: Pamet Marsh – Vegetation showing (left to right) *Spartina alterniflora*, *Salicornia spp.*, **and** *Spartina patens* **zonation along a man-made dike.**

Table 5.1: Flight parameters of NCALM July 20th, 2010.

Flight Parameter	Value
Flying Speed (m/sec)	60
Altitude (m)	600
Swath Overlap (%)	50
Laser Beam Divergence (mrad)	0.25
Pulse Rate Frequency (kHz)	70
Transmit Pulse Width (ns)	12
Scan Rate (kHz)	40
Scan Angle (degrees)	± 21
Nominal Point Density (pts/m^2)	5
Laser Footprint Diameter (m)	0.15

Table 5.2: Waveform metrics and surface characteristics available to the model predictor variables.

Source	Symbol	Metric Name	Description
Waveform and Surface Metrics			
Full-waveform	A	Waveform amplitude	Maximum of received echo (i.e., peak value)
	AUC	Area under curve	Trapezoidal numerical integration of echo
	μ_ω	Waveform mean	A measure of the "center" of the return pulse
	g_1	Waveform skewness	A measure of the asymmetry of the return pulse; positive for our waveforms, which are right skewed
	w	Waveform width	Width (FWHM) of return pulse
Derived from Discrete Lidar	γ	Curve	The curvature of a surface is the fourth-order polynomial calculated on a cell-by-cell basis.
	γ_{pl}	Curve Plan	This is the curvature of the surface in the direction perpendicular to slope
	γ_{pr}	Curve Profile	This is the curvature of the surface in the direction of slope
	d	Distance	Distance (m) from the -1 mean high water (MHW) contour line (or lowest extent of vegetation). Positive values for shoreward and negative values for seaward distances.
	Z	Elevation	Lidar elevation as derived from the discrete-return dataset using a 1 x 1 m cell size and inverse distance weighting interpolation method.
	i	Intensity	Lidar intensity is the magnitude, of the return pulse. It represents the reflectivity of the surface at the laser wavelength scaled between 0-255.
	R	Rugosity	Measure of terrain variation of grid cells within a neighborhood in three-dimensions. Output raster values range from 0 (no terrain variation) to 1 (complete terrain variation).
	m	Slope	Slope is the maximum rate of change in value from each cell to its neighbors calculated as a percent.

Table 5.3: Regression and classification models used with their descriptions, benefits and detriments.

Model	Description	Pros	Cons	References
Classification and Regression Trees (CART)	Creates classification trees using binary recursive partitioning to predict the group association based on one or more predictor variables.	Ability to handle missing data; Can often reveal important data relationships that sometimes remain concealed using other analytical methods	Regression based models are limited in the output response to data clustering based on the terminal node assignment	(Breiman et al. 1984)
Multivariate Adaptive Regression Splines (MARS)	Approximates functions by capturing essential nonlinearities and interactions but still produces results in a form similar to a traditional regression	Predicts continuous numeric outcome; Uncovers important data patterns; Produces output equations similar to those used in traditional regression approaches.	Not capable of categorical classifications	(Friedman 1991)
TreeNet - Stochastic Gradient Boosting	Generates thousands of small decision trees, less than 6 terminal nodes, from a random sample of the data that sequentially eliminate residuals and converge on a highly accurate model	Highly resistant to over fitting of the data since very small trees are used instead of one large tree and the models produce substantially higher accuracies	Does not produce equation style regression output; lacks interpretable decision trees as are found with CART	(Friedman 2002)
Random Forests	Random Forests is an ensemble of many CART trees that are not influenced by each other	Ability to spot outliers/anomalies; Discovering data patterns; Identifying important predictors; Predict future outcomes.	Produces somewhat more accurate classification models than regression	(Breiman 2001)
Generalized Path Seeker Model (GPSM)	A forward stepping model that builds linear regressions that are additive with predictors and cannot discover on its own nonlinear relationships or interactions without the help of an analyst.	Well suited to using more predictor columns than observation records; Can handle highly correlated predictors (colinearity); Finds a compact model with good performance	Does not handle missing values and will enforce row deletions to compensate for missing predictor values.	(Friedman 2012)

Table 5.4: Model results from full-waveform and discrete-return lidar based models. The "learn" sample was used to build the model while the "test" sample is independent and used for confirming model results. The scored data column is the results of the model on the combined learn and test samples. The regression line equation for the scored model is displayed to give an indication of how close to a 1:1 relationship the model created. A perfect model would have an R^2 value of 1 and an equation of y = x. Models results are sorted in order by performance (best to worst), which is determined using three criteria: a high independent "test" sample R^2 result, similarity of R^2 results between the "learn" and "test" results, and closeness of fit of the final regression equation line to a 1:1 correlation. * (The learn sample R^2 for Random Forest [RF] models, otherwise known as "OOB" [out-of-bag], is always 1 and therefore not reported.)

Type	Models	Learn (n = 560)	Test (n = 225)	Scored (n = 785)	Equation
Waveform	TreeNET	0.990	0.963	0.982	y = 0.9748x - 0.0103
	MARS	0.967	0.960	0.964	y = 0.9642x - 0.0169
	GPSM	0.934	0.948	0.938	y = 0.9329x - 0.0327
	Regression	0.934	0.947	0.938	y = 0.9326x - 0.0327
	RF	*	0.959	0.984	y = 0.8971x - 0.0488
	CART	0.939	0.919	0.934	y = 0.9964x - 0.0009
Discrete	TreeNET	0.934	0.910	0.926	y = 0.9126x - 0.0388
	RF	*	0.911	0.959	y = 0.8652x - 0.0649
	MARS	0.857	0.872	0.862	y = 0.8567x - 0.0720
	CART	0.917	0.880	0.905	y = 0.9139x - 0.0407
	GPSM	0.817	0.832	0.827	y = 0.7992x - 0.0990
	Regression	0.820	0.828	0.823	y = 0.8201x - 0.0872
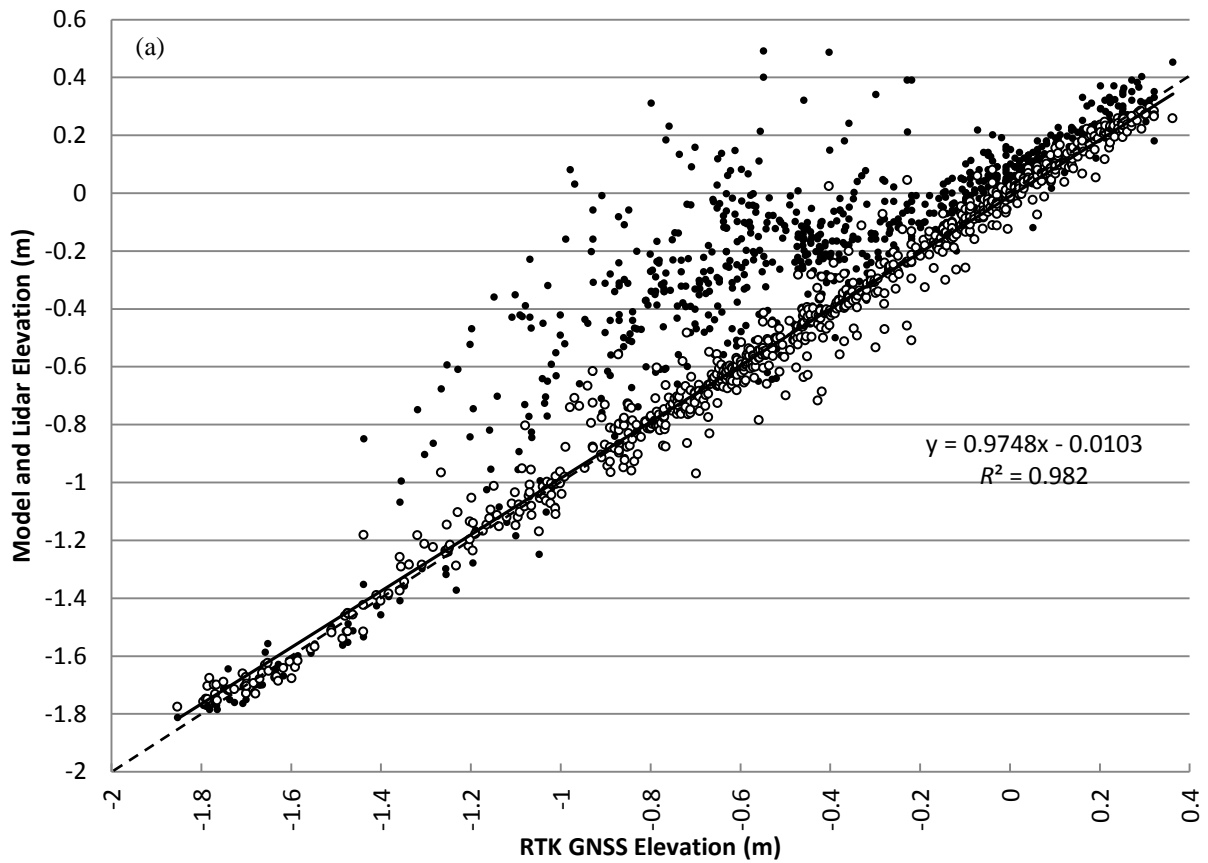
Figure 5.5a: Plot of RTK GNSS elevations to raw lidar elevation (red) and the same lidar points corrected with the TreeNet model (open circles) using full-waveform and discrete-return lidar data. All elevations are in local mean high water (MHW) tidal datum.
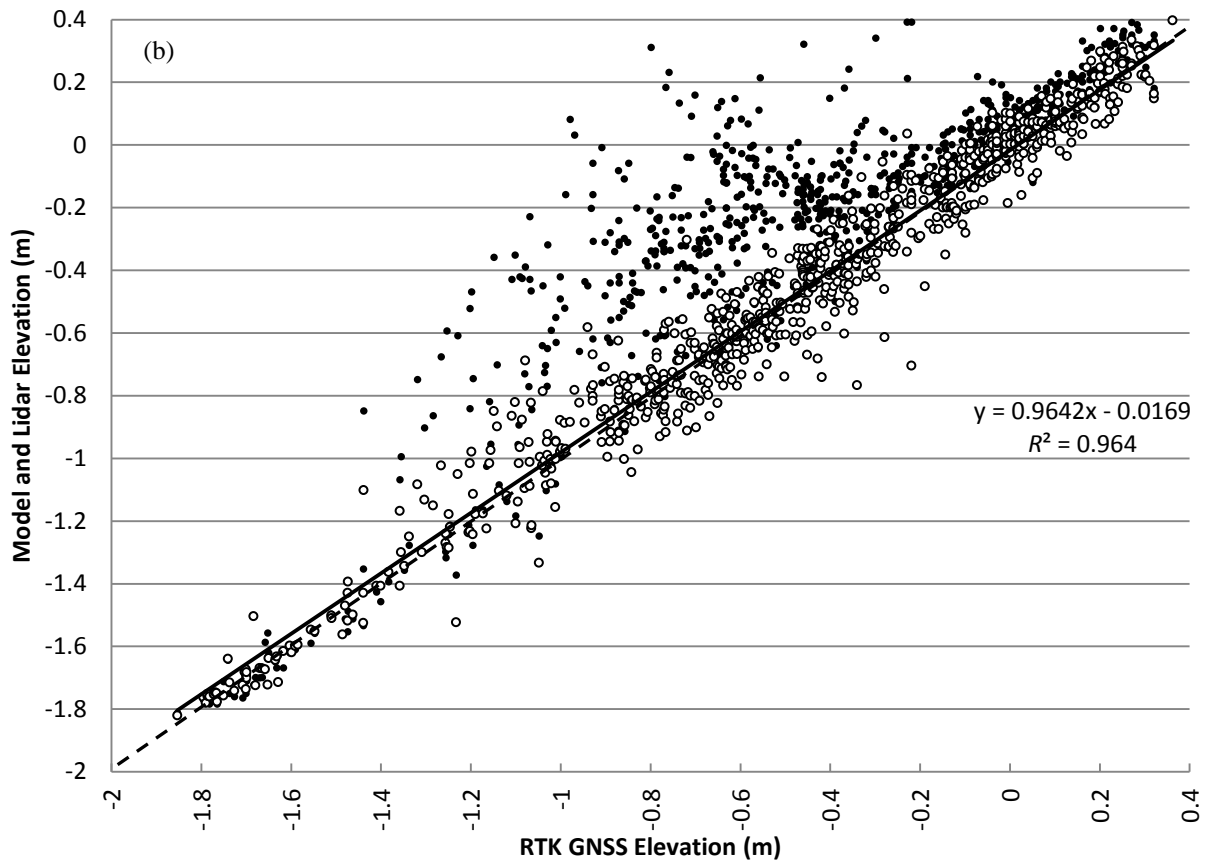
Figure 5.5b: Plot of RTK GNSS elevations to raw lidar elevation (closed circles) and the same lidar points corrected with the MARS model (open circles) using full-waveform and discrete-return lidar data. All elevations are in local mean high water (MHW) tidal datum.

Table 5.5: Variable importance is presented for each of the models that use full-waveform and discrete-return lidar data predictors. The most important variable is given a score of 100 and all other variables importance are reported are rescaled relative to the most important variable. The top 3 important variable from each model run are highlighted in bold.

Symbol	Predictor Variable	TreeNet	MARS	GPSM	RF	CART
A	Amplitude	9.05	3.16	**8.54**	0.24	2.71
AUC	Area under curve	7.71	-	1.8	0.21	1.96
μ_ω	Waveform mean	9.85	3.02	-	0.07	10.7
g_1	Waveform skewness	7.77	4.15	2.19	0.07	4.58
w	Width	**52.11**	**42.62**	**39.16**	**24.11**	**30.26**
Z	Elevation	**100**	**100**	**100**	**100**	**100**
γ	Curve	6.58	**7**	4.91	0.05	6.13
γ_{pl}	Curve Plan	7.55	-	-	0.02	2.5
γ_{pr}	Curve Profile	7.32	-	6.21	0.08	3.28
d	Distance	**16.77**	2.86	1.27	**3.22**	**65.95**
R	Rugosity	8.49	5.21	-	-	14.14
m	Slope	7.92	3.83	4.08	-	4.89

Table 5.6: Bias by species for uncorrected lidar and top two models for both full-waveform and discrete-return lidar model results

Model	Species	N	Mean	Min	Max	SD	RMS
Uncorrected Lidar	All Vegetation	694	0.24	-0.20	1.11	0.23	0.33
	S. alterniflora	446	0.35	-0.20	1.11	0.22	0.41
	S. patens	123	0.06	-0.17	0.18	0.05	0.08
	Distichlis spicata	39	0.05	-0.07	0.11	0.05	0.07
	Salicornia spp.	86	0.06	-0.12	0.32	0.08	0.10
TreeNet Waveform	All Vegetation	694	0.00	-0.43	0.29	0.07	0.07
	S. alterniflora	446	-0.01	-0.43	0.27	0.08	0.08
	S. patens	123	0.01	-0.08	0.16	0.04	0.04
	Distichlis spicata	39	0.02	-0.05	0.14	0.04	0.04
	Salicornia spp.	86	0.02	-0.10	0.29	0.06	0.06
MARS Waveform	All Vegetation	694	0.00	-0.42	0.49	0.10	0.10
	S. alterniflora	446	-0.02	-0.42	0.43	0.11	0.11
	S. patens	123	0.01	-0.10	0.26	0.07	0.07
	Distichlis spicata	39	0.03	-0.06	0.16	0.06	0.06
	Salicornia spp.	86	0.05	-0.11	0.49	0.09	0.10
TreeNet Discrete	All Vegetation	694	-0.01	-0.72	0.57	0.14	0.14
	S. alterniflora	446	-0.05	-0.72	0.37	0.14	0.15
	S. patens	123	0.04	-0.14	0.48	0.10	0.11
	Distichlis spicata	39	0.04	-0.11	0.57	0.11	0.12
	Salicornia spp.	86	0.10	-0.07	0.37	0.09	0.13
Random Forest Discrete	All Vegetation	694	-0.01	-0.60	0.56	0.11	0.11
	S. alterniflora	446	0.03	-0.22	0.56	0.11	0.11
	S. patens	123	-0.07	-0.47	0.04	0.08	0.11
	Distichlis spicata	39	-0.07	-0.60	0.04	0.10	0.12
	Salicornia spp.	86	-0.08	-0.33	0.08	0.07	0.11
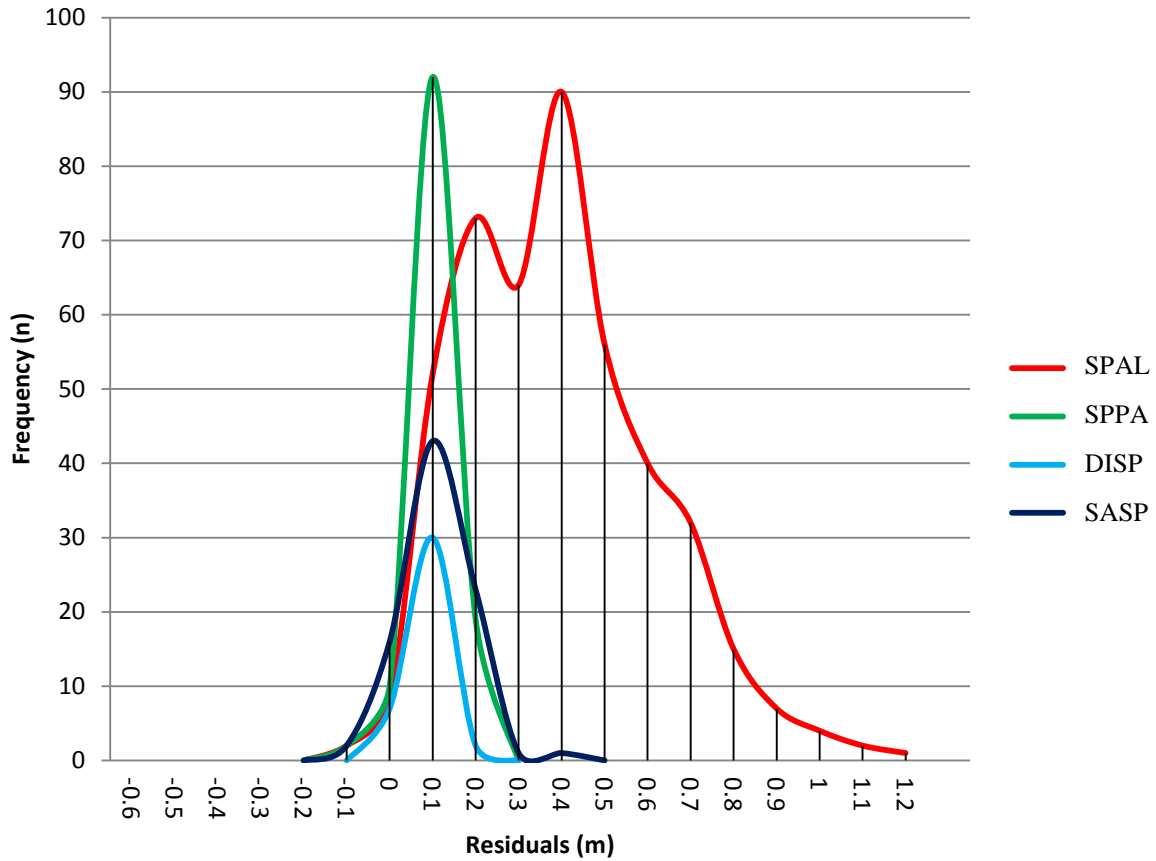
Figure 5.6: Frequency of occurrence for lidar residuals (lidar – RTK GNSS = ΔZ) by vegetation species (n = 694) across all three marsh sites. The red solid line represents the combined total of all *S. alterniflora* ecophenes residuals. (SPAL - *Spartina alterniflora*, DISP - *Distichlis spicata*, SPPA - *Spartina patens*, SASP - *Salicornia spp.*)
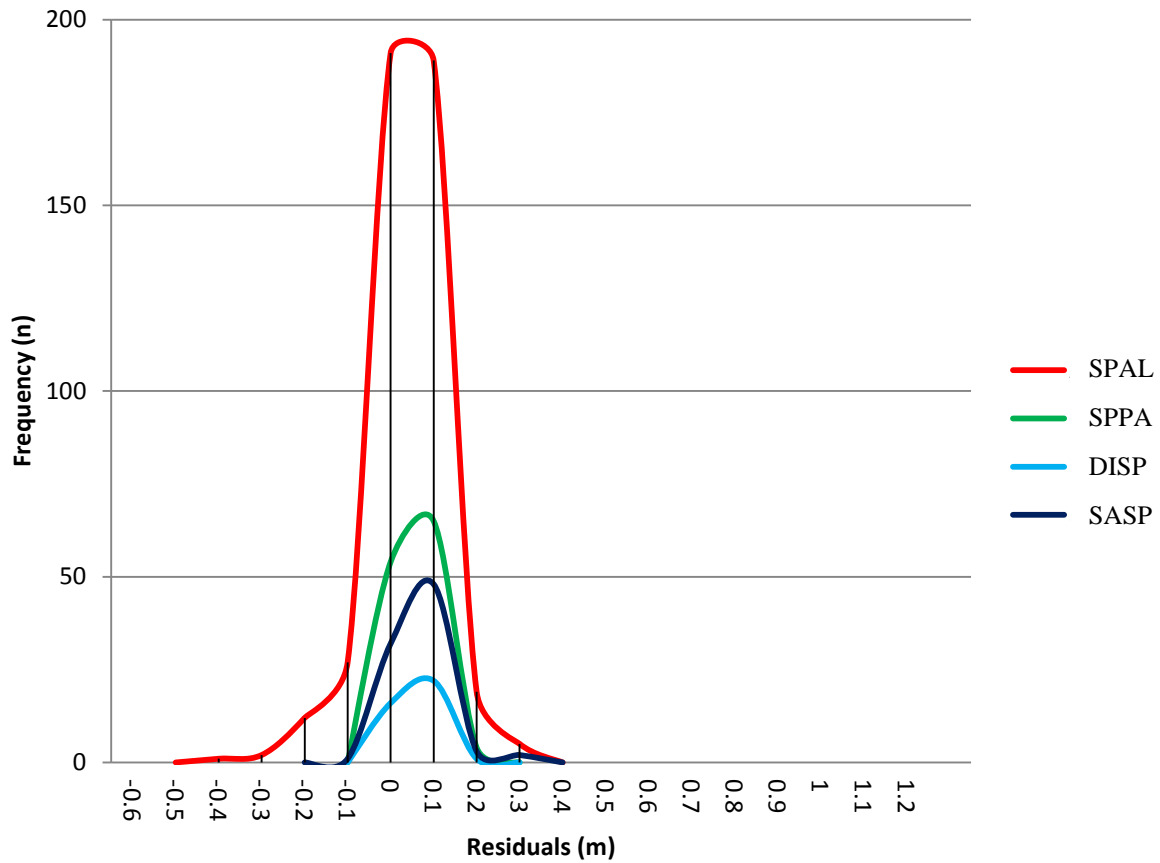
Figure 5.7: Frequency of occurrence for residuals as corrected by the TreeNet model (Lidar – RTK GNSS = ΔZ) using full-waveform and discrete-return lidar predictors (n = 694). (SPAL - *Spartina alterniflora***, DISP -** *Distichlis spicata***, SPPA -** *Spartina patens***, SASP -** *Salicornia spp.***)**
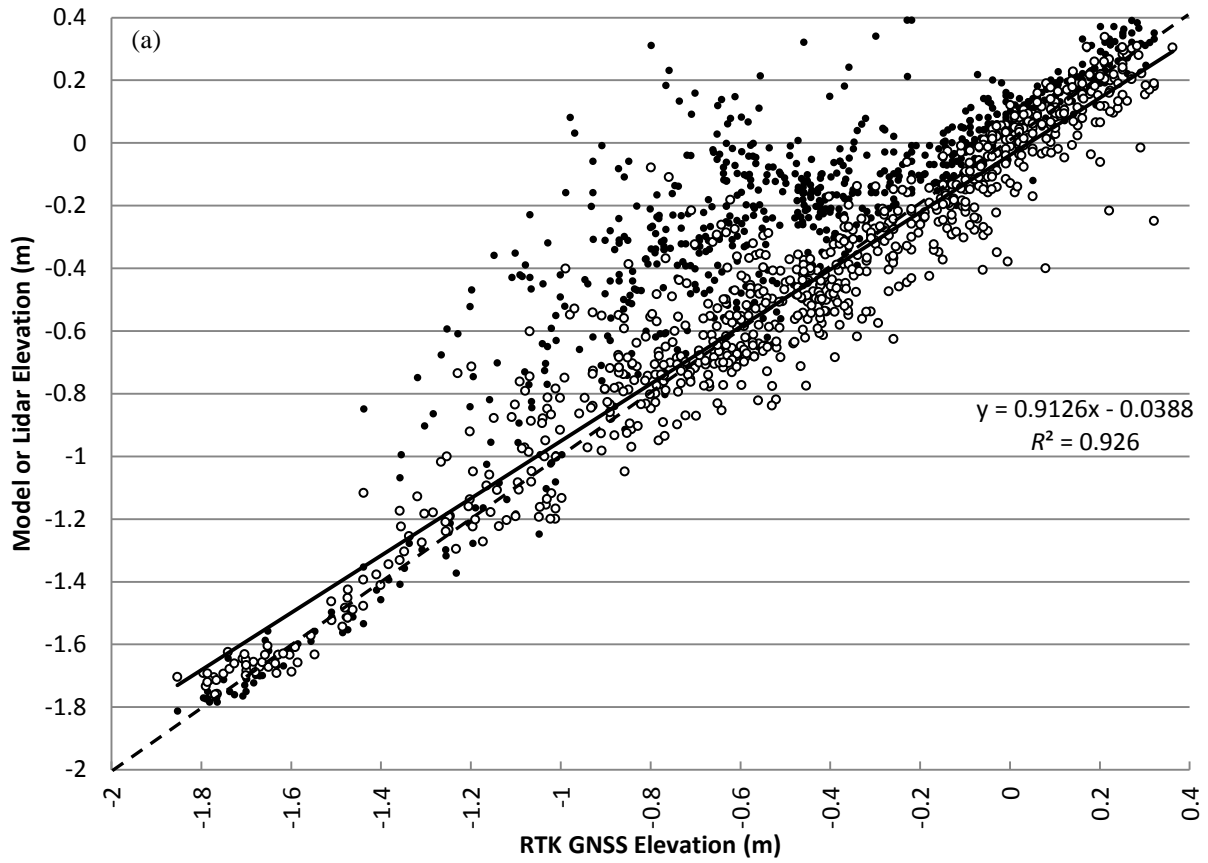
Figure 5.8a: Plot of RTK GNSS elevations to raw lidar elevation (red) and the same lidar points corrected with the TreeNet model (open circles) using only discrete-return lidar data sources. All elevations are in local mean high water (MHW) tidal datum.
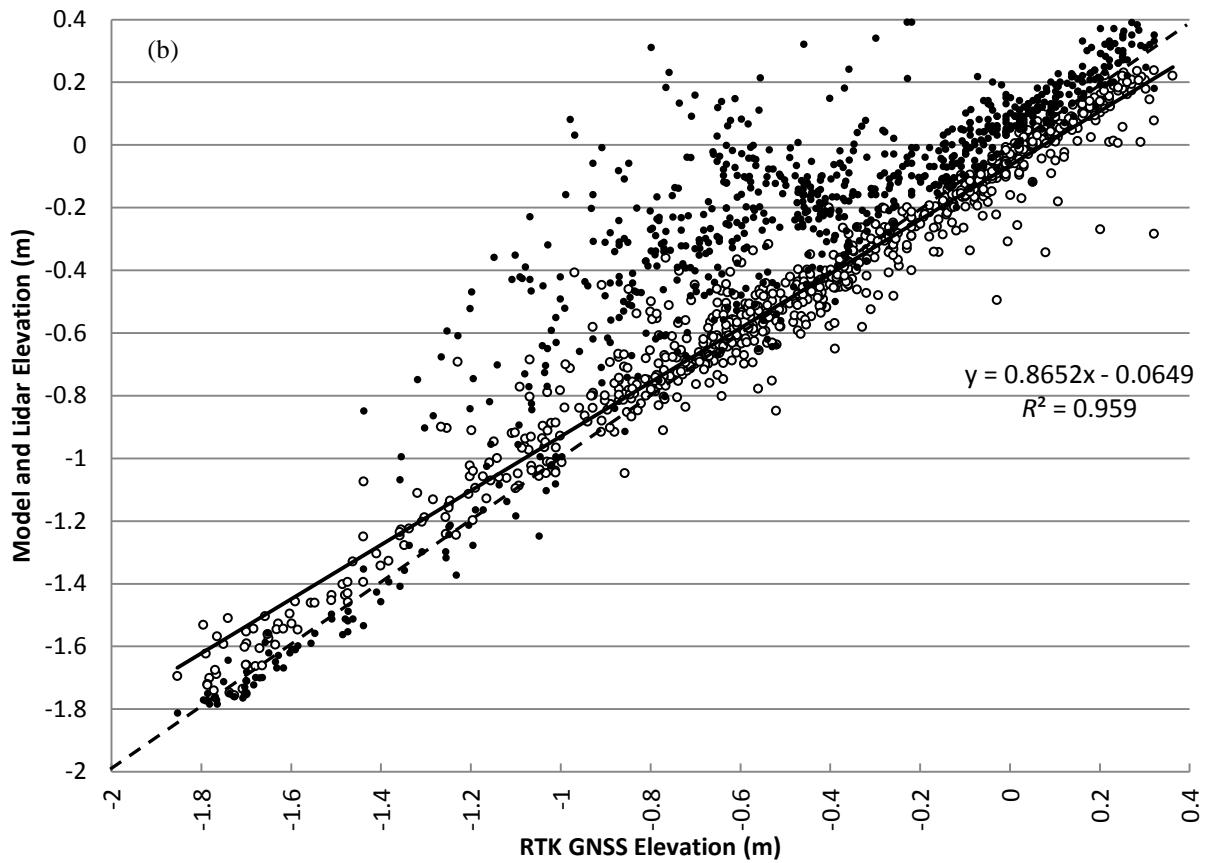
Figure 5.8b: Plot of RTK GNSS elevations to raw lidar elevation (closed circles) and the same lidar points corrected with the Random Forest model (open circles) using only discrete-return lidar data sources. All elevations are in local mean high water (MHW) tidal datum.

Table 5.7: Variable importance is presented for each of the models that use only the discrete-return lidar data predictors. The most important variable is given a score of 100 and all other variables importance are reported are rescaled relative to the most important variable. The top 3 important variable from each model run are highlighted in bold. "–" represents not found significant or used by the model.

Symbol	Predictor Variable	TreeNet	MARS	GPSM	Random Forest	CART
γ	Curve	14.21	-	1.23	0.45	0.78
γ_{pl}	Curve Plan	12.29	-	-	-	3.18
γ_{pr}	Curve Profile	17.9	**13.78**	2.186	0.72	7.51
d	Distance	20.79	-	1.86	**0.73**	**65.17**
Z	Elevation	**100**	**100**	**100**	**100**	**100**
i	Intensity	**23.87**	-	-	**2.44**	14.68
R	Rugosity	**24.72**	**14.92**	**55.33**	2.2	**21.96**
m	Slope	14.68	-	**6.28**	0.2	14.74
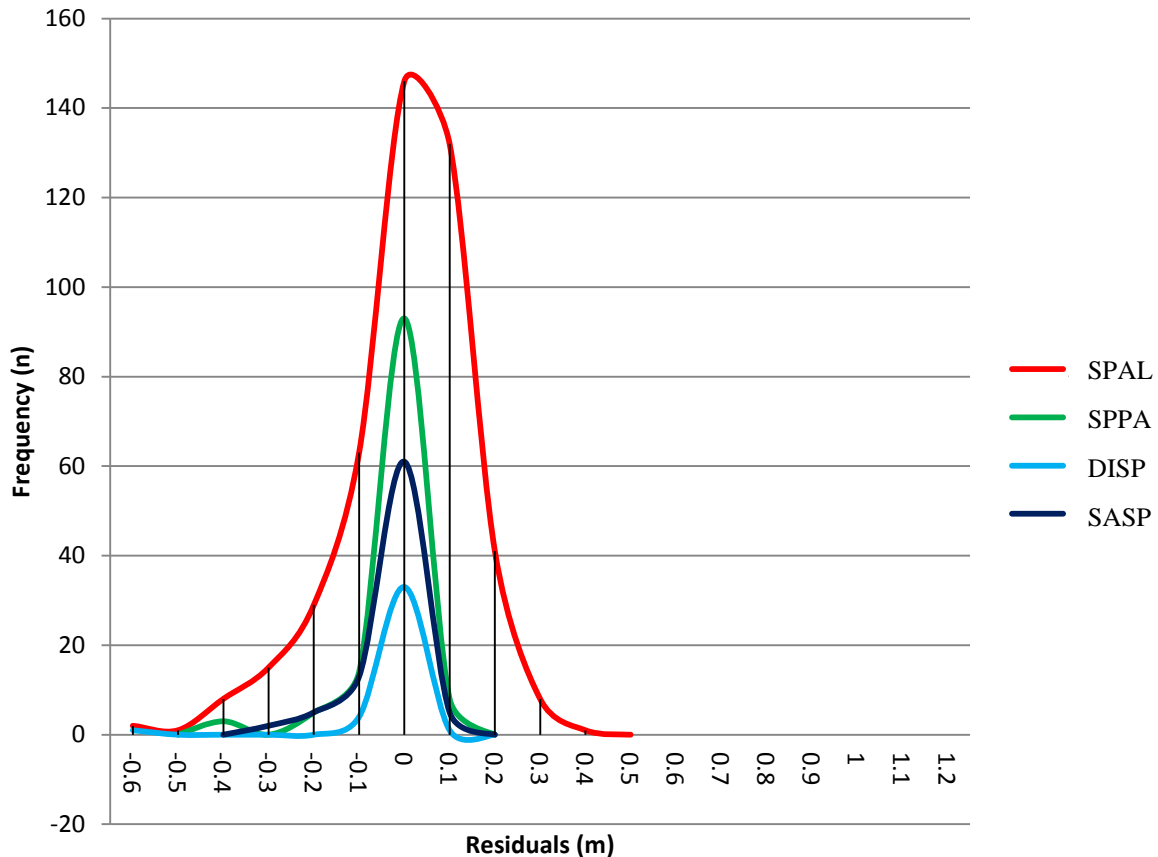
Figure 5.9: Histogram of TreeNet model residuals (Lidar – RTK GNSS = ΔZ) for discrete-return lidar predictors (n = 694). (SPAL - *Spartina alterniflora***, DISP -** *Distichlis spicata***, SPPA -** *Spartina patens***, SASP -** *Salicornia spp.***)**

Table 5.8: Confusion matrices for the three classification models created to identify vegetation zonation. The three zones are bare ground (GR), high marsh vegetation [*S. patens*, *Salicornia spp.*, *D. spicata*, short-form *S. alterniflora*] (HM), and low marsh vegetation [tall-form and medium-form *S. alterniflora*] (LM). The shaded diagonal (grey) contains the cases of agreement between the model and the learn or test datasets.

Model	Class	Learn Dataset					Test Dataset				
		N	Correct	GR	HM	LM	N	Correct	GR	HM	LM
TreeNet	GR	58	94.8%	55	2	1	33	81.8%	27	2	1
	HM	179	98.9%	0	177	2	69	92.8%	0	64	5
	LM	230	99.6%	0	1	229	89	95.5%	1	3	85
	Total	467	98.7%	55	180	232	191	92.1%	28	72	91
Random Forest	GR	58	89.7%	52	5	1	33	97.0%	32	1	0
	HM	265	77.4%	9	205	51	110	83.6%	4	92	14
	LM	237	82.3%	15	27	195	82	86.6%	6	5	71
	Total	560	80.7%	76	237	247	225	86.7%	42	98	85
CART	GR	58	91.4%	53	4	1	33	87.9%	29	4	0
	HM	265	83.4%	1	221	43	110	86.4%	0	95	15
	LM	237	81.9%	12	31	194	82	78.0%	5	13	64
	Total	560	83.6%	66	256	238	225	83.6%	34	112	79

Table 5.9: Variable importance is presented for each of the zonation models using all available predictors. The most important variable is given a score of 100 and all other variables importance are reported are rescaled relative to the most important variable. The top three important variables from each model run are highlighted in bold.

| Symbol	Predictor Variable	TreeNet	Random Forest	CART
A	Waveform Amplitude	35.66	12.4885	7.4541
AUC	Area under curve	26.15	10.5998	10.2763
m_w	Waveform mean	29.18	10.3625	19.2795
g_1	Waveform skewness	21.36	8.1181	15.1362
w	Waveform Width	**100**	**100**	92.5945
Z	Elevation	**68.63**	**98.8685**	**100**
γ	Curve	15.64	4.79	7.1263
γ_{pl}	Curve Plan	21.33	3.8031	0.9588
γ_{pr}	Curve Profile	24.25	7.3549	1.8469
d	Distance	**60.37**	**68.5338**	**77.8668**
i	Intensity	51.62	25.7267	38.6824
R	Rugosity	32.92	22.667	41.7609
m	Slope	29.32	9.5455	8.0322
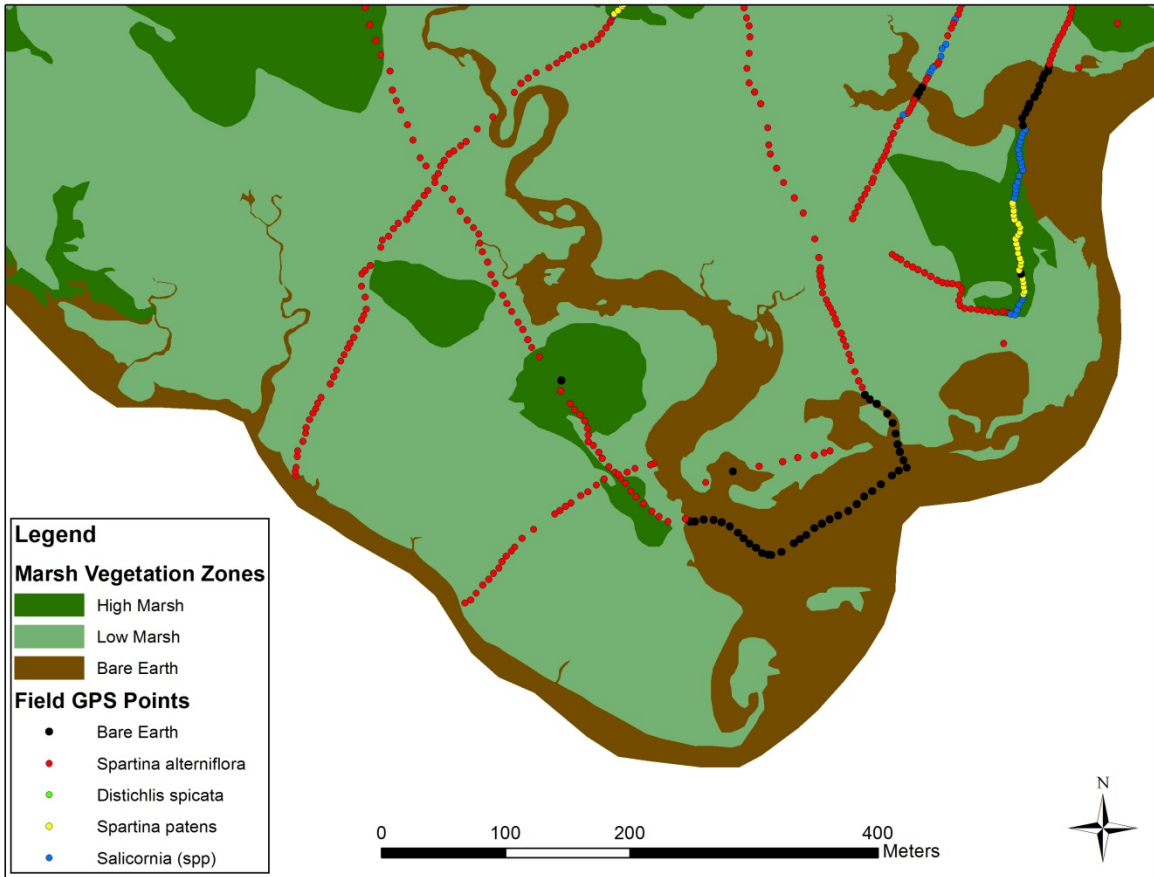
Figure 5.10: Vegetation map of Moors marsh vegetative zones developed from field collected data and interpretation from a 2009 high resolution aerial photograph. Salt ponds are not identified on this map.
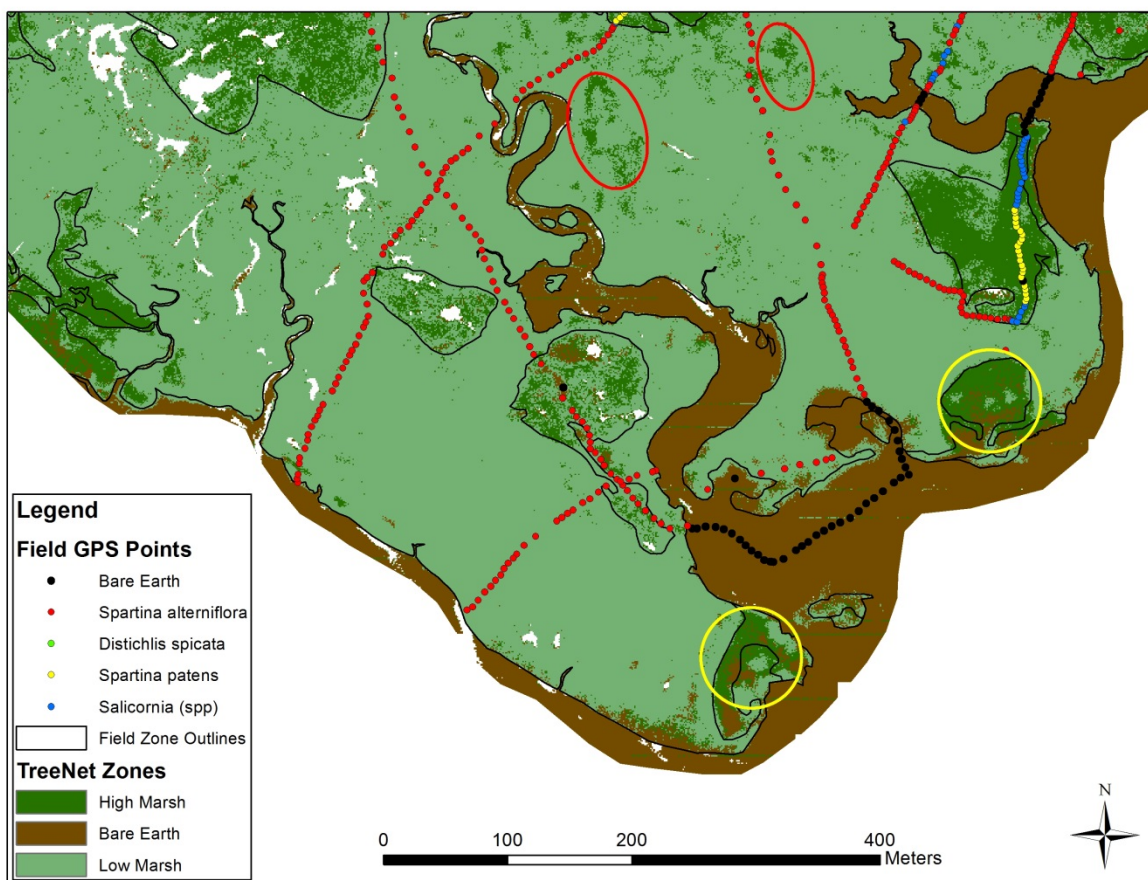
Figure 5.11: Vegetation map of marsh vegetative zones derived from the TreeNet model using all available predictors. Salt ponds and other water features are visible as data voids (white). Red ovals represent areas of high marsh vegetation (SF *Spartina alterniflora*) not interpreted using standard techniques but detected by the full-waveform nonparametric model. Yellow circles are "bare ground" that has been misclassified as high marsh possibly due to the presence of macroalgae.
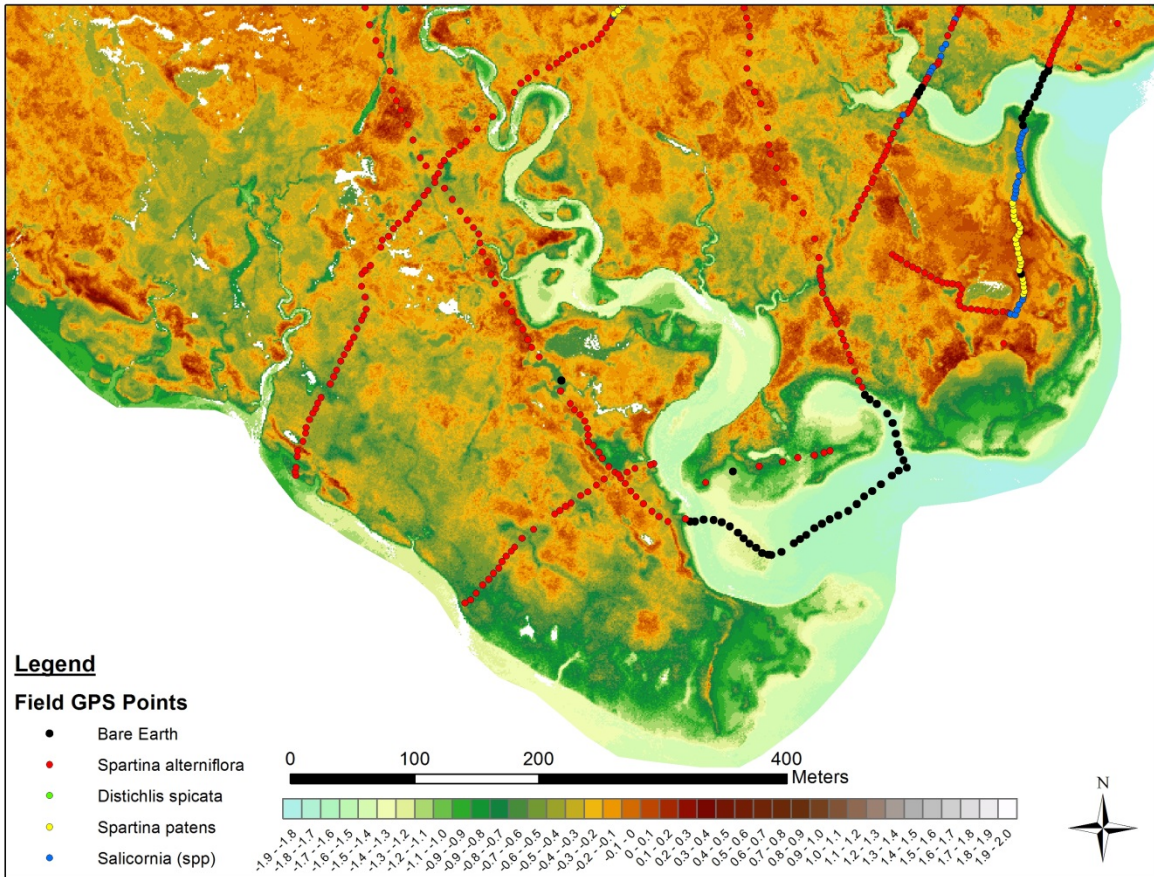
Figure 5.12: Uncorrected lidar DEM of last (single) returns using an Inverse Distance Weighting algorithm with a radius of 1 cell. Elevations are in meters and referenced to local MHW datum.
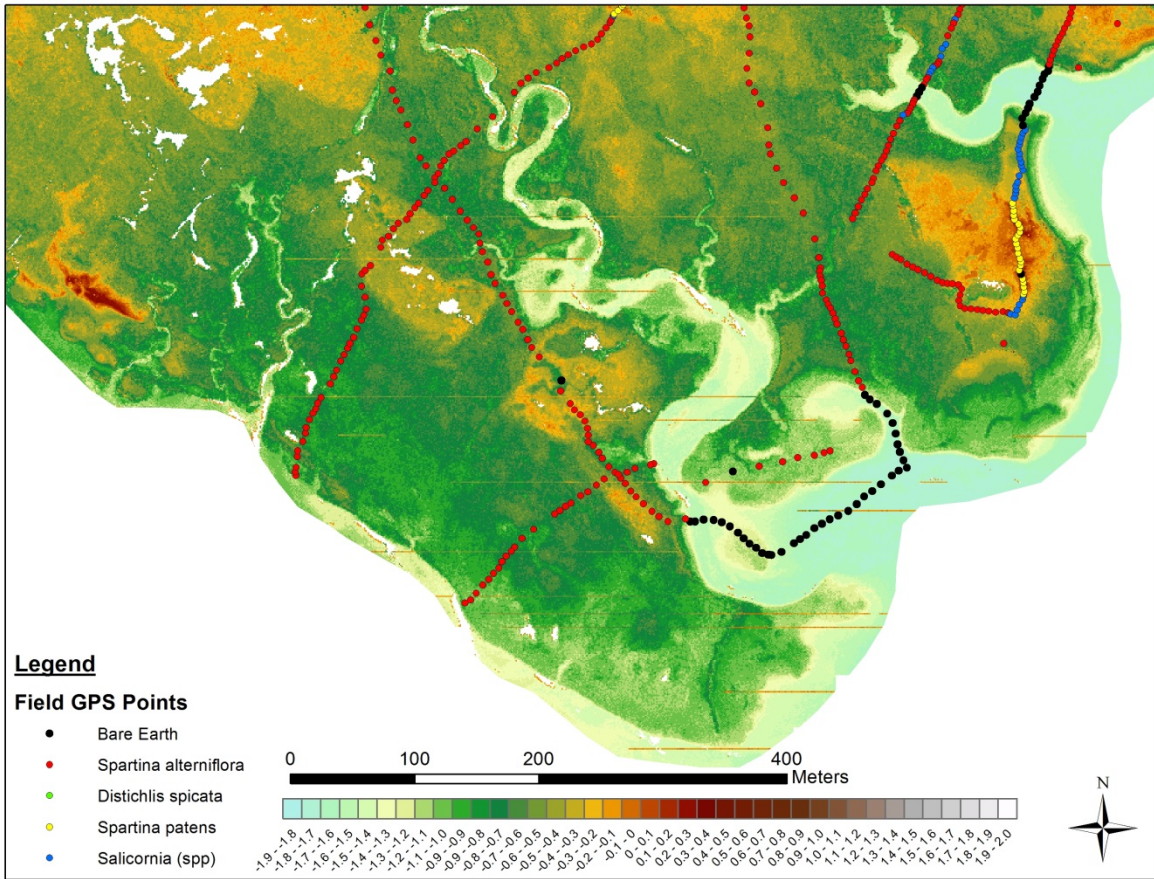
Figure 5.13: Waveform corrected DEM using the developed TreeNet model. Notice the visible topography that was hidden in the uncorrected DEM by vegetation-induced bias. Elevations are in meters and referenced to local MHW datum.
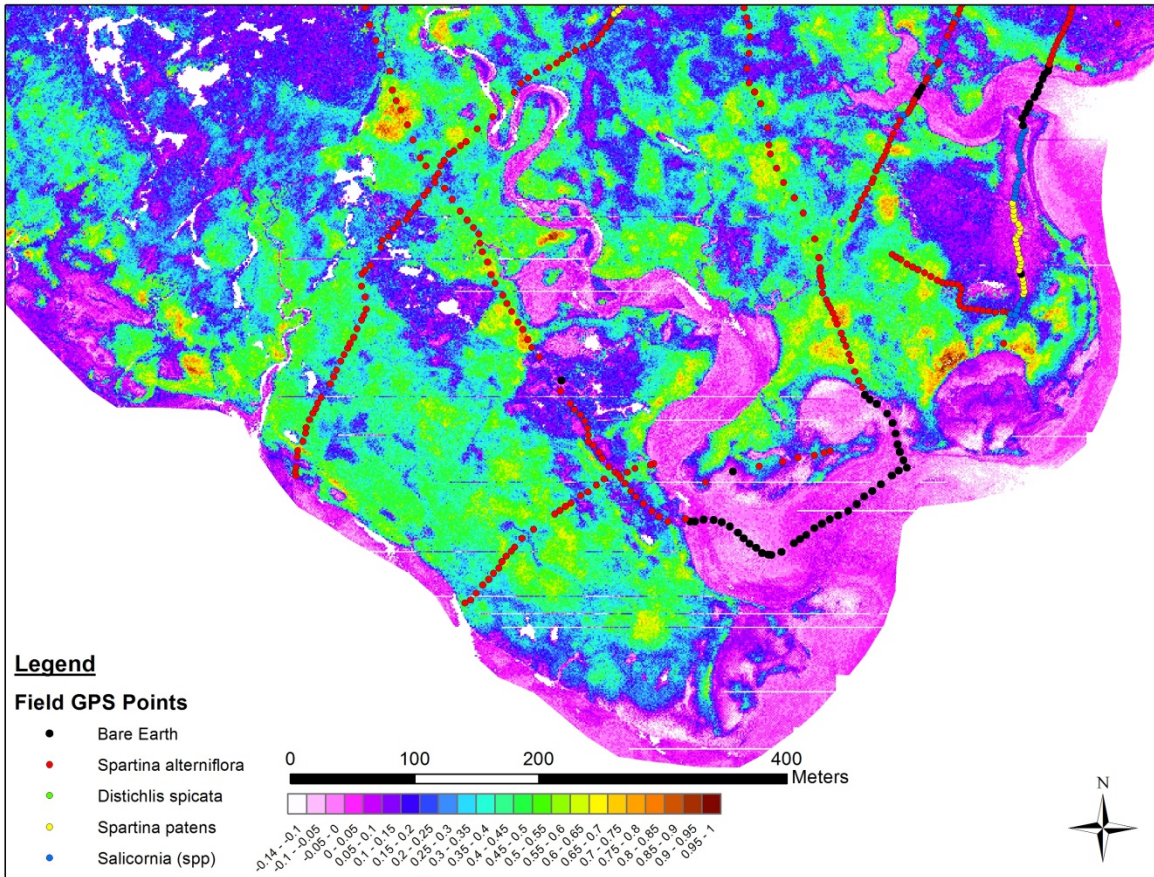
Figure 5.14: Difference map between the uncorrected lidar DEM and the Waveform TreeNet model corrected DEM. Differences are attributed to model "removed" vegetation-induced bias and are measured in meters.
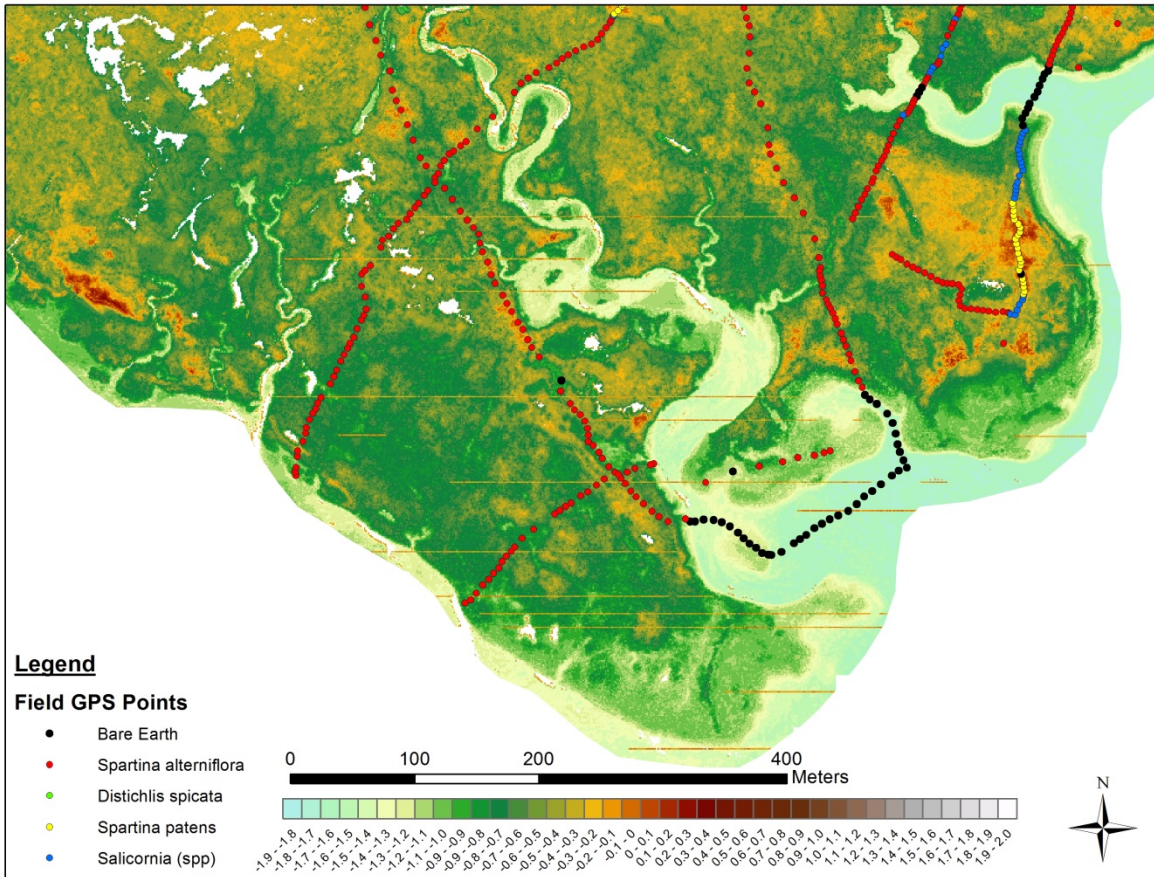
Figure 5.15: Corrected DEM using discrete-return lidar derived predictor TreeNet model. Results are an improvement over the uncorrected DEM but still contain significant vegetation-induced bias as compared to the full-waveform corrected DEM. Elevations are in meters and referenced to local MHW datum.

179
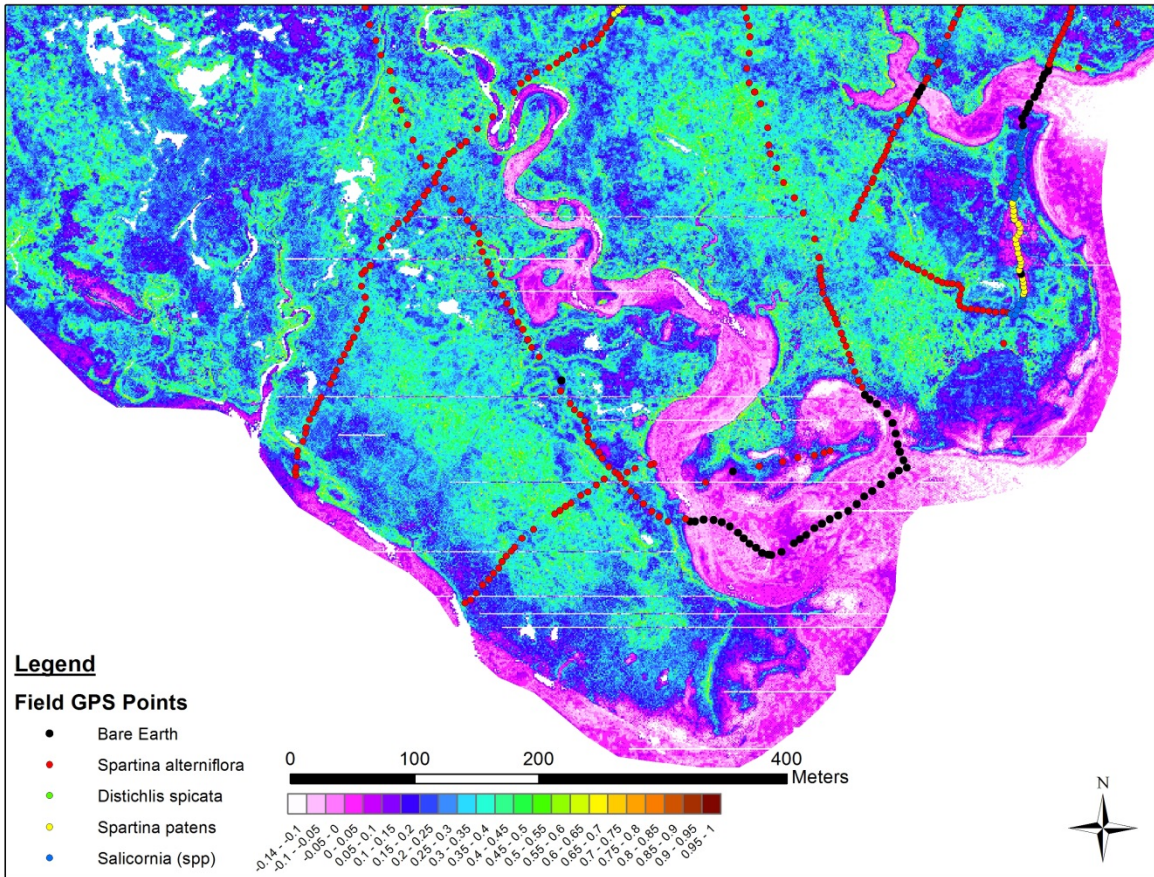
Figure 5.16: Difference map between the uncorrected lidar DEM and the discrete-return lidar corrected DEM using the developed TreeNet model. Differences are attributed to model "removed" vegetation-induced bias and are measured in meters.
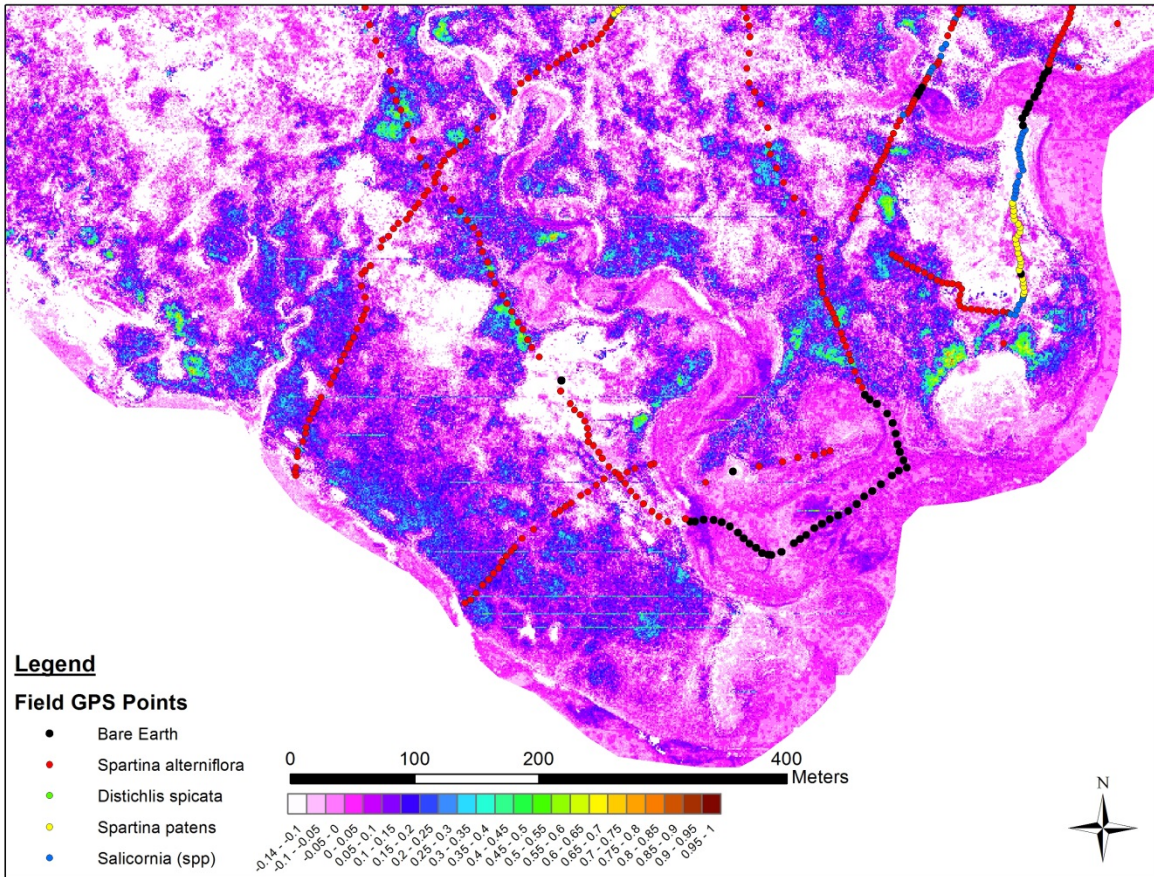
Figure 5.17: Difference map between the full-waveform corrected difference map and the discrete-return lidar corrected difference map. These differences (m) are the "improvement" of the full-waveform model over the discrete-return lidar model at removing the vegetative induced bias.

181

CHAPTER VI

CONCLUSIONS

This research investigated the utility and uncertainty of discrete-return (DRL) and full-waveform lidar in salt marsh environments. Vegetation-induced DRL uncertainty continues to challenge researchers and coastal managers considering the use of lidar in salt marshes for regional or site specific detailed topographic analysis. As observed in other environments, lidar uncertainty varies as a function of the terrain and vegetation cover. More specifically, the lidar uncertainty in salt marsh environments appears to be driven by the light blocking characteristics of individual species, which is also function of the physical location in the marsh. Without correction, digital elevation models (DEM) developed from DRL sources are not acceptable for applications where fine topographic details are necessary such as sea level rise resilience studies, hydrologic modeling, restoration planning, or storm impact analysis. The most effective approaches to salt marsh DEM correction to date have been based on vegetation species specific bias removal. However these methods assume *a priori* knowledge of species location, which is a level of detail typically unavailable in most projects. This vegetation detail can be acquired by extensive fieldwork or additional flight sensors such as hyperspectral imaging, but these require processing and interpretation that will add to time, cost and the possible introduction of errors. These vegetation-based methods also assume that each mapped zone that requires DEM modification has a constant correction factor across its entire extent when vegetation conditions and lidar bias vary continuously across the salt marsh surface. Waveform data offers additional information about the target not available in DRL datasets. Through conducting a series of

182

analyses of DRL and full-waveform data from salt marshes in Cape Cod Massachusetts, as well as a field experiment, the primary conclusions from this study can be summarized as follows:

(1)   Using a new photographic field method for imaging *in situ* vegetation, there was a clear relationship between vertical biomass (VB) density and vertical obscuration (VO). However, this relationship was found to be species dependent and may not be appropriate for other vegetation species with different growth habits. Correlations of VB and VO in individual sample locations of *Spartina alterniflora* often had r values > 0.9. The VB and VO methods were determined to yield important information that is useful for future salt marsh and lidar investigations.

(2)   Full waveform lidar are useful in estimating salt marsh biophysical parameters. Waveform width and amplitude had significant correlations with vegetation height, planimetric obscuration, and proportion vegetated area (PVA) [a measure of the cross-sectional area and the light obscuring properties of the vegetation].

(3)   DRL returns in salt marsh environments from the peak vegetation, IDW interpolation exhibited a positive bias of 0.14 m ($\sigma = 0.17$ m) across all survey locations. However, a DRL accuracy assessment based on bias estimates across the entire salt marsh is grossly misleading since a majority of the observed bias could be attributed to just one species, *Spartina alterniflora*.

(4)   Regardless of flight capture season, DRL returns in salt marsh environments exhibit positive bias. Temporal measurements of change in vegetation-induced-bias between peak

and senescent growth conditions are possible from lidar datasets. Collecting lidar during senescent conditions helped to significantly reduce uncertainty in the elevation measurements and had the effect of lowering overall lidar bias from 0.14 m at peak vegetation growth to 0.04 m at senescent conditions.

(5) Different marsh species were found to have diverse ranges of bias that are found in a continuous distribution of residuals rather than a constant value. While most species observed in this study have unimodal distributions, *S. alterniflora* was observed to have a multimodal distribution as a result of its three distinct ecophenes. The distribution of bias will complicate DRL correction techniques that are vegetation-based using a constant factor for bias.

(6) Custom interpolation and filtering techniques such as minimum bin may improve overall DRL accuracy, but does not address a majority of the species-specific bias and can introduce additional errors that might create negative bias considerations. This technique should probably only be used with caution in the instance where other methods such as species specific or nonparametric modeling are not possible.

(7) Waveform feature-based metrics can be used to create relative uncertainty surfaces (RUS) that are useful to predict regions of variable uncertainty within the marsh and can be confidently used for targeted ground truth or other field work activities. These areas may also be used to quickly identify and monitor locations of change within the marsh since areas of higher uncertainty should be related to vegetation height, which in most cases will imply changes in inundation frequency.

(8) Non-parametric predictive modeling techniques, coupled with full waveform feature-based metrics, reduce elevation uncertainty due to salt marsh vegetation, even during peak vegetation growth conditions. The highest performing model, TreeNet, produced an R^2 of 0.98, a slope within 4% of a 1:1 correlation, and reduced bias, μ, from 0.24 m to 0.00 m, and standard deviation, σ, from 0.23 to 0.07 m. The developed model reduced systematic and random error for the entire data set by applying location-specific, point-by-point corrections obtained via the nonparametric regression methods.

(9) Reasonably successful models were built with predictors that were based solely on DRL sources (with the addition of intensity), which provides adequate correction in some circumstances particularly when working with historic datasets. The best models resulted in an R^2 of 0.92, slopes within 9% of 1:1 correlation, and reduced bias to -0.01m, and standard deviation to 0.14 m .

(10) The most significant predictor variable in nearly all models that used waveform feature-based metrics was waveform width after DRL starting elevation.

(11) Accurate classification maps (>90%) of salt marsh vegetation zones were created using only a lidar data source and without the use of other imagery or spectral data.

Field techniques for elevation data collection are often inadequate in salt marsh environments especially for projects covering large spatial extents. Full-waveform lidar holds

the promise to deliver more accurate salt marsh elevation models by distinguishing coastal vegetation biophysical parameters such as height and planimetric obscuration, as well as detecting the ground within the DRL dead zone of less than 2 m. The results of this study suggest that it should be possible to achieve at least a coarse understanding of lidar bias across an entire marsh by the creation of RUS maps that can be used to minimize the amount of expensive, time-consuming field work, target field investigations, or monitor changes over time. Waveform width was determined to be a very valuable parameter for evaluating key marsh characteristics such as uncertainty and vegetation height. It may be that waveform width will also provide important information that can be used in other applications and should potentially be considered by instrument manufacturers as a standard deliverable with future DRL datasets such as intensity is today. Predictive modeling tools that use variables derived from full-waveform lidar appears to deliver highly accurate salt marsh elevation models by removing vegetation induced uncertainty. Corrected elevation surfaces will minimizing the amount of expensive, time-consuming fieldwork and better support coastal research and management objectives such as studying the impacts of sea level rise on marsh health and resilience as well as plan and monitor the results of salt marsh restoration projects. Five different nonparametric model algorithms and one parametric algorithm were employed in this study to correct for vegetation-based uncertainty. These models used a wide range of different algorithms, but produced a relatively narrow range of results. This provided further validation of a lack of overfitting and individual model success despite the complex variable relationships and interactions.

It is recommended that the methods developed in this research be tested further. Specific goals of follow-on studies should include: a) extending these methods and analyses to marshes in different regions of the country with differing vegetation species and geomorphology; b)

186

investigating the extensibility of the full-waveform methods to lidar systems with shorter transmit pulse widths; c) determining if models created in this study can be successfully scored against full waveform data from other northeastern salt marshes without reworking the developed model; d) analyzing full waveform data taken from marsh systems in winter (senescent conditions) to determine if this correction technique is adaptable to data collected at different times of the year.

LITERATURE CITED

Abdallah, H., Baghdadi, N., Bailly, J.S., Pastol, Y., & Fabre, F. (2012). Wa-LiD: A New LiDAR Simulator for Waters. *Ieee Geoscience and Remote Sensing Letters, 9*, 744-748

Adamowicz, S.C., & Roman, C.T. (2005). New England salt marsh pools: a quantitative analysis of geomorphic and geographic features. *Wetlands, 25*, 279-288

Adams, T., Beets, P., & Parrish, C. (2012). Extracting More Data from LiDAR in Forested Areas by Analyzing Waveform Shape. *Remote Sensing, 4*, 682-702

Allen, J.R.L. (1995). Salt-marsh growth and fluctuating sea level: implications of a simulation model for Flandrian coastal stratigraphy and peat-based sea-level curves. *Sedimentary Geology, 100*, 21-45

Anderson, C.M., & Treshow, M. (1980). A Review of Environmental and Genetic Factors That Affect Height in *Spartina alterniflora* Loisel (Salt-Marsh Cord Grass). *Estuaries, 3*, 168-176

Anderson, J.E., Plourde, L.C., Martin, M.E., Braswell, B.H., Smith, M.L., Dubayah, R.O., Hofton, M.A., & Blair, J.B. (2008). Integrating waveform lidar with hyperspectral imagery for inventory of a northern temperate forest. *Remote Sensing of Environment, 112*, 1856-1870

Argitas, F.J., & Yang, J. (2006). Spectral discrimination of marsh vegetation types in the New Jersey Meadowlands, USA. *Wetlands, 26*, 271-277

Argow, B.A., & Fitzgerald, D.M. (2006). Winter processes on northern salt marshes: evaluating the impact of in-situ peat compaction due to ice loading, Wells, ME. *Estuarine Coastal and Shelf Science, 69*, 360-369

Artigas, F.J., & Yang, J.S. (2005). Hyperspectral remote sensing of marsh species and plant vigour gradient in the New Jersey Meadowlands. *International Journal of Remote Sensing, 26*, 5209-5220

Bachmann, C.G. (1979). *Laser Radar Systems and Techniques*. Norwood, MA: Artech House

Baily, B., & Pearson, A.W. (2007). Change detection mapping and analysis of salt marsh areas of central Southern England from Hurt Castle Spit to Pagham Harbour. *Journal of Coastal Research, 23*, 1549-1564

Barnett, T.P., Pierce, D.W., AchutaRao, K.M., Gleckler, P.J., Santer, B.D., Gregory, J.M., & Washington, W.M. (2005). Penetration of Human-Induced Warming into the World's Oceans. *Science, 309*, 284-287

Barnhardt, W.A., Belknap, D.F., & Kelley, J.T. (1997). Stratigraphic evolution of the inner continental shelf in response to late Quaternary relative sea-level change, northwestern Gulf of Maine. *Geological Society of America Bulletin, 109*, 612-630

Barnhardt, W.A., Gehrels, W.R., Belknap, D.F., & Kelley, J.T. (1995). Late Quaternary Relative Sea-Level Change in the Western Gulf of Maine - Evidence for a Migrating Glacial Forebulge. *Geology, 23*, 317-320

Belknap, D.F., Anderson, B.G., Anderson, R.S., Anderson, W.A., Borns Jr., H.W., Jacobson Jr., G., Kelley, J.T., Shipp, R.C., Smith, D.C., Stuckenrath Jr., R., Thompson, W.B., & Tyler, D.A. (1987a). Late Quaternary sea level changes in Maine. In D. Nummedal, O.H. Pilkey, & J.D. Howard (Eds.), *Sea Level Fluctuation and Coastal Evolution, Special Publication 41* (pp. 71-85): SEMP

Belknap, D.F., & Shipp, R.C. (1991). Seismic stratigraphy of glacial marine units, Maine inner shelf. *Geological Society of America Special Papers, 261*, 137-157

Belknap, D.F., Shipp, R.C., & Kelley, J.T. (1987b). Quaternary stratigraphy of representative Maine estuaries: initial examination by high resolution seismic reflection profiling. In D.M. FitzGerald, & P.S. Rosen (Eds.), *Glaciated Coasts* (pp. 177-207). San Diego: Academic Press

Belluco, E., Camuffo, M., Ferrari, S., Modenese, L., Silvestri, S., Marani, A., & Marani, M. (2006). Mapping salt marsh vegetation by multispectral and hyperspectral remote sensing. *Remote Sensing of Environment, 105*, 54-67

Bertness, M.D., & Ellison, A.M. (1987). Determinants of Pattern in a New England Salt Marsh Plant Community. *Ecological Monographs, 57*, 129-147

Bertness, M.D., Ewanchuck, P.J., & Silliman, B.R. (2002). Anthropogenic modification of New England salt marsh landscapes. *Ecology, 99*, 1395-1398

Bockelmann, A.C., Bakker, J.P., Neuhaus, R., & Lage, J. (2002). The relation between vegetation zonation, elevation and inundation frequency in a Wadden Sea salt marsh. *Aquatic Botany, 73*, 211-221

Boggs, S. (1987). *Principles of Sedimentology and Stratigraphy*. New York: Macmillan Publishing Company

Bork, E.W., & Su, J.G. (2007). Integrating LIDAR data and multispectral imagery for enhanced classification of rangeland vegetation: A meta analysis. *Remote Sensing of Environment, 111*, 11-24

Boumans, R.M.J., Burdick, D.M., & Dionne, M. (2002). Modeling habitat change in salt marshes after tidal restoration. *Restoration Ecology, 10*, 543-555

Bourennane, H., Couturier, A., Pasquier, C., Chartin, C., Hinschberger, F., Macaire, J.-J., & Salvador-Blanes, S. (2014). Comparative performance of classification algorithms for the development of models of spatial distribution of landscape structures. *Geoderma, 219–220*, 136-144

Breiman, L. (2001). Random forests. *Machine Learning, 45*, 5-32

Breiman, L., Friedman, J.H., Olshen, R.A., & Stone, C.J. (1984). *Classification and Regression Trees*. Belmont, CA: Wadsworth

Bretar, F., Chauve, A., Bailly, J.S., Mallet, C., & Jacome, A. (2009). Terrain surfaces and 3-D landcover classification from small footprint full-waveform lidar data: application to badlands. *Hydrology and Earth System Sciences, 13*, 1531-1544

Brinson, M.M., Christian, R., & Blum, L.K. (1995). Multiple states in the sea level induced transition from terrestrial forest to estuary. *Estuaries, 18*, 648-659

Brock, J., & Sallenger, A. (2001). Airborne topographic LIDAR mapping for coastal and resource management. In (p. 4): U.S. Geological Survey Open File Report

Broome, S.W., Seneca, E.D., & Woodhouse, W.W. (1988). Tidal Salt Marsh Restoration. *Aquatic Botany, 32*, 1-22

Brovelli, M., Cannata, M., & Longoni, U. (2004). LIDAR data filtering and DTM interpolation within GRASS. *Transactions in GIS, 8*, 155-174

Brown, C.A., & Kraus, N.C. (1998). Numerical gauge approach to water-level datum determination. *Journal of Hydraulic Engineering-Asce, 124*, 321-324

Burrough, P.A., & McDonell, R.A. (1998). *Principles of Geographical Information Systems*. New York: Oxford University Press

Butera, M.K. (1983). Remote sensing of wetlands. *Ieee Transactions on Geoscience and Remote Sensing, 21*, 383-392

Byrd, K.B., & Kelly, M. (2006). Salt marsh vegetation response to edaphic and topographic changes from upland sedimentation in a pacific estuary. *Wetlands, 26*, 813-829

Cahoon, D.R. (2006). A review of major storm impacts on coastal wetland elevations. *Estuaries and Coasts, 29*, 889-898

Cahoon, D.R., Reed, D.J., & Day, J.W. (1995). Estimating shallow subsidence in microtidal salt marshes of the southeastern United States: Kaye and Barghoorn revisited. *Marine Geology, 128*, 1-9

Chapman, V.J. (1940). Studies in Salt-Marsh Ecology: Sections VI and VII. Comparison with Marshes on the East Coast of North America. *Journal of Ecology, 28*, 118-152

Charlier, R.H. (2003). Hold the sea back - Is it sustainable? Retrospective and Projection. *Journal of Coastal Research, 19*, 875-883

Chmura, G.L., Anisfeld, S.C., Cahoon, D.R., & Lynch, J.C. (2003). Global carbon sequestration in tidal, saline wetland soils. *Global Biogeochemical Cycles, 17*

Chmura, G.L., Burdick, D.M., & Moore, G.E. (2012). Recovering Salt Marsh Ecosystem Services through Tidal Restoration. In C.T. Roman, & D.M. Burdick (Eds.), *Tidal Marsh Restoration: A Synthesis of Science and Practice* (pp. 233-251). Washington: Island Press

Chu-Agor, M.L., Munoz-Carpena, R., Kiker, G., Emanuelsson, A., & Linkov, I. (2011). Exploring vulnerability of coastal habitats to sea level rise through global sensitivity and uncertainty analyses. *Environmental Modelling & Software, 26*, 593-604

Church, J.A., & White, N.J. (2006). A 20th century acceleration in global sea-level rise. *Geophysical Research Letters, 33*, L01602

Church, J.A., White, N.J., Aarup, T., Wilson, W.S., Woodworth, P.L., Domingues, C.M., Hunter, J.R., & Lambeck, K. (2008). Understanding global sea levels: past, present and future. *Sustainability Science, 3*, 9-22

Church, J.A., White, N.J., & Hunter, J.R. (2006). Sea-level rise at tropical Pacific and Indian Ocean islands. *Global and Planetary Change, 53*, 155-168

Chust, G., Galparsoro, I., Borja, A., Franco, J., & Uriarte, A. (2008). Coastal and estuarine habitat mapping, using LIDAR height and intensity and multi-spectral imagery. *Estuarine Coastal and Shelf Science, 78*, 633-643

Costanza, R., D'Arge, R., DeGroot, R., Farber, S., & Grasso, M. (1997). The value of the world's ecosystem services and natural capital. *Nature, 387*, 253-280

Craft, C., Clough, J., Ehman, J., Joye, S., Park, R., Pennings, S., Guo, H.Y., & Machmuller, M. (2009). Forecasting the effects of accelerated sea-level rise on tidal marsh ecosystem services. *Frontiers in Ecology and the Environment, 7*, 73-78

Crooks, S., Schutten, J., Sheern, G.D., Pye, K., & Davy, A.J. (2002). Drainage and elevation as factors in the restoration of salt marsh in Britain. *Restoration Ecology, 10*, 591-602

Dionne, M., Short, F.T., & Burdick, D.M. (1999). Fish utilization of restored, created, and reference salt-marsh habitat in the Gulf of Maine. In, *American Fisheries Society Symposium* (pp. 384-404)

Domingues, C.M., Church, J.A., White, N.J., Gleckler, P.J., Wijffels, S.E., Barker, P.M., & Dunn, J.R. (2008). Improved estimates of upper-ocean warming and multi-decadal sea-level rise. *Nature, 453*, 1090-U1096

Donnelly, J.P., & Bertness, M.D. (2001a). Rapid shoreward encroachment of salt marsh cordgrass in response to accelerated sea-level rise. *Geology, 98*, 14218-14223

Donnelly, J.P., & Bertness, M.D. (2001b). Rapid shoreward encroachment of salt marsh cordgrass in response to accelerated sea-level rise. *Proceedings of the National Academy of Sciences of the United States of America, 98*, 14218-14223

Donnelly, J.P., Cleary, P., Newby, P., & Ettinger, R. (2004). Coupling instrumental and geological records of sea-level change: evidence from southern New England of an increase in the rate of sea-level rise in the late 19th century. *Geophysical Research Letters, 31*, 1-4

Drake, J.B., Dubayah, R.O., Clark, D.B., Knox, R.G., Blair, J.B., Hofton, M.A., Chazdon, R.L., Weishampel, J.F., & Prince, S.D. (2002). Estimation of tropical forest structural characteristics using large-footprint lidar. *Remote Sensing of Environment, 79*, 305-319

Dubayah, R.O., & Drake, J.B. (2000). Lidar remote sensing for forestry. *Journal of Forestry, 98*, 44-46

Erwin, K.L. (2009). Wetlands and global climate change: the role of wetland restoration in a changing world. *Wetlands Ecology and Management, 17*, 71-84

Ewanchuk, P.J., & Bertness, M.D. (2004). Structure and organization of a northern New England salt marsh plant community. *Journal of Ecology, 92*, 72-85

Fagherazzi, S., Carniello, L., D'Alpaos, L., & Defina, A. (2006). Critical bifurcation of shallow microtidal landforms in tidal flats and salt marshes. *Proceedings of the National Academy of Sciences of the United States of America, 103*, 8337-8341

Fitzgerald, D.M., Fenster, M.S., Argow, B.A., & Buynevich, I.V. (2008). Coastal impacts due to sea-level rise. *Annual Review of Earth and Planetary Sciences* (pp. 601-647). Palo Alto, CA: Annual Reviews

Fowler, R. (2001). The Thorny Problem of Lidar Specifications. *EOM, 10*, 25-28

Friedman, J.H. (1991). Multivariate Adaptive Regression Splines. *Annals of Statistics, 19*, 1-67

Friedman, J.H. (2002). Stochastic gradient boosting. *Computational Statistics & Data Analysis, 38*, 367-378

Friedman, J.H. (2012). Fast sparse regression and classification. *International Journal of Forecasting, 28*, 722-738

Gedan, K.B., Silliman, B.R., & Bertness, M.D. (2009). Centuries of Human-Driven Change in Salt Marsh Ecosystems. *Annual Review of Marine Science* (pp. 117-141). Palo Alto, CA: Annual Reviews

Gehrels, W.R., & Belknap, D.F. (1993). Neotectonic history of eastern Maine evaluated from historic sea level data and 14C dates on salt marsh peats. *Geology, 21*, 615-618

Gehrels, W.R., Belknap, D.F., & Kelley, J.T. (1996). Integrated high-precision analyses of Holocene relative sea level changes: Lessons from the coast of Maine. *Geological Society of America Bulletin, 1089*, 1073-1088

Gibson, W.M., & Gill, S.K. (1999). Tides and water level requirements for NOS hydrographic surveys. *International Hydrographic Review, 76*, 141-150

Giese, G.S., & Aubrey, D.G. (1987). Losing coastal upland to relative sea level rise - 3 scenarios for Massachusetts. *Oceanus, 30*, 17-22

Goodman, J.E., Wood, M.E., & Gehrels, W.R. (2007). A 17-yr record of sediment accretion in the salt marshes of Maine (USA). In (pp. 109-121): Elsevier Science Bv

Gopfert, J., & Heipke, C. (2006). Assessment of Lidar DTM in coastal vegetated areas. *International Archives of Photogrammetry, Remote Sensing, and Spatial Information Sciences, 36*, 79-85

Graham, D., Sault, M., & Bailey, C.J. (2003). National Ocean Service shoreline - Past, present, and future. *Journal of Coastal Research*, 14-32

Green, J., Carswell, D., & Gutelius, B. (1996). Topographic terrain mapping using scanning airborne laser radar. In, *Annual conference and exposition on GIS and LIS*

Gutierrez, A.G., Schnabel, S., & Contador, J.F.L. (2009). Using and comparing two nonparametric methods (CART and MARS) to model the potential distribution of gullies. *Ecological Modelling, 220*, 3630-3637

Habib, A., Bang, K.I., Kersting, A.P., & Lee, D.C. (2009). Error Budget of Lidar Systems and Quality Control of the Derived Data. *Photogrammetric Engineering and Remote Sensing, 75*, 1093-1108

Harris, L.D. (1963). Characteristics of the hurricane storm surge, Technical Paper 48. In U.S.D.o. Commerce (Ed.). Washington, D.C.: Weather Bureau

Hartig, E.K., Gornitz, V., Kolker, A., Mushacke, F., & Fallon, D. (2002). Anthropogenic and climate-change impacts on salt marshes of Jamaica Bay, New York City. *Wetlands, 22*, 71-89

Hazelden, J., & Boorman, L.A. (2001). Soils and 'managed retreat' in South East England. *Soil Use Management, 17*, 150-154

Hladik, C. (2012). Use of Remote Sensing Data for Evaluating Elevation and Plant Distribution in a Southeastern Salt Marsh. In, *Dissertation* (p. 222). Athens, GA: University of Georgia

Hladik, C., & Alber, M. (2012). Accuracy assessment and correction of a LIDAR-derived salt marsh digital elevation model. *Remote Sensing of Environment, 121*, 224-235

Hladik, C., Schalles, J., & Alber, M. (2013). Salt marsh elevation and habitat mapping using hyperspectral and LIDAR data. *Remote Sensing of Environment, 139*, 318-330

Hodgson, M.E., & Bresnahan, P. (2004). Accuracy of airborne lidar-derived elevation: Empirical assessment and error budget. *Photogrammetric Engineering and Remote Sensing, 70*, 331-339

Hodgson, M.E., Jensen, J.R., Raber, G.T., Tullis, J.A., Davis, B.A., Thompson, G., & Schuckman, K. (2005). An evaluation of Lidar-derived elevation and terrain slope in lea-off conditions. *Photogrammetric Engineering and Remote Sensing, 71*, 817-823

Hopkinson, C., Chasmer, L.E., Zsigovics, G., Creed, I.F., Sitar, M., Treitz, P., & Maher, V. (2004). Errors in Lidar Ground Elevation and Wetland Vegetation Height Estimates. *International Archives of Photogrammetry, Remote Sensing, and Spatial Information Sciences, 36*, 108-113

Horton, B.P., Rahmstorf, S., Engelhart, S.E., & Kemp, A.C. (2014). Expert assessment of sea-level rise by AD 2100 and AD 2300. *Quaternary Science Reviews, 84*, 1-6

Howes, B.L., Dacey, J.W.H., & Goehringer, D.D. (1986). Factors Controlling the Growth Form of Spartina alterniflora - Feedbacks Between Aboveground Production, Sediment Oxidation, Nitrogen and Salinity. *Journal of Ecology, 74*, 881-898

Hughes, Z.J., FitzGerald, D.M., Wilson, C.A., Pennings, S.C., Wieski, K., & Mahadevan, A. (2009). Rapid headward erosion of marsh creeks in response to relative sea level rise. *Geophysical Research Letters, 36*, 5

Irish, J.L., & Lillycrop, W.J. (1999). Scanning laser mapping of the coastal zone: the SHOALS system. *Isprs Journal of Photogrammetry and Remote Sensing, 54*, 123-129

Jones, C.G., Lawton, J.H., & Shachak, M. (1994). Organisms as ecosystem engineers. *Oikos, 69*, 373-386

Jutzi, B., & Stilla, U. (2006). Range determination with waveform recording laser systems using a Wiener Filter. *Isprs Journal of Photogrammetry and Remote Sensing, 61*, 95-107

Kearney, M., Stevenson, J., & Ward, L.G. (1994). Spatial and temporal changes in marsh vertical accretion rates at Monie Bay: implications for sea level rise. *Journal of Coastal Research, 10*, 1010-1020

Kearney, M., & Ward, L.G. (1986). Accretion rates in brackish marshes of a Chesapeake Bay estuarine marsh. *Geo-Marine Letters, 6*, 41-49

Kelley, J.T., Dickson, S.M., Belknap, D.F., & Stuckenrath Jr., R. (1992). Sea level change and late Quaternary sediment accumulation on the southern Maine inner continental shelf. In C. Fletcher, & J. Wehmiller (Eds.), *Quaternary Coasts of the United States: Marine and Lacustrine Systems* (pp. 23-34): SEMP

Kelley, J.T., Gehrels, W.R., & Belknap, D.F. (1995). Late Holocene Relative Sea-Level Rise and the Geological Development of Tidal Marshes at Wells, Maine, USA. *Journal of Coastal Research, 11*, 136-153

Kennish, M.J. (2001). Coastal salt marsh systems in the US: A review of anthropogenic impacts. *Journal of Coastal Research, 17*, 731-748

King, M.A. (2009). The GPS Contribution to the Error Budget of Surface Elevations Derived From Airborne LIDAR. *Ieee Transactions on Geoscience and Remote Sensing, 47*, 874-883

Kirwan, M., & Temmerman, S. (2009). Coastal marsh response to historical and future sea-level acceleration. In (pp. 1801-1808): Pergamon-Elsevier Science Ltd

Kirwan, M.L., Murray, A.B., Donnelly, J.P., & Corbett, D.R. (2011). Rapid wetland expansion during European settlement and its implication for marsh survival under modern sediment delivery rates. *Geology, 39*, 507-510

Konisky, R. (2012). Role of Simulation Models in Understanding the Salt Marsh Restoration Process. In R.C. T., & D. Burdick (Eds.), *Tidal Marsh Restoration: A Synthesis of Science and Practice* (pp. 253-276). Washington: Island Press

Konisky, R.A., & Burdick, D.M. (2004). Effects of stressors on invasive and halophytic plants of New England salt marshes: a framework for predicting response to tidal restoration. *Wetlands, 24*, 434-447

Kukko, A., & Hyyppa, J. (2009). Small-footprint Laser Scanning Simulator for System Validation, Error Assessment, and Algorithm Development. *Photogrammetric Engineering and Remote Sensing, 75*, 1177-1189

Kukko, A., Kaasalainen, S., & Litkey, P. (2008). Effect of incidence angle on laser scanner intensity and surface data. *Applied Optics, 47*, 986-992

Latypov, D. (2002). Estimating relative lidar accuracy information from overlapping flight lines. *Isprs Journal of Photogrammetry and Remote Sensing, 56*, 236-245

Lee, D.S., & Shan, J. (2003). Combining Lidar elevation data and IKONOS multispectral imagery for coastal classification mapping. *Marine Geodesy, 26*, 117-127

Lefor, M.W., Kennard, W.C., & Civco, D.L. (1987). Relationship of salt marsh plant distributions to tidal levels in Connecticut, USA. *Environmental Management, 11*, 61-68

Lefsky, M.A., Cohen, W.B., Harding, D.J., Parker, G.G., Acker, S.A., & Gower, T. (2002a). Lidar remote sensing of above-ground biomass in three biomes. *Global Ecology and Biogeography, 11*, 393-399

Lefsky, M.A., Cohen, W.B., Parker, G.G., & Harding, D.J. (2002b). Lidar remote sensing for ecosystem studies. *BioScience, 52*, 19-30

Li, J.L., Yang, X.P., & Tong, Y.Q. (2009). Relationship Between Spartina alterniflora Belt on Tidal Flats and Tidal Water Levels: A Case Study on Jiangsu Coast and Hangzhou Bay, China. *Philippine Agricultural Scientist, 92*, 77-84

Liu, J.M., & Zhang, J.S. (2014). Spectral Unmixing via Compressive Sensing. *Ieee Transactions on Geoscience and Remote Sensing, 52*, 7099-7110

Mallet, C., & Bretar, F. (2009). Full-waveform topographic lidar: State-of-the-art. *Isprs Journal of Photogrammetry and Remote Sensing, 64*, 1-16

Marani, M., Belluco, E., D'Alpaos, A., Defina, A., Lanzoni, S., & Rinaldo, A. (2003). On the drainage density of tidal networks. *Water Resources Research, 39*, 1040

Mckee, K., & Patrick, J.W.H. (1988). The Relationship of Smooth Cordgrass (*Spartina alterniflora*) to Tidal Datums: A Review. *Estuaries, 11*, 143-151

Meissner, K., Fiorentino, D., Schnurr, S., Arbizu, P.M., Huettmann, F., Holst, S., Brix, S., & Svavarsson, J. (2014). Distribution of benthic marine invertebrates at northern latitudes - An evaluation applying multi-algorithm species distribution models. *Journal of Sea Research, 85*, 241-254

Mendelssohn, I.A., & Kuhn, N.L. (2003). Sediment subsidy: effects on soil-plant responses in a rapidly submerging coastal salt marsh. *Ecological Engineering, 21*, 115-128

Mendelssohn, I.A., McKee, K.L., & Patrick, W.H. (1981). Oxygen Deficiency in Spartina alterniflora Roots - Metabolic Adaptation to Anoxia. *Science, 214*, 439-441

Miller, W.D., Neubauer, S.C., & Anderson, I.C. (2001). Effects of Sea Level Induced Disturbances on High Salt Marsh Metabolism. *Estuaries, 24*, 357-367

Millette, T.L., Argow, B.A., Marcano, E., Hayward, C., Hopkinson, C.S., & Valentine, V. (2010). Salt Marsh Geomorphological Analyses via Integration of Multitemporal Multispectral Remote Sensing with LIDAR and GIS. In, *Journal of Coastal Research* (pp. 809-816): Allen Press Publishing Services Inc.

Mitsch, W.J., & Gosselink, J.G. (2000). *Wetlands*. (third ed.). New Jersey: John Wiley & Sons

Möller, I. (2006). Quantifying saltmarsh vegetation and its effects on wave height dissipation: results from a UK East coast salt marsh. *Estuarine Coastal and Shelf Science, 69*, 337-351

Möller, I., Spencer, T., & Rawson, J. (2002). Spatial and temporal variability of wave attenuation over a UK East-coast saltmarsh. In, *Proceedings of the 38th International Conference on Coastal Engineering*. Cardiff Spain

Montane, J.M., & Torres, R. (2006). Accuracy assessment of lidar saltmarsh topographic data using RTK GPS. *Photogrammetric Engineering and Remote Sensing, 72*, 961-967

Morris, J.T., & Bradley, P.M. (1999). Effects of nutrient loading on the carbon balance of coastal wetland sediments. *Limnology and Oceanography, 44*, 699-702

Morris, J.T., & Haskin, B. (1990). A 5-yr Record of Aerial Primary Production and Stand Characteristics of Spartina alterniflora. *Ecology, 71*, 2209-2217

Morris, J.T., Porter, D., Neet, M., Noble, P., Schmidt, L., Lapine, L.A., & Jensen, J.R. (2005). Integrating Lidar elevation data, multispectral imagery and neural network modeling for marsh characterization. *International Journal of Remote Sensing, 26*, 5221-5234

Morris, J.T., Sundareshwar, P.V., Nietch, C.T., Kjerfve, B., & Cahoon, D.R. (2002). Responses of coastal wetlands to rising sea level. *Ecology, 83*, 2869-2877

Muss, J.D., Aguilar-Amuchastegui, N., Mladenoff, D.J., & Henebry, G.M. (2013). Analysis of Waveform Lidar Data Using Shape-Based Metrics. *Ieee Geoscience and Remote Sensing Letters, 10*, 106-110

Nayegandhi, A., Brock, J.C., & Wright, C.W. (2009). Small-footprint, waveform-resolving lidar estimation of submerged and sub-canopy topography in coastal environments. *International Journal of Remote Sensing, 30*, 861-878

Nayegandhi, A., Brock, J.C., Wright, C.W., & O'Connell, M.J. (2006). Evaluating a small footprint, waveform-resolving lidar over coastal vegetation communities. *Photogrammetric Engineering and Remote Sensing, 72*, 1407-1417

Neumeier, U. (2005). Quantification of vertical density variations of salt-marsh vegetation. *Estuarine Coastal and Shelf Science, 63*, 489-496

NOAA (2013). Tides and Currents. In: NOAA Center for Operational Oceanographic Products and Services

Nobis, M., & Hunziker, U. (2005). Automatic thresholding for hemispherical canopy-photographs based on edge detection. *Agricultural and Forest Meteorology, 128*, 243-250

Nyman, J.A., Walters, R.J., Delaune, R.D., & Patrick, J.W.H. (2006). Marsh vertical accretion via vegetative growth. *Estuarine Coastal and Shelf Science, 69*, 370-380

Optech (2005). ALTM 3100 specifications. In

Optech (2009). ALTM 3100EA Specification Sheet. In

Ornes, W.H., & Kaplan, D.I. (1989). Macronutrient status of tall and short forms of Spartina alterniflora in a South Carolina salt marsh *Marine Ecology-Progress Series, 55*, 63-72

Orson, R.A., Simpson, R.L., & Good, R.E. (1990). Rates of sediment accumulation in a tidal fresh-water marsh. *Journal of Sedimentary Petrology, 60*, 859-869

Orson, R.A., Warren, R.S., & Niering, W.A. (1998). Interpreting Sea Level Rise and Rates of Vertical Marsh Accretion in a Southern New England Tidal Salt Marsh. *Estuarine Coastal and Shelf Science, 47*, 419-429

Parrish, C.E., Jeong, I., Nowak, R.D., & Smith, R.B. (2011). Empirical Comparison of Full-Waveform Lidar Algorithms: Range Extraction and Discrimination Performance. *Photogrammetric Engineering and Remote Sensing, 77*, 825-838

Parrish, C.E., Rogers, J.N., & Calder, B.R. (2014). Assessment of Waveform Features for Lidar Uncertainty Modeling in a Coastal Salt Marsh Environment. *Ieee Geoscience and Remote Sensing Letters, 11*, 569-573

Pe'eri, S., & Philpot, W.D. (2007). Increasing the existence of very shallow-water Lidar measurements using the red-channel waveforms. *Ieee Transactions on Geoscience and Remote Sensing, 45*, 1217-1223

Pei-Yin, C., Chien-Chuan, H., Yeu-Horng, S., & Yao-Tung, C. (2009). A VLSI Implementation of Barrel Distortion Correction for Wide-Angle Camera Images. *Circuits and Systems II: Express Briefs, IEEE Transactions on, 56*, 51-55

Pennings, S.C., & Bertness, M.D. (2001). Salt Marsh Communities. In M.D. Bertness, S.D. Gaines, & M.E. Hay (Eds.), *Marine Community Ecology* (pp. 289-316). Sunderland, MA: Sinauer Associates Inc.

Peterson, C.H., Able, K.W., DeJong, C.F., Piehler, M.F., Simenstad, C.A., & Zedler, J.B. (2008). Practical Proxies for Tidal Marsh Ecosystem Services: Application to Injury and Restoration. *Advances in Marine Biology, Vol 54* (pp. 221-266). San Diego: Elsevier Academic Press Inc

Plag, H.P., & Tsimplis, M.N. (1999). Temporal variability of the seasonal sea-level cycle in the North Sea and Baltic Sea in relation to climate variability. *Global and Planetary Change, 20*, 173-203

Populus, J., Barreau, G., Faxilleau, J., Kerdreux, M., & L'Yavanc, J. (2001). Assessment of the Lidar topographic technique over a coastal area. In, *Proceedings of CoastGIS'01: 4th International Symposium on GIS and Computer Mapping for Coastal Zone Management* (p. 11). Halifax, Nova Scotia

Portnoy, J.W., Roman, C.T., Smith, S.M., & Gwilliam, E. (2003). Estuarine habitat restoration at Cape Cod National Seashore: the Hatches Harbor prototype. *Park Science, 22*, 8

Provost, M.W. (1976). Tidal Datum Planes Circumscribing Salt Marshes. *Bulletin of Marine Science, 26*, 558-563

Raber, G.T., Jensen, J.R., Hodgson, M.E., Tullis, J.A., Davis, B.A., & Berglund, J. (2007). Impact of lidar nominal post-spacing on DEM accuracy and flood zone delineation. *Photogrammetric Engineering and Remote Sensing, 73*, 793-804

Redfield, A.C. (1965). Ontogeny of a salt marsh estuary. *Science, 147*, 50-55

Redfield, A.C. (1972). Development of a New England Salt Marsh. *Ecological Monographs, 42*, 201-237

Redfield, A.C., & Rubin, M. (1962). The Age of Salt Marsh Peat and its Relation to Recent Changes in Sea Level at Barnstable, MA. *Proceedings of the National Academy of Sciences of the United States of America, 48*, 1728-1735

Reed, D.J. (2002). Sea-level rise and coastal marsh sustainability: geological and ecological factors in the Mississippi delta plain. *Geomorphology, 48*, 233-243

Reed, D.J., Bishara, D.A., Cahoon, D.R., Donnelly, J.P., & Kearney, M. (2007). Site-specific scenarios for wetlands accretion as sea level rises in the mid-Atlantic region. In U.S.E.P. Agency (Ed.). Washington D.C.

Reed, D.J., & Cahoon, D.R. (1992). The relationship between marsh surface topography, hydroperiod, and growth of *Spartina alterniflora* in a deteriorating Louisiana salt marsh. *Journal of Coastal Research, 8*, 77-87

Reimold, R.J., Gallagher, J.l., & Thompson, D.E. (1973). Remote Sensing of Tidal Marsh. *Photogrammetric Engineering and Remote Sensing, 39*, 477-488

Rogers, J.N., Parrish, C.E., Ward, L.G., & Burdick, D.M. (2015). Evaluation of field-measured vertical obscuration and full waveform lidar to assess salt marsh vegetation biophysical parameters. *Remote Sensing of Environment, 156*, 264-275

Rogers, J.N., Parrish, C.E., Ward, L.G., & Burdick, D.M. (In Review). Assessment of Elevation Uncertainty in Salt Marsh Environments Using Discrete-Return and Full-Waveform Lidar. *Journal of Coastal Research, In Review*

Roman, C.T., & Burdick, D. (2012). *Tidal Marsh Restoration: A Synthesis of Science and Practice*. Washington: Island Press

Roman, C.T., Niering, W.A., & Warren, R.S. (1984). Salt marsh vegetation change in response to tidal restrictions. *Environmental Management, 8*, 141-149

Roman, C.T., Peck, J., Allen, J.R.L., King, J., & Appleby, P. (1997). Accretion of a New England (USA) Salt Marsh in Response to Inlet Migration, Storms, and Sea Level Rise. *Estuarine Coastal and Shelf Science, 45*, 717-727

Rosso, P.H., Ustin, S.L., & Hastings, A. (2005). Use of lidar to study changes associated with *Spartina* invasion in San Francisco Bay marshes. *Remote Sensing of Environment, 100*, 295-306

Rosso, P.H., Ustin, S.L., & Hastings, A. (2006). Use of lidar to study changes associated with *Spartina* invasion in San Francisco Bay marshes. *Remote Sensing of Environment, 100*, 295-306

Sadro, S., Gastil-Buhl, M., & Melack, J. (2007). Characterizing patterns of plant distribution in a southern California salt marsh using remotely sensed topographic and hyperspectral data and local tidal fluctuations. *Remote Sensing of Environment, 110*, 226-239

Sappington, J.M., Longshore, K.M., & Thompson, D.B. (2007). Quantifying landscape ruggedness for animal habitat analysis: A case study using bighorn sheep in the Mojave Desert. *Journal of Wildlife Management, 71*, 1419-1426

Sasian, J.M. (1992). Image Plane Tilt in Optical-Systems. *Optical Engineering, 31*, 527-532

Schalles, J.F., Hladik, C.M., Lynes, A.A., & Pennings, S.C. (2013). Landscape Estimates of Habitat Types, Plant Biomass, and Invertebrate Densities in a Georgia Salt Marsh. *Oceanography, 26*, 88-97

Schmid, K.A., Hadley, B.C., & Wijekoon, N. (2011). Vertical Accuracy and Use of Topographic LIDAR Data in Coastal Marshes. *Journal of Coastal Research, 27*, 116-132

Schmidt, K.S., & Skidmore, A.K. (2003). Spectral discrimination of vegetation types in a coastal wetland. *Remote Sensing of Environment, 85*, 92-108

Schureman, P. (1975). Tide and current glossary. In U.S.D.o. Commerce (Ed.) (p. 25). Washington D.C.: National Oceanic and Atmospheric Administration

Schwimmer, R.A., & Pizzuto, J.E. (2000). A model for the evolution of marsh shorelines. *Journal of Sedimentary Research, 70*, 1026-1035

Shrestha, R., & Carter, W.E. (1998). Engineering applications of airborne scanning lasers: Reports from the field. *Photogrammetry Engineering and Remote Sensing, 64*, 256

Shuman, C.S., & Ambrose, R.F. (2003). A comparison of remote sensing and ground-based methods for monitoring wetland restoration success. *Restoration Ecology, 11*, 325-333

Silvestri, S., Marani, M., & Marani, A. (2003). Hyperspectral remote sensing of salt marsh vegetation, morphology and soil topography. *Physics and Chemistry of the Earth, 28*, 15-25

Smith, S.M. (2009). Multi-decadal Changes in Salt Marshes of Cape Cod, MA: Photographic Analyses of Vegetation Loss, Species Shifts, and Geomorphic Change. *Northeastern Naturalist, 16*, 183-208

Stoddart, D., Reed, D.J., & French, J.R. (1989). Understanding Satl Marsh Accretion, Scolt Head Island, Norfolk, England. *Estuaries, 12*, 228-236

Straatsma, M.W., Warmink, J.J., & Middelkoop, H. (2008). Two novel methods for field measurements of hydrodynamic density of floodplain vegetation using terrestrial laser scanning and digital parallel photography. *International Journal of Remote Sensing, 29*, 1595-1617

Swanson, R.L. (1974). Variability of tidal datums and accuracy in determining datums from short series of observations, Tech Report 64. In U.S.D.o. Commerce (Ed.). Washington D.C.: NOAA NOS

Swanson, R.L., & Thurlow, C.I. (1979). Uniform Tidal Datum System for the United States of America. *International Hydrographic Review, 56*, 143-151

Swatantran, A., Dubayah, R., Roberts, D., Hofton, M., & Blair, J.B. (2011). Mapping biomass and stress in the Sierra Nevada using lidar and hyperspectral data fusion. *Remote Sensing of Environment, 115*, 2917-2930

Tayyebi, A., & Pijanowski, B.C. (2014). Modeling multiple land use changes using ANN, CART and MARS: Comparing tradeoffs in goodness of fit and explanatory power of data mining tools. *International Journal of Applied Earth Observation and Geoinformation, 28*, 102-116

Timm, B.C., & McGarigal, K. (2012). Fine-scale remotely-sensed cover mapping of coastal dune and salt marsh ecosystems at Cape Cod National Seashore using Random Forests. *Remote Sensing of Environment, 127*, 106-117

Tiner, R.W.J. (1987). *A Field Guide to Coast Wetland Plants of the Northeastern United States*. University of Massachusetts Press

Tolley, P., & Christian, R. (1999). Effects of Increased Inundation and Wrack Deposition on a High Salt Marsh Plant Community. *Estuaries, 22*, 944-954

Torres, R., & Styles, R. (2007). Effects of topographic structure on salt marsh currents. *Journal of Geophysical Research-Earth Surface, 112*, 14

Toyra, J., Pietroniro, A., Hopkinson, C., & Kalbfleisch, W. (2003). Assessment of airborne scanning laser altimetry (lidar) in a deltaic wetland environment. In (pp. 718-728): Canadian Aeronautics Space Inst

Uchupi, E., Giese, G.S., Aubrey, D.G., & Kim, D.J. (1996). The Late Quaternary Construction of Cape Cod, Massachusetts: A Reconstruction of the W.M. Davis Model. *The Geological Society of America, Special Paper 309*, 69

van Proosdij, D., Ollerhead, J., & Davidson-Arnott, R.G.D. (2006). Seasonal and annual variations in the volumetric sediment balance of a macro-tidal salt marsh. *Marine Geology, 225*, 103-127

Varnell, L.M., Evans, D.A., & Havens, K.J. (2003). A geomorphological model of intertidal cove marshes with application to wetlands management. *Ecological Engineering, 19*, 339-347

Vincent, R.E., Burdick, D.M., & Dionne, M. (2014). Ditching and Ditch-Plugging in New England Salt Marshes: Effects on Plant Communities and Self-Maintenance. *Estuaries and Coasts, 37*, 354-368

Wagner, W., Hollaus, M., Briese, C., & Ducic, V. (2008). 3D vegetation mapping using small-footprint full-waveform airborne laser scanners. In (pp. 1433-1452): Taylor & Francis Ltd

Wang, C., Menenti, M., Stoll, M.-P., Belluco, E., & Marani, M. (2007). Mapping mixed vegetation communities in salt marshes using airborne spectral data. *Remote Sensing of Environment, 107*, 559-570

Wang, C., Menenti, M., Stoll, M.P., Feola, A., Belluco, E., & Marani, M. (2009). Separation of Ground and Low Vegetation Signatures in LiDAR Measurements of Salt-Marsh Environments. *Ieee Transactions on Geoscience and Remote Sensing, 47*, 2014-2023

Ward, L.G., Kearney, M., & Stevenson, J. (1998). Variations in sedimentary environments and accretionary patterns in estuarine marshes undergoing rapid submergence, Chesapeake Bay. *Marine Geology, 151*, 111-134

Ward, L.G., Zaprowski, B.J., Trainer, K.D., & Davis, P.T. (2008). Stratigraphy, pollen history and geochronology of tidal marshes in a Gulf of Maine estuarine system: Climatic and relative sea level impacts. *Marine Geology, 256*, 1-17

Warren, R.S., & Niering, W.A. (1993). Vegetation Change on a Northeast Tidal Marsh: Interaction of Sea-Level Rise and Marsh Accretion. *Ecology, 74*, 96-103

White, S.A., Parrish, C.E., Calder, B.R., Pe'eri, S., & Rzhanov, Y. (2011). LIDAR-Derived National Shoreline: Empirical and Stochastic Uncertainty Analyses. *Journal of Coastal Research*, 62-74

Wiegert, R.G., & Freeman, B.J. (1990). *Tidal salt marshes of the southeast Atlantic Coast : a community profile*. Washington, D.C.: U.S. Dept. of the Interior, Fish and Wildlife Service

Wright, C.W., & Brock, J.C. (2002). EAARL: A Lidar for mapping shallow coral reefs and other coastal environments. In, *Proceedings of the Seventh International Conference on Remote Sensing for Marine and Coastal Environments*. Miami, FL: Veridian International Conferences

Yang, Z., Myers, E., Jeong, I., & White, S. (2013). VDatum for the Gulf of Maine: Tidal Datums and Topography of the Sea Surface. In: NOAA Technical Memorandum NOS CS 31

Zedler, J.B., Callaway, J.C., Desmond, J.S., Vivian-Smith, G., Williams, G.D., & Sullivan, G. (1999). Californian salt-marsh vegetation: An improved model of spatial pattern. *Ecosystems, 2*, 19-35

Zehm, A., Nobis, M., & Schwabe, A. (2003). Multiparameter analysis of vertical vegetation structure based on digital image processing. *Flora, 198*, 142-160

Zevenbergen, L.W., & Thorne, C.R. (1987). Quantitative Analysis of Land Surface Topography. *Earth Surface Processes and Landforms, 12*, 47-56

APPENDIX A

OPTICAL CALIBRATION

There are several potential sources of uncertainty in the Vertical Obscuration (VO) photographic measuring method. The first of these potential sources involve optical distortions that may be present as a result of the camera lens and mirror assembly. Although great care was taken to compensate for introduced errors by using precision leveling devices, the geometry of the camera, mirror and background could play a role in increasing uncertainty. Camera rotation along the three axes may create erroneous angles to the image, lengthening or shortening pixel dimensions. Similarly, mirror angles less than or greater than 45 degrees may add to potential geometric distortion. Additionally, a non-perpendicular background board and scale bar may affect the geometry of the scale bar, but would not create geometrical distortion in the vegetation portion of the image. Finally, the digital extraction of background from the vegetation, creating a binary image, has the potential to be a source of uncertainty. In the case of this analysis, the spectral properties of the background and the vegetation are mixed. Spectrally mixed pixels are a combination of end member spectral properties weighted by the corresponding abundances (Liu and Zhang 2014). The frequency of occurrence of spectrally mixed pixels in this study is primarily dependent on camera resolution, the vegetation density, and the size of air spaces or gaps. As a consequence this could lead to a positive bias towards the bottom of the image where the stems/leaves are often the densest and small gaps are not easily detected. Spectral unmixing algorithms are sometimes employed to extract the percentage of each end member material present in each pixel (Liu and Zhang 2014).

Various fully-automated extraction techniques were attempted to extract the vegetation pixels from the background such as supervised and unsupervised classification, histogram stretch and thresholding using image processing software including ENVI 4.3. After extensive tests, a semi-automated approach was selected utilizing SideLook software (Zehm et al. 2003; Nobis and Hunziker 2005), which was found to produce superior results in the least time. Fully automated approaches were not as successful due to the inconsistent red color of the back-board from top to bottom in the image. The color variation was caused by diminishing light levels as a result of tall vegetation. Therefore when the classification or thresholding techniques could separate the board from the vegetation at the top of the image, it was unsuccessful at the bottom. Unfortunately, manual thresholding does not necessarily resolve this issue because it can also be somewhat subjective, introducing uncertainty to the measurement (Neumeier 2005; Nobis and Hunziker 2005).

Threshold values and spectral mixing are very closely related parameters and for the purposes of this analysis are investigated together since threshold is an easily controllable parameter. Starting with a field collected, vegetation image that was arbitrarily selected to represent "truth" (i.e., assumed to have no other distortions such as those caused by the lens and mirror), optimal VO (vo_{true}) was first computed, and then the 8-bit threshold (0-255) was systematically varied between 255 to 235 in 1 DN (digital number) increments. For each iteration, Δvo ($vo_{\text{true}} - vo$) was computed. The results of this analysis showed that the change in vo was < 1% for the entire image, up to a variation of threshold ±3 DN values from the empirically-determined "best threshold." Therefore, for the purposes of this study mixed pixel issues do not significantly impact the results. If the objective were to investigate small air gaps, higher resolution imagery would be necessary.

A calibration was conducted for the camera and mirror assembly to determine potential optical distortions, which may contribute to erroneous results or increased uncertainty. Two calibration images, one with only the camera lens optics (**Figure AA1a**) and a second with the mirror assembly (**Figure AA1b**), were taken of a standard black and white checkerboard with 9.4 cm squares at full field of view (i.e. minimum zoom). Using ArcGIS 10, polygons and line segments of the calibration checkers were hand digitized to the nearest pixel and coded for row number (**Figure AA2**). Quantifiable barrel distortion was observed in the camera lens calibration photo, where checkers varied in size from the center of the image to the outer extremities (corners) (**Figure AA3**). Barrel distortion is defined as when the image magnification decreases with distance from the optical axis with the apparent effect of an image appearing to be mapped around a barrel (Pei-Yin et al. 2009). Deviation in calibration checker area due to the barrel lens distortion appears to be very symmetrical varying by as much as 13% in the center column from centermost checker to bottom or top of the image **(Figure AA4a)** and 8% from center to the left and right edges **(Figure AA4b)**. The center checker area, across all the columns, varied by a minimum of 1% in the adjacent columns to approximately 7% in the outermost columns in the center of the image and 11% at the bottom and top. Length variation by area followed similar patterns with variation from top to bottom being as large as 8-10% and sided to side by as much as 6% (**Figure AA5**).

The rectangular mirror assembly was imaged by the camera as a trapezoidal shape, where the top, closer to the camera, is wider than the bottom (**Figure AA6a**). This type of optical distortion was first thought to be keystone, which is sometimes observed using remote sensing imaging platforms (Sasian 1992). However, calibration checkers and therefore marsh vegetation photos, did not exhibit this keystone distortion. Checkers at the top and bottom of the image are

not trapezoidal in shape, as would be expected if this was true keystone distortion. Instead, it was observed that the field of view is wider at the top than at the bottom.

The portion of the calibration image visible in the mirror and used for VO analysis was located in the center calibration columns of the camera image, which contained the least amount of observed error (**Figure AA6b**). During preprocessing and analysis of the imagery, the edges around the mirror where the most extreme errors are found were cropped away and the calibration checkers within the mirror were digitized (**Figure AA7**). This method of image cropping was similar to that used by another researcher that cropped the center columns from multiple images, where image distortion is minimal, to create a composite mosaic (Straatsma et al. 2008). Measuring the observed differences in checker area from the mirror it was found that they differ by as much as 12% from the center to the bottom but the upper 72% of the image contained less than 4% variation (**Figure AA8**). With the exception of the bottom most row, row area variation from the center to sides was within 1%. The length variation analysis produced very similar results (**Figure AA9**). Therefore, checkers at the bottom of the mirror were observed to contain the greatest error from the combined lens and mirror distortion as compared to the center squares.

Ideally, each image should be geometrically corrected for the observed optical distortions using a predetermined camera model or rectified to a known grid by an affine transformation (**Figure AA10**) (Zehm et al. 2003); However, this may not be necessary, if the effect on the computed VO can be shown to be negligible. For example, Zehm et al. (2003) showed in their calibration photos that results on vertical height measurements differed by approximately 3% on average from standard digital photos to their geometrically corrected version. Other researchers conducting similar photographic measurements of vegetation also did not perform geometric

correction and determined the errors to be negligible when compared to the other potential sources of error within their analysis (Neumeier 2005; Nobis and Hunziker 2005; Möller 2006; Straatsma et al. 2008).

Further evaluation of rectified image uncertainty was conducted by correcting a calibration image for lens distortion with ArcGIS to a perfect grid (**Figure AA11a**) before digitizing checkers visible in the mirror (**Figure AA11b**). After lens correction was completed, image distortions related to the mirror and camera geometry could be isolated from the optical lens distortion. Checker polygons were color coded by area in **figure AA12** to visualize the variability found in the image by sources other than the camera lens. This same rectification can then be applied to field photos (**Figure AA13**). Additional analysis of the camera rectified image reveals at least two other sources of error are present (**Figure AA14**) (**Figure AA15**). The first source is suggested by a lineation of area and length differences from the bottom of the image to the top. Imaging through the mirror assembly produced a 4% difference in area and less than 2% variability in length between the top and bottom of the image with the center. It should be noted that the seemingly chaotic points of **figure AA15a** only deviate from a straight line by at most 1% and could easily be caused by slight digitizing errors in the line segment lengths. Several of the line segments that were significantly off were a known error caused by the seam between two sheets of calibration paper. Secondly, a slight rotation was observed in which the cause could be the orientation of the mirror to the calibration board, the orientation of the camera mount to the mirror or possibly a warp in the mirror frame assembly. This observed rotation produced area variability from left to right of 0.5 to 2% and length variability of approximately 1 to 3% to the center measurement with the greatest differences located at the bottom of the image.

A mirror correction model could be created to remove the remaining distortions (**Figure AA16a**). However, such a model would require mirror conditions to be identical in each image. Although conditions were similar they were not identical in each captured image (**Figure AA16b**). There was some variation in the placement of the mirror assembly within each image. Using the model created in **figure AA16a**, a good portion of the observed mirror error could be corrected, but it may not eliminate all distortion and could introduce additional errors. Image specific calibration models are not possible due to a lack of calibration checkers in each field image.

The VO analysis used in this study of uncorrected images measured the percent obscured of an area in 5 cm increments in height (i.e. a binary image of how much is vegetation versus how much is background in a given area). Therefore, the resulting measurements of VO are unit-less and the area discrepancies observed as a result of barrel and mirror distortions should not materially affect the results. However, in the absence of that assumption or when the VO digital imaging method is used for measuring vegetation height, the following uncertainty assessment is made. Based on the analysis presented above, height measurements at the bottom of the mirror could vary as much as 8% from those at the center. Yet, approximately 80% of the image varies by less than 5% of the center checker. Based on measurements, imaged vegetation with heights less than 20 cm will fall within the image 6-8% error zone equivalent to 1.6 cm of error. This project contained only one sample of *Spartina patens* that imaged at a height below 20 cm. Field observations were consistently lower than photographically derived heights with *Spartina alterniflora* exhibiting a mean difference of 8.6-14 cm and the other taxa differing by a mean of 10.4-16.8 cm. According to the calibration findings, uncorrected VO imaging of height will always be underestimated due to the lens and mirror distortions. That underestimate will be

variable over the mirror length increasing as the distance increases from the center of the mirror. The combined lens and mirror distortion produce up to a maximum of 3.71 cm of error over the total height of the mirror, which is a 2.8% variance in height. This error is significantly less than the difference between the field observed heights and the photographically derived heights.

The use of the VO method in the field does appear to have some limitations and may not be suitable for extremely dense or woody vegetation. The colored board and mirror assembly are difficult to maneuver in these settings and damage may be caused to the apparatus and/or the vegetation, thereby introducing the potential for erroneous results. For instance the mirror and background apparatus may not work well in an invasive *Phragmites australis* stand, because of lack of maneuverability and due to height constraints as a result of the tall stalks. For denser vegetated areas the method may need to be modified to exclude the mirror, which is more analogous to the Möller and Zehm design (Zehm et al. 2003; Möller 2006).
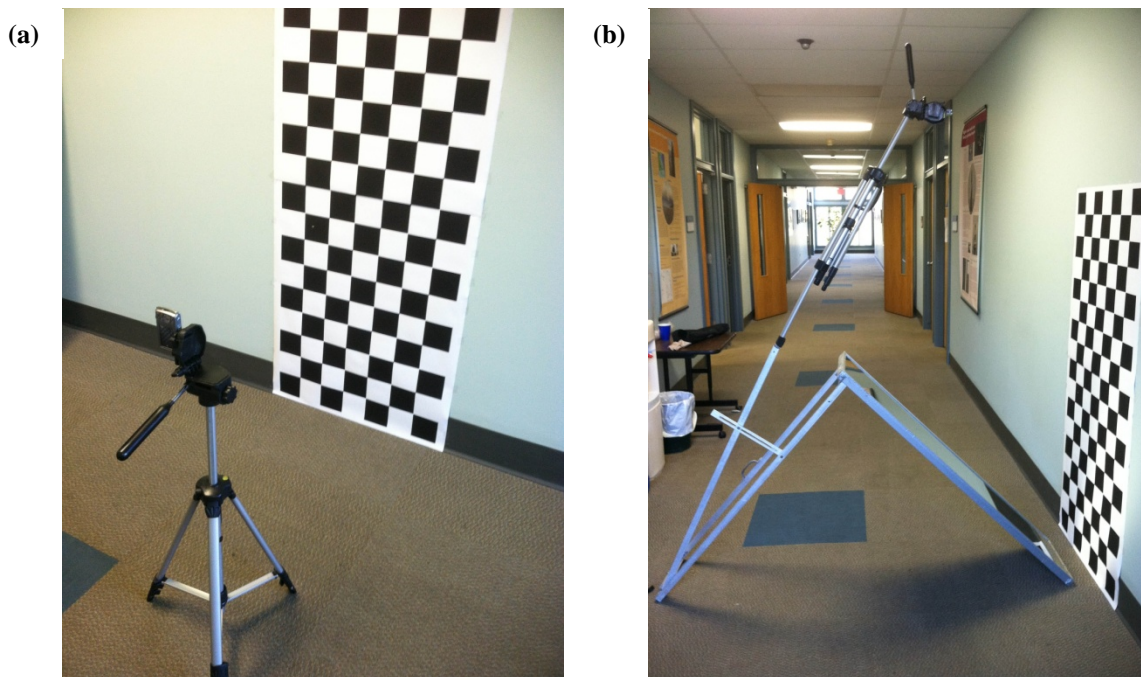
Figure AA1: a) Digital camera on a tripod capturing an image of a calibration checker board. b) Camera and mirror assembly capturing an image of a calibration checker board.
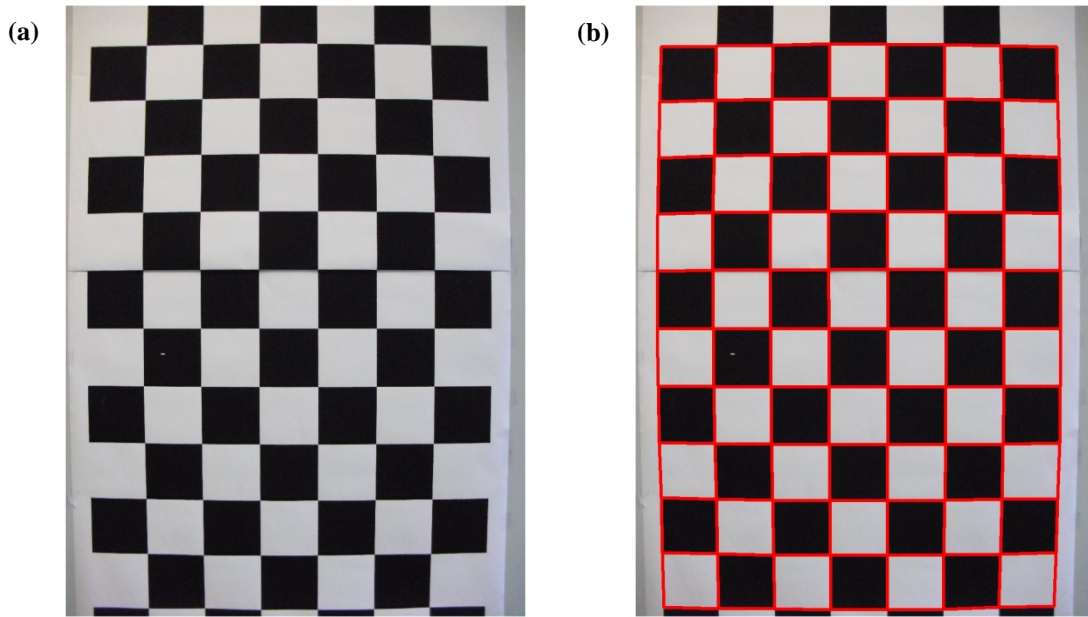
Figure AA2: a) Camera photo of calibration board. b) Digitized (in red) calibration checkers. Notice arcing barrel shape to the red digitized lines.
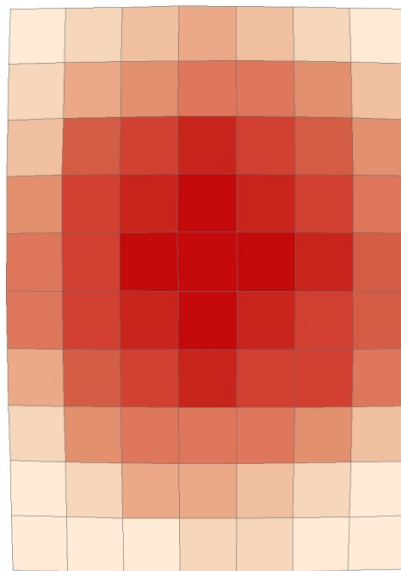
Figure AA3: Polygons colored by area for camera calibration. Center squares (red) are larger in unitless area than corner squares (pink).

(a) Camera Area Column Analysis

(b) Camera Area Row Analysis
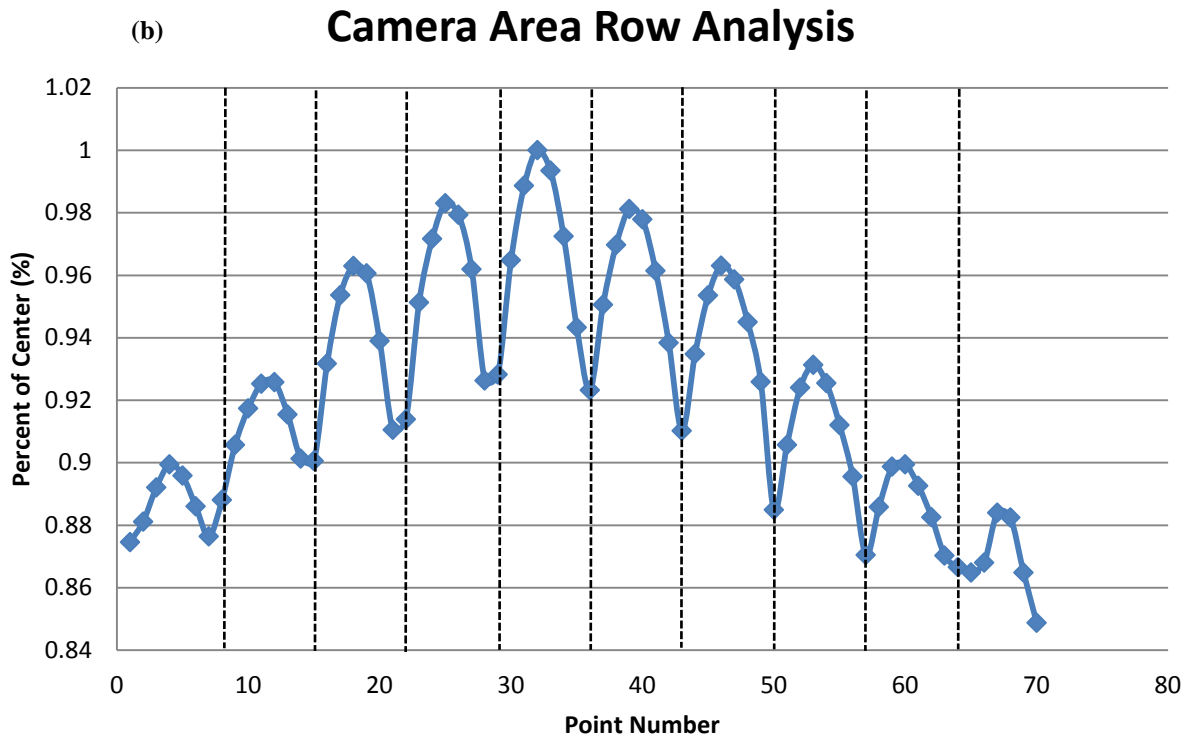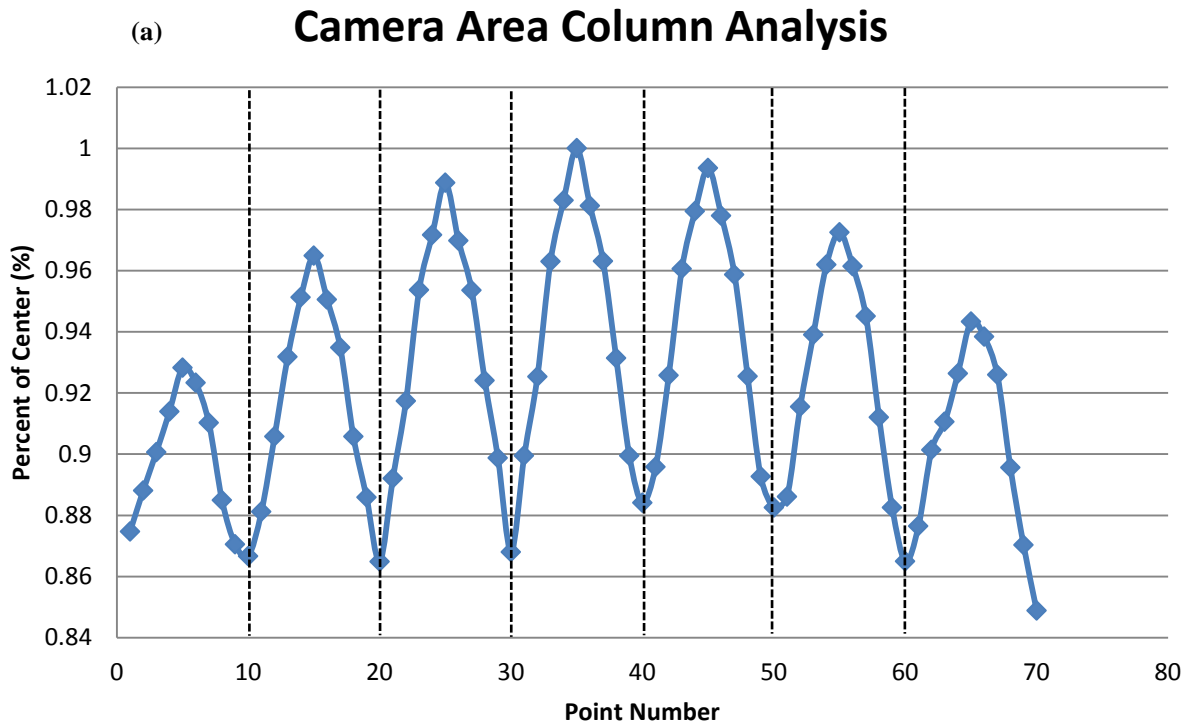
Figure AA4: From bottom of image/calibration grid to top a) Camera lens distortion for checker area by columns. b) Camera lens distortion for checker area by rows. The center checker's area (largest) was used to calculate the percent variance of other checkers. Dashed lines are column/row separators.

(a) Camera Length Column Analysis

(b) Camera Length Row Analysis
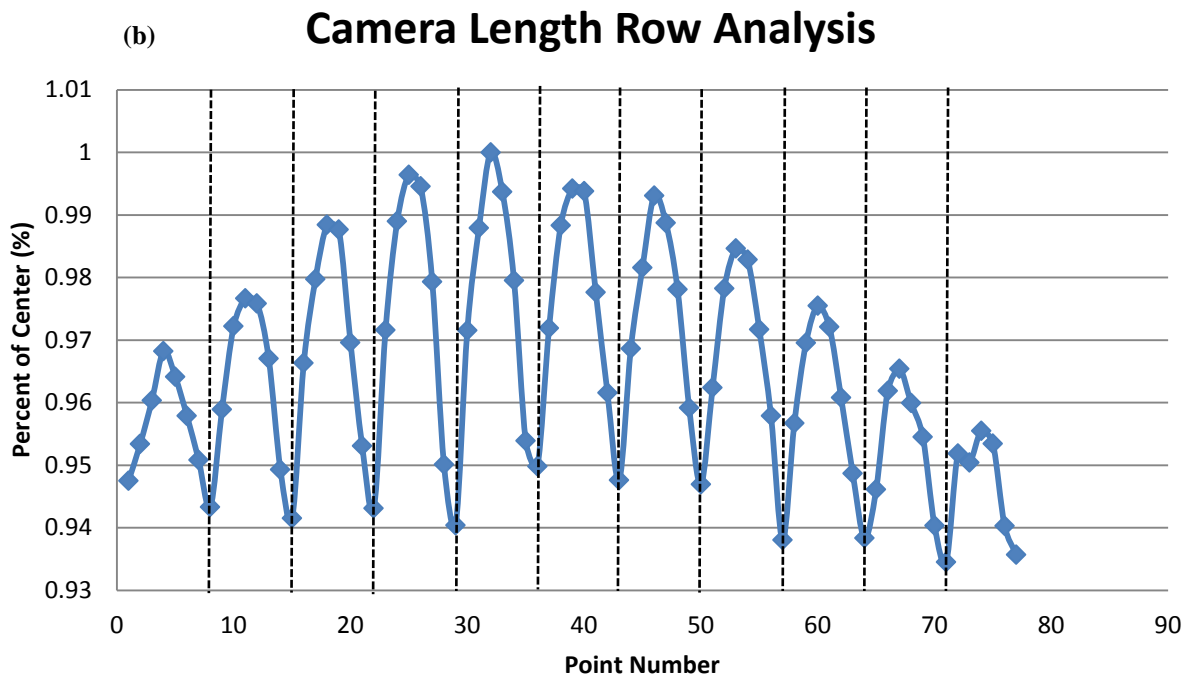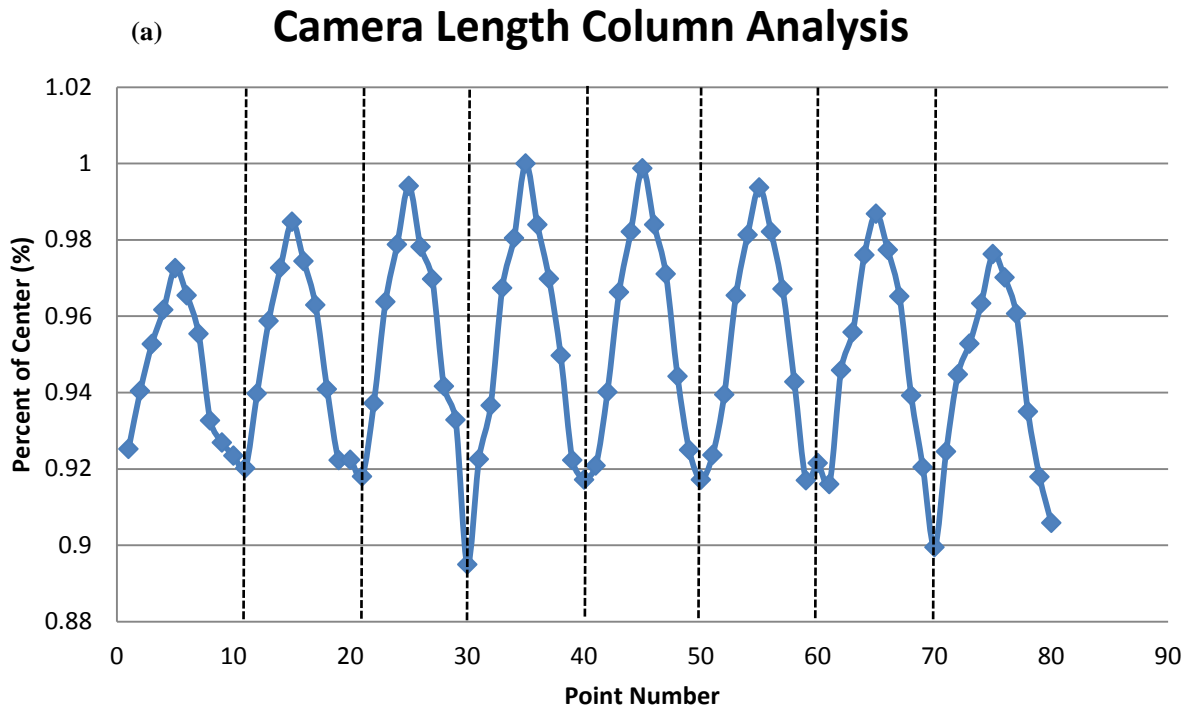
Figure AA5: **From bottom of image/calibration grid to top a) Camera lens distortion for checker length by columns. b) Camera lens distortion for checker length by row. The center checker's length (largest) was used to calculate the percent variance of other checkers. Dashed lines are column/row separators.**
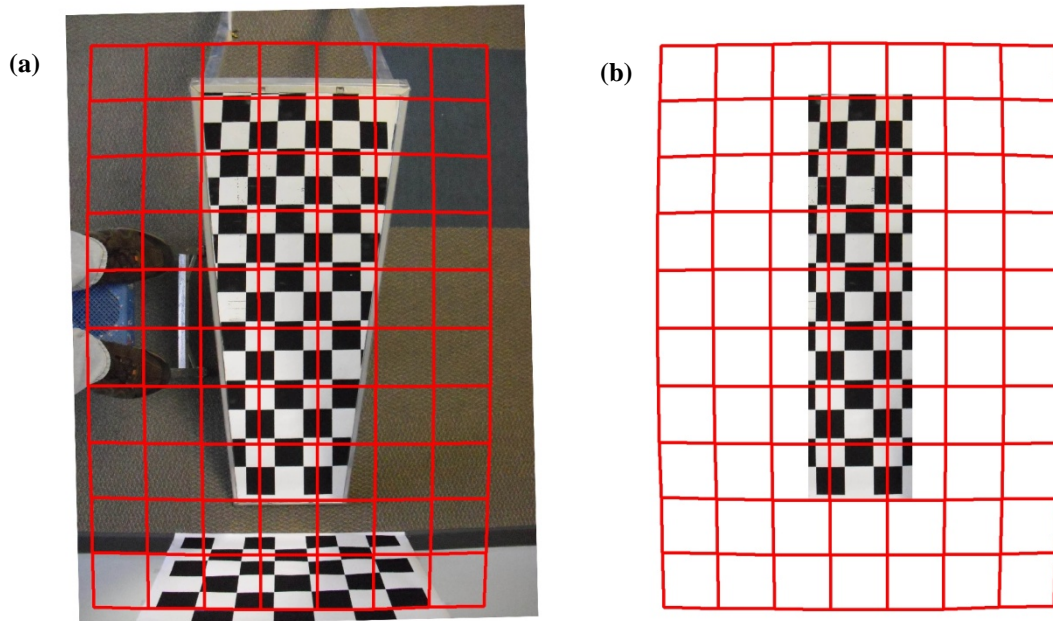
Figure AA6: a) Digitized calibration checkers over photo of mirror apparatus b) Digitized calibration checkers over cropped, usable portion of mirror.

Figure AA7: Calibration checkers from mirror digitized (in yellow).
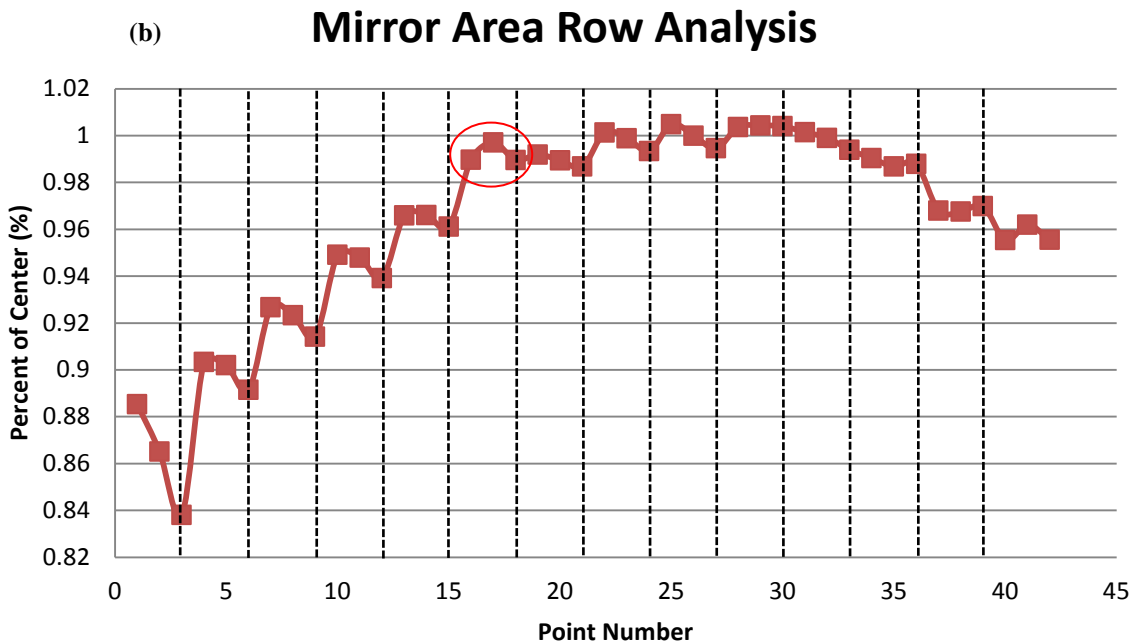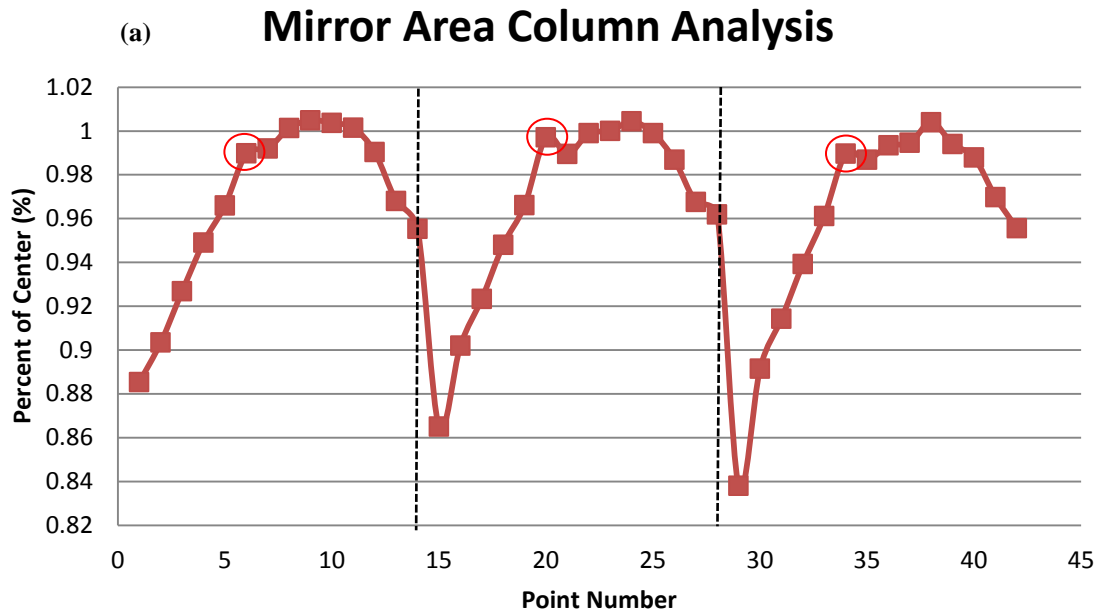
Figure AA8: From bottom of image/calibration grid to top, a) Deviation in area within the mirror portion of the image for each checker by column. b) Deviation in area within the mirror portion of the image for each checker by rows. The center checker's area was used to calculate the percent variance of other checkers. Dashed lines are column/row separators. Red ovals represent points with digitizing error from the calibration board (seam between two sheets of paper). These graphs contain both lens optical distortion and mirror distortion.

(a) Mirror Length Column Analysis

(b) Mirror Length Row Analysis
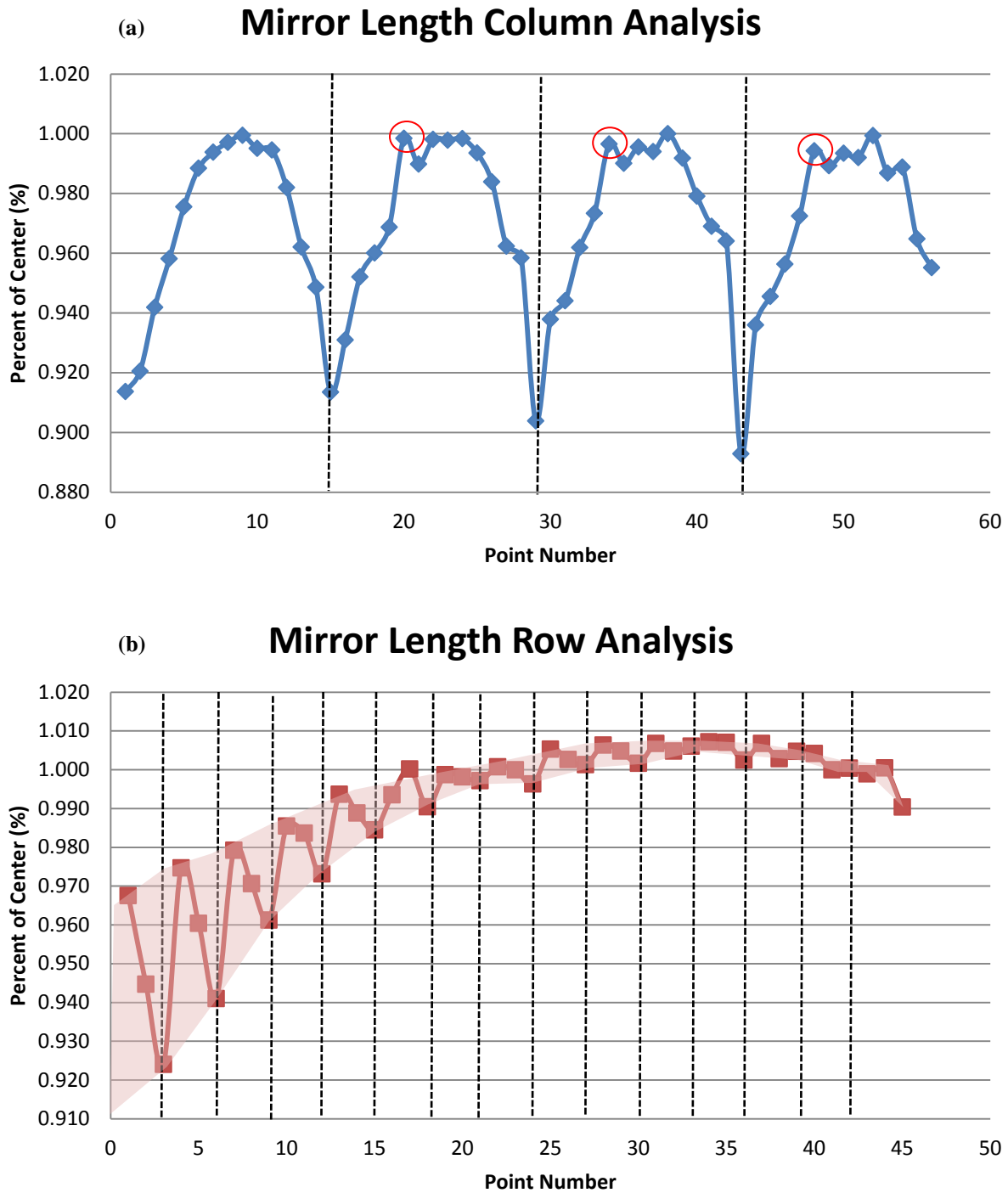
Figure AA9: From bottom of image/calibration grid to top, a) Deviation in length within the mirror portion of the image for each checker by column. b) Deviation in length within the mirror portion of the image for each checker by rows. The center checker's area was used to calculate the percent variance of other checkers. Dashed lines are column/row separators. Red ovals represent points with digitizing error from the calibration board (seam between two sheets of paper).   These graphs contain both lens optical distortion and mirror distortion. The shaded area essentially represents the cone of error with the bottom of the mirror on the left with the largest errors.
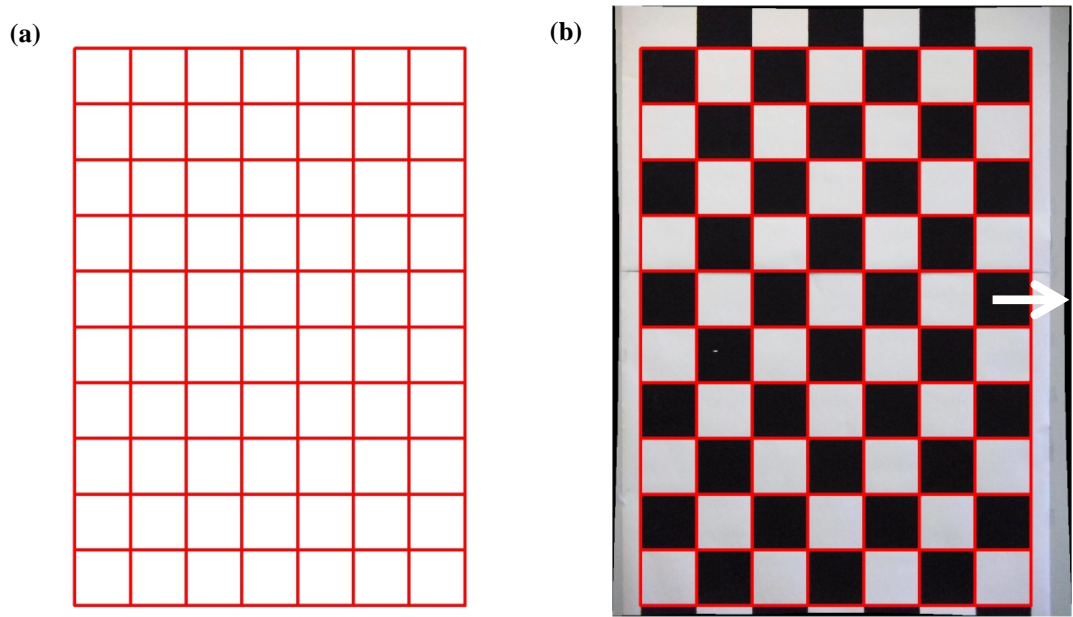
Figure AA10: a) A perfect grid the same size as the original calibration checker board with right angles and no distortion. b) Calibration photo has been rectified to perfect grid removing camera lens barrel distortion. Notice black, arcing slivers (white arrow) at the edges of the photo and the perfect grid matching exactly the photo checkers. This is the same photo as shown in figure AA2a, b.
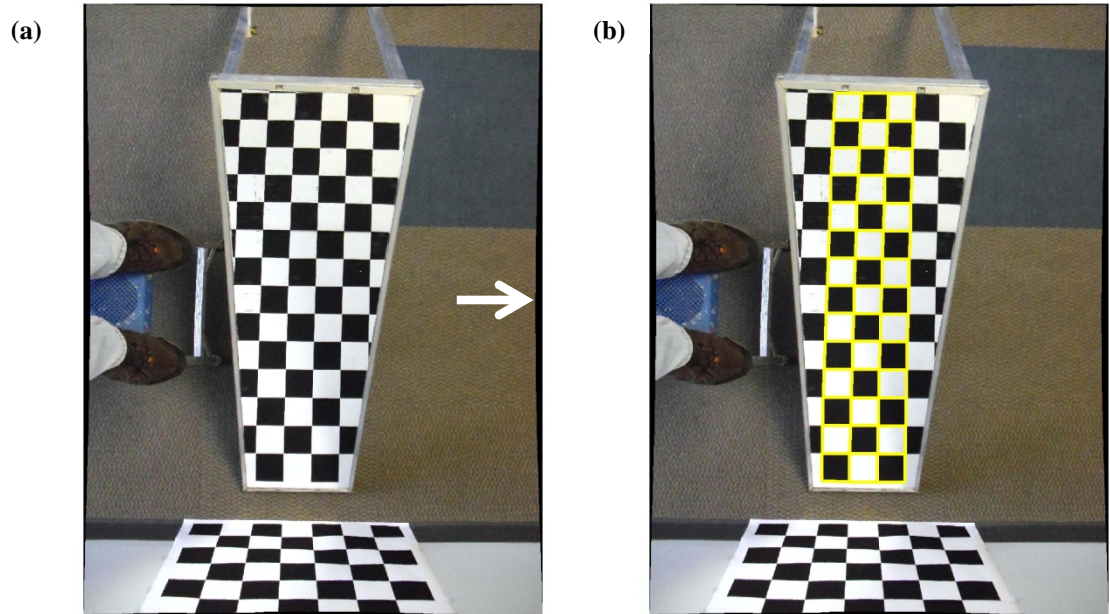
Figure AA11: Using the camera lens correction model based on the perfect grid from figure AA10b, a) Rectified image of mirror apparatus. Barrel lens distortion has been removed from the image (white arrow points to black slivers as seen in figure AA10b). b) Calibration checkers visible in the mirror portion have been digitized (in yellow) from the now rectified image.
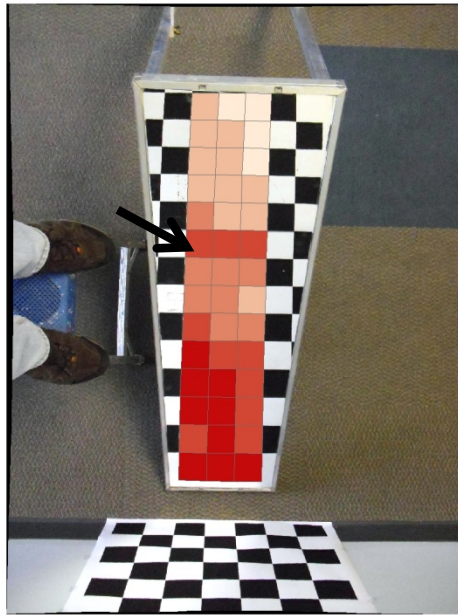
Figure AA12: Digitized polygons colored by area after lens optics correction. A diagonal pattern of decreasing area is observed from upper right to lower left. This is likely the combined effect of both a top to bottom increase in area as a result of the mirror optics and a slight camera rotation from left to right. The center strip of larger area located in row 6 (black arrow) from the top is the result of a calibration board error (seam between two sheets of calibration paper).

(a)

(b)
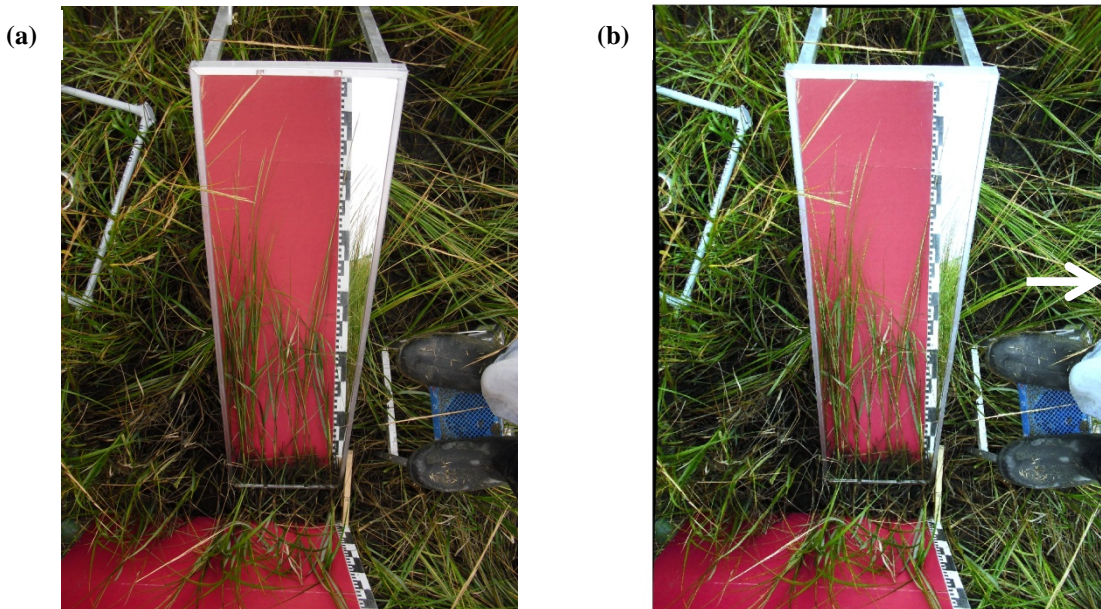
Figure AA13: a) Unrectified field image. b) Using the same model developed in figure AA10b, the rectified image of salt marsh vegetation (Sample station GA3) with camera lens distortion removed is shown. Notice slender black arcing border along all four sides of the image (white arrow).

(a) Camera Rectified Mirror Area by Column

(b) Camera Rectified Mirror Area by Row
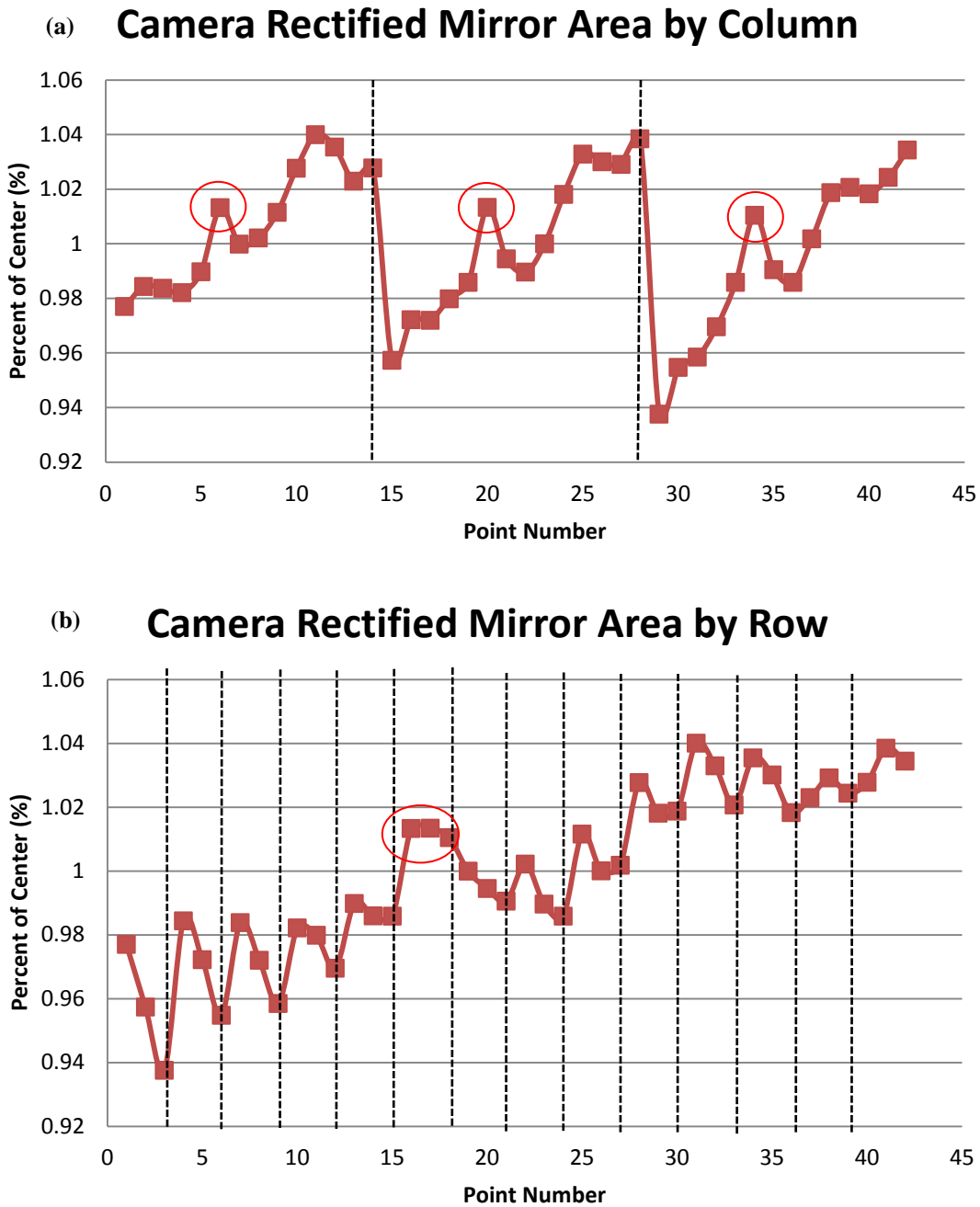
Figure AA14: Camera lens rectified image containing only the mirror related distortions. a) Plot of area for each checker by column. Areas are smaller at the top of the mirror than the bottom. b) Plot of area for each checker by row. The mirror's centermost checker area was used to calculate the percent variance of other checkers. Dashed lines are column/row separators. Red circle represents points with digitizing error from the calibration board (seam between two sheets of calibration paper). There is also a slight change in area from left to right suggesting the calibration mirror may not have been exactly perpendicular to the background board or there was some distortion of the mirror within the A-frame.
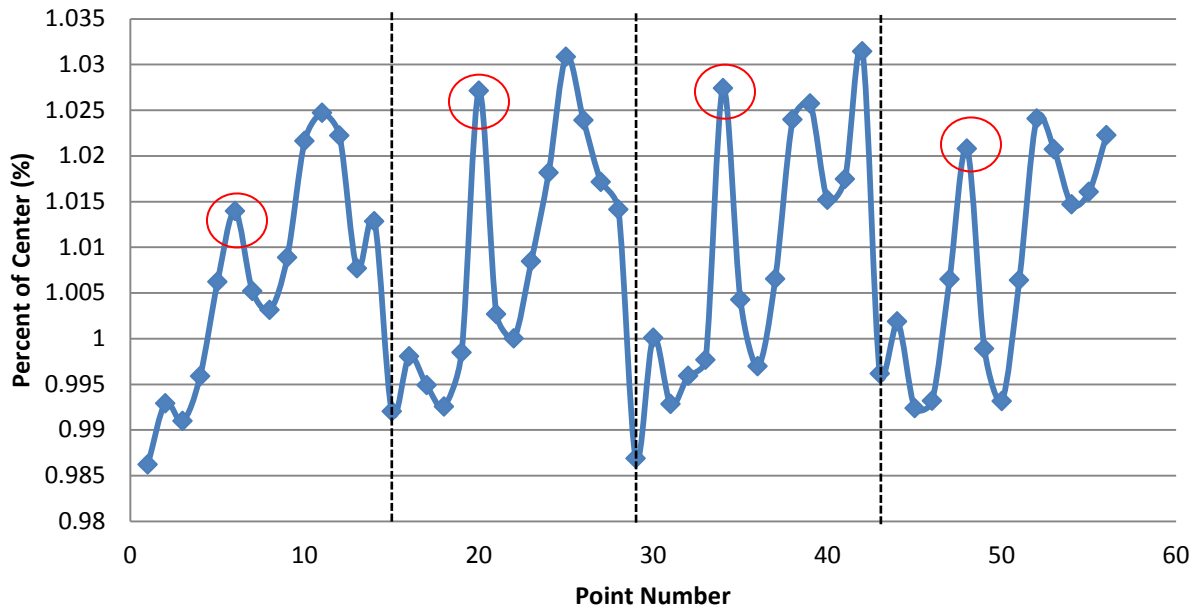
Figure AA15: Camera lens rectified image containing only mirror related distortions. a) Plot of lengths for each checker by column. Red circles represent points with digitizing error from the calibration board (seam between two sheets of calibration paper). b) Plot of lengths for each checker by row. The mirror's centermost checker length was used to calculate the percent variance of other checkers. Dashed lines are column/row separators. Lengths are smaller at the top of the mirror than the bottom. There is also a slight change in length from left to right suggesting the calibration mirror may not have been exactly perpendicular to the camera or there was some distortion of the mirror within the A-frame.

(a) **(b)**
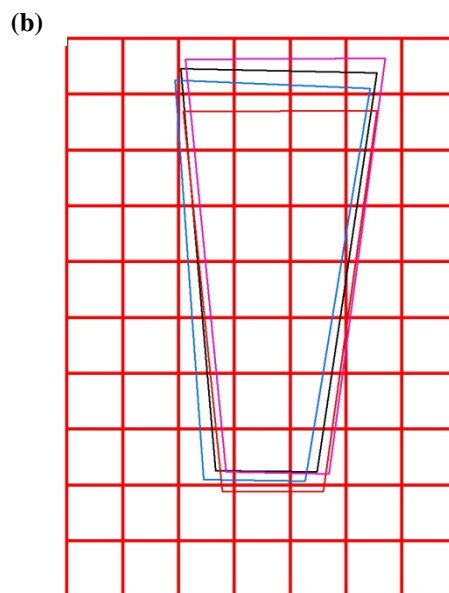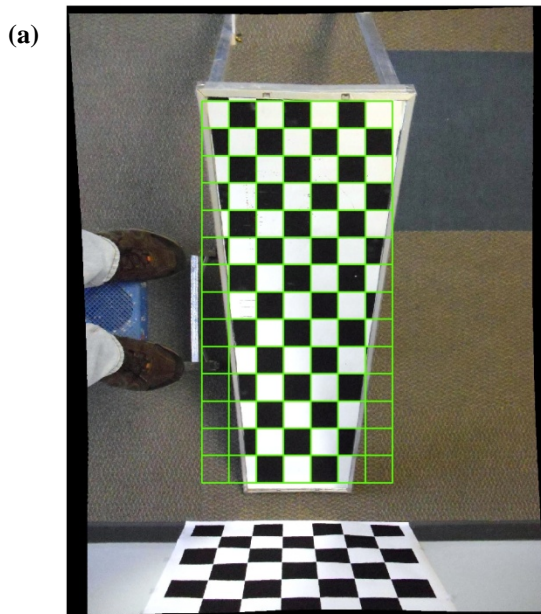
Figure AA16: a) A second rectification of the mirror image is possible to a known perfect grid. This process can remove any of the remaining mirror and rotation distortions. However, unless the mirror is always in the exact position within the photo boundary for every image then this process will introduce its own error and an exact mirror correction cannot be made. Since the calibration checkers are not available in each vegetation field plot image, an image specific mirror model cannot be generated. b) Four lens rectified images with their mirror trapezoid outlines digitized showing the slight variability in mirror position.

APPENDIX B

NONPARAMETRIC MODELS

Investigating problems with numerous independent variables and complex, possibly nonlinear response curves, requires the use of machine learning, nonparametric modeling techniques. Unlike typical statistical analysis of dependent and independent variables that utilize single or multiple regression techniques to make predictions of variable outcome, non-parametric modeling does not necessitate any assumption concerning variable distribution (i.e. a normal distribution is not necessary) as prerequisite of analysis (Bourennane et al. 2014). Non-linear approaches are often required in environmental modeling problems due to the complex and often concealed relationships between predictor variables (Tayyebi and Pijanowski 2014). In this research there were 12 to 13 predictor variables used in the construction of the models including: discrete return lidar elevation, distance from shoreline, waveform amplitude (**Figure AB1**), waveform area-under-the-curve (**Figure AB2**), surface curvature (**Figure AB3**), surface planimetric curvature (**Figure AB4**), surface profile curvature (**Figure AB5**), surface rugosity (**Figure AB6**), waveform skewness (**Figure AB7**), discrete return lidar (DRL) intensity (**Figure AB8**), waveform mean (**Figure AB9**), surface slope (**Figure AB10**), and waveform width (**Figure AB11**).

Modeling algorithms typically have between two or three analysis types: regression, classification or logistic binary depending if the response outcome is categorical or continuous. Regression algorithms are used when the response variable is continuous and use a regression-based model such as Multivariate Adaptive Regression Splines (MARS) where the response

variable (y) is fit based on one or more independent predictor variables $(x_1, x_2, \ldots, x_n)$ (Friedman 1991). Classification models such as Classification and Regression Trees (CART) are used to separate data based on its homogeneity into two or more discrete classes belonging to a categorical response variable (Breiman et al. 1984). Logistic binary methods are similar to classification but contain only two binary "yes/no" classes and can often be run from regression-based models.

Classification and Regression Trees (CART)

The CART algorithm creates regression (**Figure AB12**) and classification (**Figure AB13**) trees using binary recursive partitioning to predict the group association based on one or more predictor variables (Breiman et al. 1984). A tree consists of a series of binary "yes/no" rules that are applied to the predictor variables until each record is classified into categories. These trees can be simplified into splitter variables as shown in **Figure AB14.** The decision rules are applied first to the root node and then subsequently progressed until terminal nodes are reached. CART creates an optimal tree based on an extensive search of all possible variable splits and pruning to minimize residuals and overfitting the data (Breiman et al. 1984). Data outputs can be continuous or discrete values using regression or classification methods. However, regression-based CART models are limited in the output response to data clustering based on the terminal node assignment. CART has the ability to handle missing data and can often reveal important data relationships that sometimes remain concealed using other analytical methods by capturing non-linear, hierarchical relationships as well as interactions among predictor variables (Byrd and Kelly 2006).

Multivariate Adaptive Regression Splines (MARS)

MARS is a mathematical model that approximates functions by capturing essential nonlinearities and interactions but still produces results in a form similar to a traditional regression (Friedman 1991). This algorithm was the successor to CART and constructed specifically for regression type modeling where the model outputs are designed to predict a continuous numeric outcome. In addition to regression, MARS is also capable of producing high quality binary classifications with a "yes/no" outcome. MARS effectively uncovers important data patterns and relationships and produces output equations similar to those used in traditional regression approaches (**Figure AB15**). To accomplish this, MARS creates a sequence of basis functions by fitting piecewise linear segments with their own individual slopes and knots (boundaries between each linear section) allowing MARS to capture patterns (**Figure AB16**) (Friedman 1991). Basis functions are then systematically eliminated in a backward stepwise fashion with all knots being removed that do not substantially contribute to the goodness-of-fit. Each basis function is then used as new predictor variables in the model. Models run with interaction between variables result in basis functions that are 3d planar in nature similar to plotted output from parametric multiple regression. MARS can adapt to different basis function intervals as well as different predictor variables. The response variable mean square error is successively lowered through applying basis functions until an optimal model is achieved (**Figure AB17**).

TreeNet - Stochastic Gradient Boosting

The TreeNet algorithm, otherwise known as stochastic gradient boosting, is capable of consistently generating extremely accurate models for both regression and classification. To

accomplish this, TreeNet generates thousands of small decision trees (< 6 terminal nodes), from a random sample of the data that sequentially eliminate residuals and converge on a highly accurate model (Friedman 2002). TreeNet has the ability to handle contaminated or missing data that can be very challenging for other data mining methods, such as neural networks, by rejecting training data points that are too much at variance with the existing model. TreeNet is highly resistant to overfitting of the data since very small trees are used instead of one large tree and the models produce substantially higher accuracies (Friedman 2002). TreeNet uses several regularization techniques to minimize overfitting such as a gradually building up the model through successive gradient boosting iterations (trees). Variables are introduced one at a time but are only permitted to adjust the model outcome by very small coefficients (Friedman 2002). Increasing the number of trees reduces the error on the learn dataset and the model determines the optimal tree that minimizes overfitting and error. In addition, another method of overfitting regularization employed by TreeNet consists of the subsample size, which is a constant fraction of the size of the training set. A small subsample size of 0.5 has been determined optimal and introduces randomness into the algorithm by forcing the regression trees to be fit to reduced datasets at each boosting iteration (Friedman 2002). The response variable mean square error or average negative log likelihood is successively lowered through applying numerous trees until an optimal model is achieved (**Figure AB18, AB19**).

Random Forests

The Random Forests (RF) algorithm is an ensemble of many independent CART trees (Breiman 2001). RF interjects randomness into the selection of the best tree splitters by evaluating a random subset of predictors at each of the nodes. The overall prediction is

determined from the sum of the predictions made from individual decision trees. Due to the randomness of data selected from the learn sample, approximately 37% of the dataset is never used in the model creation, which forms the out-of-bag (OOB) observations and is used for testing purposes. These OOB records are subsequently run through each regression tree to produce error estimates and are used for cross-validation of the model errors (Breiman 2001). Overfitting is considerably reduced as OOB errors are averaged over hundreds of trees. RF models perform best with a small to moderate number of observations but up to millions of predictor columns. The principal strengths of RF are in spotting outliers/anomalies, discovering data patterns, identifying important predictors, and predicting future outcomes (Breiman 2001).

Generalized Path Seeker Model (GPSM)

Generalized Path Seeker (known in the literature as GPS but here it will be GPSM since Global Positioning System has the same acronym) is a flexible regression and logistic binary modeling approach. Some of the principal benefits of using GPSM over other models is its simplicity in design and speed (Friedman 2012). GPSM is well-suited to handle models built with more predictor columns then observation records, highly correlated predictors (colinearity), and finding a compact model with good performance. The GPSM algorithm is a forward stepping model that builds linear regressions that are additive and cannot discover on its own nonlinear relationships or interactions without the help of an analyst. Three principle strategies are employed in GPSM: Ridge, Lasso and Compact (Friedman 2012). Ridge functions by optimally shrinking the coefficients, preventing any coefficient from reaching an unreasonable value while still retaining overall model quality and keeping all predictor variables. Lasso also shrinks the coefficients but it selects variables for either inclusion or exclusion from the model.

Finally, compact attempts to use as few of the predictor variables as possible. The response variable mean square error is successively lowered through the addition of predictors until an optimal model is achieved (**Figure AB20**). One weakness is that the GPSM algorithm does not handle missing values and will enforce row deletions to compensate for missing predictor values.

Regression

The Salford Systems Regression algorithm uses a traditional forward, stepwise least squares regression. In this algorithm the best predictor variable is found and introduced to the model and a traditional linear regression is built. Subsequently, another variable is chosen and added that best improves the coefficient of determination. Each variable available is added until either there are no predictor variables remaining or they no longer improve the coefficient of determination.
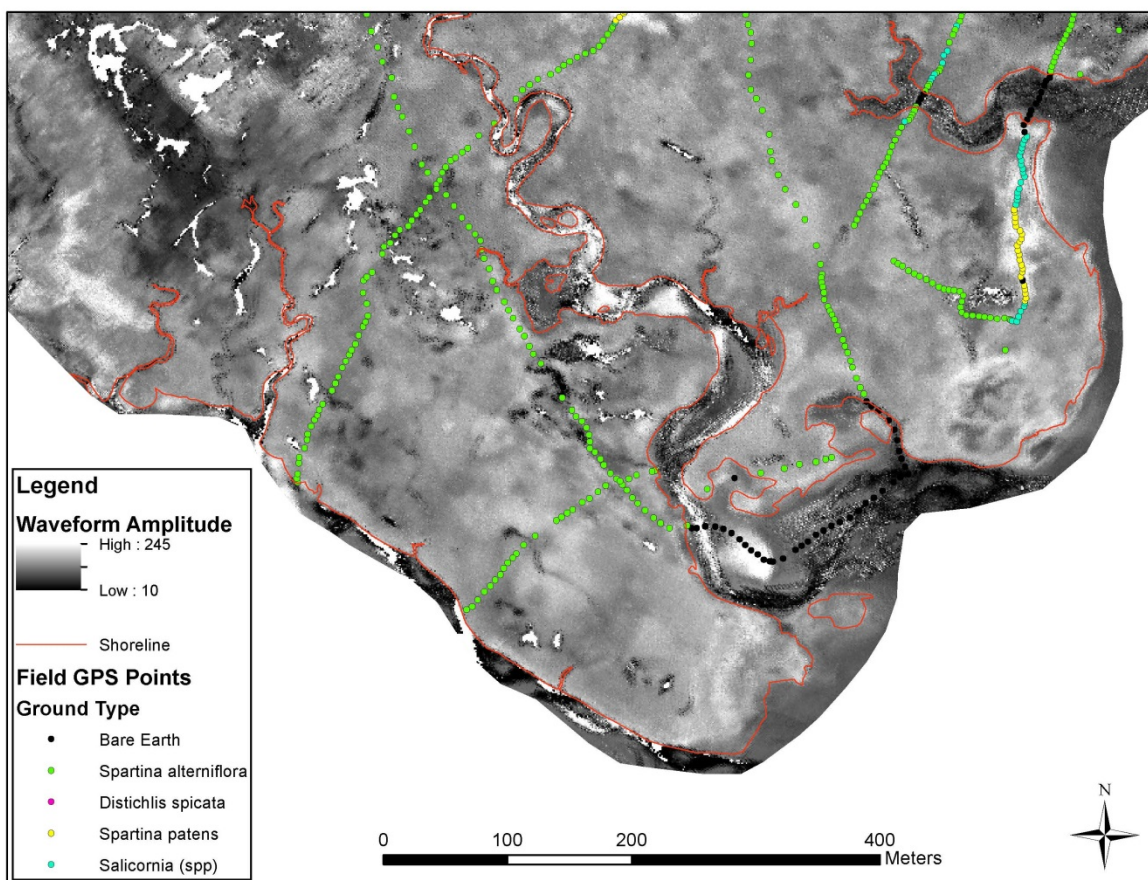
Figure AB1: Predictor variable waveform amplitude interpolated to a 1 m grid for Moors Marsh.
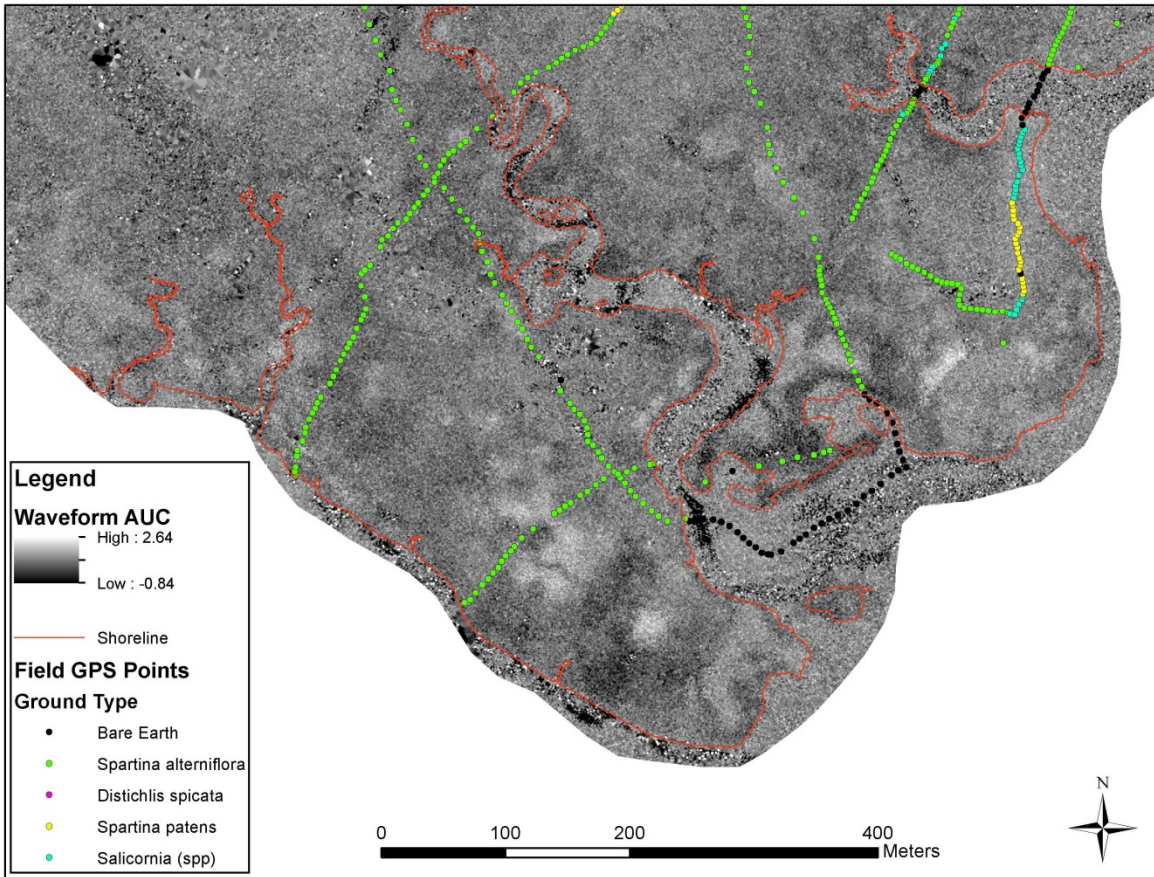
Figure AB2: Predictor variable waveform area-under-the-curve interpolated to a 1 m grid for Moors Marsh.
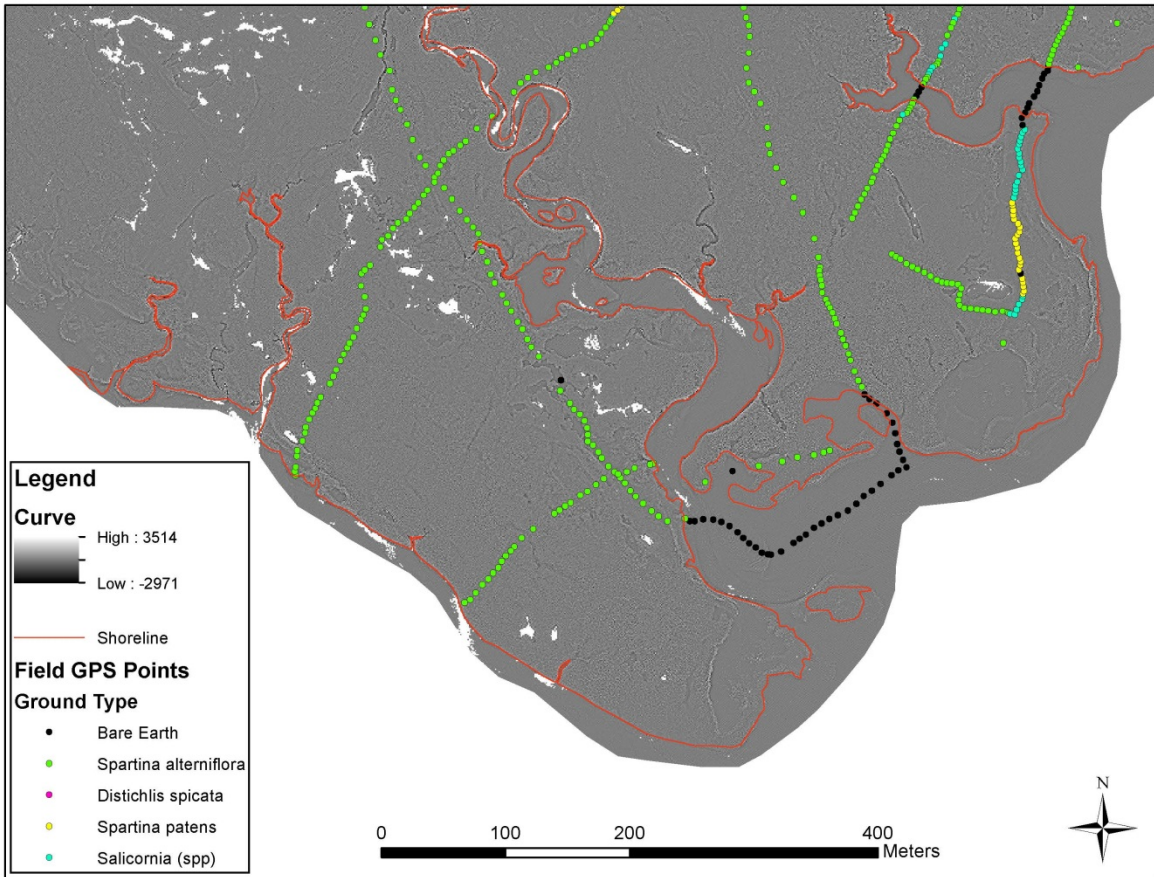
Figure AB3: Predictor variable surface curvature interpolated to a 1 m grid for Moors Marsh.
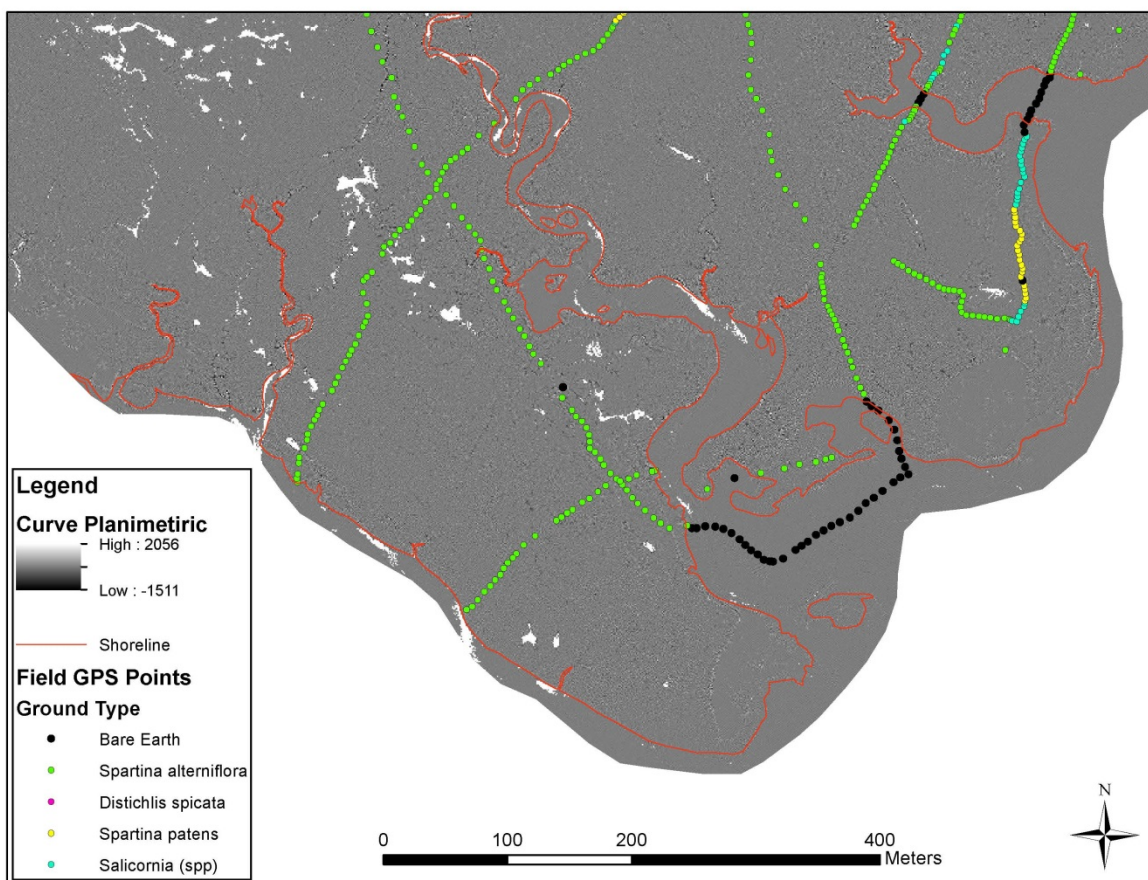
Figure AB4: Predictor variable surface planimetric curvature interpolated to a 1 m grid for Moors Marsh.
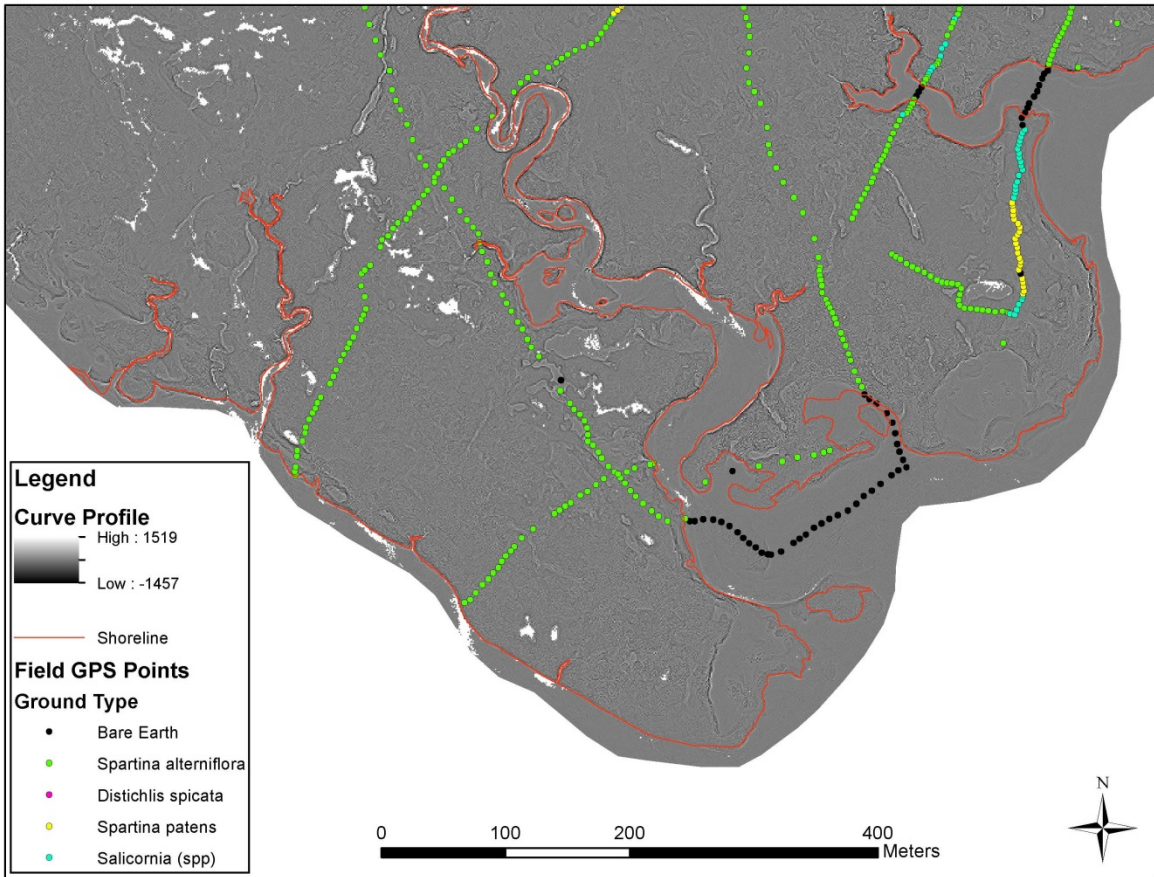
Figure AB5: Predictor variable surface profile curvature interpolated to a 1 m grid for Moors Marsh.
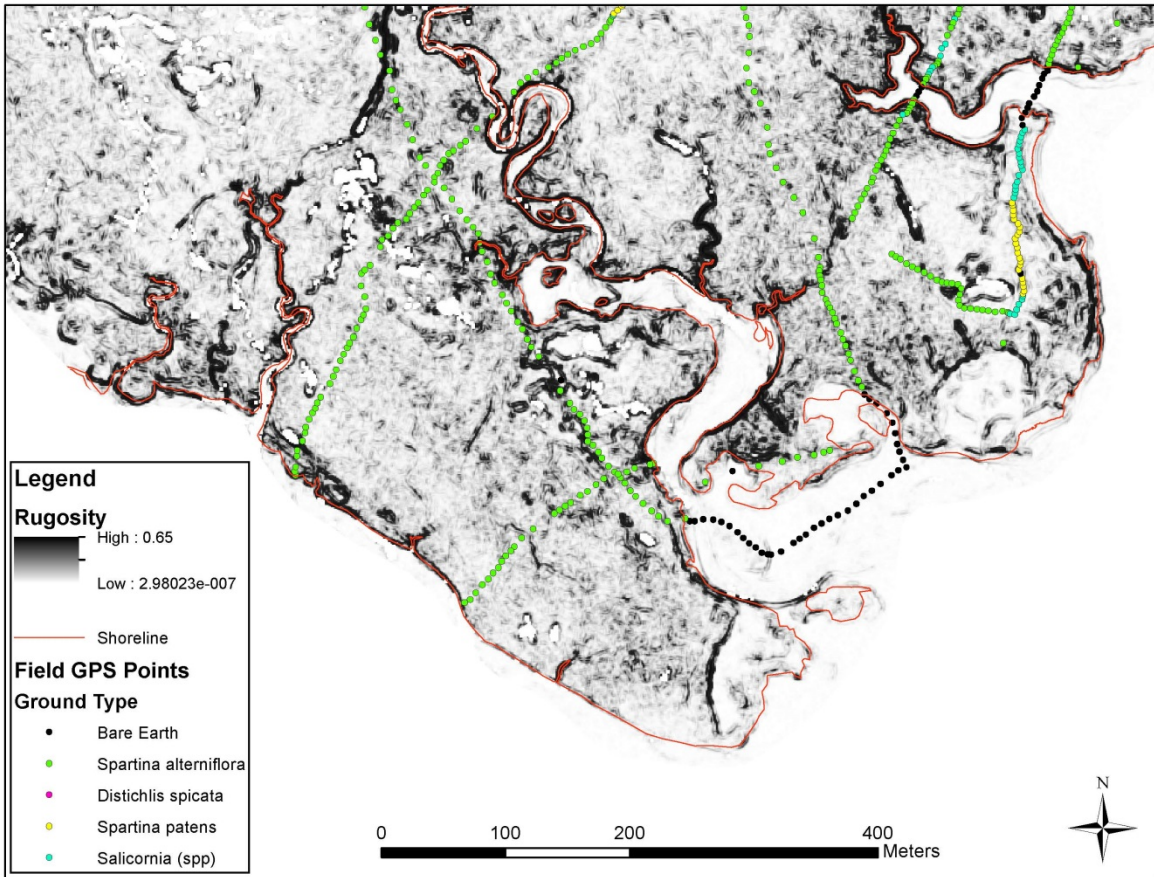
Figure AB6: Predictor variable surface rugosity interpolated to a 1 m grid for Moors Marsh.
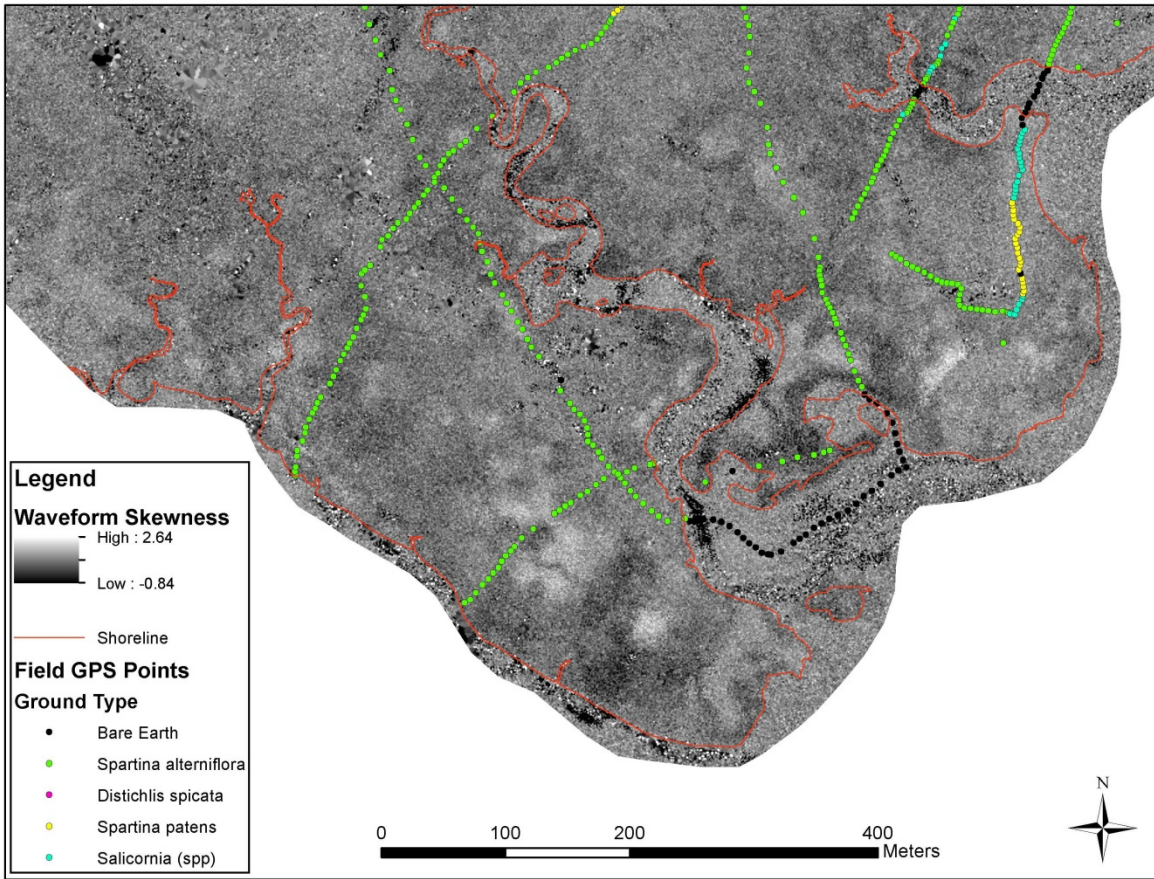
Figure AB7: Predictor variable waveform skewness interpolated to a 1 m grid for Moors Marsh.
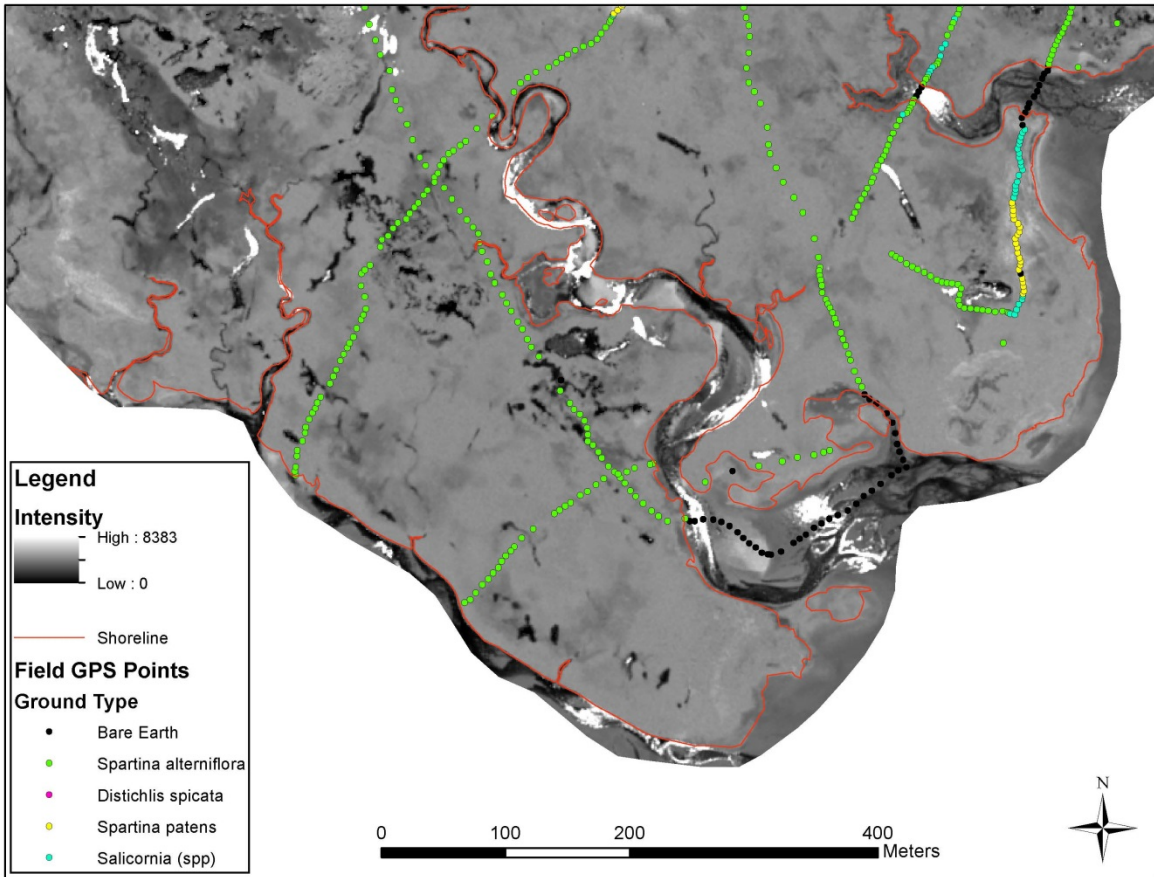
Figure AB8: Predictor variable discrete lidar intensity interpolated to a 1 m grid for Moors Marsh.
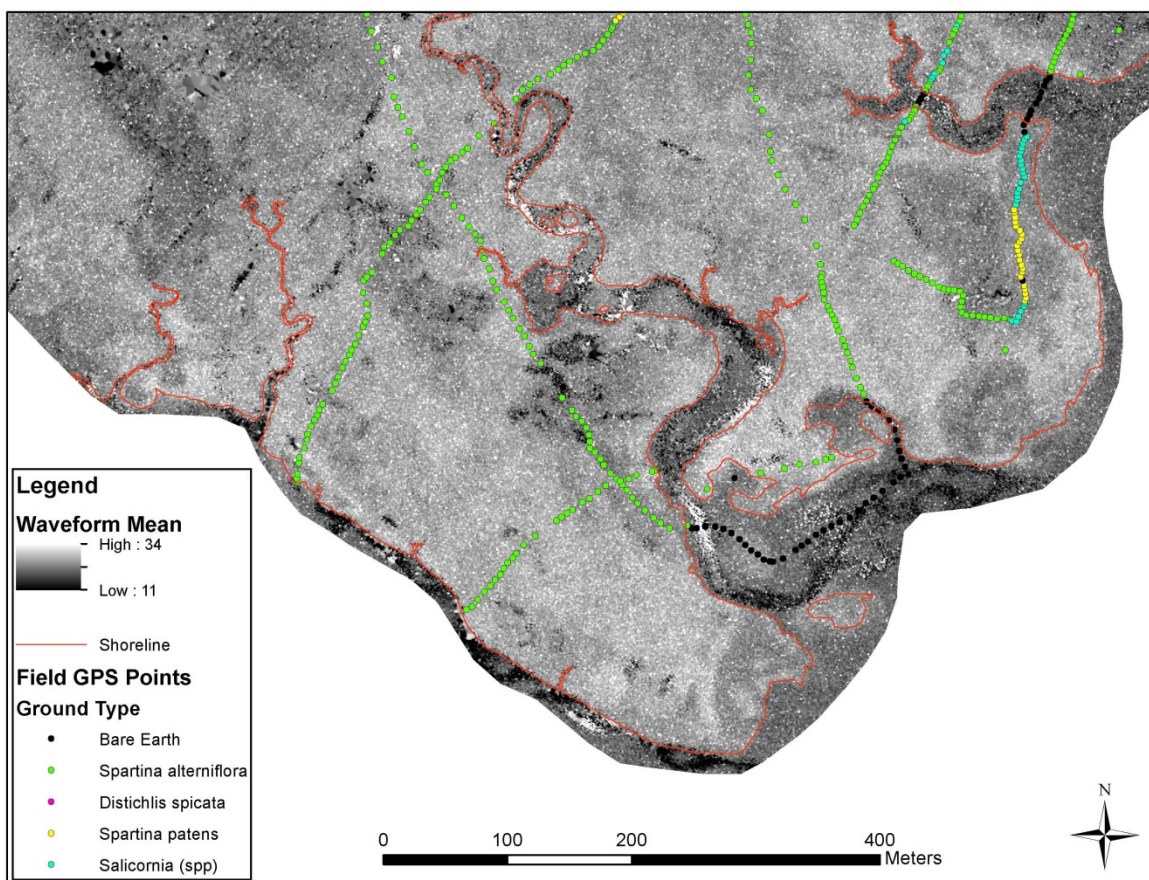
Figure AB9: Predictor variable waveform mean interpolated to a 1 m grid for Moors Marsh.
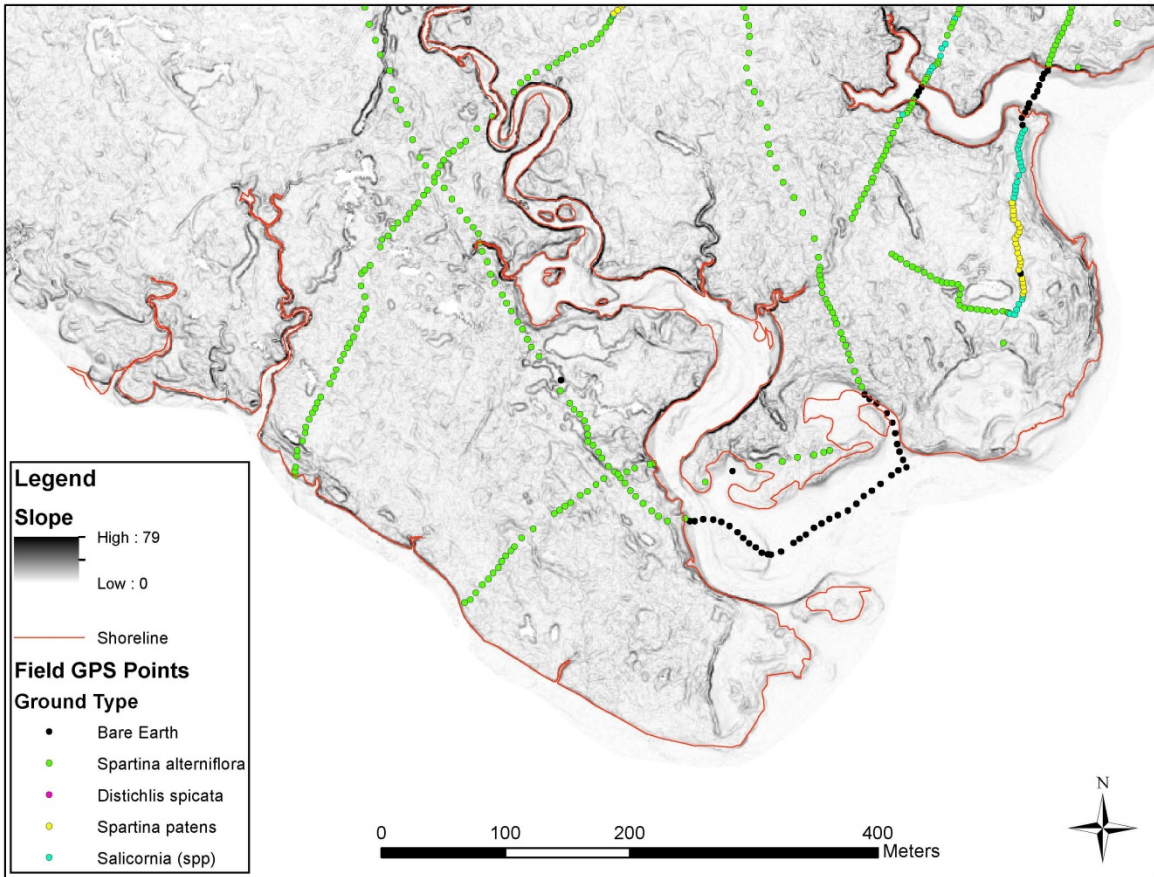
Figure AB10: Predictor variable surface slope interpolated to a 1 m grid for Moors Marsh.
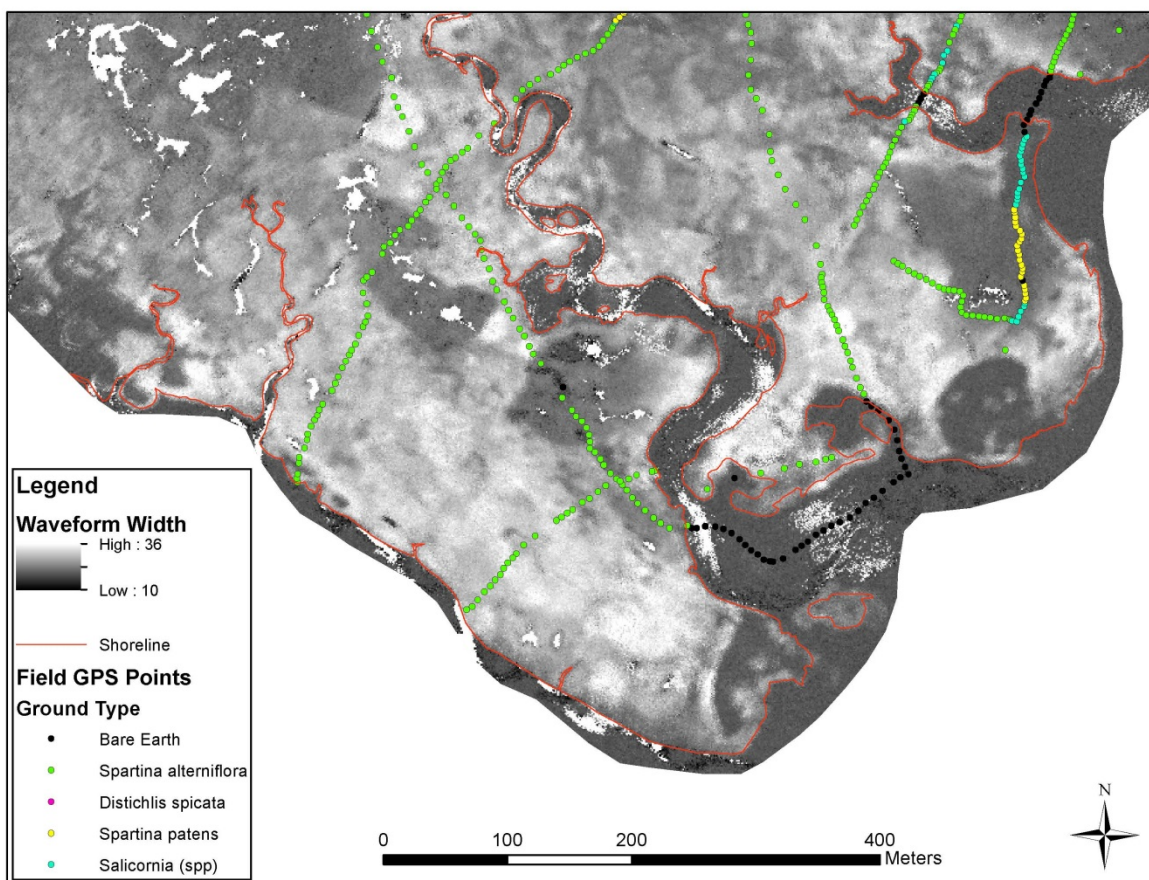
Figure AB11: Predictor variable waveform width interpolated to a 1 m grid for Moors Marsh.
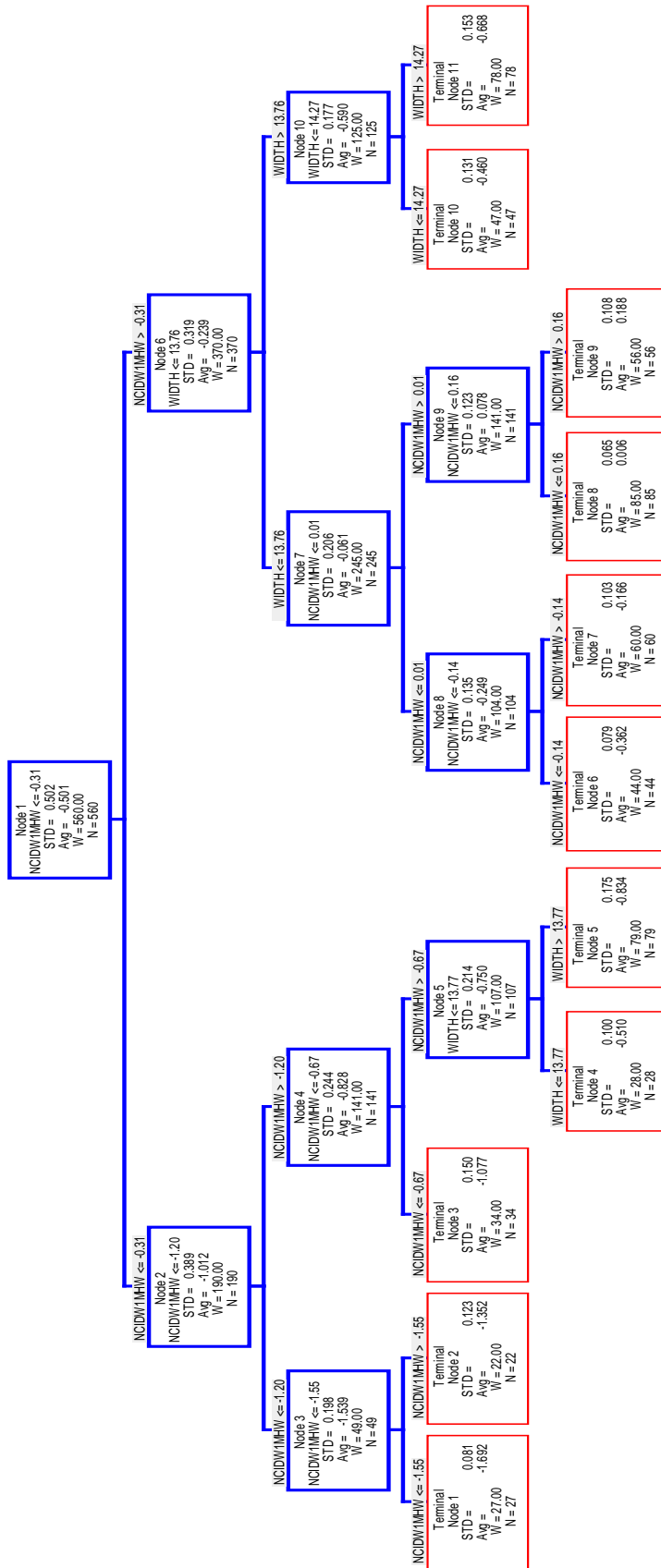
Figure AB12: Regression trees from CART elevation correction model. Each successive split refines the regression. The variables are as follows: NCIDWMHW = elevation in mean high water and WIDTH = waveform width. N is the number of samples in the node, STD is the standard deviation of the N sample and AVG is the average. The optimal model was found to have 11 nodes.
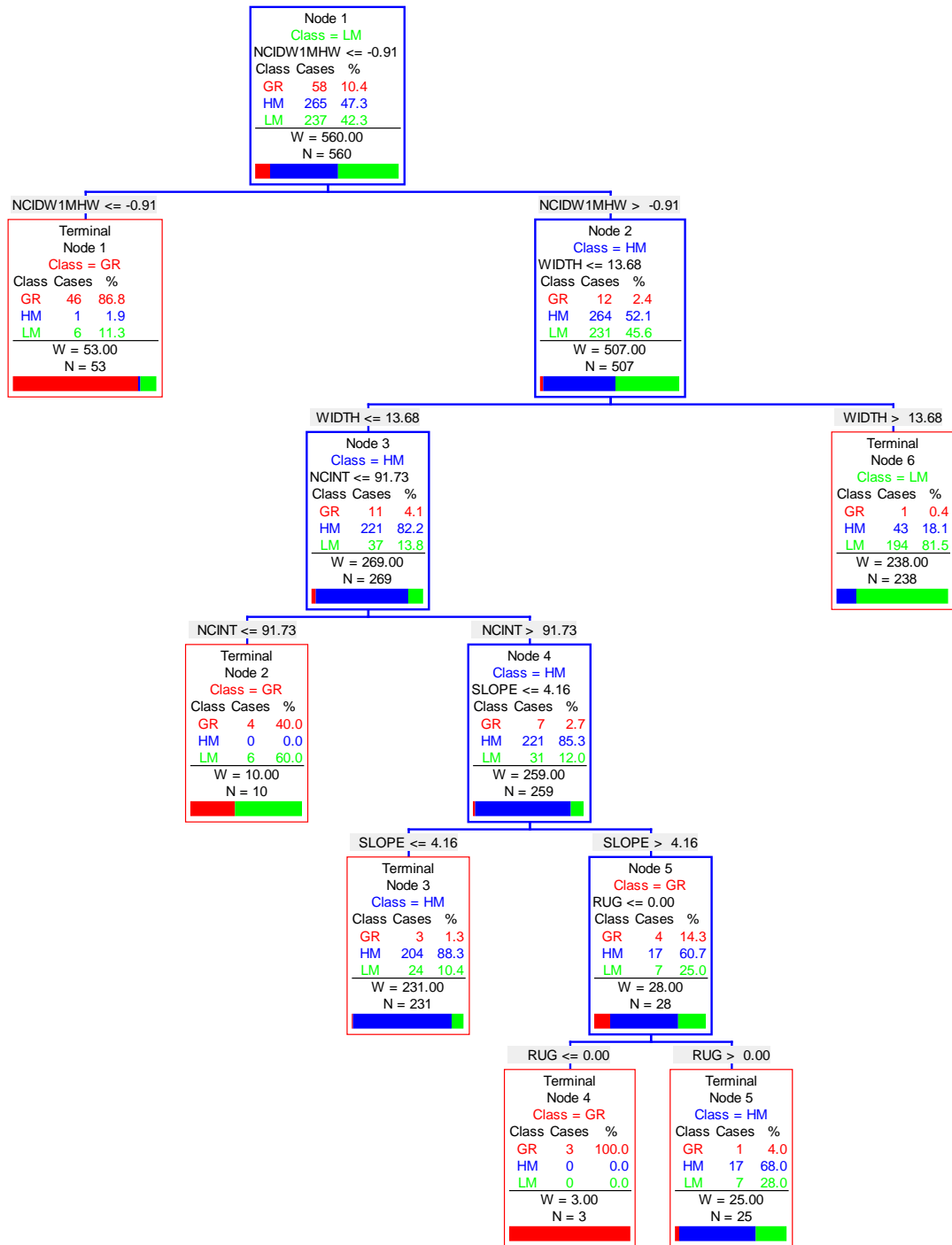
Figure AB13: CART classification trees for vegetation zone model. Each successive split refines the classification into three classes ("GR" ground - red, "HM" high marsh – blue, and "LM" low marsh – green). The variables are as follows: NCIDWMHW = elevation in mean high water, WIDTH = waveform width, NCINT = lidar intensity, SLOPE = ground slope, and RUG = rugosity. N is the number of samples in the node, "cases" are the subset of N that have been placed in the class followed by its percentage of N at that node. The optimal model was found to have 6 nodes.
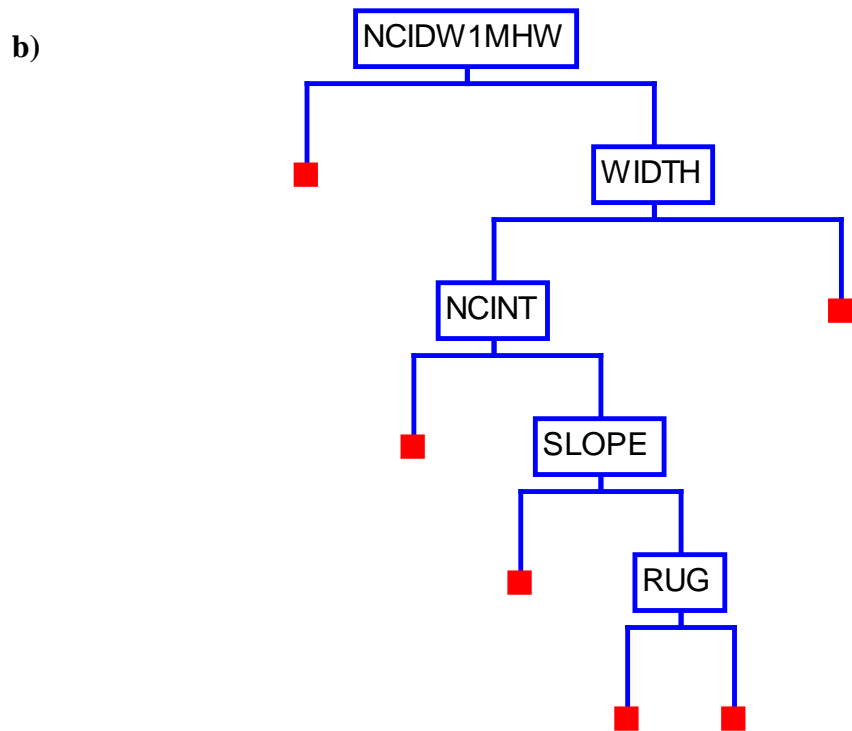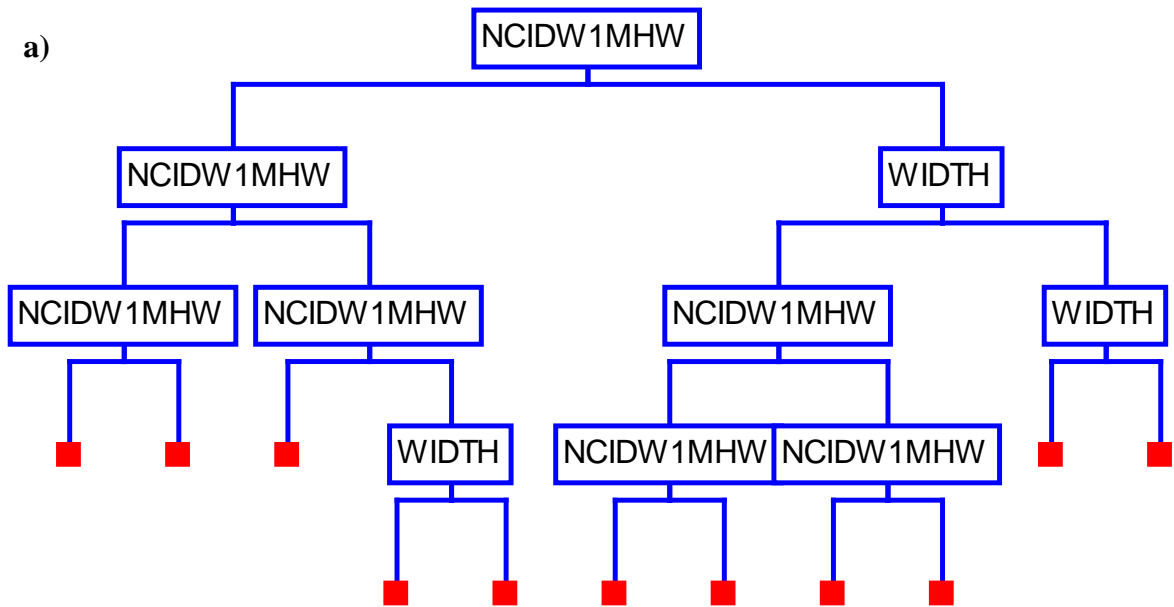
Figure AB14: a) CART regression tree model splitter variables. b) CART classification tree model splitter variables. These diagrams are simplified versions of figures AB1 and AB2, respectively, without the split values and number of samples.

```
BF1  = max(0, NCIDW1MHW + 0.3516);
BF2  = max(0, -0.3516 - NCIDW1MHW);
BF3  = max(0, WIDTH - 13.1143);
BF6  = max(0, 0.3113 - NCIDW1MHW) * BF3;
BF7  = max(0, CURVE - 16);
BF8  = max(0, 16 - CURVE);
BF9  = max(0, WIDTH - 14.3601);
BF10 = max(0, 14.3601 - WIDTH);
BF11 = max(0, WIDTH - 13.4489) * BF1;
BF12 = max(0, 13.4489 - WIDTH) * BF1;
BF13 = max(0, SKEW - 0.072488) * BF9;
BF15 = max(0, 0.00318962 - RUG) * BF9;
BF16 = max(0, RUG - 1.16415E-010);
BF17 = max(0, DISTANCE - 41.2531) * BF10;
BF19 = max(0, SLOPE - 1.40682) * BF16;
BF22 = max(0, 0.00206113 - RUG) * BF3;
BF25 = max(0, NCIDW1MHW + 0.5929) * BF9;
BF28 = max(0, 20.2412 - MEAN) * BF9;
BF34 = max(0, -0.4287 - NCIDW1MHW) * BF7;
BF38 = max(0, 19.4165 - MEAN) * BF3;
BF39 = max(0, AMP - 10);

Y = -0.459127 + 1.11029 * BF1 - 0.956923 * BF2 - 0.437193 * BF3
              + 0.147079 * BF6 + 0.00179318 * BF8
              + 0.671852 * BF9 - 0.370747 * BF11
              - 0.432482 * BF12 - 0.996613 * BF13
              - 135.885 * BF15 - 0.00207991 * BF17
              - 0.394268 * BF19 + 40.2244 * BF22
              + 0.427146 * BF25 - 0.136851 * BF28
              - 0.0362495 * BF34 + 0.0461106 * BF38
              + 0.000439638 * BF39;

MODEL ELEVMHW = BF1 BF2 BF3 BF6 BF8 BF9 BF11 BF12 BF13 BF15 BF17
                BF19 BF22 BF25 BF28 BF34 BF38 BF39;
```
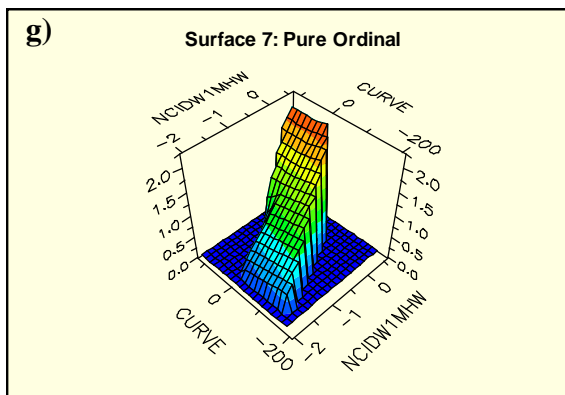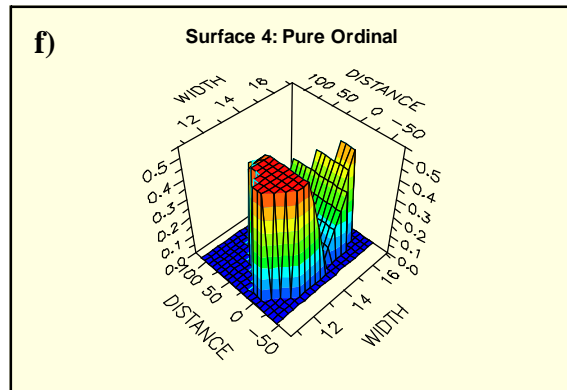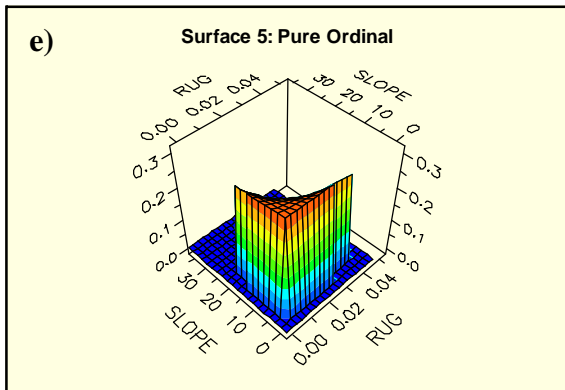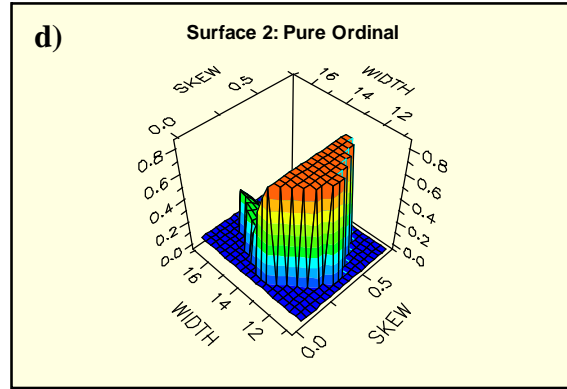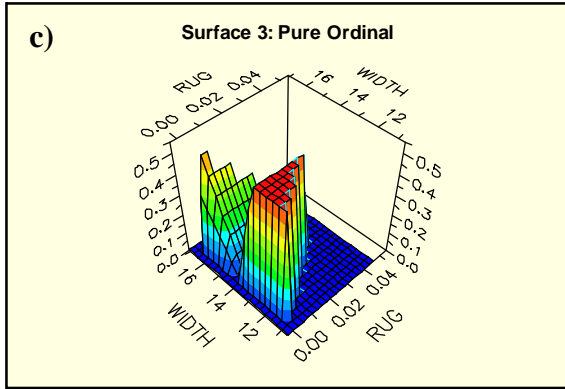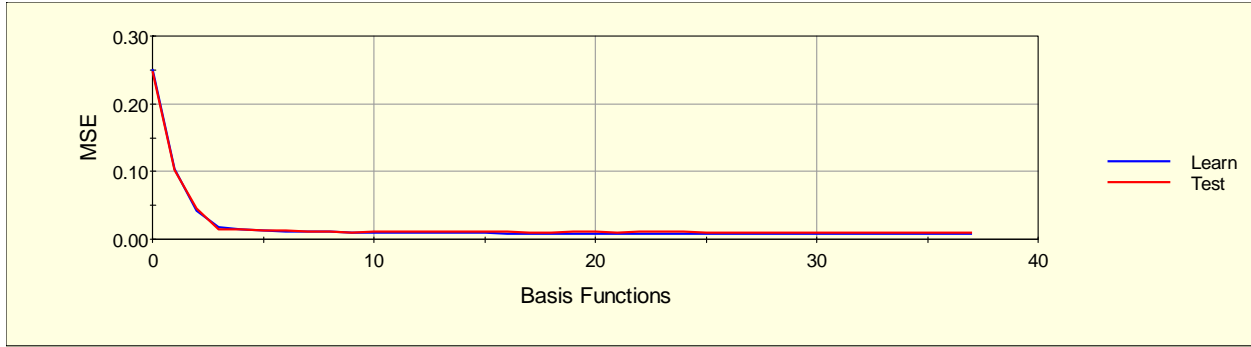
Figure AB15: MARS regression basis functions of the elevation correction model. MARS is the only model used in this study that creates a formula that is similar to a traditional regression equation.
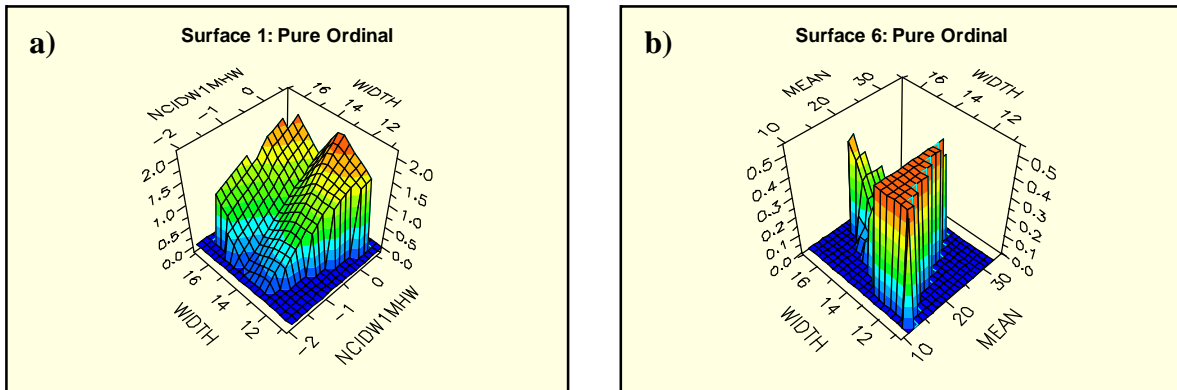

Figure AB16: Graphical representations of MARS regression basis functions from the elevation correction model. Each three dimensional graph (a-g) represents an interaction between variables. The contribution to the model is measured in the y axis and the scale varies from graph to graph. a) waveform width and elevation in mean high water. b) waveform width and waveform mean;
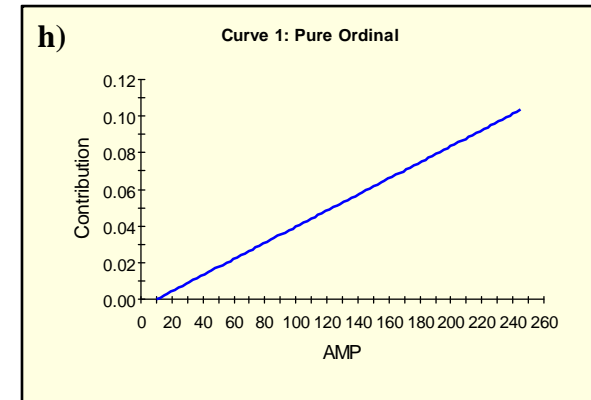
Figure AB16: Graphical representations of MARS regression basis functions from the elevation correction model. Each three dimensional graph (a-g) represents an interaction between variables. The contribution to the model is measured in the y axis and the scale varies from graph to graph. c) waveform width and surface rugosity; d) waveform width and waveform skewness; e) surface slope and surface rugosity; f) distance from shoreline in meters and waveform width; g) surface curvature and elevation in mean high water; h) waveform amplitude with no interaction terms.
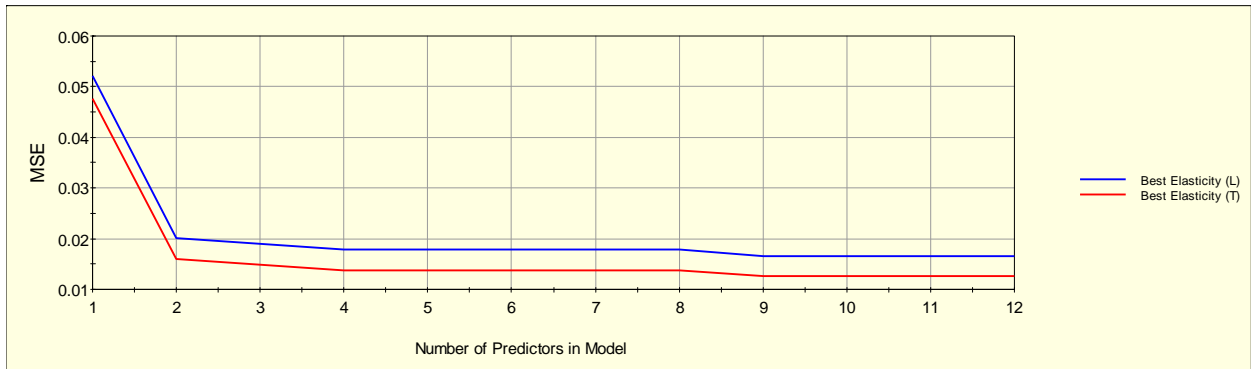
Figure AB17: MARS regression elevation correction model Mean Square Error (MSE) curve as a function of the number of basis function. The blue line is the learn sample (n = 560) and the red line is the model performance on the independent test sample (n = 225). In this model the learn and test samples are almost completely overlapping with an optimal model have 18 basis functions.
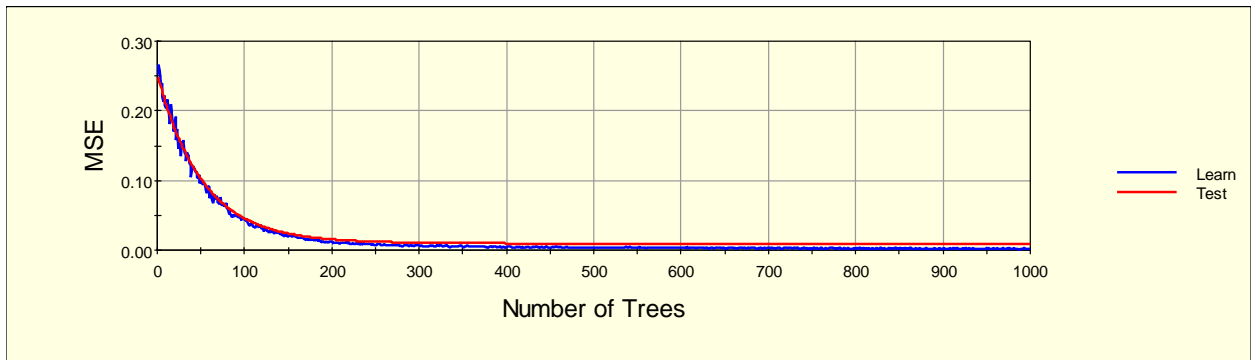
Figure AB18: TreeNet regression elevation correction model Mean Square Error (MSE) curve as a function of the number of trees built. The blue line is the learn sample (n = 560) and the red line is the model performance on the independent test sample (n = 225). In this model the the learn and test samples are almost completely overlapping with an optimal model having 772 trees.
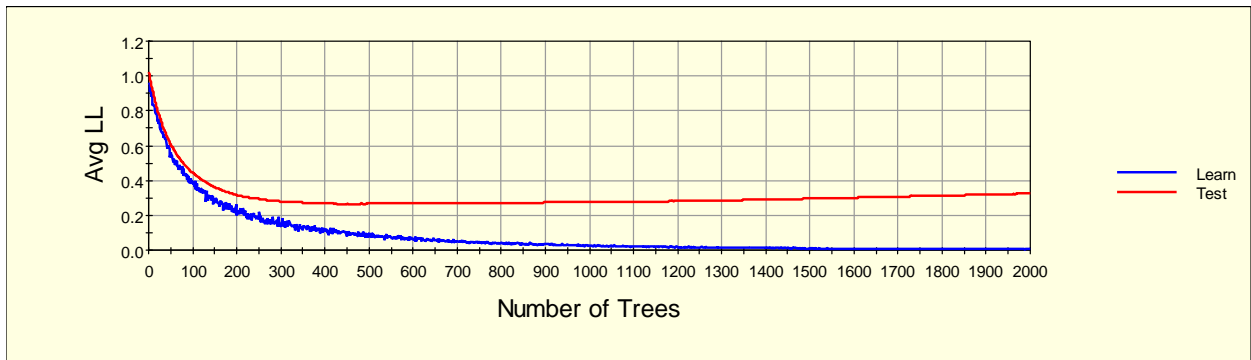
Figure AB19: TreeNet classification of vegetation zones average negative log likelihood (AvgLL) curve as a function of the number of trees built. The blue line is the learn sample (n = 467) and the red line is the model performance on the independent test sample (n = 191). In this model the learn and test samples slightly diverge with an optimal model having 470 trees.

244

Figure AB20:   GPSM regression elevation correction model Mean Square Error (MSE) curve as a function of the number of predictors. The blue line is the learn sample (n = 560) and the red line is the model performance on the independent test sample (n = 225). In this model the two slightly offset with the test data performing better than the model based on the learn sample with an optimal model using 9 predictors.

APPENDIX C

GLOSSARY OF UNCERTAINTY-RELATED TERMINOLOGY

Various terms related to lidar elevation uncertainty are used throughout this dissertation. This appendix defines these terms, as used in this work. While it is recognized that no universally-accepted, standard terminology exits and that other works define many of these terms differently, the goals in choosing terminology were to: 1) adhere, to the extent feasible, with usage in recognized standards documents, such as those of the International Standards Organization (ISO) and the American Society of Mechanical Engineers (ASME); and 2) to be self-consistent.

Accuracy – nearness to truth (generally a qualitative concept). Where the term accuracy is used in this dissertation, it usually refers to an empirical accuracy assessment (i.e., a comparison against GNSS ground truth), which contrasts to a stochastic uncertainty assessment, based on probability distributions.

Bias – the mean elevation residual from an empirical assessment (comparison against ground control), defined as:

$$\text{bias} = \mu = \frac{\sum_{i=1}^{N} \Delta Z_i}{N}$$

Elevation residual – also called "vertical difference" or "vertical error," an elevation residual is defined in this dissertation as the difference between a lidar-derived elevation at a particular

246

location and a corresponding reference or "ground truth" elevation, typically obtained by GNSS. Elevation residual is denoted by ΔZ and calculated as follows:

$$\Delta Z = Z_{lidar} - Z_{GPS}$$

Error – the difference between the (theoretically unknowable) "true" value of a quantity and its measured value. Errors can be categorized as systematic and random. Since the true value can never be known, the exact error can also not be known.

Root mean square error (RMSE) – perhaps better termed the root mean square residual (as used here), the RMSE is given by:

$$RMSE = \left[\frac{\sum_{i=1}^{N}(\Delta Z_i)^2}{N}\right]^{1/2}$$

For large N, it is expected that the following relationship will hold:

$$RMSE^2 \approx \mu^2 + \sigma^2$$

Standard deviation – quantifies the dispersion of the lidar residuals about the field surveyed data. Standard deviation is given by:

$$\sigma = \left[\frac{\sum_{i=1}^{N}(\Delta Z_i - \mu)^2}{N-1}\right]^{1/2}$$

Uncertainty – an estimate of the limits of error in a measured or computed quantity. Uncertainty estimation is typically based on probability distributions. Standard uncertainty refers to the uncertainty expressed as a standard deviation. Expanded uncertainty refers to uncertainty expressed at other confidence intervals, such as U_{95}, corresponding to the 95% confidence interval. Component uncertainties can be random or systematic.